

**School of Engineering
PhD Thesis**

Laser Curing of Inks for Plastic Electronic Applications

Thesis submitted in accordance with the requirements of the University
of Liverpool for the degree of Doctor in Philosophy

By

Liwei Fu

September 2014

Laser Engineering Group

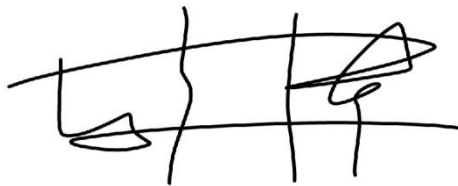
Centre for Materials and Structures
School of Engineering
University of Liverpool
UK



UNIVERSITY OF
LIVERPOOL

Declaration

I hereby declare that my thesis, entitled "Laser Curing of Inks for Plastic Electronic Applications", has not been submitted for any degree, diploma, or other qualification. This thesis is my own work and contains nothing which is the outcome of work done in collaboration with others, except as specified in the text and acknowledgements.

A handwritten signature in black ink, consisting of several loops and a horizontal line across the middle.

Signed: _____

Date: 18/09/2014

Abstract

The development of the plastic electronics industry has drawn great interest and inspired technology innovations in a broad area. This has stimulated the rapid development of flexible circuitry manufacturing technologies, including advances in conductive inks, printing technology and most importantly the novel curing technology - laser based curing (or Laser Direct Write). This has the ability to replace the conventional environmentally damaging and time consuming chemical etching method in current Printed Circuit Board (PCB) manufacturing.

The work presented in this thesis is an investigation into a frequency doubled Nd:YAG laser curing process of epoxy-based micro-sized particulate silver inks. This 532nm laser curing process filled the gap as no research reported for solidifying conductive microparticle silver ink using this particular laser wavelength at 532nm. This 532nm laser curing process also extended the curing technology with a fast localized heating process.

The composition of the epoxy-based conductive silver ink was studied in this investigation. The laser wavelength of 532nm was selected as the silver microparticles can absorb the laser energy more efficiently without the risk of damaging the material compared to infrared wavelength. Liquid-phase epoxy-based particulate silver inks deposited on flexible substrates were irradiated by laser beam at the wavelength of 532nm. This produced a smooth and cured ink with an effectively reduced electrical resistivity.

A new laser curing mechanism theory was proposed based on the presented experimental research. 532nm has shown benefits in protecting the flexible substrate used from thermal damage, owing to the high transmittance of the wavelength through the substrate material. Unlike massive solvent evaporation observed in CO₂ laser curing at 10.6 μ m, laser curing at 532nm, transported the solvent component by expelling solvent liquid from the ink system as a result of a radical change in solvent dynamic viscosity at an increased temperature and the

molecular excitation followed by the Marangoni effect. Chemical cross-linking reactions to resin system were evidenced by Fourier Transform Infrared Spectroscopy (FTIR), resulting in a fully cured ink with reduced electrical resistivity.

Epoxy-based silver ink's physical properties such as density, thermal conductivity were mathematically defined based on a new temperature evolution for use in a 3-D finite element (FE) modelling. A Time-dependent solver was chosen for modelling the thermal field in a 532nm laser curing process of epoxy-based conductive silver ink within COMSOL Multiphysics 4.3b. The modelling results were compared to the experimental thermal images for FE model validation. The impact to laser curing results by changing the absorption of the epoxy-based conductive silver ink was investigated in this FE model.

Acknowledgement

I would like to thank everyone who has supported and encouraged me during my PhD. In particular I would like to thank the following people.

Firstly, I would like to thank my supervisors Dr Geoff Dearden and Dr Stuart Edwardson, as well as my previous supervisor Prof. Ken Watkins, for their unwavering support, advice and guidance during my studies and researches in Liverpool's Laser Engineering group, in particular assisting me with resources, and helping me for theory development, as well as Finite Element (FE) modelling process. Without their support and encouragement this Thesis would never have come about. Thank you all.

I would like to thank Dr Eamonn Fearon, for his constant support in assisting my PhD, in particular his expertise and invaluable suggestion in supporting and guiding my theory development, as well as experiment optimization. I would also like to express my appreciation for his advice, encouragement during my research at Liverpool, thank you.

Thanks must also go to Dr Walter Perrie, and Mr Doug Eckford for their invaluable advice and support in both theory development and experiment set-up.

I thank Dr Andrew Fogg and Dr Jennifer Nicholls in Chemistry department of the University of Liverpool for their expertise in the help of supporting resin chemical cross-linking theory, running FTIR analysis and interpreting FTIR spectrograms.

I would also like to thank Dr Tim Joyce at Nano Investigation Centre at Liverpool University (NiCaL) for his expertise in the help of running SEM and EDX analysis.

I would also like to thank Gwent Electronic Materials, Ltd. (GEM) and Goodfellow for supplying material and helping out with resources.

I would also like to thank Dr Shuo Shang, Dr Taku Sato, Dr Khairilhijra Khirotdin, Dr Zheng Kuang, Dr Dun Liu, Dr Wei Zhang, Dr Jian Cheng, Dr Paul Fitzsimons, Dr Oliver Allegre, Dr Dan Wellburn, Dr Jonathan Griffiths, Mr Yang Jin, Mr Lingyi Ye, Mr Jinglei Ouyang, Miss Ghazal Sheikholeslami, and everyone, past and present, in this lovely Laser Engineering group at Liverpool, thank you all for offering help, joy and fun during my time at Liverpool.

Finally I would like to thank my mom and dad, thank you both for your constant support, encouragement and always offering warm hugs whenever I met difficulties. Without your constant support and encouragement I would never have made this achievement. I love you all.

List of Symbols

Symbol	Description	SI Unit
λ	Wavelength	nm
κ	Thermal conductivity	$\text{JK}^{-1}\text{m}^{-1}\text{s}^{-1}$
ρ	Electrical resistivity	$\text{Ohm}\cdot\text{m}$
v	Velocity	m/s
R	Electrical resistance	Ohm
ℓ	Length	m
I_0	Maximum intensity	Wm^{-2}
w_0	Gaussian peak width	m
Q	Heat source	J
c	Specific heat capacity	$\text{JKg}^{-1}\text{K}^{-1}$
C	Heat capacity	JK^{-1}

List of Figures

Figure 2.1: A typical continuous ink jet (CIJ) printing system [2.8].	6
Figure 2.2: A demonstration shows that the ink breaks up into drops as a result of Rayleigh instability [2.6].	7
Figure 2.3: Kodak's stream inkjet technology increases the printing efficiency by deploying an array of ink jet printing heads [2.9].	8
Figure 2.4: A printing head from a typical thermal-based Drop on Demand (DOD) printer [2.5].	9
Figure 2.5: Illustration of the printing process in a typical piezoelectric-based Drop on Demand (DOD) printer [2.8].	10
Figure 2.6: A micro-battery fabricated by a piezoelectric-based Drop on Demand (DOD) printer [2.11].	11
Figure 2.7: A typical aerosol jet [®] system developed by Optomec [2.14].	11
Figure 2.8: An example shows the micro deposition capability of writing 60 μm Ag lines over a 500 μm trench, by using an Optomec aerosol jet [®] system [2.15].	12
Figure 2.9: A typical Laser Chemical Vapour Deposition (LCVD) process [2.19].	13
Figure 2.10: SEM images of silicon wires deposited on polysilicon (a,d) and silicon dioxide (b,c) surfaces using the LCVD technology [2.22].	14
Figure 2.11: A typical Laser Induced Forward Transfer (LIFT) working process [2.26].	15
Figure 2.12: Polystyrene microbead (PS- μbead) microarrays are transferred from the support onto substrate by Laser Induced Forward Transfer (LIFT) technology with a pulsed laser energy at 2.25J $\cdot\text{cm}^{-2}$ (scare bar: 100 μm) [2.27].	16
Figure 2.13: A typical material deposition process for Matrix Assisted Pulsed Laser Evaporation Direct Write (MAPLE DW) technology [2.36].	17
Figure 2.14: A sample of temperature sensor application was produced by using Matrix Assisted Pulsed Laser Evaporation Direct Write (MAPLE DW) technology (a), and (b) shows the sample can respond to applied heat [2.35].	18
Figure 2.15: A typical Focused Ion Beam (FIB) technology where the metal ions are directly deposited on to the substrate [2.37].	19
Figure 2.16: nScrypt printing head with a dispensing tip [2.40].	20
Figure 2.17: A sample produced by using nScrypt technology shows clean ends at each starting/stopping point [2.39].	20
Figure 2.18: Variation in flow rate of material from the dispensing tip with gap between the tip and substrate [2.38].	21
Figure 2.19: A typical Dip-Pen Nanolithography (DPN) process which can deposit molecules on to the substrate [2.44].	22
Figure 2.20: An example of printing a Jefferson Nickel image on the surface of a probe chip by using the Dip-Pen Nanolithography (DPN) technology [2.45].	22

Figure 2.21: A typical structure for Nanofountain Pen (NFP) (a) where nano-pipette is used as the dispensing tip (b) [2.46].	23
Figure 2.22: Ferritin proteins are deposited on a silicon dioxide substrate using the Nanofountain Pen (NFP) technology (a), where (b) and (c) shows magnified view of area A and area B in (a), respectively [2.50].	23
Figure 2.23. Illustration of a typical screen printing process [2.64].	25
Figure 2.24. Silver nanoparticle (NP) ink track samples made by screen printing technology with different mesh of the screen. The electrical resistivity of 400 mesh ink track after heat treatment at 200°C for 5 min is measured as 180 $\mu\text{O}\cdot\text{cm}$, nearly ~ 100 times the resistivity of the bulk silver [2.65].	26
Figure 2.25. The progresses in screen mesh in screen printing technology, where the more holes of the screen per square inch (mesh), the finer the mesh and hence the better printing quality can be achieved [2.66].	27
Figure 2.26. Advanced 3-D structure of crystalline silicon solar cell created by screen printing (right) can increase efficiency for its narrower line width and thicker structure, to overcome the shadowing problem caused by conventional thinner lines (left) [2.67].	27
Figure 2.27. A typical relationship between percolation concentration (x-axis) and the percolation probability (y-axis) [2.69].	29
Figure 2.28. A cross-sectional illustration of a conductive joint after cure showing an example of the formation of one big conductive cluster that electrically connects the ink [2.74].	30
Figure 2.29. Size distributions of silver microparticles in ink used in Roberson et al.'s research [2.68].	32
Figure 2.30. Electrical resistivity is a function of silver content, as experimentally investigated by Faddoul et al., with all ink samples on alumina substrate (ink1 $\sim 70\%$ Ag, ink2 $\sim 72.5\%$ Ag, ink3 $\sim 75\%$ Ag, ink4 $\sim 77.5\%$ Ag, C1075 $\sim 85\%$ Ag) cured in Oven with a heating temperature at 700°C for 15 min [2.76].	32
Figure 2.31. Results for Ohmic curing different silver micro particle inks on Polyimide substrate [2.77].	33
Figure 2.32. Electrical resistivity of cured Cu micro-particle ink samples with one-part resin (a), and with two-part resin (b). Conventional oven curing results (heating temperature $\sim 150^\circ\text{C}$) were compared [2.86].	34
Figure 2.33. The melting point temperature of gold particles is a function of particle size, which was investigated and plotted by Buffat et al. in 1976 [2.83].	35
Figure 2.34. Illustration of the necking formation during the sintering process for 0.8 μm Ag particles at 700°C [2.87].	35
Figure 2.35. Illustration for electrical resistivity as a function of sintering time for different sintering temperature for silver nano-particle ink ($\sim 40\text{nm}$) [2.93].	36
Figure 2.36. Sintering comparison between conventional thermal sintering with various temperatures (a), and time-reduced 532nm laser based sintering process (b) [2.94].	38

Figure 2.37. Comparison of electrical resistivities of silver nano-particle ink on PI substrate by Ar+ laser at 488nm and by Laser Diode laser at 980nm [2.97].	39
Figure 2.38. Comparison of electrical resistivity values achieved by laser sintering gold nano-particle ink on different substrate materials at 514nm at laser output power of 0.4W (a), and 0.8W (b) [2.84].	40
Figure 2.39. Electrical resistivity for silver nano-particle ink (~20-30nm) as a function of plasma sintering power and sintering time, the temperature for plasma sintering power working on 150W were measured less than 70°C [2.90].	41
Figure 2.40: In Liverpool's LA-DW method, the ink is dispensed on top of the PET by using a doctor blade method (a) to form an ink track shape (b) [2.51].	43
Figure 2.41: A SYNRAD® CO ₂ laser processing workstation used in LA-DW investigation [2.51].	43
Figure 2.42: Electrical Resistance of ink track as a function of the curing speed [1.3].	44
Figure 2.43: A Towards a Wireless Aircraft (TaWA) demonstrator shows antennas which were cured onto a foam wing by a CO ₂ laser of the existing Liverpool's LA-DW process [2.52].	45
Figure 2.44: Substrate and ink track can be damaged as a result of extensive heat caused by laser irradiations at an infrared wavelength [2.52].	45
Figure 2.45: Laser curing mechanism of LA-DW at 10.6µm [2.52].	46
Figure 2.46: Temperature evolution as a function of total heat input during the LA-DW curing process at 10.6µm [2.51].	47
Figure 2.47: Absorbance spectrum of silver and gold particles [2.54].	49
Figure 2.48: Absorbance spectrum of PET polymer substrate, the red curve labelled '0 minutes' can be treated as a clean PET substrate as it has not been irradiated by UV irradiations [2.55].	50
Figure 2.49: Both UV and infrared wavelengths can cause damage to polymer substrate, leaving the visible wavelength as a suitable range for curing functional materials on polymer substrate [2.58].	51
Figure 3.1: Goodfellow® PET film used in this investigation.	55
Figure 3.2: Illustration shows D58 silver ink composition by weight percentage (Data from Gwent Electronic Materials, Ltd. (GEM)).	57
Figure 3.3: A typical SEM image of silver flakes used in D58 conductive silver ink.	58
Figure 3.4: A BMI® Lyra 100/60 frequency doubled Nd:YAG laser with wavelength at 532nm.	60
Figure 3.5: A isel® automation's CNC controlled working stage.	61
Figure 3.6: The experimental set-up for curing a conductive silver ink track using a Nd:YAG DPSS laser and CNC controlled working stage.	61
Figure 3.7: Illustration of laser beam scanning path.	62
Figure 3.8: Laser output power for Nd:YAG laser used in this investigation is a function of laser driving currents.	63
Figure 3.9: Illustration of the SYNRAD® CO ₂ laser marker system in experiment.	64
Figure 3.10: A SYNRAD® CO ₂ laser marker with DH scanning head.	64

Figure 3.11: A memmert® SM100 drying cabinet used in this investigation.	65
Figure 3.12: Temperature comparisons between temperature measured by a Type-K thermocouple and temperature measured by a thermometer of the Oven.	65
Figure 3.13: Fisher Scientific® FB15001 heating magnetic stirrer.	66
Figure 3.14: A silver ink track sample prepared by screen-printing method.	67
Figure 3.15: Illustration shows the sequence of Liverpool laser group's doctor blading method. (a) Equipment for doctor blading method, (b) PET substrate was covered by two layers of masking tape, (c) A negative track shape image was carved by a knife along internal edges of the stencil, (d) The carved tape was peeled off for followed printing process, (e) A scraper was used for printing epoxy-based conductive silver ink along the negative track shape image, (f) A finished epoxy-based conductive silver ink track, and (g) A finished epoxy-based conductive silver ink track with masking tape removed.	68
Figure 3.16: The Veeco®'s WYKO NT1100 white light interferometer used in this investigation.	69
Figure 3.17. The working principle of WYKO white light interferometer working in vertical scanning interferometry (VSI) mode [3.10].	70
Figure 3.18: The four-point probes configuration in this investigation.	72
Figure 3.19: Illustration of the working principle of the four-point probe method for measuring resistivity.	72
Figure 3.20. The finite width correction factor f_2 as a function of d/S , a linear extension line within the domain $[0, 2]$ is reproduced for the ease of the calculation of f_2 within this domain [3.8].	75
Figure 3.21. A WYKO interferometer measurement shows the thickness of the D58 silver ink track cured in oven at 110°C for 1 hour.	77
Figure 3.22: A conductive silver ink track was measured by Elcometer® 501 pencil hardness tester for Wolff-Wilborn hardness test to measure ink track hardness property.	79
Figure 3.23: Illustration of the hardness index marked on graphite pencils, from the lowest hardness index 6B (1) to the highest hardness index 6H (14).	79
Figure 3.24: FLIR® SC 660 IR camera used in this investigation (a), a typical IR image recorded for curing the D58 conductive silver ink track at the speed of 5mm/s under Nd:YAG laser irradiations with laser output power at 17.94W is shown in (b).	80
Figure 3.25. Working principle of a typical IR camera [3.12].	80
Figure 3.26. Experimental set-up for measuring emissivity of D58 silver ink.	81
Figure 3.27. Temperature recording of the black tape.	82
Figure 3.28. Emissivity adjustment and calibration for D58 silver ink, the temperature value should be kept a same reading of that measured from the black tape in Figure 3.27.	82
Figure 3.29. Dynamic temperature comparisons between temperature measured by an IR camera and temperature measured by a Type-K thermocouple.	85
Figure 3.30. Working principle for SEM based on electron secondary irradiation [3.13].	86
Figure 3.31: A FEI Phenom™ desktop SEM system used in this investigation.	87

Figure 3.32. JEOL's JSM-6610 SEM with x-ray detector fitted in Liverpool's NiCaL.	87
Figure 3.33. Sample can be exposed to infrared beam due to Attenuated Total Reflectance (ATR) for a FTIR measurement [3.15].	88
Figure 3.34: PerkinElmer® Spectrum 100 Spectrometer used in samples' FTIR measurement (The FTIR measurements were carried out in Department of Chemistry, the University of Liverpool).	89
Figure 3.35: A typical FTIR sample analysis procedure [3.4].	89
Figure 4.1. D58 epoxy-based silver ink can be cured (a), undercured (b), or overcured (c).	93
Figure 4.2: The electrical resistance of the ink track as a function of laser working parameters and the laser scanning pass, showing how the multiple-pass scanning method can significantly reduce the electrical resistance pass by pass.	96
Figure 4.3: Electrical resistivity comparisons for ink track samples cured by CO ₂ laser (red triangles) at 10.6µm and Nd:YAG laser (green dots) at 532nm	99
Figure 4.4. Electrical resistivity of laser cured D58 silver ink track samples as a function of effective laser energy density per unit scanning pass.	101
Figure 4.5: Electrical resistivities for oven cured D58 ink track samples.	102
Figure 4.6: Hardness Index comparisons for ink track samples cured by CO ₂ laser (red triangles), and 532nm Nd:YAG laser (green dots).	103
Figure 4.7: Hardness Index comparisons for oven cured D58 ink track samples.	104
Figure 4.8: SEM cross-sectional images with 1000x magnification on the left, and 5450x magnification on the right for: CO ₂ laser cured ink track sample (a), (b); 532nm Nd:YAG laser cured sample (c), (d); and oven cured sample (e), (f), respectively.	106
Figure 4.9. EDX spectrums for D58 silver ink track samples cured by CO ₂ laser at 10.6µm (a), Nd:YAG laser at 532nm (b), and oven (c).	107
Figure 4.10. Carbon and Oxygen content in D58 silver ink for different curing processes.	109
Figure 4.11. Thermogravimetric analysis (TGA) graph of uncured D58 silver ink shows the mass loss as a function of curing temperature, investigated by Sato [2.52].	110
Figure 4.12. Silver content in D58 silver ink for different curing processes.	111
Figure 4.13: Temperature profiles for D58 conductive silver ink track samples irradiated by CO ₂ (red triangles) laser at 10.6µm and Nd:YAG (green dots) laser at 532nm. A window for suitable working parameters is given between resin cross-linking temperature at around 90°C (gray) and the PET melting temperature at 260°C (yellow).	113
Figure 4.14. Curing window for curing D58 silver ink.	114
Figure 4.15. Demonstration of the PET substrate materials which were not entirely burnt through by infrared wavelength by CO ₂ laser at 10.6µm (pictures were not taken with the same scale).	119
Figure 4.16. the width of damage on PET substrate as a function of CO ₂ laser working parameters, measured by a WYKO measurement.	119
Figure 4.17. Electrical resistivity of laser cured laser curable D5 silver ink track samples as a function of effective laser energy density per unit scanning pass.	122

Figure 4.18. Electrical resistivity of laser cured graphite doped D5 silver ink track samples as a function of effective laser energy density per unit scanning pass.	124
Figure 5.1: Surface temperature comparisons for D58 silver ink components - silver flakes.	128
Figure 5.2: Surface temperature comparisons for D58 silver ink components - resin complex.	128
Figure 5.3: Surface temperature comparisons for D58 silver ink components - organic solvent.	129
Figure 5.4: Surface temperature comparisons for D58 silver ink components - silver flakes (blue), resin complex (green), and organic solvent (red).	130
Figure 5.5. The reflectance of silver, for laser irradiation at 532nm, the reflectance of silver is at ~95% [5.11].	131
Figure 5.6: Illustration for silver flakes rising up temperature during the laser curing process due to Geometric scattering and laser beam multiple reflections among silver flakes within the D58 ink. ·	131
Figure 5.7: Illustration of the experimental set-up to investigate solvent removal theory.	132
Figure 5.8: Experimental set-up for solvent removal investigation, which can represents the conditions by which the solvent removal mechanism in D58 silver ink system during thermal-based laser curing process at the wavelength of 532nm.	133
Figure 5.9: Sequence of captured images showing the evolution of solvent transport at 40°C.	134
Figure 5.10: Sequence of captured images showing the evolution of solvent transport at 50°C.	135
Figure 5.11: Sequence of captured images showing the evolution of solvent transport at 60°C.	136
Figure 5.12: Sequence of captured images showing the evolution of solvent transport at 70°C.	137
Figure 5.13: The rate of solvent expansion against temperature and duration of heating.	138
Figure 5.14: The rate of expansion against temperature and time for solvent, BI, and epoxy resin components.	139
Figure 5.15: Illustration of how the laser beam energy excites solvent molecular movements within a D58 silver ink during the laser curing process at the wavelength of 532nm.	140
Figure 5.16: Variation in dynamic viscosity of solvent with temperature (graph reproduced based on NOAA data) [5.1].	141
Figure 5.17: Variation in dynamic viscosity of a typical two part epoxy resin with temperature [5.2].	141
Figure 5.18: Tide marks have been observed at both sides of the D2 ink, cured by 532nm laser at 7 Watts, with a curing speed at 10 mm/s for 4 scanning passes.	143
Figure 5.19. SEM images for silver ink D2 (Spectrum 2 – on track; Spectrum 1 – off track).	144
Figure 5.20. SEM images of nanoparticles carried off the track of D2 silver ink.	145
Figure 5.21. EDX Spectrum for silver ink D2 on ink track (Spectrum 2) and off track (Spectrum 1). ·	146
Figure 5.22. Illustration of the Marangoni effect during the 532nm laser curing process shows how solvent is being transported from the centre of the ink track towards to area ahead of the laser beam.	147

Figure 5.23. Illustration of the Marangoni effect during the 532nm laser curing process shows how solvent is being transported from the centre of the ink track towards to area at both sides of the laser beam.	147
Figure 5.24. Temperature within the silver ink measurement for 532nm laser curing a D58 epoxy-based silver ink (Laser Power=20W, traverse speed=15mm/s) at the middle position of the ink track by a Type-K thermocouple for the first 3 scanning passes. The high temperature measured in the first pass was observed, this was caused by a reduction in specific heat capacity of the ink due to solvent removal in area of the laser irradiation due to the Marangoni effect ahead of the laser beam irradiation.	148
Figure 5.25: Solvent watermark observed at the edge of D58 silver ink track immediately after the laser cure process – the greater amount of expelled solvent liquid seen on one side is assumed to be as a result of the operation of the fume extractor system during the laser curing process.	149
Figure 5.26: The unblocking reaction process for Blocked Isocyanates (BI).	150
Figure 5.27: Trimerization of Isocyanates to generate Isocyanurate.	150
Figure 5.28: Resin cross-linking process between Isocyanates and Epoxy resin.	151
Figure 5.29: Resin cross-linking process between Isocyanurate and Epoxy resin.	151
Figure 5.30: FTIR spectrum of resin complex with curing temperature recorded at 35°C.	152
Figure 5.31: FTIR spectrum of resin complex with curing temperature recorded at 70°C.	153
Figure 5.32: FTIR spectrum of resin complex with curing temperature recorded at 105°C.	154
Figure 5.33: FTIR spectrum of resin complex with curing temperature recorded at 160°C.	155
Figure 5.34: FTIR spectrum of resin complex with curing temperature recorded at 180°C.	156
Figure 5.35: FTIR spectrum of resin complexes shows two increasing peaks at 1681cm^{-1} and 1739cm^{-1} are observed for samples with increased curing temperatures (blue:35°C green:70°C light yellow:105°C brown:160°C red:180°C).	158
Figure 5.36: FTIR spectrum of resin complexes shows five decreasing peaks at 830cm^{-1} , 901cm^{-1} , 1182cm^{-1} , 1241cm^{-1} and 1510cm^{-1} are observed for samples with increased curing temperatures (blue:35°C green:70°C light yellow:105°C brown:160°C red:180°C).	160
Figure 6.1: The structure of modules in COMSOL Multiphysics FE modelling software [6.2].	164
Figure 6.2: FE Modelling strategy [6.3].	164
Figure 6.3: Drawing of the temperature evolution as a function of overall heat input for Nd:YAG laser curing a D58 silver ink track at the laser irradiation wavelength of 532nm.	166
Figure 6.4: Dynamic absorbance of D58 silver ink is a function of an increasing temperature.	171
Figure 6.5: Dynamic density of D58 silver ink is a function of an increasing temperature.	172
Figure 6.6: Dynamic specific heat capacity of D58 silver ink is a function of an increasing temperature.	173
Figure 6.7: Dynamic thermal conductivity of D58 silver ink as a function of temperature.	175
Figure 6.8: Interface of COMSOL Multiphysics 4.3b.	177
Figure 6.9. FE model construction for laser curing a D58 silver ink track.	179

Figure 6.10: The meshing of the model, more nodes on the ink track than PET substrate material ensures smooth and accurate mathematical solutions can be achieved.	181
Figure 6.11. The comparison of thermal field constructed and simulated from FE modelling results (top) and the thermal data recorded by an IR camera in experiment (bottom) for D58 silver ink track in 532nm laser curing process at 3.86W, 12mm/s.	183
Figure 6.12. The comparison of thermal field constructed and simulated from FE modelling results (top) and the thermal data recorded by an IR camera in experiment (bottom) for D58 silver ink track in 532nm laser curing process at 10.95W, 12mm/s.	184
Figure 6.13. The comparison of thermal field constructed and simulated from FE modelling results (top) and the thermal data recorded by an IR camera in experiment (bottom) for D58 silver ink track in 532nm laser curing process at 17.94W, 12mm/s.	185
Figure 6.14. The comparison of thermal field constructed and simulated from FE modelling results (top) and the thermal data recorded by an IR camera in experiment (bottom) for D58 silver ink track in 532nm laser curing process at 17.94W, 8.33mm/s.	186
Figure 6.15. The comparison of thermal field constructed and simulated from FE modelling results (top) and the thermal data recorded by an IR camera in experiment (bottom) for D58 silver ink track in 532nm laser curing process at 3.86W, 5mm/s.	187
Figure 6.16. The comparison of thermal field constructed and simulated from FE modelling results (top) and the thermal data recorded by an IR camera in experiment (bottom) for D58 silver ink track in 532nm laser curing process at 17.94W, 5mm/s.	188
Figure 6.17. Temperature evolution result in the middle position of the ink track from the FE model for 532nm laser curing the D58 epoxy-based silver ink over the processing time of 4 passes.	189
Figure 6.18. Temperature evolution result in the middle position of the ink track from the FE model for 532nm laser curing the D58 epoxy-based silver ink over the processing time of 4 passes.	190
Figure 6.19. Curing temperature comparison between modelling results and experimental data. ..	192
Figure 6.20. Modelling results of temperature evolution in the middle of the ink track of the D58 epoxy-based silver ink over the laser scanning time for four scanning passes.	194
Figure 6.21. Modelling results of temperature evolution in the middle of the ink track of the D58 epoxy-based silver ink over the laser scanning time for four scanning passes.	195
Figure 6.22. Electrical resistivity comparison between derived data from the FE model and the experimental measurement.	196
Figure 6.23. An example of the thermal field modelled from the FE model of 532nm laser curing of a D58 epoxy-based silver ink track with the laser output power at 17.94W, and the laser traverse speed at 5mm/s. This shows the temperature distribution surrounding the laser beam. The cooler temperature surrounding the laser beam can result in the Marangoni effect removing the liquid solvent component out of the ink system towards both sides of the ink track and ahead of the laser beam prior to the laser beam irradiation, which fits well to the mechanism theories discussed in Chapter 5.	197

Figure 6.24. Temperature evolution graphs in the middle of the ink track for a repeating 532nm laser curing process in this FE model can only predict the thermal field property, it needs improvement to predict the optimized number of scanning passes to suggest a fully cured situation. 199

Figure 6.25. Thermal field modelled (top) and the temperature evolution graph in the middle of the ink track of the laser curing process (bottom) for 4 passes from the FE model for initial D58 silver ink (Laser power=12.972W, scanning speed=8mm/s). 201

Figure 6.26. Thermal field (top) and the temperature evolution graph in the middle of the ink track of the laser curing process (bottom) for 4 passes modelled from the FE model for silver ink with absorbance to laser energy at 0.52. 202

Figure 6.27. Thermal field (top) and the temperature evolution graph in the middle of the ink track of the laser curing process (bottom) for 4 passes modelled from the FE model for silver ink with absorbance to laser energy at 0.61. 203

Figure 6.28. Comparison of electrical resistivities of epoxy based silver inks discussed in this thesis to the output from the FE model (this graph is reproduced based on experimental results presented in Chapter 4). As can be seen from this figure, the curing efficiency of the epoxy based silver ink can be significantly increased by (i) increasing the silver content (Laser curable Ag ink D5), or (ii) adding the optical absorbing agent (Graphite doped Ag ink D5), or (iii) increasing the overall absorption to laser energy (Ag ink modelled in the FE model). 205

List of Tables

Table 2.1. Resistivities of common materials (Silver, Copper and Gold) [2.75].....	31
Table 2.2. Commercial conductive silver ink used for Roberson et al.'s investigation [2.59, 2.102, 2.103].	31
Table 2.3. Typical prices for silver-based conductive materials (source: Sigma-Aldrich) [2.80].....	42
Table 3.1: Typical material properties of Goodfellow® PET films [3.1]	56
Table 3.2. Approximated compositions for silver inks used in this investigation. (Data from GEM) ...	57
Table 3.3: Laser output power measurement for Nd:YAG laser used in this investigation.....	62
Table 3.4: Temperature calibration measurements for memmert® SM100 Oven.....	65
Table 3.5. Emissivity calibration for different materials used in this thesis.	83
Table 4.1: D58 epoxy-based conductive silver ink track samples cured by CO ₂ laser at 10.6µm.....	92
Table 4.2: D58 epoxy-based conductive silver ink track samples cured by Nd:YAG laser at 532nm. ..	92
Table 4.3: D58 epoxy-based conductive silver ink track samples cured by Oven.	93
Table 4.4: Electrical resistance measured for 532nm Nd:YAG laser curing D58 epoxy-based silver ink track samples at 15mm/s with multiple laser scanning passes.	95
Table 4.5. Electrical resistivity comparison of D58 epoxy-based silver microparticle ink after cure. ..	99
Table 4.6: D58 conductive silver ink track samples cured by CO ₂ laser at 10.6µm.	100
Table 4.7: D58 conductive silver ink track samples cured by Nd:YAG laser at 532nm.....	100
Table 4.8. Elemental analysis in D58 ink.....	108
Table 4.9. Elemental composition in D58 silver ink	108
Table 4.10. Investigation of damage caused to the PET substrate at infrared wavelength by CO ₂ laser at 10.6µm.....	118
Table 4.11: Laser curable D5 silver ink track samples cured by Nd:YAG laser at 532nm.	121
Table 4.12: Graphite doped D5 silver ink track samples cured by Nd:YAG laser at 532nm.	123
Table 5.1: Temperature profiles of D58 epoxy based silver ink components (silver flakes, resin complex, and organic solvent) irradiated under Nd:YAG laser beam irradiation at 532nm.	127
Table 5.2. Elemental analysis to element content in silver ink D2	145
Table 5.3: FTIR spectrum absorbance of resin complex at the wavenumber 1681cm ⁻¹ and 1739cm ⁻¹	157
Table 5.4: FTIR spectrum absorbance of resin complex at the wavenumber 830cm ⁻¹ , 901cm ⁻¹ , 1182cm ⁻¹ , 1241cm ⁻¹ and 1510cm ⁻¹	159
Table 6.1: Assumption to change-in-ink's composition below 70°C.	169
Table 6.2: Assumption to change-in-ink's composition above 70°C.....	169
Table 6.3: Laser working parameters used as the input to the FE model.	176
Table 6.4 Laser working variables used as the input to the FE model.....	176

Table 6.5: Mesh data of the FE model.	180
Table 6.6. Laser working parameters as the input into the FE model.	182
Table 6.7. Curing temperature comparison between modelling results and experimental data.	191
Table 6.8. Laser working parameters as the input into the FE model.	192
Table 6.9. Derived electrical resistivity compares to experimental measurement.	195
Table 6.10: Assumptions for different ink compositions as the input to the FE model.	200
Table 6.11. Electrical resistivity comparison for modelled results with different absorbance to laser energy.	204

Contents

Chapter 1

1. INTRODUCTION	1
1.1 Overview	1
1.2 Aim and Objectives	2
1.3 Thesis Structure Review	3

Chapter 2

2. LITERATURE REVIEW	5
2.1 Classification of Direct Writing Technology	5
2.1.1 Droplet-based Direct Writing Technology	5
2.1.1.1 Ink Jet Printing Technology	5
2.1.1.1.1 Continues Ink Jet (CIJ) Printing Technology	6
2.1.1.1.2 Drop on Demand (DOD) Printing Technology	8
2.1.1.1.2.1 Thermal-based Transducer DOD Printing Technology	9
2.1.1.1.2.2 Piezoelectric-based Transducer DOD Printing Technology	10
2.1.1.2 Aerosol Jet® Printing Technology	11
2.1.2 Energy Beam-based Direct Writing Technology	13
2.1.2.1 Laser Beam Direct Writing Technology	13
2.1.2.1.1 Laser Chemical Vapour Deposition (LCVD)	13
2.1.2.1.2 Laser Induced Forward Transfer (LIFT)	15
2.1.2.1.3 Matrix Assisted Pulsed Laser Evaporation Direct Write (MAPLE DW)	16
2.1.2.2 Focused Ion Beam (FIB) Direct Writing Technology	18
2.1.3 Flow-based Direct Writing Technology	19
2.1.4 Tip-based Direct Writing Technology	21
2.1.4.1 Dip-Pen Nanolithography (DPN)	21
2.1.4.2 Nanofountain Pen (NFP) Technology	23
2.2 Screen Printing Technology	24
2.3 Curing and Sintering Processes	28
2.3.1 Curing for Conductive Microparticle Ink Due To Percolation Theory ...	28
2.3.1.1 Existing Research Reported for Curing Conductive Microparticle Ink	31
2.3.2 Sintering for Conductive Nanoparticle Ink	34

2.3.2.1 Existing Research Reported for Sintering Conductive Nanoparticle Ink.....	36
2.3.3 Liverpool’s Laser Assisted Direct Writing (LA-DW) Method at an Infrared Laser Wavelength of 10.6µm.....	42
2.3.3.1 Curing Mechanism of Liverpool's Laser Assisted Direct Writing (LA-DW) at an Infrared Laser Wavelength of 10.6µm	46
2.3.3.2 The Effect of Wavelength on The LA-DW Method	48
2.4 Summary of the State of the Art & Knowledge Gaps in Solidifying Conductive Inks	52
2.5 Chapter Summary	54

Chapter 3

3. EXPERIMENTAL: METHODS, MATERIALS AND APPARATUS.....	55
3.1 Substrate Material	55
3.2 Ink System.....	56
3.2.1 Introduction to Epoxy-based Silver Ink.....	56
3.2.2 Introduction to Epoxy-based Silver Ink Components	58
3.2.2.1 Silver Micro-sized Flakes.....	58
3.2.2.2 Resin Complex.....	59
3.2.2.3 Organic Solvent.....	59
3.3 Equipment.....	59
3.3.1 Experiment Equipment	60
3.3.1.1 Frequency Doubled Nd:YAG Laser System at 532nm.....	60
3.3.1.2 Other Heating Sources.....	63
3.3.1.2.1 CO ₂ Laser System at 10.6µm.....	63
3.3.1.2.2 Oven.....	64
3.3.1.2.3 Heating Plate	66
3.3.1.3 Epoxy-based Silver Ink Doctor Blading Method	67
3.3.2 Analysis Equipment.....	69
3.3.2.1 Surface Morphology Measurement of Epoxy-based Silver Ink	69
3.3.2.2 Electrical Resistivity Measurement of Epoxy-based Silver Ink	71
3.3.2.2.1 The Thickness Correction Factor, <i>f</i> ₁	74
3.3.2.2.2 The Edge correction factor, <i>f</i> ₂	74
3.3.2.2.3 An Example of Calculating Electrical Resistivity of Epoxy-based Silver Ink	76

3.3.2.3	Hardness Measurement of Epoxy-based Silver Ink	78
3.3.2.4	Infrared (IR) Camera	79
3.3.2.5	Scanning Electron Microscope (SEM) and Energy Dispersive X-ray Spectroscopy (EDX) Measurement to Epoxy-based Silver Inks	85
3.3.2.6	Fourier Transform Infrared (FTIR) Spectroscopy Examination	88
3.4	Chapter Summary	90
 Chapter 4		
4.	RESULTS: CURING OF EPOXY-BASED CONDUCTIVE SILVER LOADED INKS.....	91
4.1	Curing Results of D58 Epoxy-based Silver Ink Cured by Lasers and by Oven	91
4.2	D58 Epoxy-based Silver Ink Curing Results At 532nm with Multiple Scanning Passes.....	94
4.3	Electrical Resistivity Results	97
4.4	Hardness Results	103
4.5	Scanning Electron Microscope (SEM) and Energy-dispersive X-ray spectroscopy (EDX) analysis for Cured D58 Epoxy-based Silver Inks.....	105
4.6	Curing Window for Laser Curing D58 Epoxy-based Silver Ink.....	112
4.7	Thermal Damage to Epoxy-based Silver Ink and Polymer Substrate Material ...	115
4.7.1	Thermal Damage to Epoxy-based Silver Ink Material.....	115
4.7.2	Thermal Damage to PET Substrate Material at an Infrared Wavelength	116
4.8	Results of Curing Epoxy-based Silver Inks with Variant Ink Compositions	120
4.8.1	Increasing Laser Coupling Efficiency by an Increased Silver Concentration	121
4.8.2	Increasing Laser Coupling Efficiency by an Added-in Optically Absorbing Agent to Laser Wavelength, or Dopant	123
4.9	Chapter Summary	124
 Chapter 5		
5.	RESULTS FROM THE STUDY OF LASER CURING MECHANISMS AT THE LASER WAVELENGTH OF 532NM	125
5.1	Analysis of Epoxy-based Silver Ink Components.....	125
5.1.1	Temperature Rise in Epoxy-based Silver Ink Due To Laser Energy Primary Absorption by Silver Flakes	126
5.1.2	Solvent Transport Theory	132
5.1.2.1	Solvent Transport Mechanism.....	139
5.1.2.1.1	Solvent Molecular Excitation.....	139
5.1.2.1.2	Solvent Transport Due To The Marangoni Effect.....	142

5.1.3 Resin Complex Crosslink Due To Chemical Reactions.....	150
5.1.3.1 Crosslinking Theory.....	150
5.1.3.2 Results of Fourier Transform Infrared Spectroscopy Examination	151
5.1.4 Nd:YAG Laser Curing Mechanism Theory At The Laser Wavelength Of 532nm	161
5.2 Chapter Summary	162
 Chapter 6	
6. FINITE ELEMENT MODELLING OF EPOXY-BASED SILVER INK CURING PROCESS BY REPEATING LASER BEAM IRRADIATIONS AT 532NM	163
6.1 Overview	163
6.2 Temperature Evolution for Modelling	165
6.3 Definition for Parameters and Variables	168
6.3.1 Material Physical Parameters Definition	168
6.3.1.1 Laser Energy Absorbance of D58 Epoxy-based Silver Ink ...	170
6.3.1.2 Dynamic Density of D58 Epoxy-based Silver Ink.....	171
6.3.1.3 Dynamic Specific Heat Capacity of D58 Epoxy-based Silver Ink	172
6.3.1.4 Dynamic Thermal Conductivity of D58 Epoxy-based Silver Ink	174
6.3.2 Laser Working Parameters Definition.....	175
6.4 Boundary Conditions for FE Modelling	176
6.5 Finite Element (FE) Model Construction.....	177
6.6 Results of Finite Element (FE) Modelling.....	182
6.6.1 Finite Element (FE) Model Validation	182
6.6.2 Experiment and Mechanism Theory Verification	192
6.6.3 How Curing Results Are Affected by A Change in Laser Absorbance of the Epoxy-based Silver Ink.....	200
6.7 Chapter Summary	205
 Chapter 7	
7. CONCLUSIONS AND RECOMMENDATIONS.....	206
7.1 Summary of Results of the Investigation and Contributions of New Knowledge	206
7.2 Recommendations for Further Investigation.....	208
REFERENCES.....	210

APPENDIX 1. Procedures of calibrating the emissivity of an IR camera (Selected from the instructional manual for FLIR SC 660 Thermal Camera)	218
APPENDIX 2. Approximated calculation of proportional mass percent of carbon and oxygen elements in D58 silver ink.....	223
APPENDIX 3. Thermal Conductivity of Silver (Source: National Bureau of Standards).....	226

1. INTRODUCTION

1.1 Overview

Laser Direct Write (DW) technology is defined as the process by which functional materials are directly added to a surface in predetermined patterns and activated by laser irradiation [1.1, 1.2]. Investigations to potential applications such as printed electronics and Printed Circuit Boards (PCBs) which can be made by Laser DW technology have been carried out worldwide, as well as in the University of Liverpool [1.3]. Different Laser-based DW using technologies with a variety of laser wavelengths have been investigated in sintering conductive nanoparticle ink on variant substrate materials [2.94, 2.96-2.101], this has an advantage of protecting the substrate material by locally heating up the ink rather than heating up the whole substrate material as in the conventional Oven heating process which uses a high temperature to sinter the conductive nanoparticle ink at temperatures above the thermal damage threshold of most polymer substrates below 200°C [2.90, 2.94, 2.95]. Materials with variant geometry or with a large size or volume can be processed efficiently by using the Laser-based DW technology, avoiding some of the problems with conventional Oven heating process. In addition, the Laser-based DW can provide a more environmentally friendly processing step compared to conventional subtractive process used in PCBs manufacturing process [1.4, 1.5].

The Laser DW technology has been investigated in the University of Liverpool [2.51]. Laser Assisted Direct Write or LA-DW, was developed by using a CO₂ laser with the laser wavelength of 10.6µm for a thermal process of heating up an epoxy-based conductive silver microparticle ink. The resin complex in this epoxy-based silver ink absorbs the infrared laser irradiation at 10.6µm, causing solvent evaporation from the top surface of the silver ink and the subsequent resin complex chemical cross-linking process, in which the silver ink is made electrically conductive [1.3, 2.51]. However this LA-DW technology has its own limitation, in that early experimental work showed both silver ink and polymer substrate materials were easily damaged at the infrared wavelength [2.52]. Therefore an improved laser DW process with a

shorter wavelength is suggested to replace the current infrared laser-based curing process at 10.6 micron, and to extend the capability of the Laser DW process.

The hypothesis for this thesis was that using a laser wavelength at 532nm can process the ink while preventing thermal damage to the flexible substrate owing to the high transparency of many polymer substrates at 532nm, whereas the infrared wavelength can thermally damage the polymer substrate [1.6, 1.7]. A typical polymer substrate – Polyethylene terephthalate (PET), for example, enables PCB manufacturing development to a new market place with advantages in flexibility and a reduced weight and cost of manufacture by using flexographic processes.

1.2 Aim and Objectives

The aim of this thesis is to harness the capabilities of 532nm laser curing process as an advantageous technology for curing epoxy based silver loaded conductive inks on polymer substrate materials. The main objectives of the research project described in this thesis are:

- To identify and study the effects of the key parameters that influence thermal-based curing results of the epoxy-based conductive silver micro-sized flake ink at the laser irradiation wavelength of 532nm.
- To investigate and compare 532nm curing of the epoxy-based conductive silver micro-sized flake ink on a low cost, flexible polymer substrate such as PET to different curing techniques, such as the CO₂ laser at 10.6µm and the Oven.
- To propose and investigate theories of the thermal mechanisms involved in curing and/or consolidating the epoxy-based conductive silver micro-sized flake ink on PET polymer substrate by laser irradiation at 532nm.
- To investigate and model the relevant thermal field properties in Finite Element (FE) model for curing the epoxy-based conductive silver micro-sized

flake ink on PET polymer substrate by laser irradiations at 532nm, and to compare results predicted by the model with the experimental results.

1.3 Thesis Structure Review

The structure of this thesis is organized as follows:

Chapter 2 commences with an introduction of the relevant background on direct writing (DW) and a literature review on different direct writing technologies and their applications in industry, followed by a review of current researches in curing and sintering conductive inks reported worldwide, as well as describing the laser assisted direct write (LA-DW) technology developed by the University of Liverpool.

Chapter 3 provides an introduction to materials, equipment and experimental set-ups employed in this study. The correction factors of calculating the electrical resistivity of the conductive material as well as the calibration of the material's emissivity are discussed in this Chapter.

Chapter 4 begins with experimental studies and results to investigate process parameters which affect curing of the epoxy-based conductive silver ink and comparing three different curing methods: Nd:YAG frequency doubled laser beam irradiation at 532nm, CO₂ laser beam irradiation at 10.6 μ m, and oven thermal treatment. The benefits of multiple laser scanning passes are discussed. Experimental results are compared and discussed, and benefits for Nd:YAG frequency doubled laser curing process at 532nm are concluded based on experimental results.

In **Chapter 5**, a study of the mechanism for Nd:YAG frequency doubled laser curing of the epoxy-based conductive silver ink at 532nm is investigated. The mechanism theory development can be divided into 2 steps, in which: 1) a discussion on experimental results of laser irradiating ink components to investigate factors affecting temperature rises in the ink; and 2) a study of solvent transport theory

(solvent molecular excitation theory and the solvent Marangoni effect). Chemical reactions for resin cross-linking are discussed to develop the resin cross-linking theory. Finally the overall mechanism for Nd:YAG frequency doubled laser curing a conductive silver ink track at 532nm is summarized.

Chapter 6 focuses on finite-element modelling (FEM) to model the thermal field of the laser curing process during curing of the epoxy-based conductive silver ink by Nd:YAG frequency doubled laser irradiation at 532nm. Temperature evolution method and a modified energy equation are defined, followed by mathematical definitions exploring temperature dependent parameters of the epoxy-based conductive silver ink material. Modelling outputs are compared to experimental thermal data for FE model validation. FE model and laser curing mechanism theories are verified by the experimental results. Assumptions of changing an ink's absorption to laser energy are made, for the purpose of investigating the impact to laser curing results by changing the absorption of the epoxy-based conductive silver ink.

Chapter 7 draws conclusions on the findings of the work carried out, providing a summary of its achievements and recommending directions in which future research may proceed based on the ideas presented.

2. LITERATURE REVIEW

2.1 Classification of Direct Writing Technology

In general, Direct Writing (DW) technology refers to techniques capable of depositing different types of material over the substrate surface in 2-D or 3-D geometry [1.2]. Such techniques are extensively used in electronics applications [2.1-2.3], and have rapidly promoted a new technology revolution in manufacturing industries.

Hon *et al.* categorized direct writing techniques into four groups depending on how a functional material is being deposited [1.2], they are:

- 1) droplet-based direct writing technology,
- 2) energy beam-based direct writing technology,
- 3) flow-based direct writing technology,
- 4) tip-based direct writing technology.

2.1.1 Droplet-based Direct Writing Technology

2.1.1.1 Ink Jet Printing Technology

The development of ink printing methodology was initiated over a century ago [2.4, 2.5]. The first practical ink jet machine was invented by William Thomson in 1858 for recording telegraph messages, which was later patented in 1867 [2.6]. In 1951, Siemens developed the world first commercial ink jet printer [2.5, 2.7], which stimulated rapid developments of ink jet printing technology. Today the use of ink jet printing technology can be found in many applications, for example, in material packaging applications, label printing applications, small office and home office (SOHO) printing applications, etc.

Ink jet printing technology could be sub-divided into two main categories: Continuous Ink Jet (CIJ) printing technology based on Plateau–Rayleigh instability [2.4, 2.6]; and Drop on Demand (DOD) printing technology based on individual droplet supply as required. The difference between two inkjet printing technologies is the method used to supply ink drops out of the printing nozzle, both ink jet printing technologies are massively used in current printing industries.

2.1.1.1.1 Continuous Ink Jet (CIJ) Printing Technology

Continuous Ink Jet (CIJ) printing technology, as its name suggests, is an ink jet printing technology in which continuously flowing ink-drops out of the printing head, or nozzle, to form a non-contact printing method. Ink drops are electrically charged prior to being printed on to the paper - this can help in recycling unused inks which were not printed on substrate to the ink chamber through an ink catcher (**Figure 2.1**).

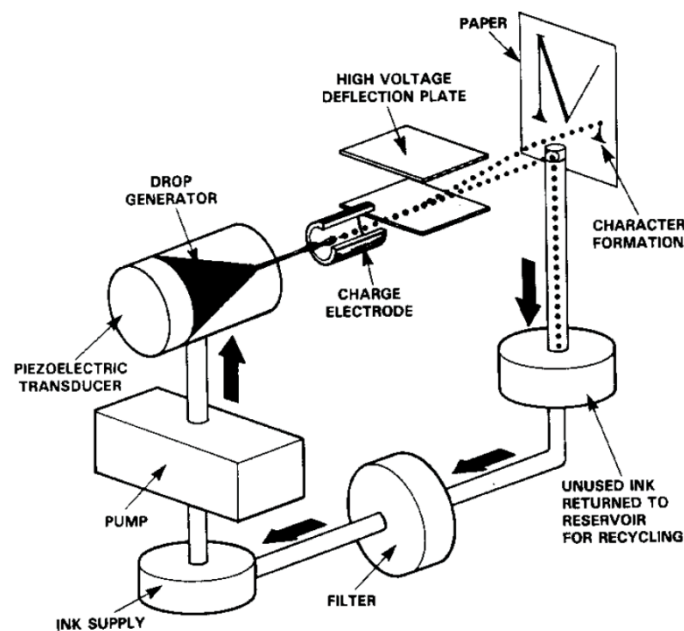


Figure 2.1: A typical continuous ink jet (CIJ) printing system [2.8].

The mechanism of CIJ printing technology is by continuously breaking up the ink into drops with a uniform geometry. This is achieved by a pressure oscillation resulting from acoustic energies being propagated from a transducer through the ink

at a high frequency (in the range of 50 kHz to 175kHz), once the mechanical vibration frequency caused by acoustic energy is equal to the ink drop formation rate, the ink stream breaks into drops of uniform mass (**Figure 2.2**). Lord Rayleigh calculated the equation in **(2-8)** for the relationship between acoustic energy vibration frequency and the ink drop formation.

$$\lambda = 4.443d \quad (2-8)$$

Where λ is the wavelength of the oscillation, and d is the jet orifice diameter. **Figure 2.2** shows the ink breaks up to ink drops due to Rayleigh instability.

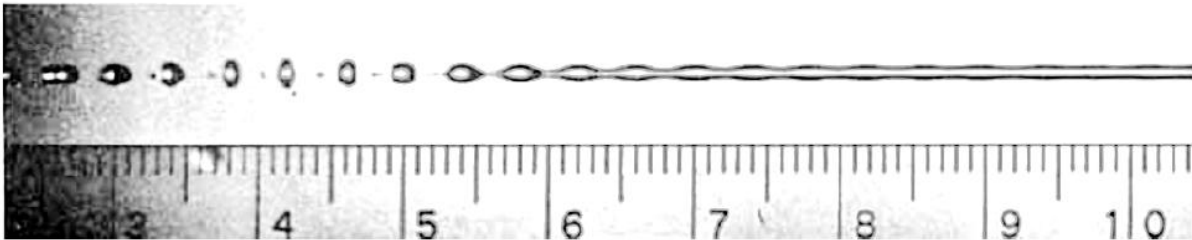


Figure 2.2: A demonstration shows that the ink breaks up into drops as a result of Rayleigh instability [2.6].

Current CIJ manufacturers include Kodak, Versamark, Domino, Imaje, etc. The overall printing quality is improved as a result of decades of technology development, an example is Stream Inkjet technology developed by Kodak. This patented technology increased the printing efficiency by deploying an array of ink jet printing heads to produce more ink drops per time (**Figure 2.3**) [2.9].

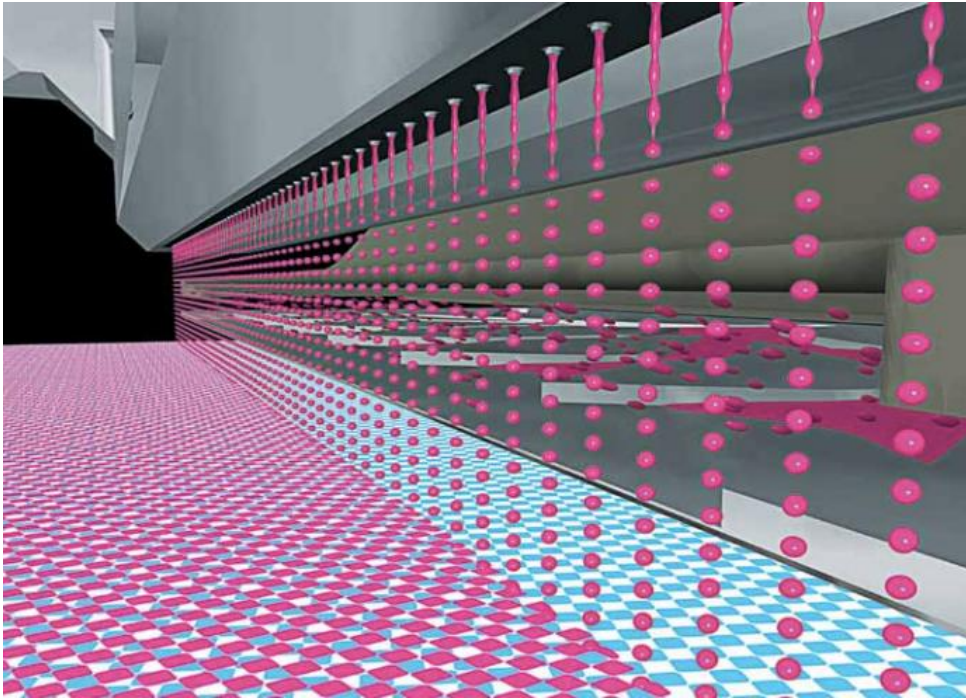


Figure 2.3: Kodak's stream inkjet technology increases the printing efficiency by deploying an array of ink jet printing heads [2.9].

Continuous ink jet technology (CIJ) is mainly used in product labelling and packaging industries for its higher printing speed as a result of greater number of ink drops per unit time in printing process, however the resolution of printing quality is relatively low ($\sim 40\text{-}60\mu\text{m}$) [2.4, 2.8, 2.10]. In addition, the recycling stage in CIJ could lead a chemical degradation to biomedical inks affecting suitability for printing biomaterials [2.5].

2.1.1.1.2 Drop on Demand (DOD) Printing Technology

Unlike the CIJ printing technology dropping the ink at all times, the Drop on Demand (DOD) printer however, drops the ink only as required. The first DOD printer was invented in the late 1940s [2.6]. The function of dropping ink on demand is controlled by an external transducer device to adjust the volume of the ink inside the ink chamber as required. Today, the Drop on Demand (DOD) printing technology could be further subcategorised into piezoelectric-based technology and thermal-based technology depending on the type of transducer used in the printer. The drop-on-demand (DOD) technology benefits the printing industry for its higher printing

resolution (sub-micron) capability [2.11], and due to the small size of nozzles, the overall size of a DOD printer can be reduced [2.7].

2.1.1.1.2.1 Thermal-based Transducer DOD Printing Technology

In thermal-based transducer DOD printing, ink is pushed out of the nozzle by a vapour bubble formed by heating the ink to 350-400°C using a heating plate attached to the wall of the ink chamber [2.12]. **Figure 2.4** illustrates a typical printing process for the thermal-based transducer DOD printing technology, where a vapour bubble is clearly seen to push the ink out of the ink chamber through a printing nozzle.

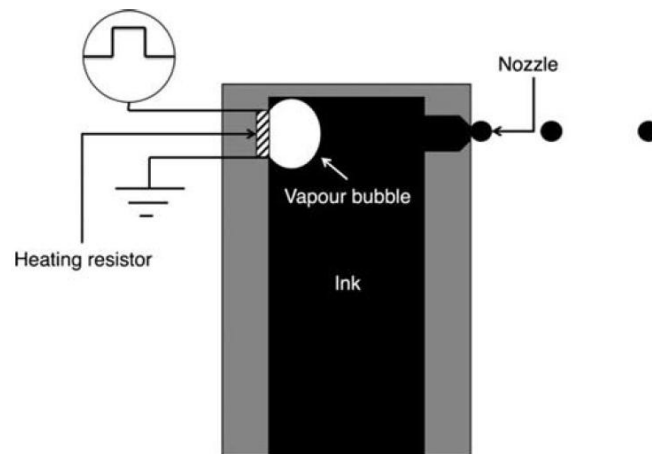


Figure 2.4: A printing head from a typical thermal-based Drop on Demand (DOD) printer [2.5].

Several drawbacks of thermal-based DOD printing technology are found. Wang *et al.* reported a restricted scope of ink materials can be printed due to the thermal effect caused by a heating plate [2.29]. Also such a thermal based technology can result a chemical reaction to biomaterial inks making thermal-based DOD technology inappropriate for printing functional materials [2.5].

2.1.1.1.2.2 Piezoelectric-based Transducer DOD Printing Technology

Figure 2.5 shows the ink drop printing process in a typical piezoelectric-based transducer DOD printer, in which the volumetric level of the ink in the chamber is controlled by deflecting a flat plate as a result of voltage changes. An ink droplet is then pushed out once the flat plate returns to its original position.

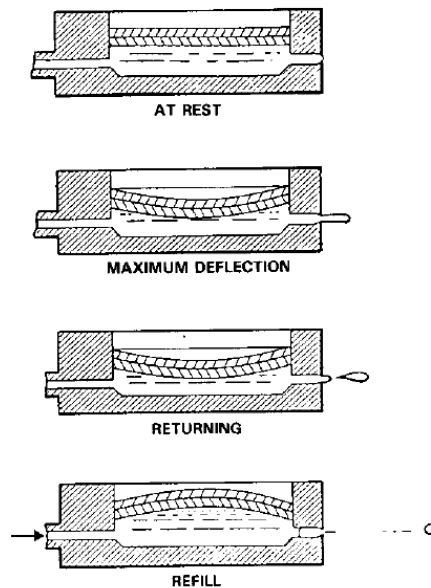


Figure 2.5: Illustration of the printing process in a typical piezoelectric-based Drop on Demand (DOD) printer [2.8].

Ho *et al.* fabricated a micro-battery using a piezoelectric-based DOD printer, comprising printed silver electrode with an average height of $40\mu\text{m}$ for pillars and with a separation distance at $100\mu\text{m}$ between each pillar (**Figure 2.6**) [2.11]. As the piezoelectric DOD process is non-thermal, these printers can print biomaterial inks such as proteins [2.30].

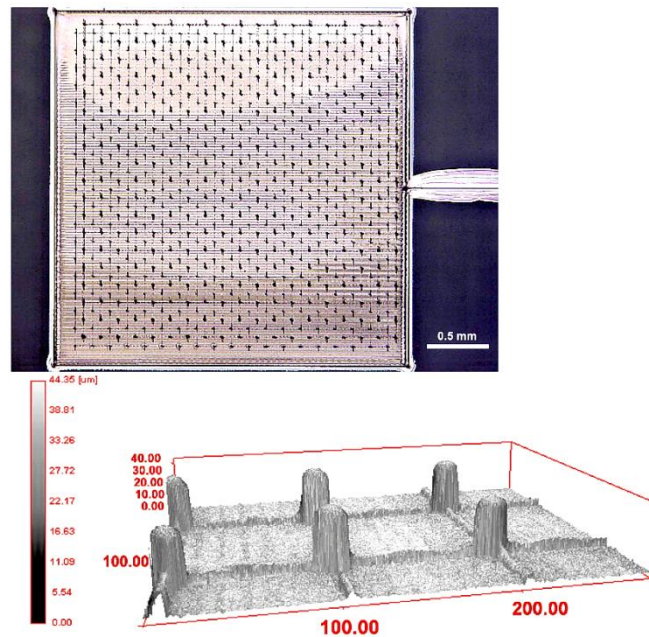


Figure 2.6: A micro-battery fabricated by a piezoelectric-based Drop on Demand (DOD) printer [2.11].

2.1.1.2 Aerosol Jet[®] Printing Technology

Aerosol Jet[®] is a droplet-based direct writing technology developed by Optomec, it uses a focused aerosol spray to print functional materials with a sub-10 μm resolution on to the substrate [2.13]. A major difference between Aerosol Jet[®] technology and ink jet printing technology is the media of transporting material, where Aerosol Jet[®] uses gas to transport material particles onto the substrate.

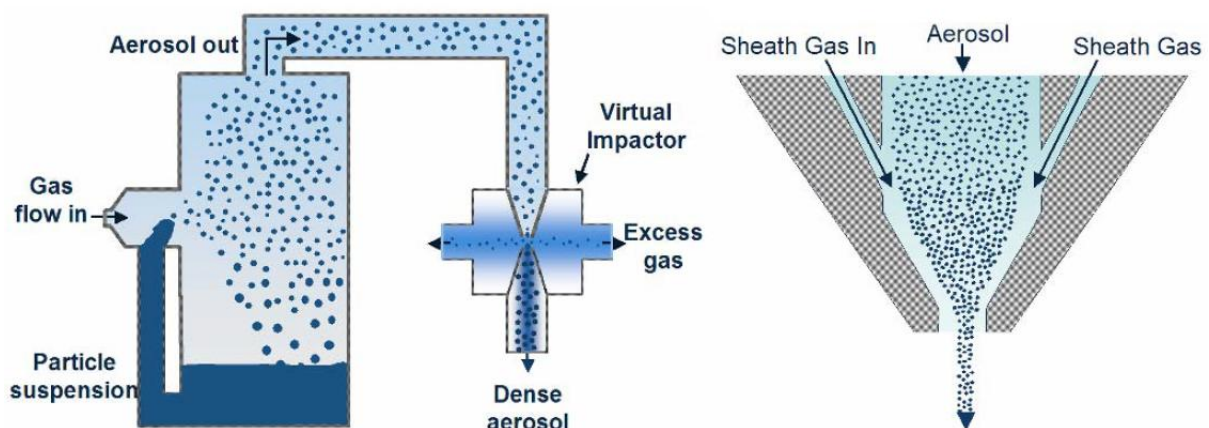


Figure 2.7: A typical aerosol jet[®] system developed by Optomec [2.14].

Figure 2.7 shows a typical aerosol jet[®] system developed by Optomec. The system contains three major components: atomizer for atomizing the source material to form aerosol, virtual impactor for removing the carrier gas, and a nozzle for dispensing aerosol stream [2.13-2.17].

In ink jet printing technology, one major disadvantage is that material with a limited scope of viscosities can be printed on to the substrate. The aerosol jet DW technology however, can deposit materials with a wide range of viscosities (0.7-2500mPa·s) and with a sub-10 μ m resolution [1.2, 2.17], therefore it can be used in micro-electronics fabrication (**Figure 2.8**) and PCB trace repair [1.2].

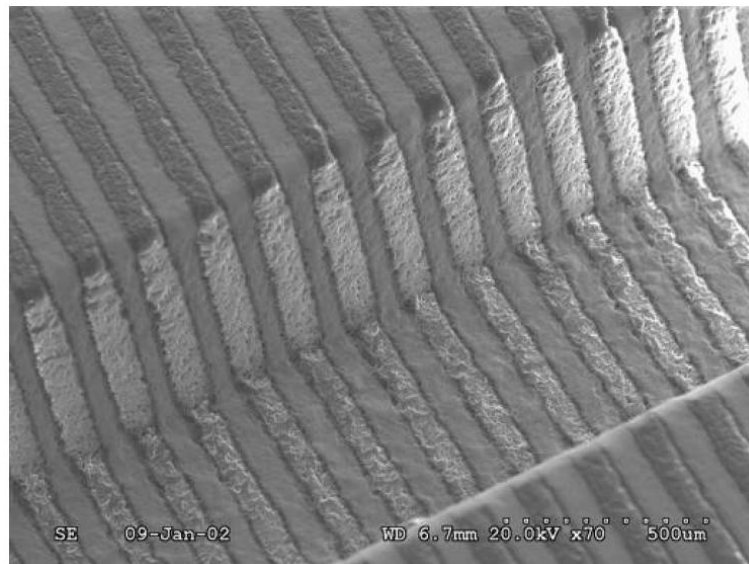


Figure 2.8: An example shows the micro deposition capability of writing 60 μ m Ag lines over a 500 μ m trench, by using an Optomec aerosol jet[®] system [2.15].

2.1.2 Energy Beam-based Direct Writing Technology

This section discusses Direct Writing Technology that utilizes an energy beam to deposit material. This includes laser beam-based DW technology and focused ion beam-based DW technology.

2.1.2.1 Laser Beam Direct Writing Technology

2.1.2.1.1 Laser Chemical Vapour Deposition (LCVD)

Laser Chemical Vapour Deposition (LCVD) is an innovative technology with a potential to replace the traditional Chemical Vapour Deposition (CVD) for a higher deposition rate, a higher deposition resolution, and localized heating area [1.2, 2.18, 2.19]. In conventional CVD, precursor gases are introduced into the heating chamber which then chemically reacts to form a thin film of material on the surface [2.20]. LCVD however, uses the laser beam to locally heat depositing materials with a higher deposition rate and its localized heating effect preserves the substrate from damage from extensive heat coupled into the substrate material (**Figure 2.9**).

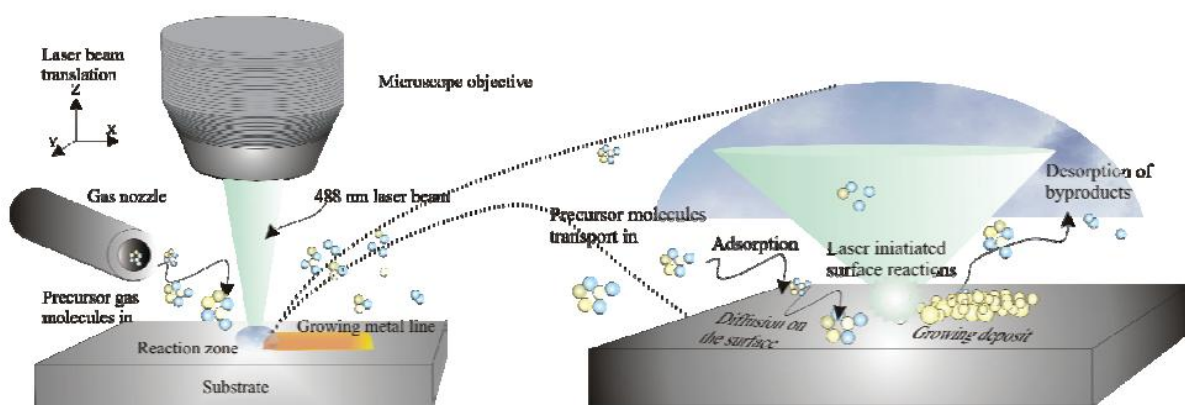


Figure 2.9: A typical Laser Chemical Vapour Deposition (LCVD) process [2.19].

James *et al.* produced silicon wires using the LCVD technology (**Figure 2.10**), with a line width from 300nm to 1.2 μ m. They demonstrated a silicon line deposited on

polysilicon by a continuous wave (CW) laser with a line width of around 600nm (**Figure 2.10 (a)**), on silicon dioxide with a line width of around 1.2 μ m (**Figure 2.10 (b)**), on silicon dioxide with a line width of around 300nm by a pulsed laser (**Figure 2.10 (c)**), and on polysilicon with a line width of around 500nm by a pulsed laser (**Figure 2.10 (d)**) [2.21].

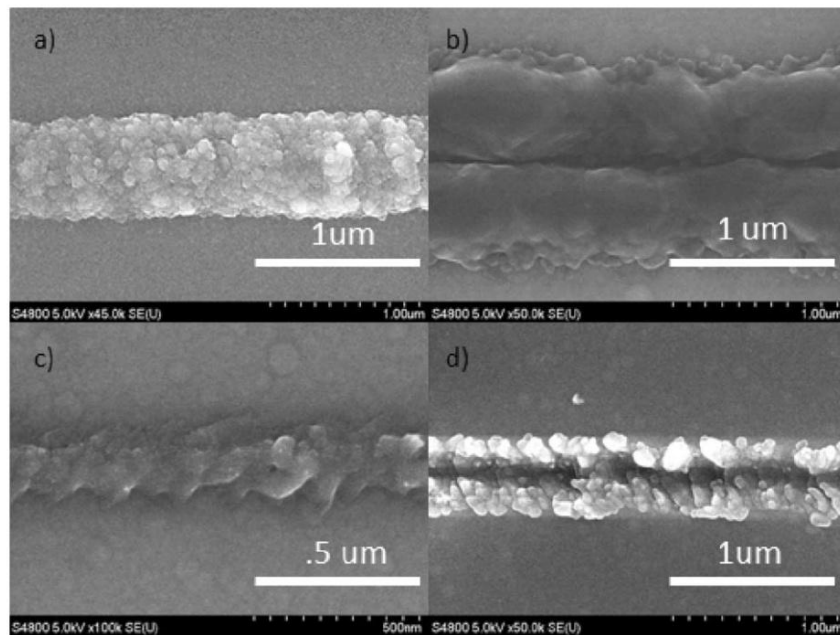


Figure 2.10: SEM images of silicon wires deposited on polysilicon (a,d) and silicon dioxide (b,c) surfaces using the LCVD technology [2.22].

Although LCVD provides a quicker deposition process without the risk of damaging the entire substrate by comparisons to conventional CVD, LCVD is slower than other laser-based direct writing methods, and biomaterials deposition by LCVD is not available. In addition, it needs a vacuum system with well developed gas, which makes this technology expensive to use and less popular in the DW industry [1.2, 2.22].

2.1.2.1.2 Laser Induced Forward Transfer (LIFT)

The concept of Laser Induced Forward Transfer (LIFT) was introduced in 1986 by Bohandy *et al.* [2.23-2.25]. It is a laser based direct write method in which material is transferred onto a target substrate from an adjacent surface by the interaction of focused laser beam irradiation [2.31]. **Figure 2.11** shows a typical LIFT operation [2.26], where the functional material is deposited on a substrate by transferring the deposition material from an optically transparent support to an acceptor substrate as a result of focused laser beam irradiations.

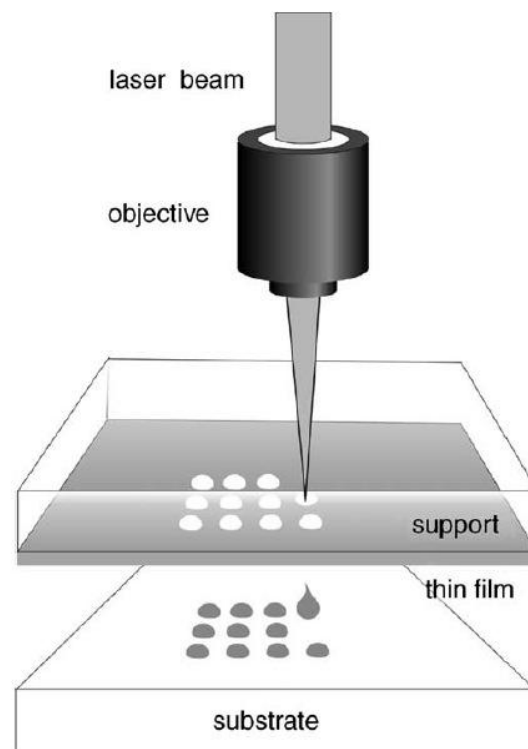


Figure 2.11: A typical Laser Induced Forward Transfer (LIFT) working process [2.26].

In **Figure 2.12**, the SEM image shows the surface morphology of the polystyrene microbead (PS- μ bead) microarrays which were transferred from the support onto substrate by LIFT technology with a pulsed laser energy at $2.25\text{J}\cdot\text{cm}^{-2}$ [2.27].

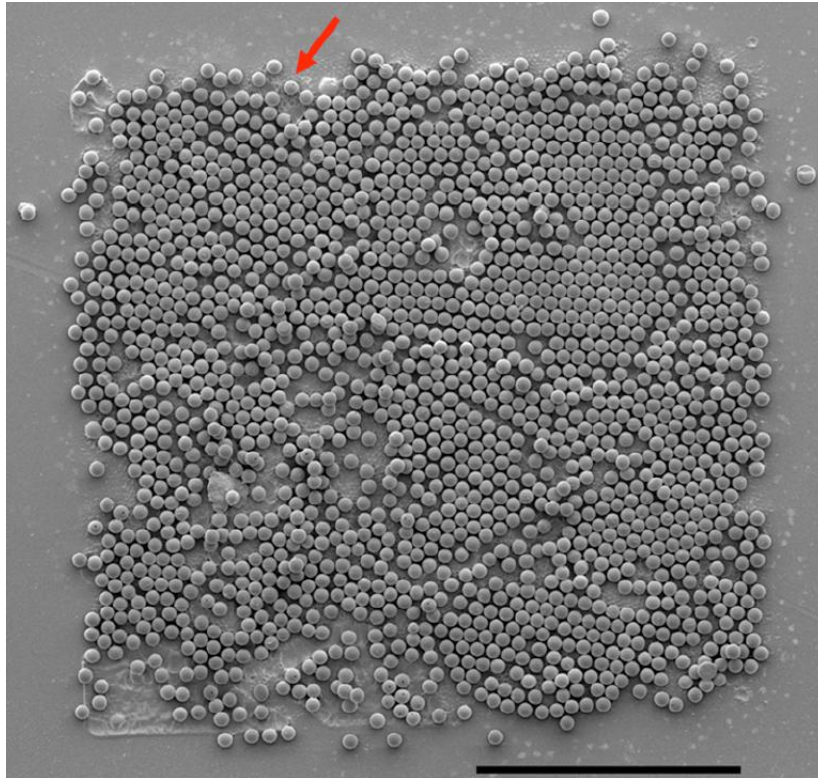


Figure 2.12: Polystyrene microbead (PS- μ bead) microarrays are transferred from the support onto substrate by Laser Induced Forward Transfer (LIFT) technology with a pulsed laser energy at $2.25\text{J}\cdot\text{cm}^{-2}$ (scale bar: $100\mu\text{m}$) [2.27].

Kattamis *et al.* reported one drawback for LIFT technology, in which a vaporization of the substrate can take place as a result of an interaction with the transmitted laser energy if such laser energy is not strongly absorbed by the ink material [2.28]. Other disadvantages include poor morphology for the finished product, as well as a limited scope of usable deposition materials due to the risk of vaporization [2.32].

2.1.2.1.3 Matrix Assisted Pulsed Laser Evaporation Direct Write (MAPLE DW)

Matrix Assisted Pulsed Laser Evaporation Direct Write (MAPLE DW) technology was developed by the Naval Research Laboratory (NRL) in the 1990s [2.33]. As a variation of the LIFT technology, MAPLE DW can deposit a thicker film than LIFT due to a stronger absorption of the laser energy for a polymer binder, which binds the deposition material on a transparent ribbon, as opposed to a rigid transparent

substrate. MAPLE DW is a mature technology to deposit conformal electronic devices, phosphor materials, micro-batteries and biomaterials [2.34, 2.35].

Figure 2.13 shows a typical material deposition process for MAPLE DW technology, the polymer binder on the ribbon absorbs the thermal energy of the laser, evaporating and separating the deposition material from polymer-ink interface and projecting down to the substrate [1.2, 2.35].

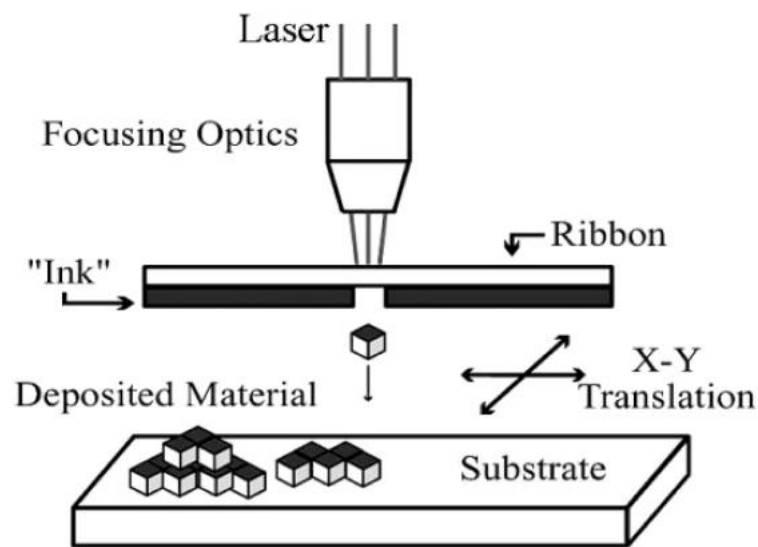


Figure 2.13: A typical material deposition process for Matrix Assisted Pulsed Laser Evaporation Direct Write (MAPLE DW) technology [2.36].

Pique *et al.* demonstrated a temperature sensor produced by MAPLE DW, as seen in **Figure 2.14** the sensor is a silver serpentine line transferred onto a polyimide substrate [2.35].

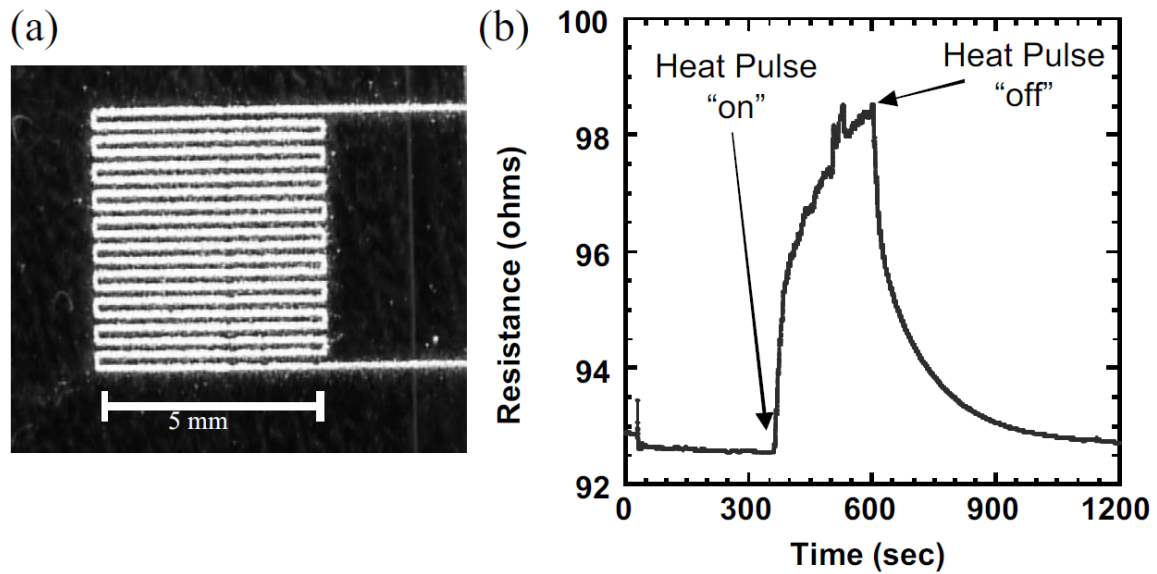


Figure 2.14: A sample of temperature sensor application was produced by using Matrix Assisted Pulsed Laser Evaporation Direct Write (MAPLE DW) technology (a), and (b) shows the sample can respond to applied heat [2.35].

2.1.2.2 Focused Ion Beam (FIB) Direct Writing Technology

Focused Ion Beam (FIB) Direct Write technology is a material deposition method that utilizes liquid metal ion sources (LMISs) to print the metal ions directly onto the substrate [2.37]. Several metallic elements including Al, Cu, Au and even Li are common ion sources used. In FIB, the focused ion beam delivers the deposited material from the LMISs on top of the substrate in the presence of shield gas (**Figure 2.15**). Due to its higher order of resolution in direct deposition, FIB has extensive uses in nanostructuring industries.

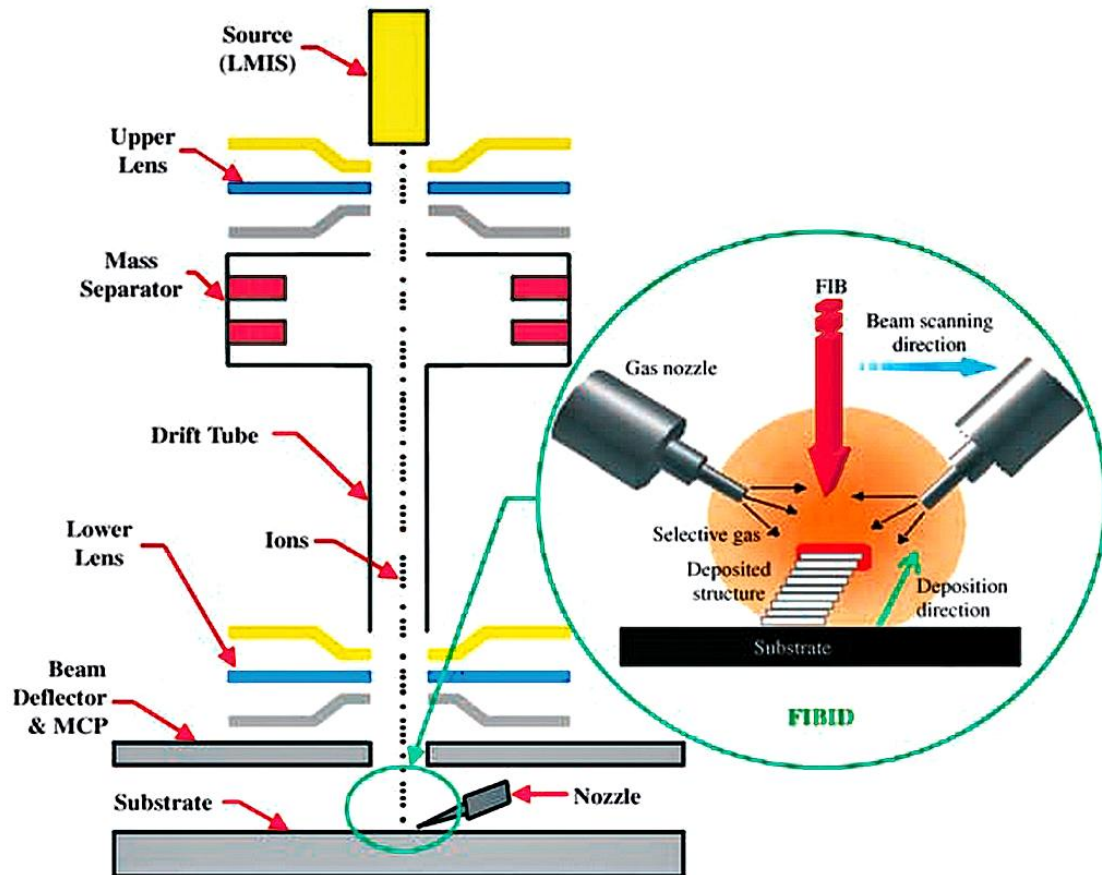


Figure 2.15: A typical Focused Ion Beam (FIB) technology where the metal ions are directly deposited on to the substrate [2.37].

The Focused Ion Beam (FIB) technology provides a better deposition resolution than LCVD, however LCVD processes are faster than FIB, and the uses of FIB restricted due to the large size of equipment [1.2].

2.1.3 Flow-based Direct Writing Technology

A novel micro-dispensing technology that could directly print materials with a higher viscosity than normal inks (the viscosity $\sim 1,000,000 \text{ mPa}\cdot\text{s}$) onto the substrate was developed by nScrypt Inc. [2.38]. Unlike Continuous Ink Jet (CIJ) printing technology which prints ink-drops with a break between each drop, nScrypt dispensing technology dispenses materials with a continuous flow (i.e filamentary). The patented design of the nScrypt pump (**Figure 2.16**) includes a process to suck back dispensing material into the nozzle once the dispensing motion stops, which

ensures a clean dispensing result with no dispensing materials accumulated at the starting/stopping point (**Figure 2.17**) [2.39].

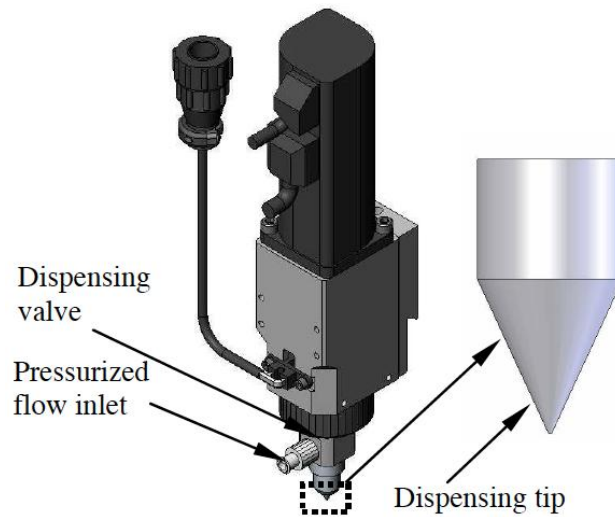


Figure 2.16: nScript printing head with a dispensing tip [2.40].

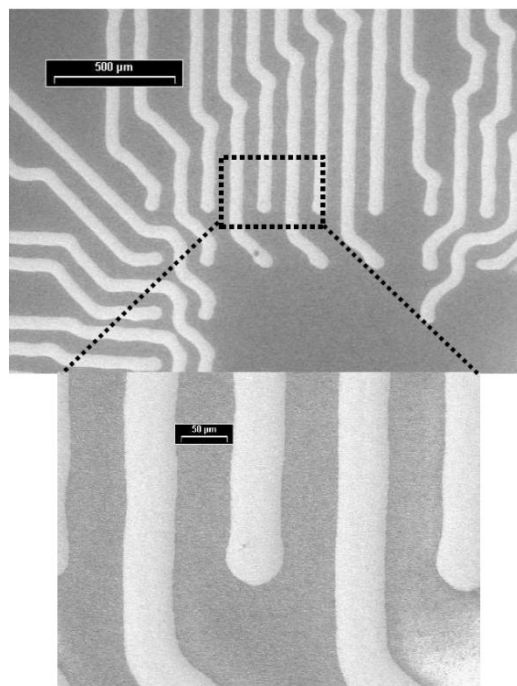


Figure 2.17: A sample produced by using nScript technology shows clean ends at each starting/stopping point [2.39].

In nScript direct writing technology, the dispensing flow rate at a constant pressure is affected by the gap between the dispensing tip and the substrate (**Figure 2.18**).

The flow rate increases with an increasing gap between the dispensing tip and the substrate material.

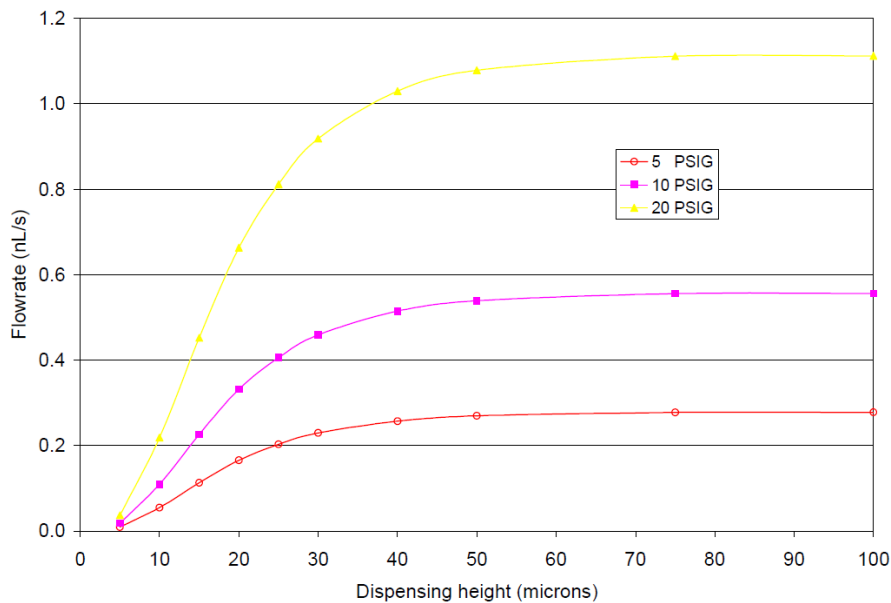


Figure 2.18: Variation in flow rate of material from the dispensing tip with gap between the tip and substrate [2.38].

2.1.4 Tip-based Direct Writing Technology

The development of Direct Writing technology also extends to micro-processing with a higher deposition resolution down to the nano-scale. Dip-Pen Nanolithography and Nanofountain Pen technology are two examples demonstrating the capability of direct composition of functional material with a nano-scale resolution.

2.1.4.1 Dip-Pen Nanolithography (DPN)

Dip-Pen Nanolithography (DPN), which is a direct writing technology using a coated atomic force microscopy (AFM) tip, was introduced in 1999 for depositing molecules on to substrates [2.41, 2.42]. Molecules are directly deposited onto a substrate via a coated AFM tip (**Figure 2.19**), resulting in deposited feature resolutions down to $\sim 14\text{nm}$ [2.43].

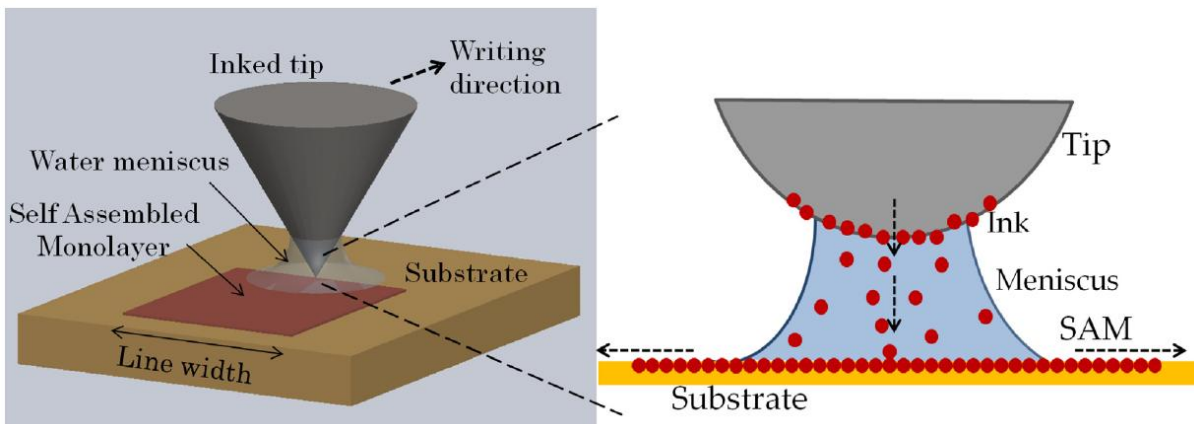


Figure 2.19: A typical Dip-Pen Nanolithography (DPN) process which can deposit molecules on to the substrate [2.44].

Hon *et al.* concluded a three-step process for DPN process where, the AFM tip deposits molecules in the first step, Self Assembled Monolayer (SAM) for molecules formed in the second step, and the final step cures the molecules by chemically binding to the substrate [1.2].

An example of utilizing the DPN technology in DW is images of a Jefferson Nickel printed on the surface of a probe chip, which is shown in **Figure 2.20** [2.45].

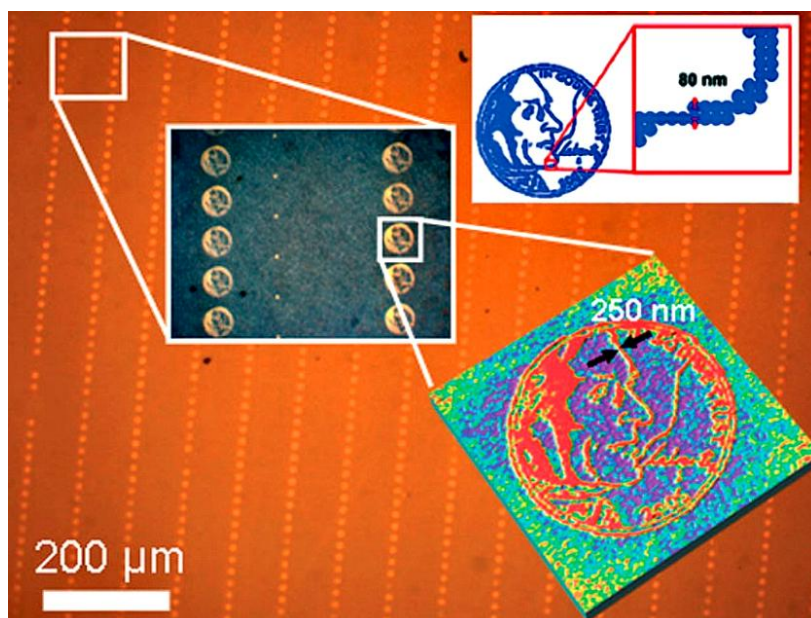


Figure 2.20: An example of printing a Jefferson Nickel image on the surface of a probe chip by using the Dip-Pen Nanolithography (DPN) technology [2.45].

2.1.4.2 Nanofountain Pen (NFP) Technology

Nanofountain Pen (NFP) technology, is a nano-scaled direct writing technology similar to DPN, but which uses a nano-pipette as the material dispensing tip rather than an AFM tip (**Figure 2.21**) [1.2, 2.46, 2.47]. The sharp tip geometry leaves the capability of writing a nanostructure with a sub-100nm resolution, which is showing a potential use in depositing proteins, active enzymes, DNA, and polymers (**Figure 2.22**) [2.48, 2.49].

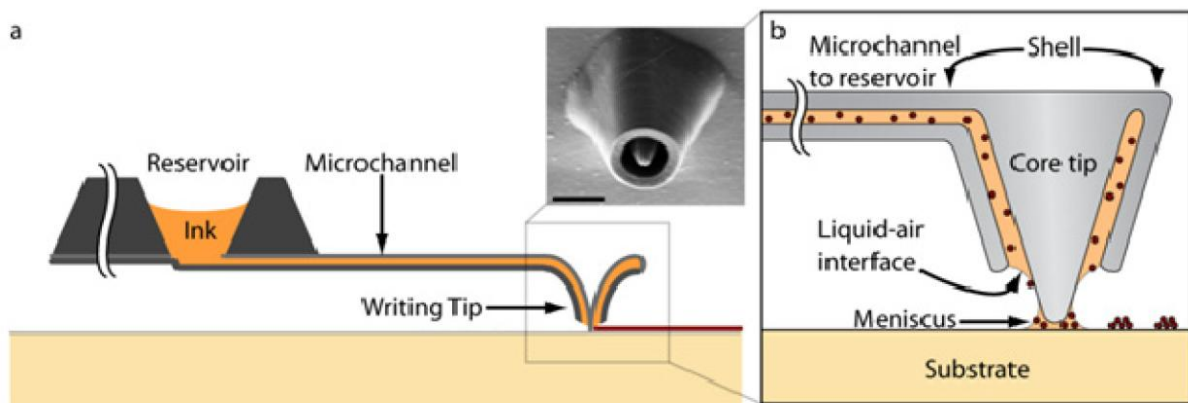


Figure 2.21: A typical structure for Nanofountain Pen (NFP) (a) where nano-pipette is used as the dispensing tip (b) [2.46].

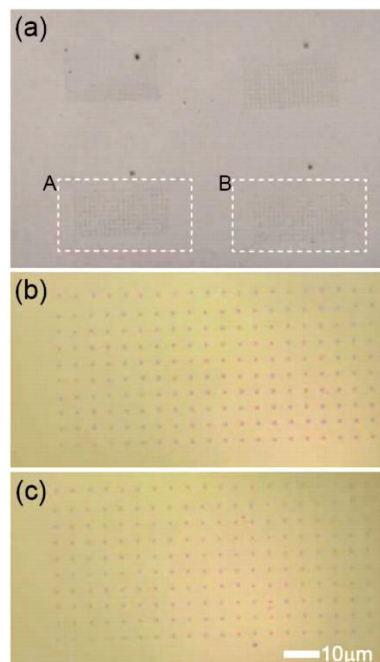


Figure 2.22: Ferritin proteins are deposited on a silicon dioxide substrate using the Nanofountain Pen (NFP) technology (a), where (b) and (c) shows magnified view of area A and area B in (a), respectively [2.50].

2.2 Screen Printing Technology

Screen Printing technology, invented in China during the Song Dynasty (960-1279 AD) [2.61, 2.62], is still in use for its advantages in simple operational procedure, low running cost, and good adaptability. Today screen printing technology has extended even to plastic electronics (PE) industries for printing electrically conductive traces on top of both rigid and flexible substrates [2.63].

A typical procedure of screen printing technology is shown in **Figure 2.23** [2.64]. A screen (usually made of nylon, polyester, or stainless steel [2.63]) is mounted in an aluminium frame, in a way that a gap is created between the substrate and the screen (this can ensure an uniform thickness of the ink that transferred on to the substrate during the screen printing process). The ink or paste is transferred to the substrate through the opening of the screen by pushing a squeegee across the screen, followed by drying the ink to remove the solvent and thermal post processing to make the ink electrically conductive [2.64, 2.65].

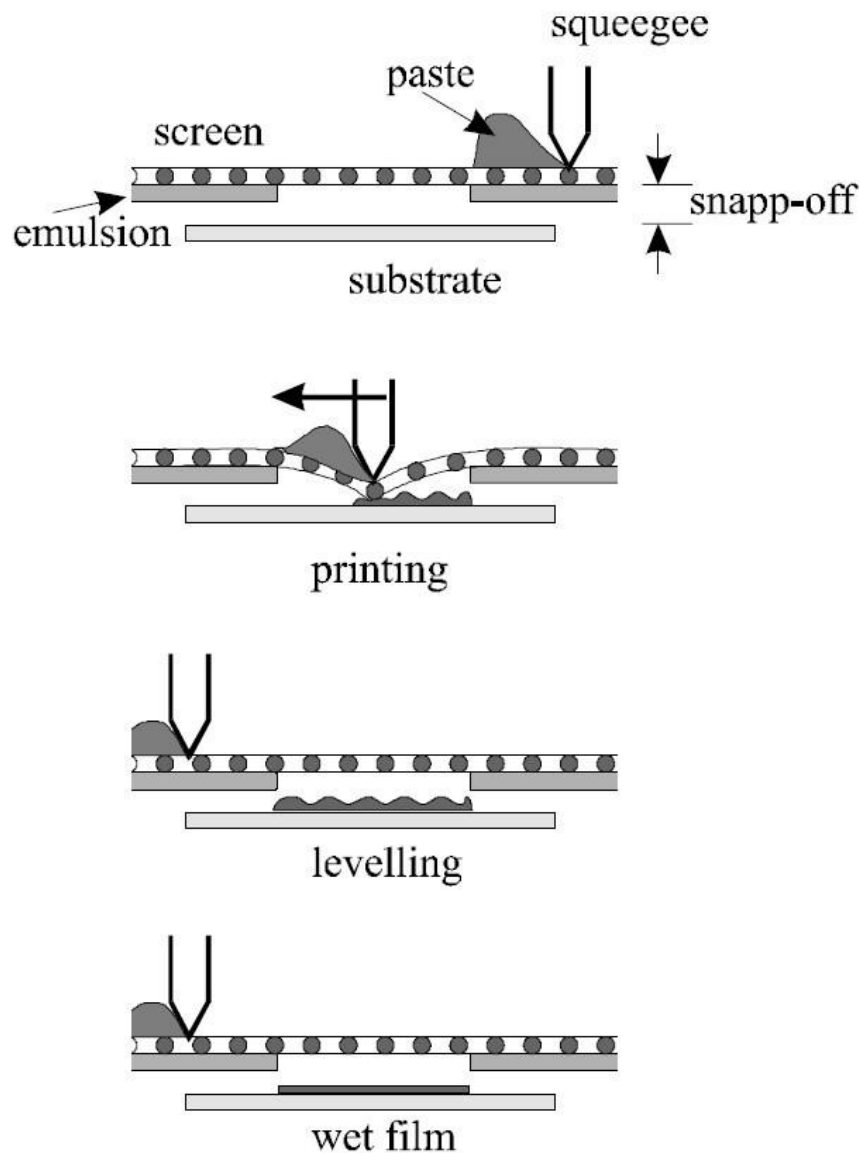


Figure 2.23: Illustration of a typical screen printing process [2.64].

The finish quality of the screen printing process is affected by several parameters, identified by Horvath *et al.* [2.61], they are: squeegee pressure, speed of the squeegee, the distance between the screen and the substrate ("snapp-off" distance), and squeegee shape. In addition, the screen printing quality can also be affected by the mesh, or the number of holes of the screen per square inch. Yin *et al.* reported the printing quality is a function of the mesh of the screen, in which the printing resolution increased with an increasing number of holes per square inch, or mesh of the screen, as shown in **Figure 2.24** [2.65]. In 2007, a Japanese stainless steel mesh manufacturer – ASADA Mesh Co., Ltd developed the world finest mesh screen – 730 mesh (730 holes in the screen per square inch), in which the diameter of the

wire of the mesh was reduced down to 13 μm , as shown in **Figure 2.25**, this made possible the screen printing of ink tracks with a linewidth narrower than 30 μm [2.63, 2.66].

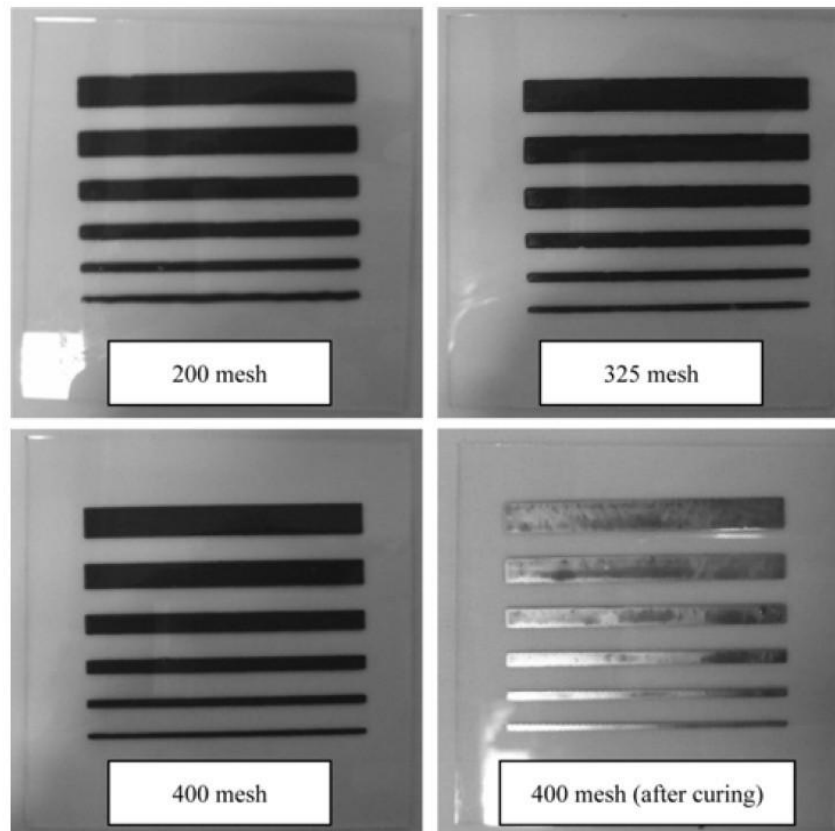


Figure 2.24: Silver nanoparticle (NP) ink track samples made by screen printing technology with different mesh of the screen. The electrical resistivity of 400 mesh ink track after heat treatment at 200°C for 5 min is measured as 180 $\mu\Omega\cdot\text{cm}$, nearly ~ 100 times the resistivity of the bulk silver [2.65].

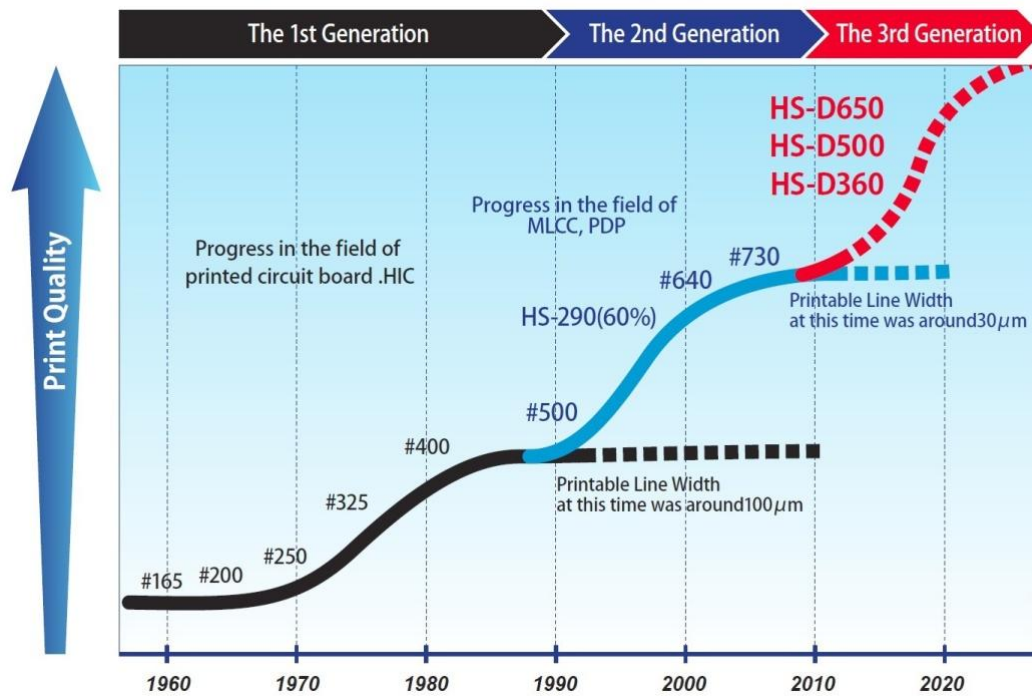


Figure 2.25: The progresses in screen mesh in screen printing technology, where the more holes of the screen per square inch (mesh), the finer the mesh and hence the better printing quality can be achieved [2.66].

An example of utilizing screen printing technology is shown in **Figure 2.26**, in which a 3-D structure has been created by Applied Materials Italia Srl, for developing crystalline silicon solar cells, this 3-D structure can overcome the shadowing problem and hence can increase the solar cell's efficiency [2.67].

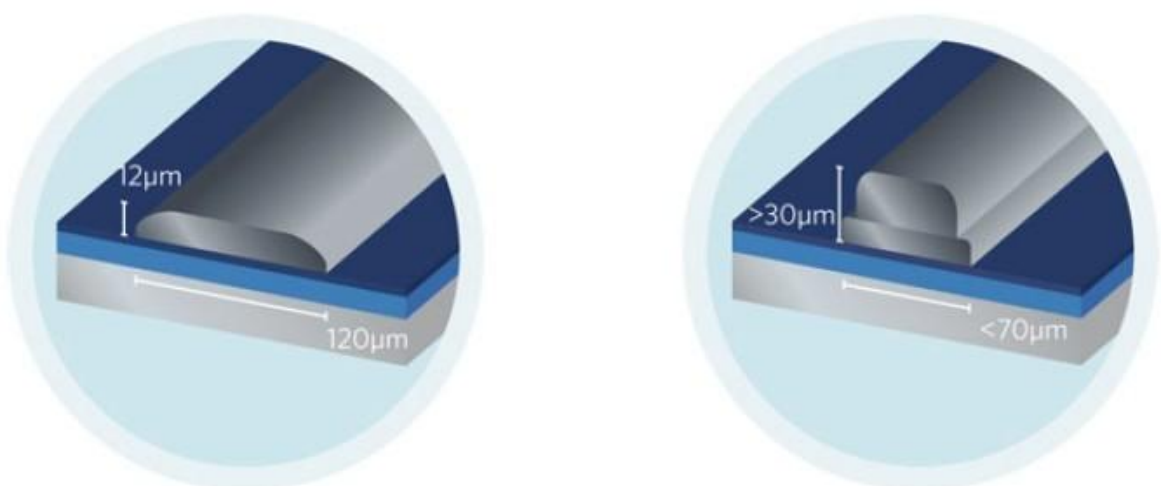


Figure 2.26: Advanced 3-D structure of crystalline silicon solar cell created by screen printing (right) can increase efficiency for its narrower line width and thicker structure, to overcome the shadowing problem caused by conventional thinner lines (left) [2.67].

2.3 Curing and Sintering Processes

For electrically conductive inks, once the electrically conductive material is dispensed/printed onto the surface of the substrate, it needs a post-processing step to solidify the material, bond the electrically conductive particles together, and hence make the material electrically conductive [1.1].

The terminology of this post-processing step (i.e. curing) to conductive material has been given various definitions in different industrial areas. In printed electronics (PE), the definition of this post-processing step is related to the particle size of electrically conductive material within the ink or gel system. Roberson *et al.* has summarized and subcategorized the definition of “curing” in the PE industry [2.68]. As reported by Roberson, the material’s electrical conduction can be achieved by: 1) percolation theory for epoxy matrix containing micro-sized metal particles; and 2) sintering effect for nanoparticle ink.

2.3.1 Curing for Conductive Microparticle Ink Due To Percolation Theory

Percolation theory was firstly reported in 1957 by Broadbent and Hammersley for describing random movements of fluid through a medium [2.69]. The percolation threshold is critical to the system in that it can radically change the state of fluid movement, e.g. to become an electrical conductor or an insulator [2.69, 2.70]. Kirkpatrick further investigated the percolation probability, in which the percolation probability is a function of concentration near the threshold (**Figure 2.27**), this can be described as below in **(2-7)**, where P is percolation probability, x is the concentration, x_c is the critical concentration at threshold, and s is a value between 0.3 and 0.4 [2.69].

$$P^s(x) \propto (x - x_c)^s \quad (2-7)$$

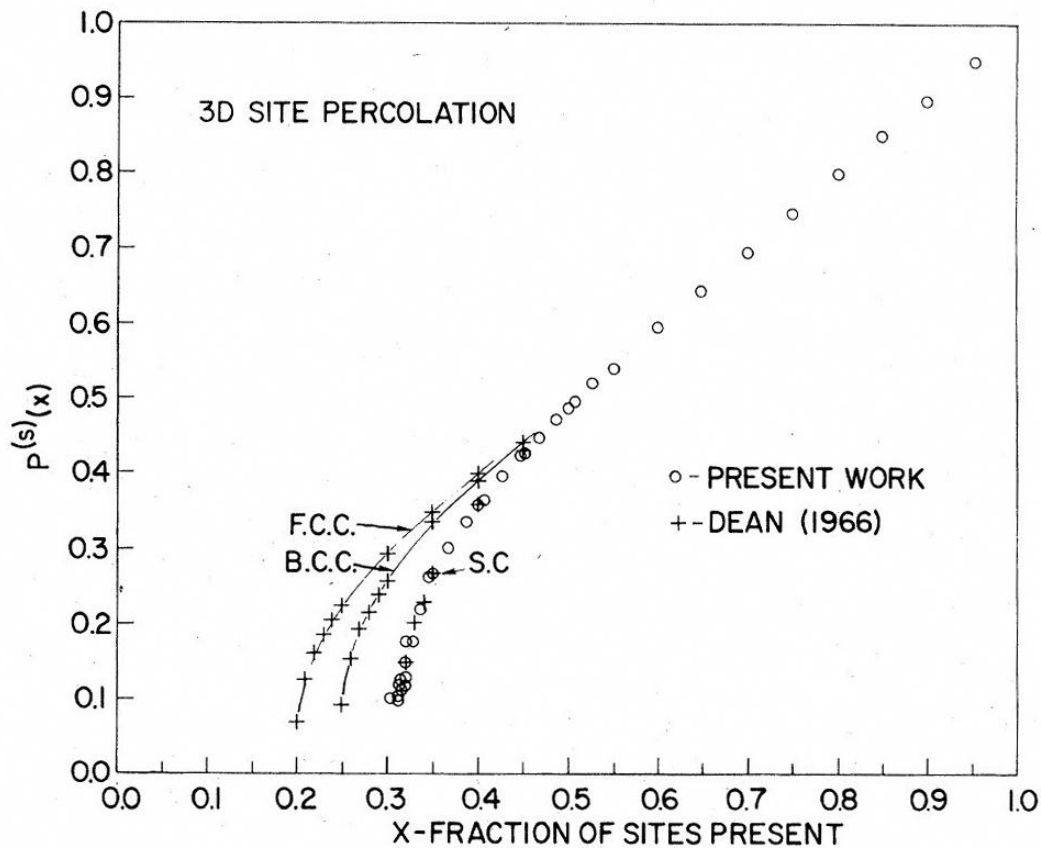


Figure 2.27: A typical relationship between percolation concentration (x-axis) and the percolation probability (y-axis) [2.69].

Percolation theory can be extended to the printed electronics (PE) industry, in which the phenomenon of metal/dielectric mixture becoming electrically conductive can be explained as the point at which the volume concentration of metal particles exceeds the percolation threshold [2.71]. This has been further explained by Don Banfield [2.72], for conductive epoxies in that when the overall volume of the mixture is reduced due to solvent evaporation during thermal processing, metal/dielectric mixture components are bonded together by the resin's chemical cross-linking process, further reducing the overall volume of the mixture, increasing the volume concentration of the conductive particles. This metal/dielectric mixture becomes electrically conductive once the metal particles' volume concentration goes beyond the percolation threshold, and provides a firm structure that can physically support the mixture to bond the conductive metal particles tightly together with a greater amount of surface contacts between metal particles.

Ye *et al.* and Nicolics *et al.* have also investigated the phenomenon of the metal/dielectric mixture becoming electrically conductive after the thermal process, in which, during the process, clusters are formed among conductive metal particles, and that these clusters are eventually formed into a single and complete cluster with multiple conducting paths by connection of these clusters to each other, as demonstrated in **Figure 2.28**, which makes the mixture become highly electrically conductive [2.73, 2.74]. The conductivity of the mixture can be affected by the shape of conductive metal particles, as has been investigated by Banfield, in which the electrical conductivity can be significantly increased by the flake shape as this shape increases the surface contact areas between particles, allowing more conducting paths to be achieved for electrons moving between particles [2.72].

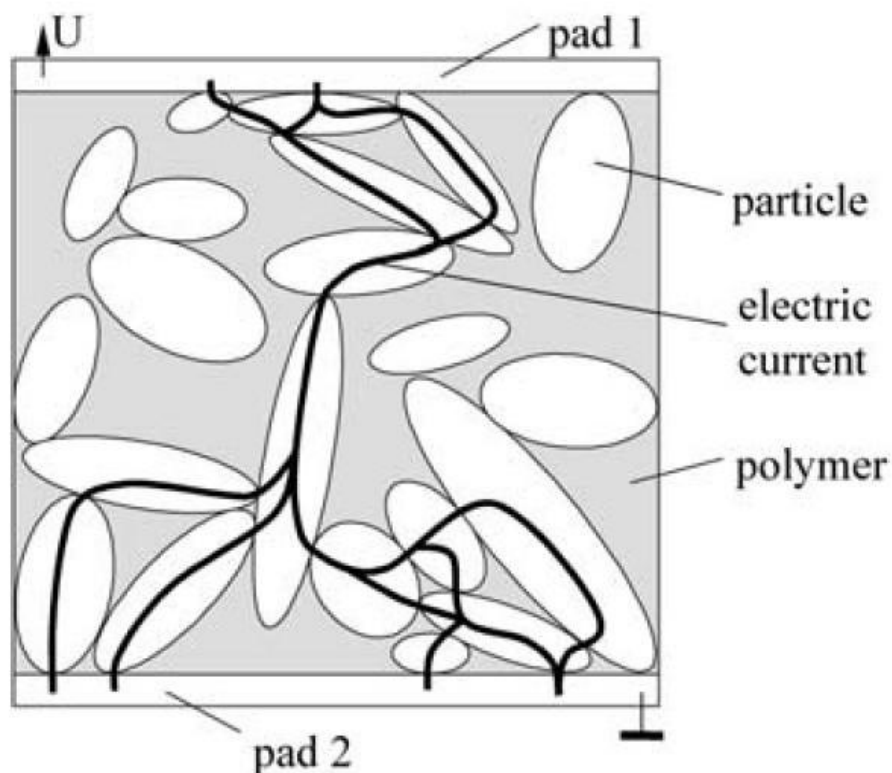


Figure 2.28: A cross-sectional illustration of a conductive joint after cure showing an example of the formation of one big conductive cluster that electrically connects the ink [2.74].

2.3.1.1 Existing Research Reported for Curing Conductive Microparticle Ink

In order to investigate and compare results in curing conductive inks carried out by different researching groups as well as the experimental results in this thesis, the resistivity of the bulk material will be used as the benchmark for resistivity comparison of the ink after different processing treatments. The bulk resistivities of common materials (Silver, Copper and Gold) are listed in **Table 2.1** [2.75].

Table 2.1: Resistivities of common materials (Silver, Copper and Gold) [2.75].

Material	Resistivity ($\Omega \cdot m$)
Silver	1.59E-08
Copper	1.72E-08
Gold	2.44E-08

Roberson *et al.* investigated oven curing silver microparticle ink (Ferro 3309F (**Figure 2.29, Table 2.2**)) on alumina substrate at 850°C for 10 min, with the best resistivity reported as $\sim 21n\Omega \cdot m \pm 5.7n\Omega \cdot m$, this is ~ 1.3 times that of bulk silver. Polyimide (PI) based substrates were also investigated in Roberson's research, in which silver microparticle ink (Ercon E1660 (**Figure 2.29, Table 2.2**)) was cured after heating by oven at 138°C for 1 hour, for which the lowest electrical resistivity was achieved at around $103n\Omega \cdot m \pm 14n\Omega \cdot m$ [2.68], which is ~ 6 times that of bulk silver. Faddoul *et al.* investigated the electrical resistivities against various silver content in ink. In his research, the electrical resistivity is shown to be a function of silver content, i.e. that the more silver in ink, the lower electrical resistivity value can be achieved. As seen in **Figure 2.30**, the lowest electrical resistivity obtained is at $18.5n\Omega \cdot m$ for commercial ink (with 85%wt Ag) on alumina substrate cured in oven at 700°C for 15 min, this is around 1.2 times that of bulk silver [2.76].

Table 2.2: Commercial conductive silver ink used for Roberson *et al.*'s investigation [2.59, 2.102, 2.103].

	Typical Curing Condition	Sheet Resistivity ($m\Omega/sq$)
Ferro 3309F	850°C for 10 minutes in Oven	0.5-1.3
DuPont CB028	160°C for 1 hour in Oven	7-10
Ercon E1660	>125°C for 15 minutes in Oven	11

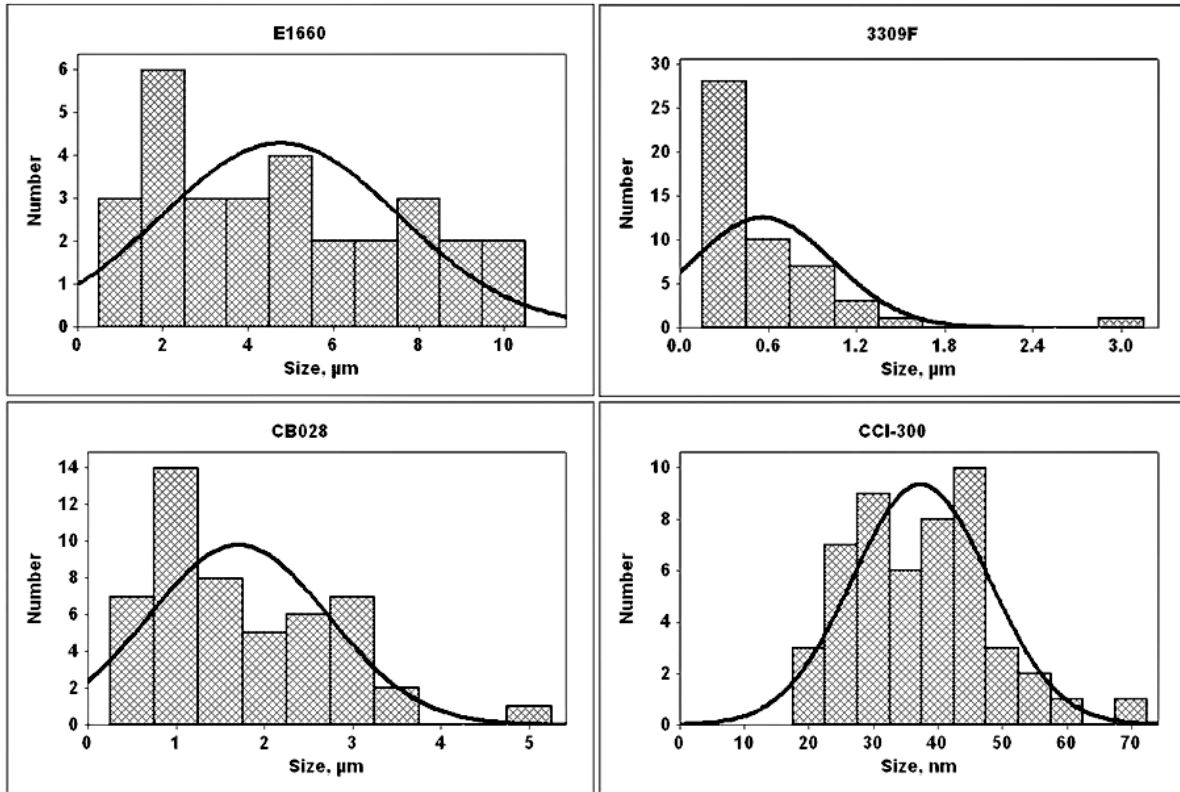


Figure 2.29: Size distributions of silver microparticles in ink used in Roberson *et al.*'s research [2.68].

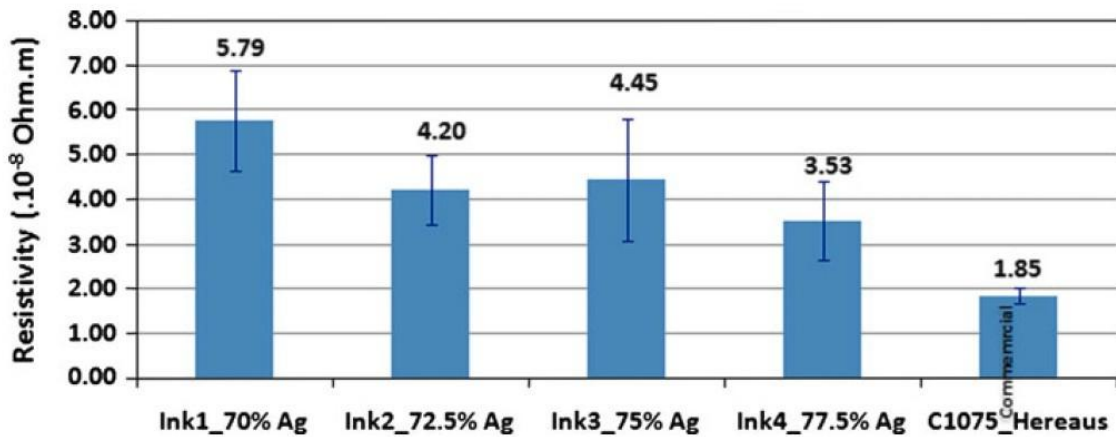


Figure 2.30: Electrical resistivity is a function of silver content, as experimentally investigated by Faddoul *et al.*, with all ink samples on alumina substrate (ink1~70%Ag, ink2~72.5%Ag, ink3~75%Ag, ink4~77.5%Ag, C1075~85%Ag) cured in Oven with a heating temperature at 700°C for 15 min [2.76].

Conventional oven curing of conductive microparticle inks has limitations: 1), oven curing technology is time-consuming, and 2), oven curing technology restricts the substrate material used in curing process as the entire substrate material is heated up at a high temperature (up to as much as $\sim 700^{\circ}\text{C}$). Therefore advanced curing

techniques have to be developed to replace the oven curing process to improve the curing result at a reduced heating area, and increased curing speed, etc. Roberson *et al.* demonstrated an ohmic curing process to cure the silver microparticle ink in 2012 [2.77], in which the silver ink is cured by applying electrical current across the silver ink trace. **Figure 2.31** shows the curing result of silver microparticle inks (the size distribution of silver particles in silver ink is shown in **Figure 2.29**) cured by using an Ohmic heating process on a polyimide (PI) substrate after an air-dry at room temperature for 7 days. The lowest electrical resistivity was achieved at $\sim 76\text{n}\Omega\cdot\text{m} \pm 1.2\text{n}\Omega\cdot\text{m}$ (CB028 ink), which is around 4.8 times that of bulk silver. However a localized discoloration of the trace was observed due to a localized melting caused by Ohmic heating.

Ink Type	Initial Preprocess	Mean Resistivity After Preprocess (n Ω m)	Applied Current Density (mA/ μm^2)	Applied Current (mA)	Duration of Current Application (s)	Mean Resistivity After Ohmic Curing (n Ω m)	Mean Resistivity of Thermal Benchmark Samples (n Ω m)
Ag microparticle CB028	Air-dried at room temp. for 7 days	253 \pm 31	0.35	500	30	129 \pm 11, N = 5	130 \pm 11, N = 5, 160°C for 1 h
Ag microparticle CB028	Air-dried at room temp. for 7 days	253 \pm 31	0.35	500	60	119 \pm 10, N = 5	
Ag microparticle CB028	Air-dried at room temp. for 7 days	253 \pm 31	0.50	750	30	76 \pm 1.2, N = 5	
Ag microparticle E1660	Air-dried at room temp. for 7 days	406 \pm 45	0.30	500	30	143 \pm 33, N = 6	

Figure 2.31: Results for Ohmic curing different silver micro particle inks on Polyimide substrate [2.77].

In addition, a microwave curing process for copper microparticle ink containing two types of resin (one-part resin and two-part resin) has been demonstrated by Qi *et al.* on glass substrate [2.86], in which the microwave cured inks were compared to the same inks cured by conventional oven at 150°C. **Figure 2.32** shows the electrical resistivities comparison for ink samples cured by both microwave and the conventional oven curing process. In **Figure 2.32(a)**, the electrical resistivity of microwave cured copper ink with one-part resin reached $1.5 \times 10^{-6} \Omega\cdot\text{m}$ after 5 minutes of the curing process. This resistivity value was further reduced to around $0.75 \times 10^{-6} \Omega\cdot\text{m}$ after 20 minutes (~ 43.6 times of that in bulk copper), for which the curing time was significantly reduced compared to 1 hour in conventional curing process. However no major differences were found in electrical resistivities for copper microparticle ink with two-part resin, as shown in **Figure 2.32(b)**. This was caused by a reduced microwave absorption for two-part resin in a microwave curing process.

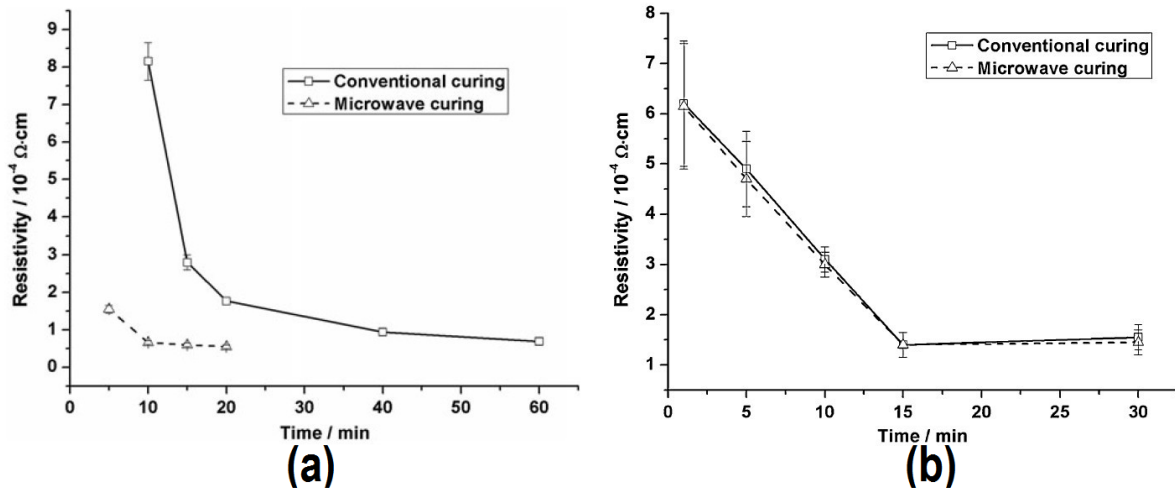


Figure 2.32: Electrical resistivity of cured Cu micro-particle ink samples with one-part resin (a), and with two-part resin (b). Conventional oven curing results (heating temperature $\sim 150^\circ\text{C}$) were compared [2.86].

2.3.2 Sintering for Conductive Nanoparticle Ink

Investigations to how an electrically conductive material's chemical and physical properties can be affected by a change in particle size started over a century ago [2.82]. Buffat *et al.* investigated and plotted a graph showing how gold nanoparticle's melting point is affected by particle size (**Figure 2.33**) [2.83]. The significantly reduced melting point of metal nanoparticles has promoted the development of sintering process in printed electronics (PE) industries [2.84, 2.85].

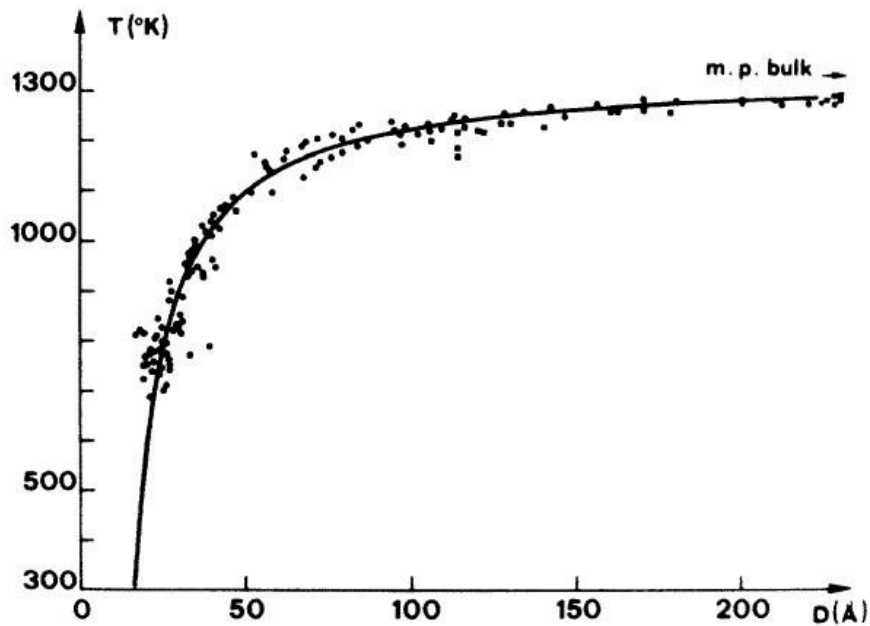


Figure 2.33: The melting point temperature of gold particles is a function of particle size, which was investigated and plotted by Buffat *et al.* in 1976 [2.83].

Sintering is a thermal process that results in the melting of nanoparticles in the range of 100-400°C and bonding these nanoparticles together through neck formations between each particle. In this way, a single cluster with a high electrical conductivity is formed in a continuous metal layer [2.87-2.91]. **Figure 2.34** demonstrates a typical neck formation of nanoparticles during the sintering process [2.87].

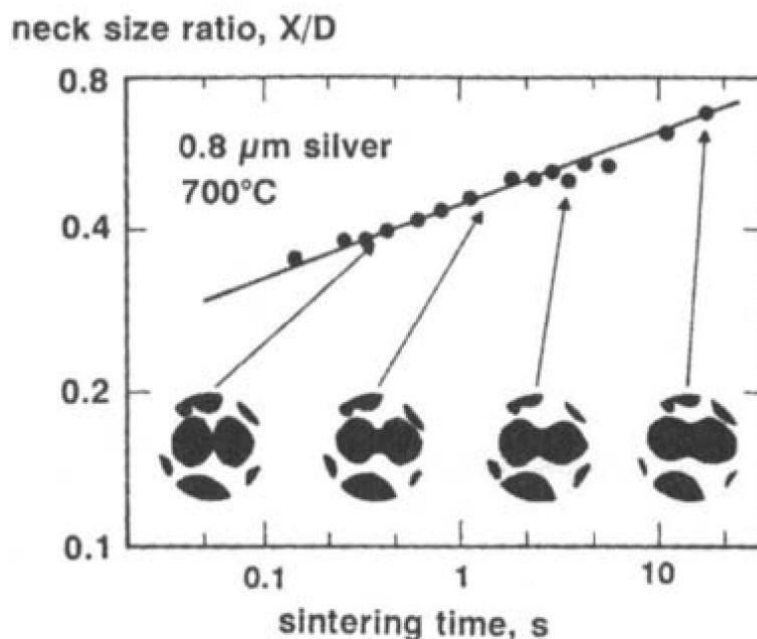


Figure 2.34: Illustration of the necking formation during the sintering process for 0.8 μm Ag particles at 700°C [2.87].

2.3.2.1 Existing Research Reported for Sintering Conductive Nanoparticle Ink

During the sintering process, the electrical conductivity of the conductive nanoparticle ink is a function of sintering temperature, in which the higher a sintering temperature, the better the electrical conductivity that can be achieved. This has been investigated by Greer *et al.* [2.93], as shown in **Figure 2.35**, in which a conductive silver nanoparticle ink with particle size at $\sim 40\text{nm}$ was sintered on silicon wafers with variant temperatures. The ink became electrically conductive more easily and quickly at a higher sintering temperature than at a lower temperature, where the lowest electrical resistivity for silver nanoparticle ink was measured as below $5 \times 10^{-8} \Omega \cdot \text{m}$ (~ 3.1 times of that in bulk silver) at a sintering temperature above 180°C for more than 10 minutes.

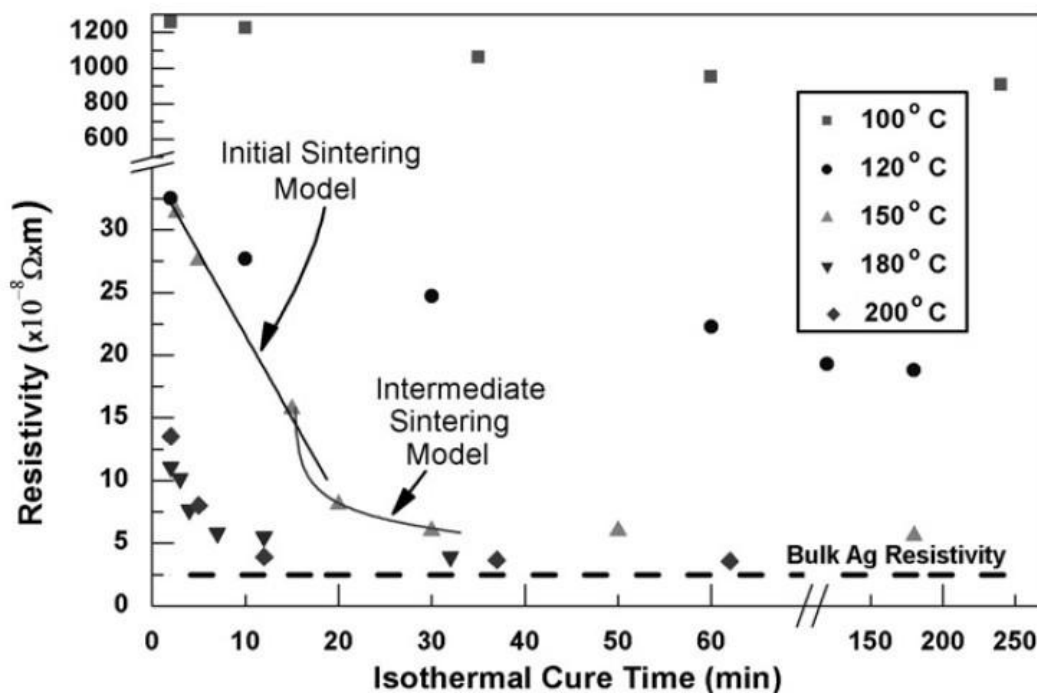


Figure 2.35: Illustration for electrical resistivity as a function of sintering time for different sintering temperature for silver nano-particle ink ($\sim 40\text{nm}$) [2.93].

Wu *et al.* investigated the thermal sintering process of conductive silver nanoparticle ink on a polyimide (PI) substrate [2.92]. In Wu's research, the silver nanoparticle ink (with particle size at $\sim 200\text{-}400\text{nm}$) was sintered on polyimide (PI) substrate in oven

at 280°C for 1 hour, and the electrical resistivity of the sintered conductive silver nanoparticle ink was measured as 88.5 $\mu\Omega\cdot\text{cm}$ (this is ~ 55.7 times of that of bulk silver). In Wu's research, variant resin compositions in nanoparticle ink were also investigated. Resin was found to help in reducing the electrical resistivity of the nanoparticle ink. The reduced electrical resistivity was reported as 2 $\mu\Omega\cdot\text{cm}$ for silver nanoparticle ink containing 5 wt% resin (~ 1.3 times of that in bulk silver).

Conventional thermal sintering has a major drawback in that its higher sintering temperatures can easily damage the substrate material [2.90, 2.94, 2.95]. In addition, the conventional thermal sintering process is a time-consuming process that requires longer times to sinter conductive nanoparticles for achieving a desired electrical conductivity [2.96]. Therefore, the localized sintering processes such as laser and plasma based sintering processes have been developed to replace conventional thermal sintering process in oven. Lee *et al.* demonstrated a low electrical resistivity achieved at $4.07 \times 10^{-8} \Omega\cdot\text{m}$ for conductive silver nanoparticle ink (with particle size $\sim 50\text{nm}$) sintered by using a 532nm continuous wave (CW) laser on a glass substrate (this is only 2.6 times of that in bulk silver). However the associated temperature was measured at around 327°C, which is still too high for sintering process on the polymer-based substrate materials with a melting point below 200°C [2.96]. Kim *et al.* further investigated conductive silver nanoparticle ink (with particle size $\sim 500\text{nm}$) sintered by 532nm laser sintering process and compared the sintering time to that of conventional thermal sintering in oven (this can be shown in **Figure 2.36**), where the overall sintering time of silver nanoparticle ink sintering process has been reduced from 30 minutes in oven down to 10 seconds for 532nm laser irradiation [2.94].

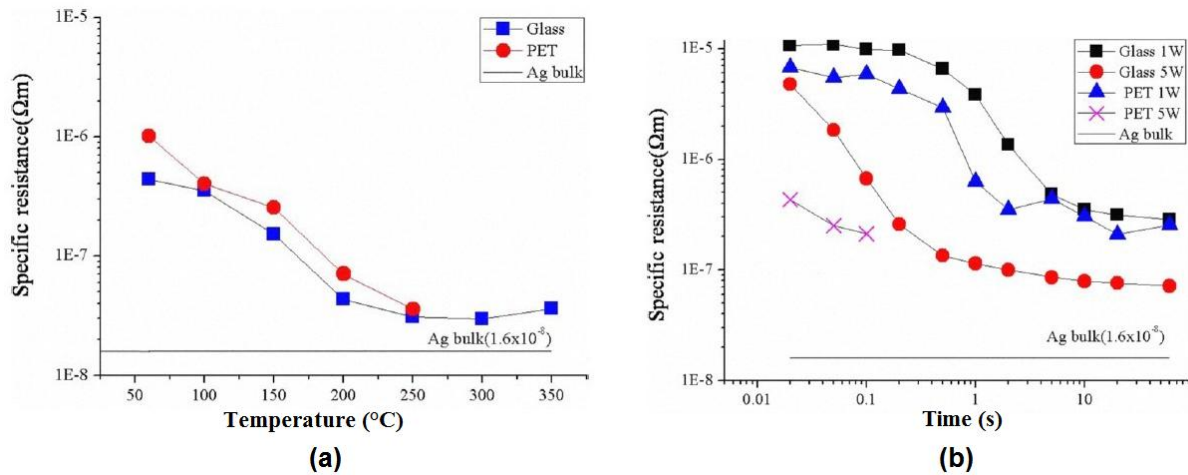


Figure 2.36: Sintering comparison between conventional thermal sintering with various temperatures (a), and time-reduced 532nm laser based sintering process (b) [2.94].

Maekawa *et al.* investigated the laser sintering process with variant laser wavelengths. In his research, conductive silver nanoparticle ink (with particle size at $\sim 5\text{nm}$) was sintered on a polyimide (PI) substrate by an Argon ion (Ar^+) laser with the laser wavelength at 488nm and a Laser Diode laser with the laser wavelength at 980nm. The electrical resistivities for sintered conductive silver nanoparticle inks are shown in **Figure 2.37** [2.97]. As seen in **Figure 2.37**, the lowest resistivity values were achieved at around $5\mu\Omega\cdot\text{cm}$ for ink samples sintered at 980nm and $8\mu\Omega\cdot\text{cm}$ at 488nm, although conductive silver nanoparticle ink sintered at 980nm by the Laser diode laser has lower electrical resistivities than those sintered at the laser wavelength of 488nm by Argon ion laser. However sintering at a longer wavelength required a higher laser power than that at 488nm, which increased the running cost and potential of damaging the substrate material with a higher laser power density.

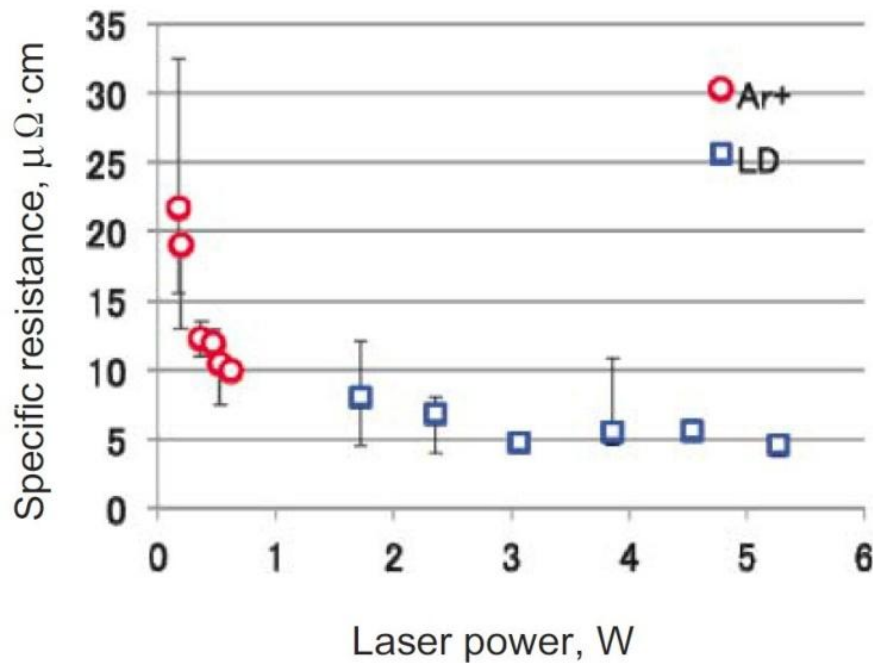


Figure 2.37: Comparison of electrical resistivities of silver nano-particle ink on PI substrate by Ar⁺ laser at 488nm and by Laser Diode laser at 980nm [2.97].

Silver has been used extensively in the sintering process of Plastic Electronics (PE) industries for its better electrical conductivity [2.75]. However scientists have also investigated the other electrically conductive materials in sintering processes, e.g. less expensive copper investigated by Halonen *et al.* [2.98]. In Halonen's research, a CW diode laser with a laser irradiation wavelength at 808nm was used to sinter conductive copper nanoparticle ink (with particle size at ~50-70nm) on a polyimide (PI) substrate. The lowest electrical resistivity was measured and calculated at around $8.25 \times 10^{-8} \Omega \cdot m$, which is about 4 times of that of bulk copper.

Gold metal based conductive nanoparticle ink has also drawn interest for its strong visible light absorption with the absorption peak at 532nm [2.99]. Ko *et al.* investigated a low power (<100mW) laser sintering process of sintering gold nanoparticle ink (with particle size at ~1-3nm) on a polyimide (PI) substrate with a laser irradiation wavelength at 514nm. The electrical resistivity of the ink was measured at around $5.41 \mu\Omega \cdot cm$, which is around 2.2 times of that of bulk gold [2.101]. Bieri *et al.* investigated and compared conductive gold nanoparticle ink sintered by 514nm Argon ion (Ar⁺) laser on different substrate materials [2.84]. As shown in **Figure 2.38**, gold nanoparticle inks were sintered with variant laser

working parameters. The lowest electrical resistivity was achieved at around $5 \times 10^{-8} \Omega \cdot \text{m}$ for gold ink sintered on AF 45 glass with laser output power at 0.8W. Despite the fact that this resistivity is only 2 times of that of bulk gold, the temperature at the laser spot was measured to be over 900°C , which is above the glass melting point at 700°C , and has softened the glass substrate. This was also observed by Chung *et al.* [2.100].

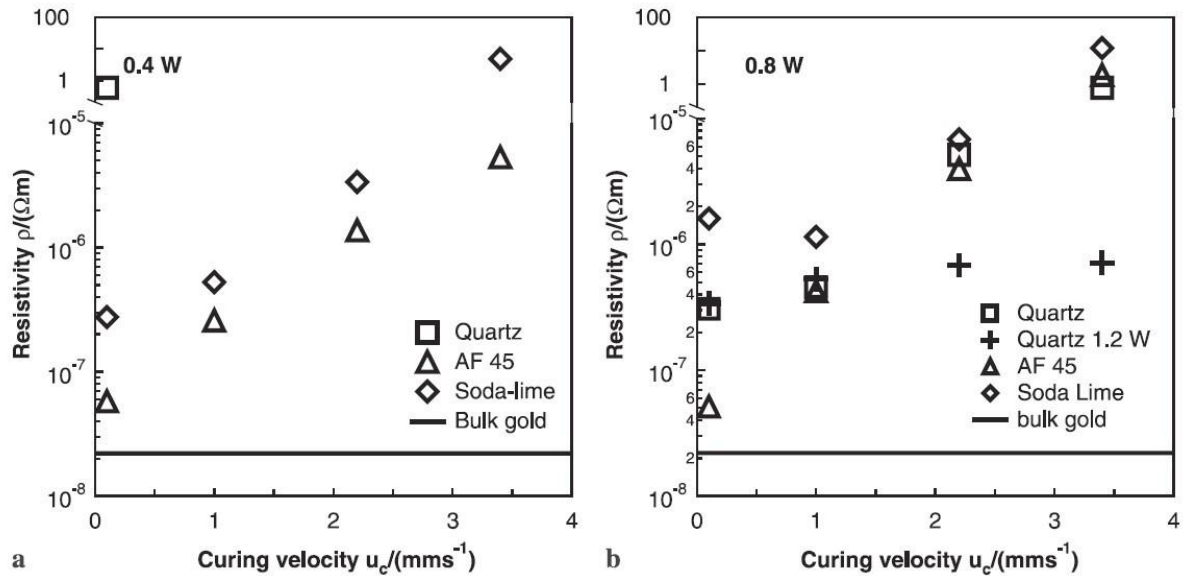


Figure 2.38: Comparison of electrical resistivity values achieved by laser sintering gold nano-particle ink on different substrate materials at 514nm at laser output power of 0.4W (a), and 0.8W (b) [2.84].

The plasma sintering process, as a localized thermal sintering process, has also been investigated for the potential to replace conventional thermal sintering processes in an oven. The plasma sintering process uses plasma exposure to sinter nanoparticles in conductive ink at a low temperature (this has been investigated by Wolf *et al.* [2.90]). In Wolf's research, conductive silver nanoparticle ink (with particle size at $\sim 20\text{-}30\text{nm}$) was sintered by plasma exposure at 150W and 300W, as shown in **Figure 2.39**, where the electrical resistivity of the ink has effectively reduced down to $< 10 \times 10^{-8} \Omega \cdot \text{m}$ after 5 minutes of the process. The resistivity value can be further reduced down to at around $4 \times 10^{-8} \Omega \cdot \text{m}$ after 60 minutes of plasma exposure, which is nearly 2.5 times of that of bulk silver.

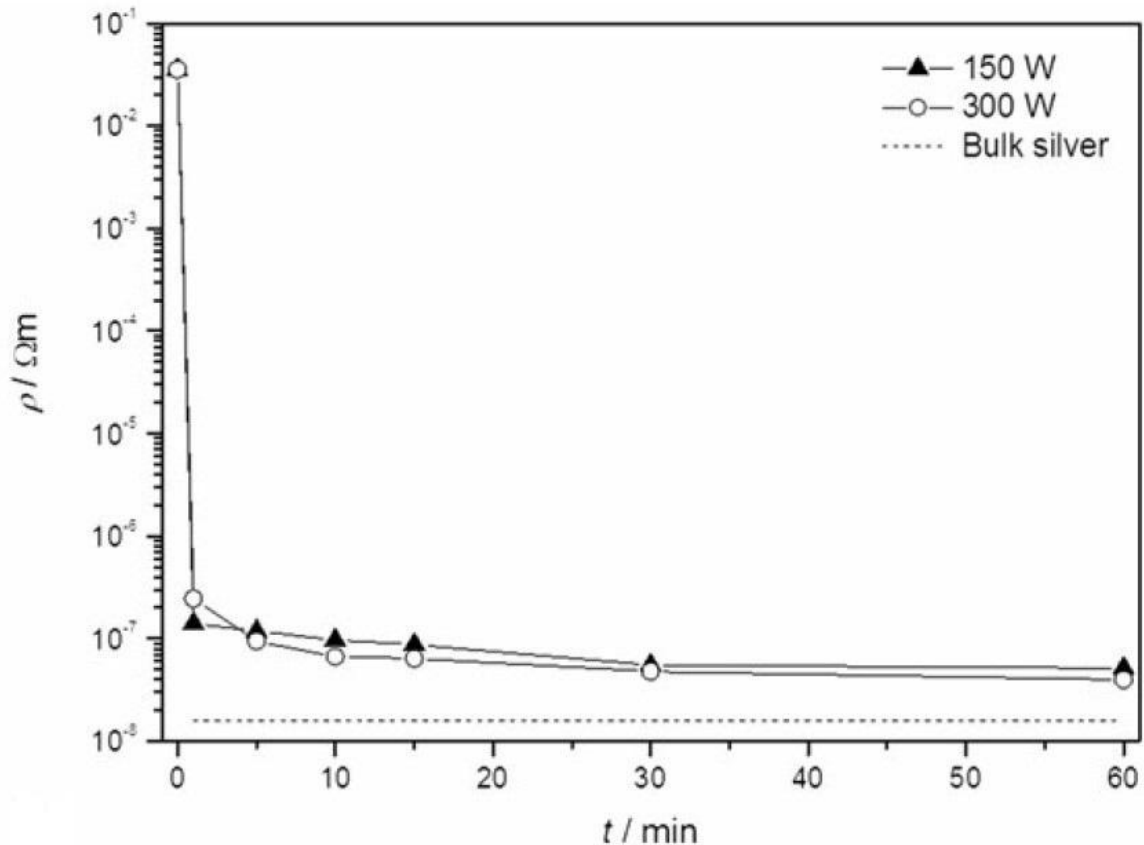


Figure 2.39: Electrical resistivity for silver nano-particle ink ($\sim 20\text{-}30\text{nm}$) as a function of plasma sintering power and sintering time, the temperature for plasma sintering power working on 150W were measured less than 70°C [2.90].

Nanoparticle ink can also be sintered by Ohmic heating, as has been investigated by Roberson *et al.* [2.77]. The lowest electrical resistivity was measured at $40 \pm 0.4 \text{ n}\Omega \cdot \text{m}$ for Ohmic heating silver nano-particle ink (with particle size at $\sim 37 \pm 10\text{nm}$) on a polyimide (PI) substrate after oven curing at 150°C for 20 hours.

Conductive nano-sized particle ink provides a better electrical conductivity after sintering treatment than that of micro-sized particle ink. Also the use of nanoparticles enables ink-jet printing technology for use in printing nanoparticle ink onto the substrate material due to its small particle size. However, one drawback for nanoparticle ink is its higher price (~ 3 times higher than that of silver flake ink [2.78]) [2.79], a typical comparison between silver inks with silver micro-sized flakes and silver nanoparticles is shown in **Table 2.3** [2.80]. The price for silver nanoparticle ink with particle size of 5nm could be costed at around USD\$30 per gram, as reported by Phil [2.81].

Table 2.3: Typical prices for silver-based conductive materials (source: Sigma-Aldrich) [2.80].

Material Type	Price (GBP)	Price per Unit Mass (GBP/gram)
Silver flakes (Micron-sized Ag)	£ 171.5 for 50g	£ 3.43
Nanoparticles (50-60wt% Ag)	£ 866 for 100g	£ 8.66

2.3.3 Liverpool's Laser Assisted Direct Writing (LA-DW) Method at an Infrared Laser Wavelength of 10.6 μ m

Laser Assisted Direct Writing, or LA-DW, is a laser-based technique in Direct Writing developed by the Laser Engineering Group at the University of Liverpool [2.51]. The process adds to direct writing technology by providing a 3-D deposition capability for depositing ink material with a higher viscosity, where the use of laser irradiation can significantly improve the deposition speed and processing quality [2.51].

Much of the earlier work on LA-DW at Liverpool has concentrated on the use of silver-loaded two-part epoxy inks, due to the cheaper price of silver than gold and its reduced oxidation properties compared to copper [2.60].

In the existing Liverpool's LA-DW method, two processing steps are involved: in the first step, liquid epoxy-based silver ink (with 59wt% Ag, 26wt% Resin, and 15wt% solvent) is dispensed on top of a PET substrate to form an ink track geometry (**Figure 2.40**); the silver ink track is solidified and cured by CO₂ laser beam irradiation in a single pass in the second step (**Figure 2.41**) [2.51].

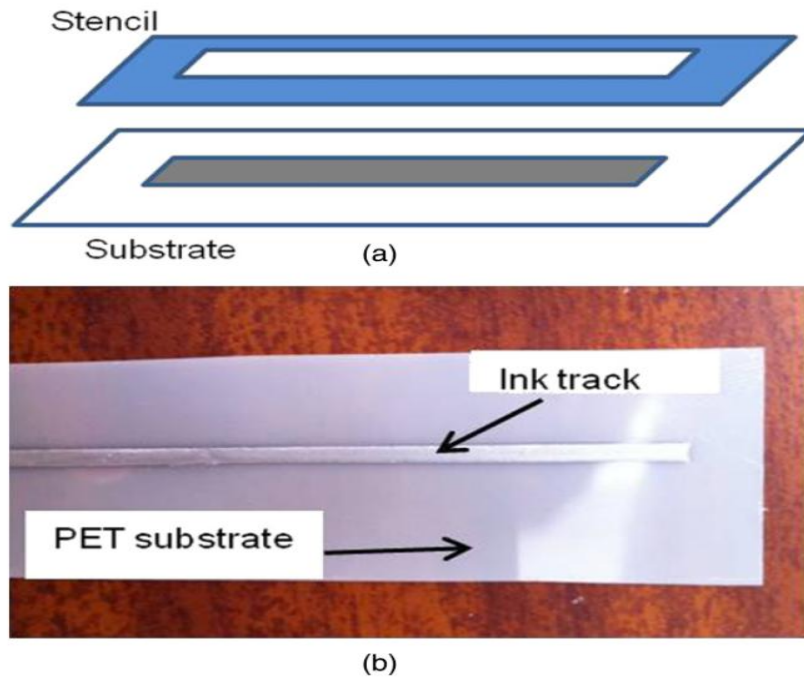


Figure 2.40: In Liverpool's LA-DW method, the ink is dispensed on top of the PET by using a doctor blade method (a) to form an ink track shape (b) [2.51].

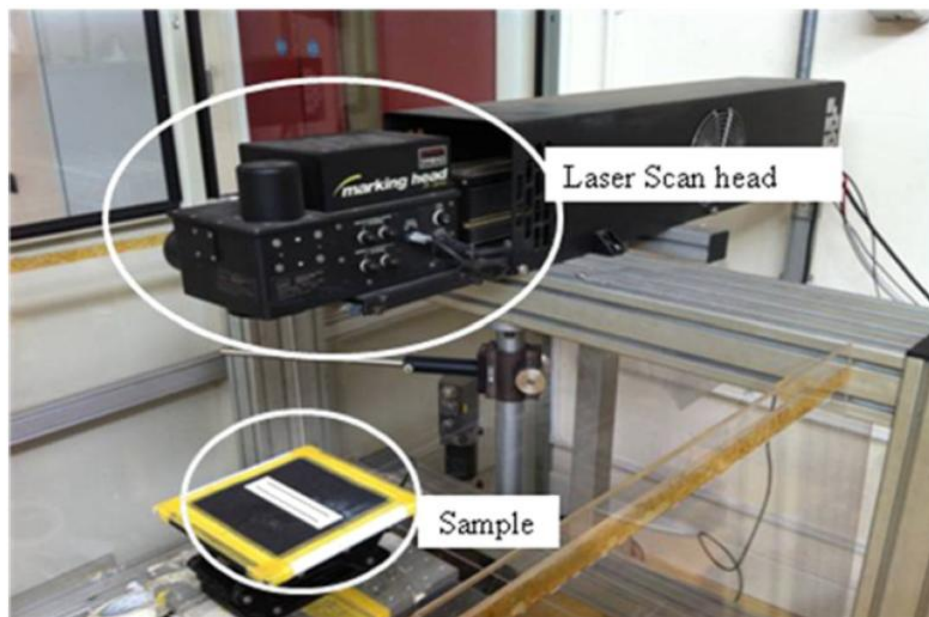


Figure 2.41: A SYNRAD[®] CO₂ laser processing workstation used in LA-DW investigation [2.51].

Figure 2.41 shows the experimental set-up for Liverpool's LA-DW method, the SYNRAD[®] CO₂ laser was used for curing the ink track sample at an infrared wavelength at 10.6 μ m. Laser scanning parameters are controlled by a computer and can form a top-hat laser beam with a maximum output power at 25 Watts.

Fearon *et al.* investigated the laser curing and found out the laser curing result depends on substrate thermal conductivity in addition to laser parameters. In his research, the best achievable resistances for a set of standardised ink tracks were found to be directly related to the substrate thermal conductivities. It was further noted that for each type of substrate that there was an optimum energy input per unit area scanned, above which the ink resistivity would be increased. It was theorised that this was due to thermal damage to the epoxy components of the ink (**Figure 2.42**) [1.3].

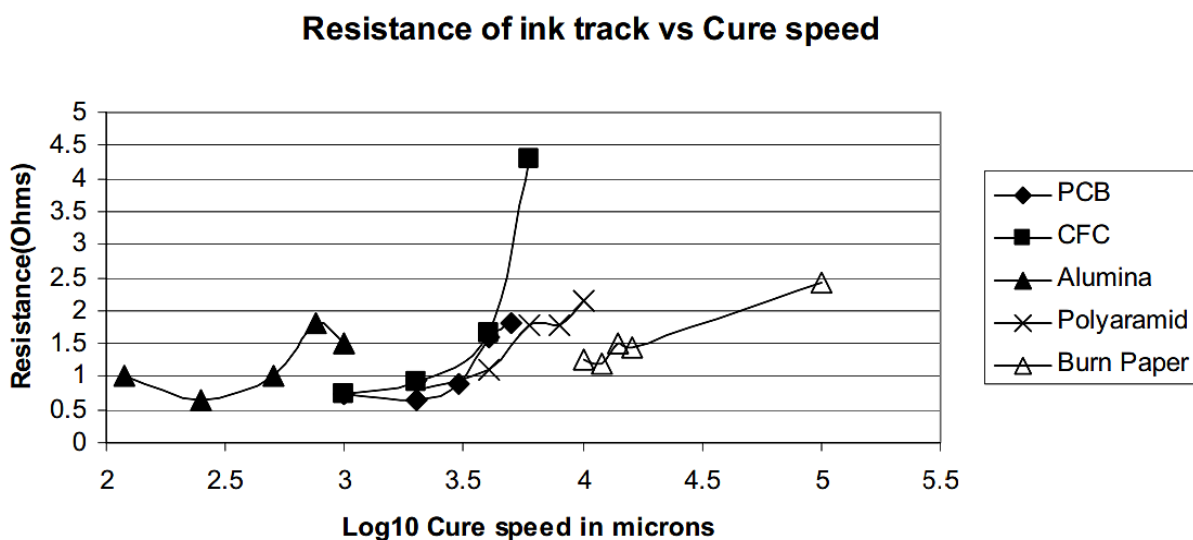


Figure 2.42: Electrical Resistance of ink track as a function of the curing speed [1.3].

One example of an application processed by LA-DW technology is shown in **Figure 2.43**, Sato demonstrated antennas which were cured by a CO₂ laser at an infrared wavelength of 10.6 μ m. Sato also demonstrated the potential of LA-DW in fabricating applications for the aerospace industry [2.52].

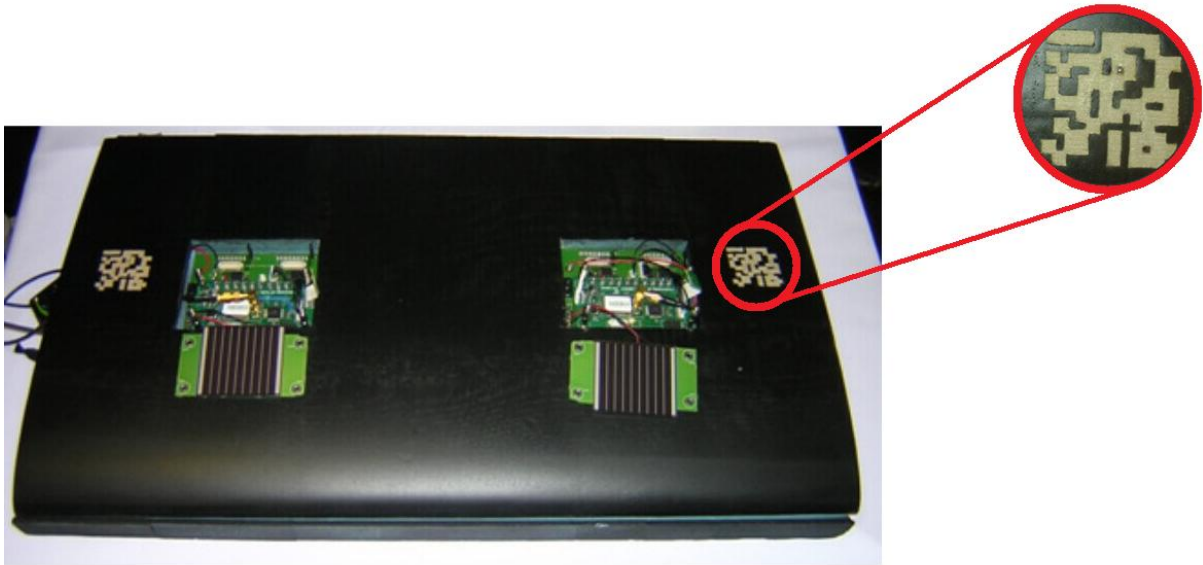


Figure 2.43: A Towards a Wireless Aircraft (TaWA) demonstrator shows antennas which were cured onto a foam wing by a CO₂ laser of the existing Liverpool's LA-DW process [2.52].

Although sensor products were successfully fabricated by using the LA-DW method at Liverpool's laser group, one major drawback was found in its potential for damaging the silver ink track and substrate materials due to the infrared wavelength easily damaging or burning ink or substrate (**Figure 2.44**) [2.52].



Figure 2.44: Substrate and ink track can be damaged as a result of extensive heat caused by laser irradiations at an infrared wavelength [2.52].

2.3.3.1 Curing Mechanism of Liverpool's Laser Assisted Direct Writing (LA-DW) at an Infrared Laser Wavelength of 10.6 μm

The silver ink used in Liverpool's LA-DW method is a D58 epoxy-based conductive silver ink which is supplied by Gwent Electronic Materials, Ltd. (GEM). Three fundamental components were contained in the D58 basic ink: silver flakes with a 59% weight composition, resin complex (mixing Blocked Isocyanates (BI) and Epoxy Resin together) with a 26% weight composition, and Diethylene Glycol Butyl Ether (an organic solvent) with the remaining 15% weight composition (for D58 ink compositions please refer to **Chapter 3** and **Appendix 2**).

Fearon *et al.* summarized the CO₂ laser curing mechanism at 10.6 micron for LA-DW as based on an increasing temperature build up on the top surface of the ink system due to laser incident energy absorbed mainly by resin at the first few microns depth. This leads to solvent evaporation and resin cross-linking as a result of heat conduction through to the bottom of the ink (**Figure 2.45**) [1.3].

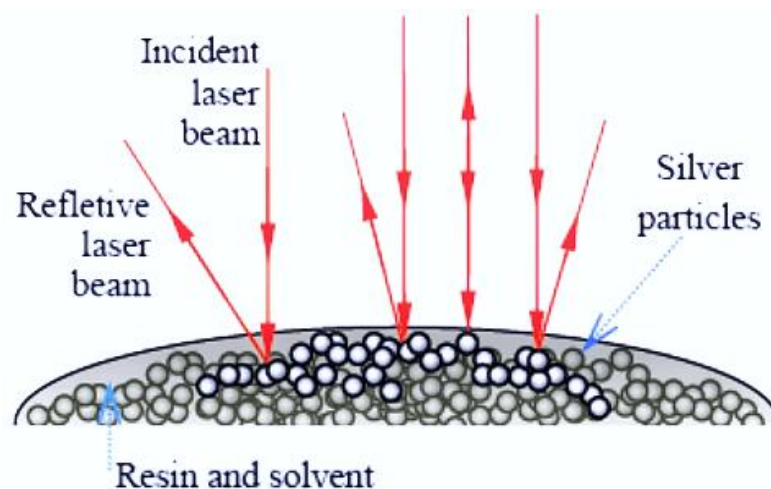


Figure 2.45: Laser curing mechanism of LA-DW at 10.6 μm [2.52].

Shang *et al.* then suggested a temperature variation model as a function of overall heat input (**Figure 2.46**), the energy balance equations (2-1) to (2-6) were mathematically defined according to the temperature variation relationship in **Figure 2.46**.

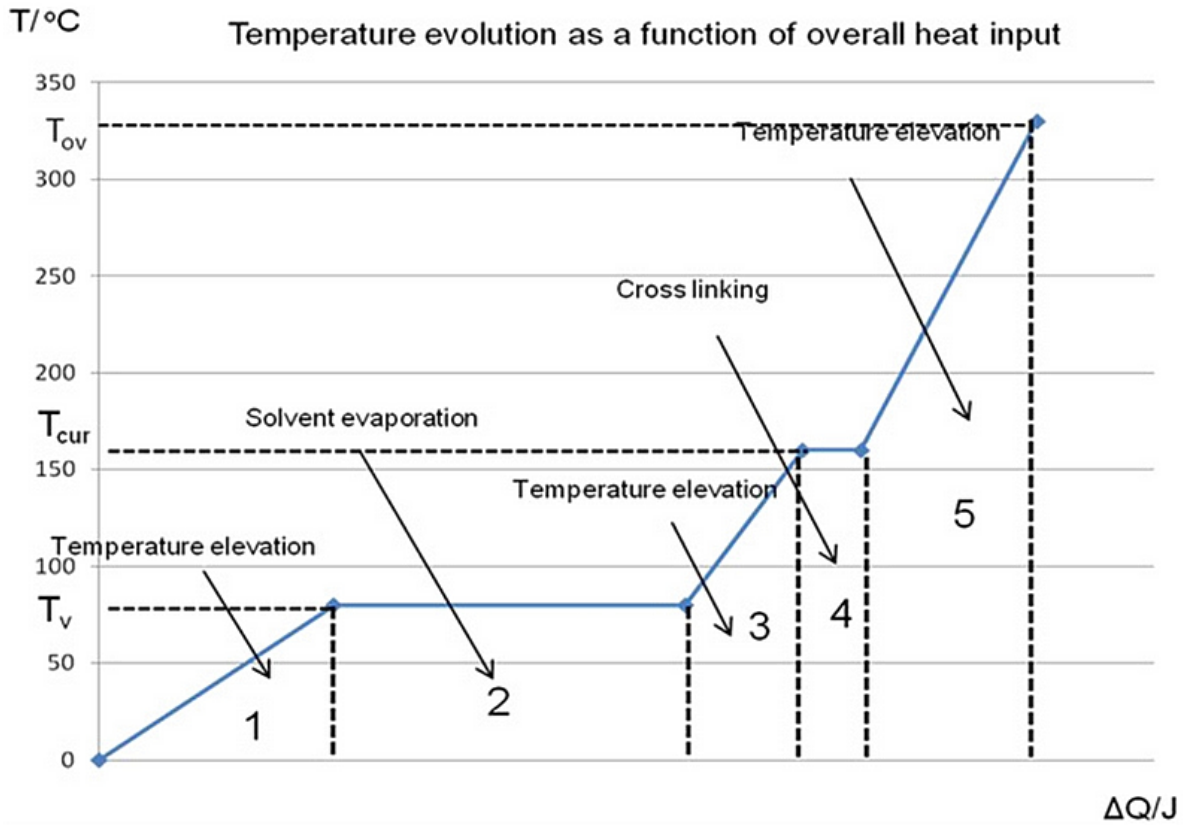


Figure 2.46: Temperature evolution as a function of total heat input during the LA-DW curing process at $10.6\mu\text{m}$ [2.51].

$$\Delta Q = \sum \Delta Q_i = \Delta Q_1 + \Delta Q_2 + \Delta Q_3 + \Delta Q_4 + \Delta Q_5 \quad (2-1)$$

$$\Delta T_1 V [(Ag\%) \rho_{Ag} C_{p(Ag)} + (r\%) \rho_r C_{p(r)} + (s\%) \rho_s C_{p(s)}] = \Delta Q_1 \quad (2-2)$$

$$V(s\%) \rho_s L_s = \Delta Q_2 \quad (2-3)$$

$$\Delta T_3 V [(Ag\%) \rho_{Ag} C_{p(Ag)} + (r\%) \rho_r C_{p(r)}] = \Delta Q_3 \quad (2-4)$$

$$V(r\%) \rho_r L_{cr} = \Delta Q_4 \quad (2-5)$$

$$\Delta T_5 V [(Ag\%) \rho_{Ag} C_{p(Ag)} + (r\%) \rho_r C_{p(r)}] = \Delta Q_5 \quad (2-6)$$

Where:

ΔQ = total energy input,

ΔQ_i = energy input at different stage,

V = unit volume of the ink,

ΔT_i = temperature change at different stage,

$Ag\%, r\%, s\%$ = composition percentages of silver micro-particles, resin and solvent,

$\rho_{Ag}, \rho_r, \rho_s$ = densities of silver micro-particles, resin and solvent,

$Cp_{(Ag)}, Cp_{(r)}, Cp_{(s)}$ = specific heat capacities of silver micro-particles, resin and solvent,

L_s = latent heat of solvent,

L_{cr} = latent heat for cross-linking.

A laser curing mechanism at 10.6 μm can be concluded based on Fearon and Shang's theories, in which the localized temperature rises due to laser energy absorption by the liquid components of the ink at 10.6 μm (*Stage 1* in **Figure 2.46**), which causes a rapid solvent evaporation (*Stage 2* in **Figure 2.46**). The composition of overall ink system is changed due to solvent evaporation at the end of *stage 2*, which reduces the overall specific heat capacity of the ink (*Stage 3* in **Figure 2.46**). Further absorption of laser induced energy cross-links the resin (*Stage 4* in **Figure 2.46**). Beyond *stage 4* the ink is cured and further temperature rise can damage the ink and substrate materials as a result of over-cure (*Stage 5* in **Figure 2.46**).

2.3.3.2 The Effect of Wavelength on The LA-DW Method

Dengler *et al.* investigated the absorbance of silver nano-particles [2.54], **Figure 2.47** shows the laser energy at the wavelength of 532nm couples into silver particles better (~14% more absorption) than that of 1064nm, which indicates that a LA-DW process at 532nm can significantly increase the laser energy absorption efficiency and therefore can result in quicker resin cross-linking process.

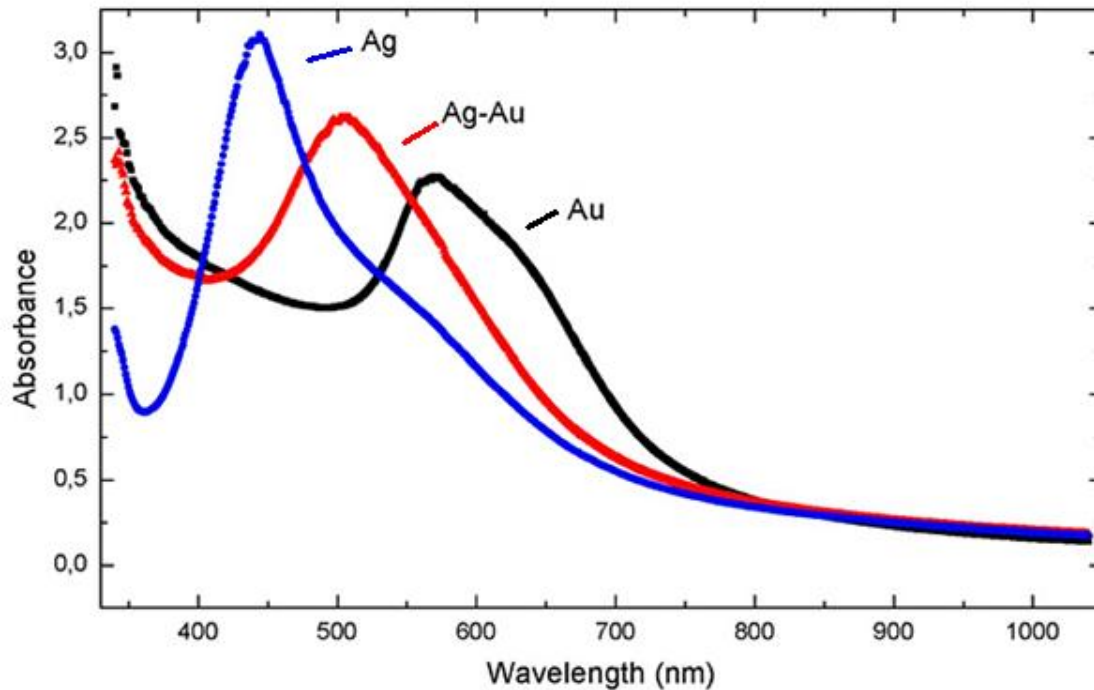


Figure 2.47: Absorbance spectrum of silver and gold particles [2.54].

Although silver particles are highly absorbed at an ultra-violet (UV) wavelength (**Figure 2.47**), it can be seen in **Figure 2.48** for the transmission spectrum of Polyethylene terephthalate (PET) [2.55], that a strong absorbance to wavelengths below 330nm at UV region is observed, in which the wavelength can cause chemical reactions to take place to damage the polymer substrate and result in polymer degradation [2.56] (**Figure 2.49**).

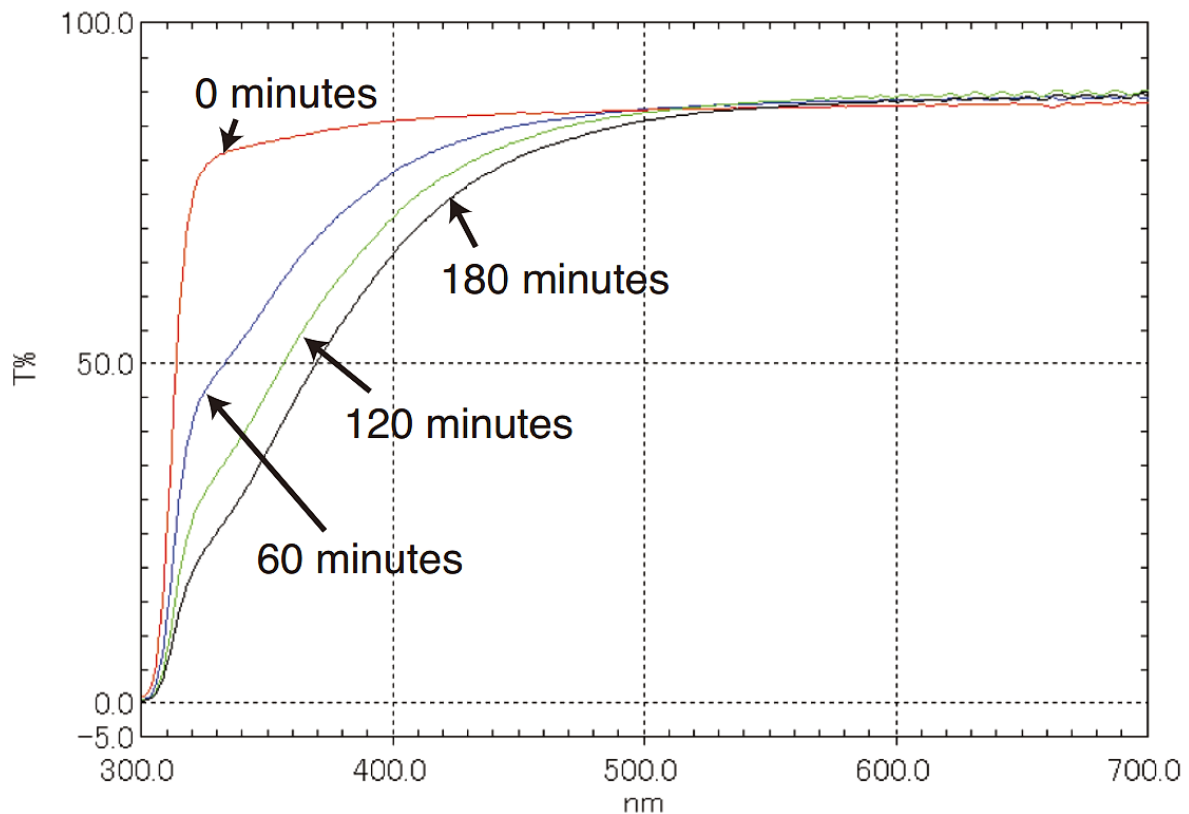


Figure 2.48: Absorbance spectrum of PET polymer substrate, the red curve labelled '0 minutes' can be treated as a clean PET substrate as it has not been irradiated by UV irradiations [2.55].

The laser wavelength used in Liverpool's LA-DW method is at $10.6\mu\text{m}$ in the infrared region, which can result in an extensive thermal effect to the polymer substrate as well as to ink materials. Lee *et al.* indicated a photothermal ablation effect to the polymer substrate as a result of molecular excitation for the infrared region [2.57].

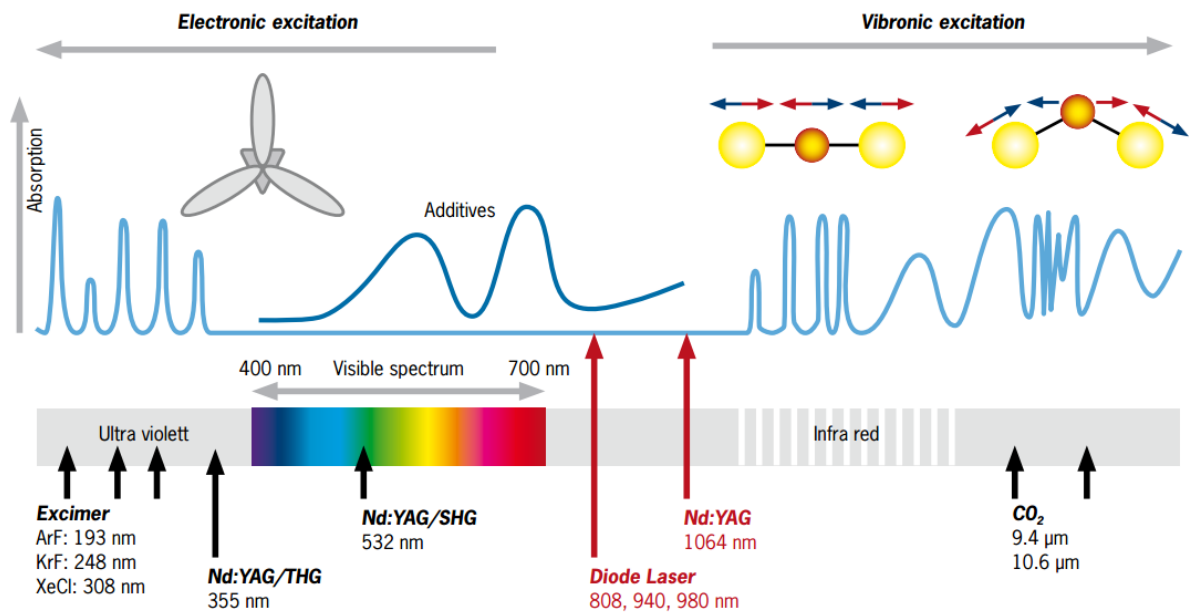


Figure 2.49: Both UV and infrared wavelengths can cause damage to polymer substrate, leaving the visible wavelength as a suitable range for curing functional materials on polymer substrate [2.58].

As both ultra-violet and infrared wavelengths are not suitable for LA-DW process, an alternative laser beam source is suggested with the laser beam irradiation within the range of the visible wavelength. The frequency-doubled Nd:YAG laser with wavelength at 532nm therefore becomes a potential replacement to CO₂ laser for improving the overall curing quality.

2.4 Summary of the State of the Art & Knowledge Gaps in Solidifying Conductive Inks

Two technologies can be categorized for the post processing step to solidify conductive inks – Curing technology and Sintering technology.

The curing technology refers to the post processing work based on the percolation theory and is the dominant post processing step for conductive inks containing microparticles. Curing microparticle ink requires a longer curing time in oven (a typical oven curing time is 1 hour for curing inks on a polymer substrate at a low temperature $<150^{\circ}\text{C}$). Alternative curing technologies have been examined to replace conventional thermal curing in oven for reduced curing time, increased curing quality (reduced electrical resistivity) and to prevent damaging the substrate at the high temperatures ($>700^{\circ}\text{C}$) usually used to fire the ink such as in Oven processing, these include: Ohmic curing process, and Microwave curing process.

Sintering technology however, refers to the post processing step based on the sintering effect for conductive inks containing nanoparticles. Conductive nanoparticle inks that can be sintered at a typical sintering temperature above 200°C have been reported. Various sintering technologies have been shown to provide a localized heating solution. These are: laser based sintering technology (488nm, 514nm, 532nm, and 980nm), and plasma sintering technology.

As compared in **section 2.3**, the processing time can be reduced from a typical one hour for curing a conductive microparticle ink in an oven down to a couple of minutes for sintering nanoparticle inks in an oven at a higher temperature. Localized sintering processes such as laser sintering technology can further reduce the processing time down to a couple of seconds. The solidification quality of the conductive ink material after post processing can be indicated by its value of electrical resistivity, in which the lower the electrical resistivity of the ink, the better processing quality of the ink can be said to have been achieved. Although the lower electrical resistivity of nanoparticle ink after the sintering process than that of

microparticle ink after curing process has been observed (~3 times lower), sintering of conductive ink risks damage to polymer substrate material due to excessive thermal input. In addition, the use of nano-sized particles in ink during a conductive ink solidification process can be more expensive (~2.5 times higher in cost) than that of micro-sized particle ink.

No research has been reported that uses a laser to cure epoxy-based conductive micro-sized particulate silver loaded ink with the laser wavelength at 532nm. To investigate this localized laser curing process is important, as this can fill a knowledge gap in the field and extend the knowledge of curing technologies. A further anticipated benefit is in reducing thermal effects on both ink and substrate by laser curing epoxy-based microparticle silver ink at 532nm.

2.5 Chapter Summary

This Chapter has discussed the current state of the art in direct writing technologies and their applications prior to the contributions of work described in this thesis.

The current technologies reviewed have included inkjet printing and aerosol methods in droplet-based direct writing technologies, laser-based and focused-ion beam-based direct writing technologies, nScrypt flow-based direct writing technology, tip-based direct writing technologies, as well as the screen printing technology.

Post processing technologies including curing and sintering techniques to solidify conductive ink have been discussed for distinguishing definitions of curing and sintering. The curing and/or sintering results of conductive inks have been compared and discussed. Sintering conductive nanoparticle ink can reduce the processing time and can also reduce the electrical resistivity of the ink after the process. However the sintering process requires a higher processing temperature which is risky to polymer-based substrate due to an excessive heating effect. In addition, nanoparticle ink is found to be more expensive than equivalent conductive ink with micro-sized particles. The only reported research into the laser curing of microparticle loaded epoxy inks has concentrated on using 10.6 μm as a direct thermal replacement for oven curing process, an approach which has limitations due to the likelihood of damage to both the ink and substrate. Therefore an opportunity arises to investigate and extend the knowledge base in laser curing processes to include the investigation of epoxy-based conductive silver microparticle ink at the laser wavelength of 532nm.

3. EXPERIMENTAL: METHODS, MATERIALS AND APPARATUS

3.1 Substrate Material

The substrate material used in this investigation is polyethylene terephthalate, or PET for short. Its flexibility and good thermoplastic properties make the PET film a suitable substrate material for this investigation. Good chemical and gas resistance makes the PET film a potential future substrate material used to replace FR4 dielectric which is commonly used for Printed Circuit Boards (PCBs) in electronics [3.1].

The PET film was supplied by Goodfellow[®] and had an average thickness of 0.35mm (**Figure 3.1, Table 3.1**). The film is useful as the substrate material in this investigation and kept below the melting point of 260°C [3.9]. In this investigation, the PET film was cut into small pieces with a uniform rectangular geometry so that the epoxy-based conductive silver ink could be directly printed on top of the PET substrate prior to undergoing further treatments in an oven or under laser beam irradiations.



Figure 3.1: Goodfellow[®] PET film used in this investigation.

Table 3.1: Typical material properties of Goodfellow® PET films [3.1]

Material Property	SI units	Value
Thermal Conductivity @23°C	$\text{W m}^{-1} \text{K}^{-1}$	0.13-0.15
Dielectric Strength @25 μm thick	kV mm^{-1}	300
Initial Tear Strength	$\text{g } \mu\text{m}^{-1}$	18-54
Specific Heat	$\text{kJ kg}^{-1} \text{K}^{-1}$	1.3
Density	g cm^{-3}	1.3-1.4
Refractive index		1.58-1.64
Coefficient of thermal expansion	$\times 10^{-6} \text{K}^{-1}$	20-80
Lower working temperature	$^{\circ}\text{C}$	-40 to -60
Upper working temperature	$^{\circ}\text{C}$	115-170

3.2 Ink System

3.2.1 Introduction to Epoxy-based Silver Ink

The epoxy-based conductive silver ink is a liquid mixture obtained by mixing silver particles, resin, solvent and other additives together. The silver ink's dynamic viscosity is maintained low at a lower temperature, which helps the ink to flow in the printing stage, the ink's viscosity increases with an increased heating temperature, until the point at which temperature rise removes the solvent and eventually cross-links the resin, which leaves a cured and highly electrical conductive solid material.

D58 epoxy-based conductive silver ink used in this investigation was supplied by Gwent Electronic Materials, Ltd. (GEM) (**Figure 3.2**). The ink contains only three basic components: silver micro-sized flakes (59% by weight), a resin complex which contains Blocked Isocyanates and Epoxy Resin mixture (26% by weight), and Diethylene Glycol Butyl Ether solvent (15% by weight). GEM also supplied amounts of each ink component (Silver micro-sized flakes, Blocked Isocyanates (BI), epoxy resin and solvent) for investigating mixtures with varying amounts of each individual component. This would simplify the study of curing mechanism theories in **Chapter 5**.

D58 silver ink composition (wt%)

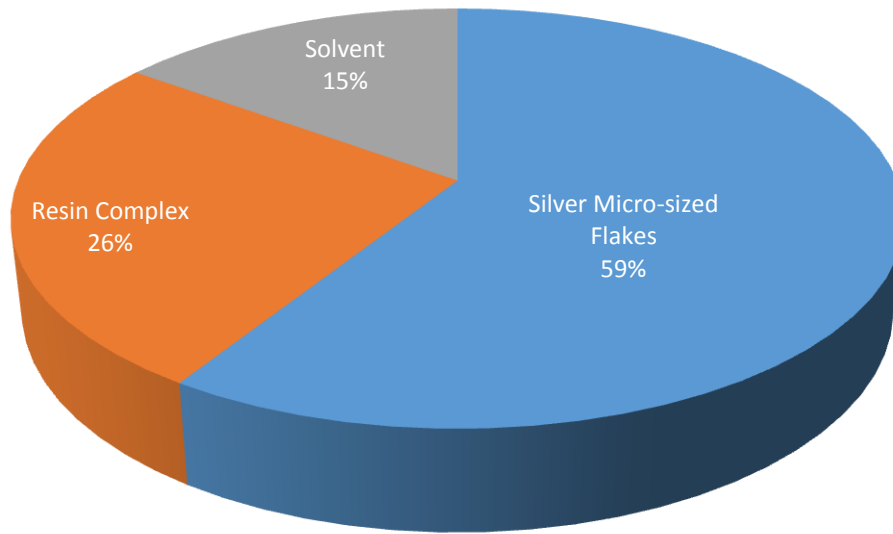


Figure 3.2: Illustration shows D58 silver ink composition by weight percentage (Data from Gwent Electronic Materials, Ltd. (GEM)).

In addition to D58 epoxy-based conductive silver ink, GEM also supplied epoxy-based silver inks with variant ink compositions for investigating curing results with a changing ink composition. Due to commercial confidential properties, only approximated ink compositions were supplied from GEM for this investigation (**Table 3.2**).

Table 3.2: Approximated compositions for silver inks used in this investigation. (Data from GEM)

Ink Name	Approximated composition	Silver content (wt%)
Silver Ink D58	Silver flakes, Epoxy resin, Blocked Isocyanates, Solvent	59%
Laser Curable Silver Ink D5	Silver flakes, Epoxy resin, Blocked Isocyanates, Solvent	78%
Graphite Doped Silver Ink D5	0.5wt% Graphite, Silver flakes, Epoxy resin, Blocked Isocyanates, Solvent	61%
Silver Ink D2	Silver particles (micro- and nano-size), Epoxy resin, Blocked Isocyanates, Solvent	45%

3.2.2 Introduction to Epoxy-based Silver Ink Components

3.2.2.1 Silver Micro-sized Flakes

The shape factor of silver flakes improves the curing result. The wider surface contact areas of silver flakes can significantly increase the electrical conductivity of the ink after cure. This improved electrical conductivity property results from improved stacking of silver flakes on top of each other within a reduced volume of the ink as a result of solvent removal from the ink system, this has been investigated by Banfield as discussed in **Chapter 2** [2.72].

A typical SEM image of Silver micro-sized flakes in D58 epoxy-based silver ink is shown in **Figure 3.3** below. As seen from the **Figure 3.3**, silver flakes were stacked on top of each other with a typical flake size at a size range of a few to tens of microns, which is larger than that of silver microparticles in conductive silver inks (Ercon E1660, DuPont CB208, and Ferro F3309F) as discussed in **Chapter 2**. This silver flake shape and size can therefore provide an increased electrical conductivity for D58 epoxy-based conductive silver ink after cure.

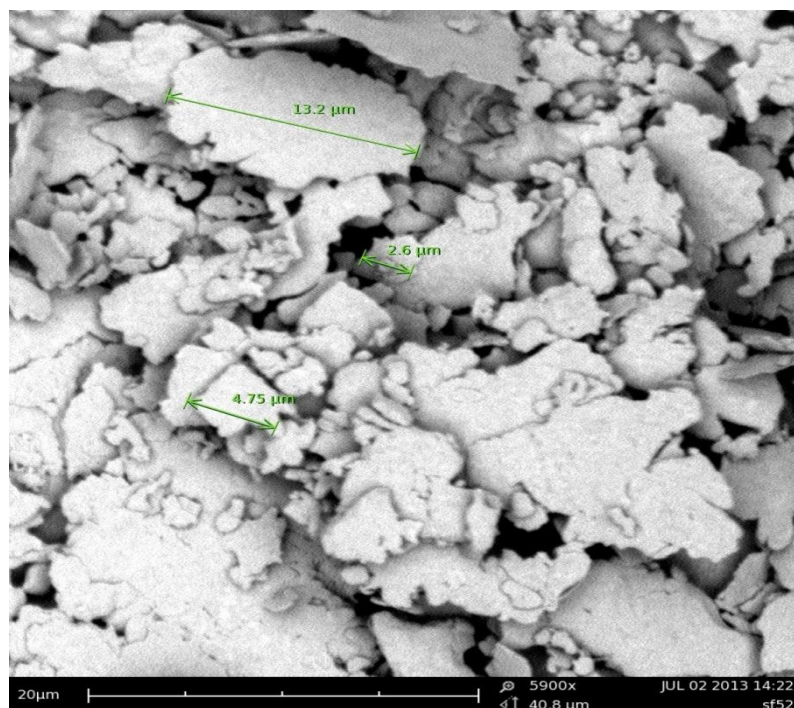


Figure 3.3: A typical SEM image of silver flakes used in D58 conductive silver ink.

3.2.2.2 Resin Complex

The resin complex, or Resin system, is a two-part resin paste that mixes the adhesion base - epoxy resin and the hardener (which is composed of Blocked Isocyanates (BI)) together with a certain mixing ratio. The hardener significantly speeds up the resin cross-linking process at a higher temperature by unblocking the polymer chains to promote a quicker cross-linking process. By adjusting the mixing ratio between epoxy resin and BI, the cross-linking rate can be controlled. In this investigation, the mixing ratio between epoxy resin and BI was suggested as 2:1 by volume composition by GEM.

3.2.2.3 Organic Solvent

The organic solvent used in this investigation is Diethylene Glycol Butyl Ether, or Butyl Carbitol. It helps to reduce the overall viscosity of the ink system and makes the liquid ink material flow more easily during the printing stage. The GEM-supplied Butyl Carbitol combines with the silver micro-sized flakes and resin complex into a D58 epoxy-based conductive silver ink paste.

3.3 Equipment

The equipment includes the experimental devices used in sample preparation and processing, including the technique used to print epoxy-based silver conductive ink to the PET substrate, as well as different heating sources used in experiment to thermally cure the sample such as infrared CO₂ laser at 10.6μm wavelength, Nd:YAG frequency doubled DPSS laser at the laser irradiation wavelength of 532nm, and a heating oven. In addition, analysis devices used to measure sample's physical and chemical properties after processing are discussed in this section, including devices that measures sample size, geometry, chemical bonding information, electrical resistivity, and hardness properties, etc.

3.3.1 Experiment Equipment

3.3.1.1 Frequency Doubled Nd:YAG Laser System at 532nm

The BMI® Lyra 100/60 Nd:YAG diode-pumped solid-state (DPSS) nanosecond laser was used as the visible wavelength laser source to cure epoxy-based conductive silver ink (**Figure 3.4**), with a frequency doubled wavelength at 532nm. The Pulse Repetition Frequency (PRF) was 15kHz with energy per pulse at 4mJ/pulse. The output laser beam with wavelength at 532nm was directed horizontally to a periscope, then directed vertically downwards and defocused by a ~50mm focal length lens to the substrate. This top-hat laser beam irradiated an ink track sample with a spot diameter of 5mm (**Figure 3.6, 3.7**) on an Isel® automation's CNC x-y working stage (**Figure 3.5**).



Figure 3.4: A BMI® Lyra 100/60 frequency doubled Nd:YAG laser with wavelength at 532nm.



Figure 3.5: A isel[®] automation's CNC controlled working stage.

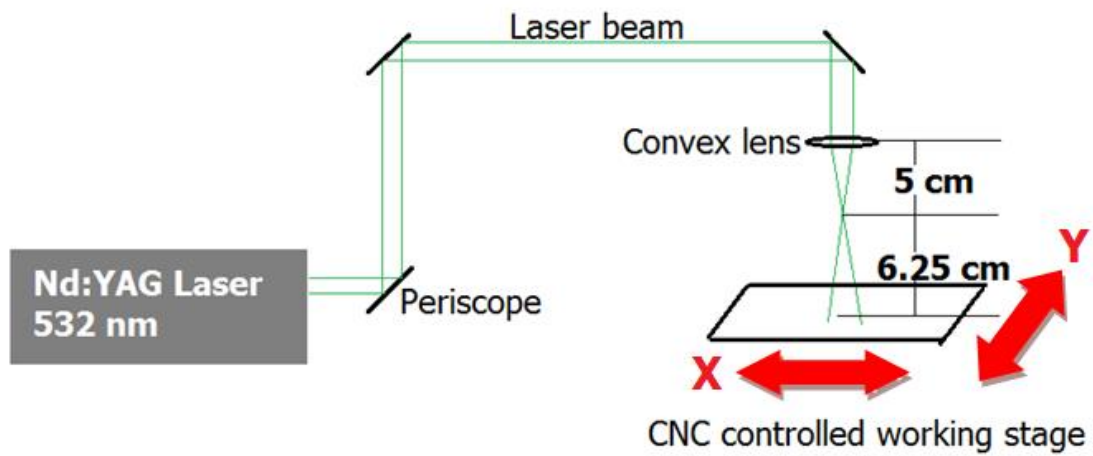


Figure 3.6: The experimental set-up for curing a conductive silver ink track using a Nd:YAG DPSS laser and CNC controlled working stage.

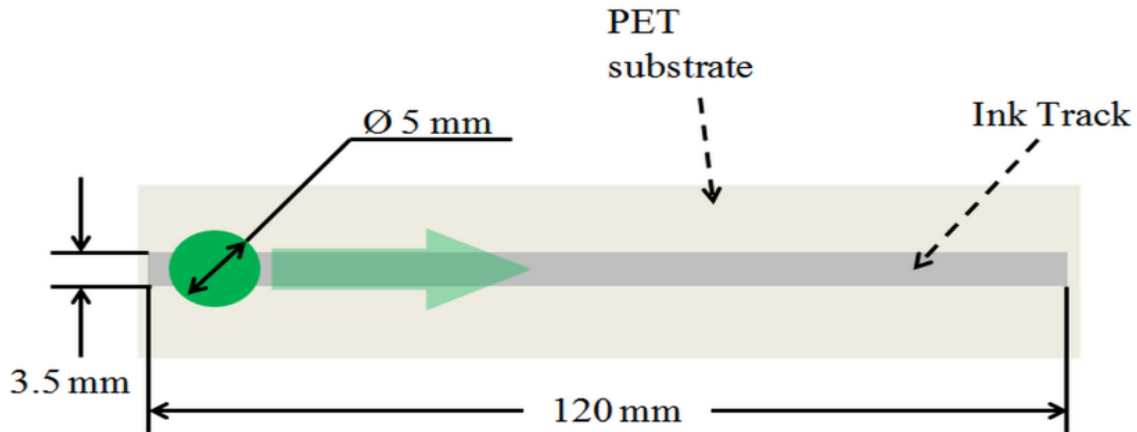


Figure 3.7: Illustration of laser beam scanning path.

The laser beam loses $\sim 8\%$ of its output power when transmitted through the convex lens, due to optical reflections at the lens surfaces; therefore, the actual laser output power is 8% less than the output power measured by a high power meter (**Table 3.3, Figure 3.8**).

Table 3.3: Laser output power measurement for Nd:YAG laser used in this investigation.

Laser Driving Current (A)	Laser Output Power (W)	Actual Power after transmitting through the lens (W)
11	0	0
11.2	0	0
11.4	0	0
11.6	0.1	0.092
11.8	0.3	0.276
12	0.5	0.46
12.2	0.7	0.644
12.4	1.4	1.288
12.6	2.3	2.116
12.8	3.3	3.036
13	4.2	3.864
13.2	5.5	5.06
13.4	7	6.44
13.6	8.5	7.82
13.8	10.1	9.292
14	11.9	10.948
14.2	14.1	12.972
14.4	15.2	13.984
14.6	16.8	15.456
14.8	18.8	17.296
15	19.5	17.94

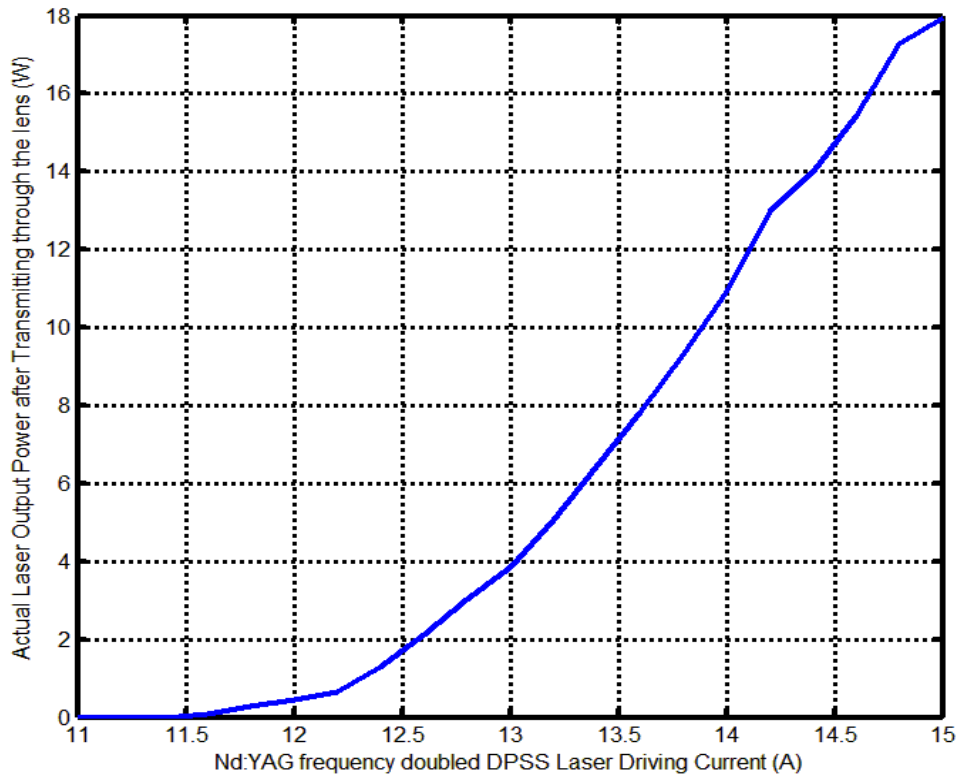


Figure 3.8: Laser output power for Nd:YAG laser used in this investigation is a function of laser driving currents.

3.3.1.2 Other Heating Sources

3.3.1.2.1 CO₂ Laser System at 10.6 μ m

A SYNRAD[®] CO₂ laser marker with a DH series DH3X-200CH beam scanning head was used in this investigation for curing the sample at an infrared wavelength of 10.6 μ m (**Figure 3.9**). This SYNRAD[®] laser system produces a top-hat mode laser beam with beam diameter of 5mm, and provides the maximum average power at 25W (**Figure 3.10**). Laser scanning speed and scanning geometry are controlled by a computer connecting to this SYNRAD[®] laser marking system.

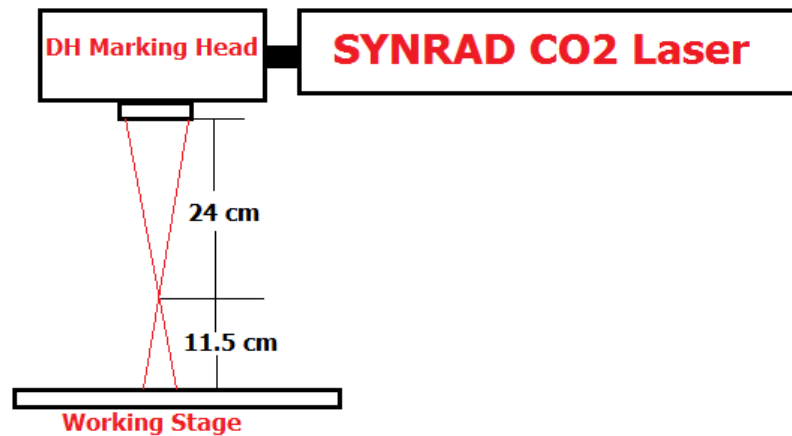


Figure 3.9: Illustration of the SYNRAD[®] CO₂ laser marker system in experiment.



Figure 3.10: A SYNRAD[®] CO₂ laser marker with DH scanning head.

3.3.1.2.2 Oven

A Memmert[®] SM100 drying cabinet (**Figure 3.11**) was used to thermally cure epoxy-based silver inks in this investigation, which provided a comparative analysis of cured ink samples. The curing temperature could be manually adjusted from 0°C to 220°C. **Table 3.4** shows a comparison between the temperature readings measured by the oven's thermometer and the temperature readings measured by a Type-K thermocouple (**Table 3.4, Figure 3.12**).



Figure 3.11: A memmert[®] SM100 drying cabinet used in this investigation.

Table 3.4: Temperature calibration measurements for memmert[®] SM100 Oven.

Temperature reading on Oven setting (°C)	Temperature reading on Oven monitor (°C)	Temperature reading on Type-K thermocouple (°C)
50	52	43
60	60	59
70	68	69
80	78	79
90	88	89
100	98	100
110	108	110
120	118	121
130	130	133
140	139	142
150	152	153

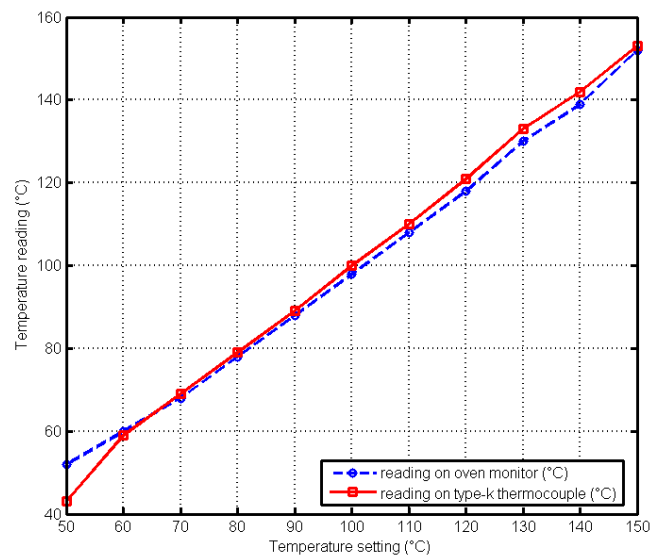


Figure 3.12: Temperature comparisons between temperature measured by a Type-K thermocouple and temperature measured by a thermometer of the Oven.

3.3.1.2.3 Heating Plate

A Fisher Scientific® FB15001 heating magnetic stirrer (**Figure 3.13**) was used as a heating platform for investigating the relationship between an increasing temperature and the dynamic viscosity for liquid components of D58 epoxy-based conductive silver ink i.e. the resin complex and organic solvent. The maximum heating temperature for this heating plate was 370°C, in this investigation the heating temperature was limited within the range between 40°C and 70°C to avoid the evaporation of liquid components. This helped to develop a curing mechanism theory in **Chapter 5**.

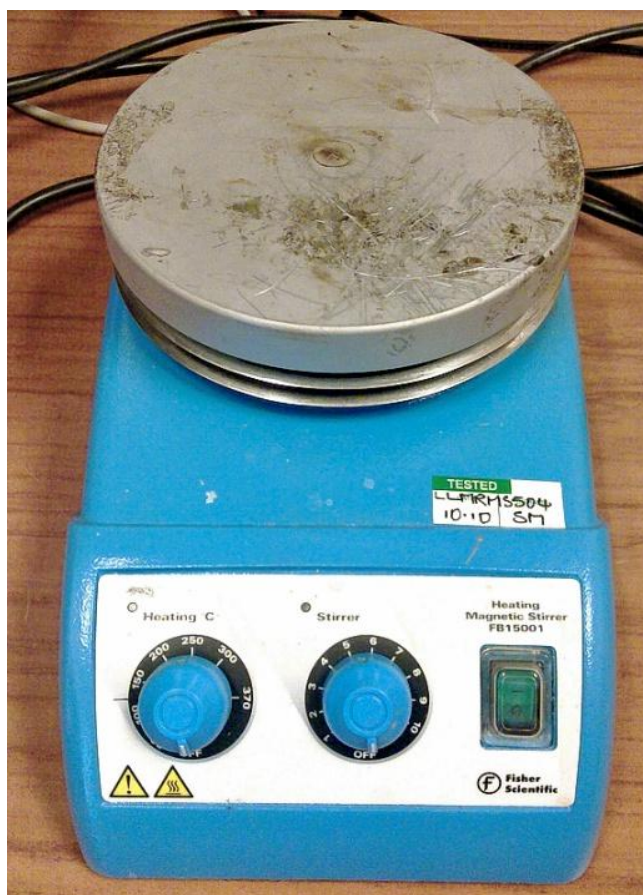


Figure 3.13: Fisher Scientific® FB15001 heating magnetic stirrer.

3.3.1.3 Epoxy-based Silver Ink Doctor Blading Method

The liquid epoxy-based conductive silver ink was dispensed onto the PET substrate by using a manual doctor blading method as discussed in **Chapter 2 (Figure 3.14)**. A metal panel was used as a stencil and placed on top of the PET and held by tape leaving a negative track-shape image. The epoxy-based silver ink was drawn above this negative image using a scraper. On removal of the stencil a finished epoxy-based silver ink track was produced with typical dimensions 120mm long and 3.5mm wide.

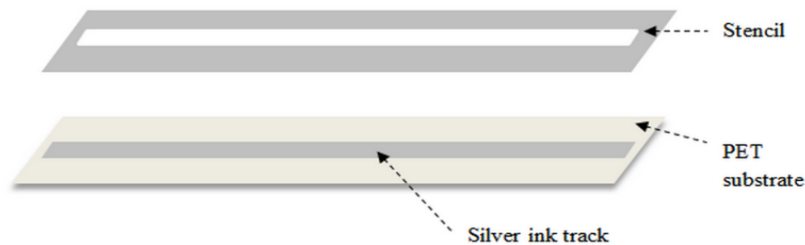


Figure 3.14: A silver ink track sample prepared by screen-printing method.

The sequence of the doctor blading method is shown in **Figure 3.15**. Two layers of masking tape were covered above the PET substrate for creating a depth of the ink track to be printed (b), a knife was used to carve a negative track shape image along internal edges of the stencil (c), then the epoxy-based conductive silver ink was printed on PET substrate by pushing the ink along the negative track shape image (e), and eventually left a finished ink track ready to cure (g).

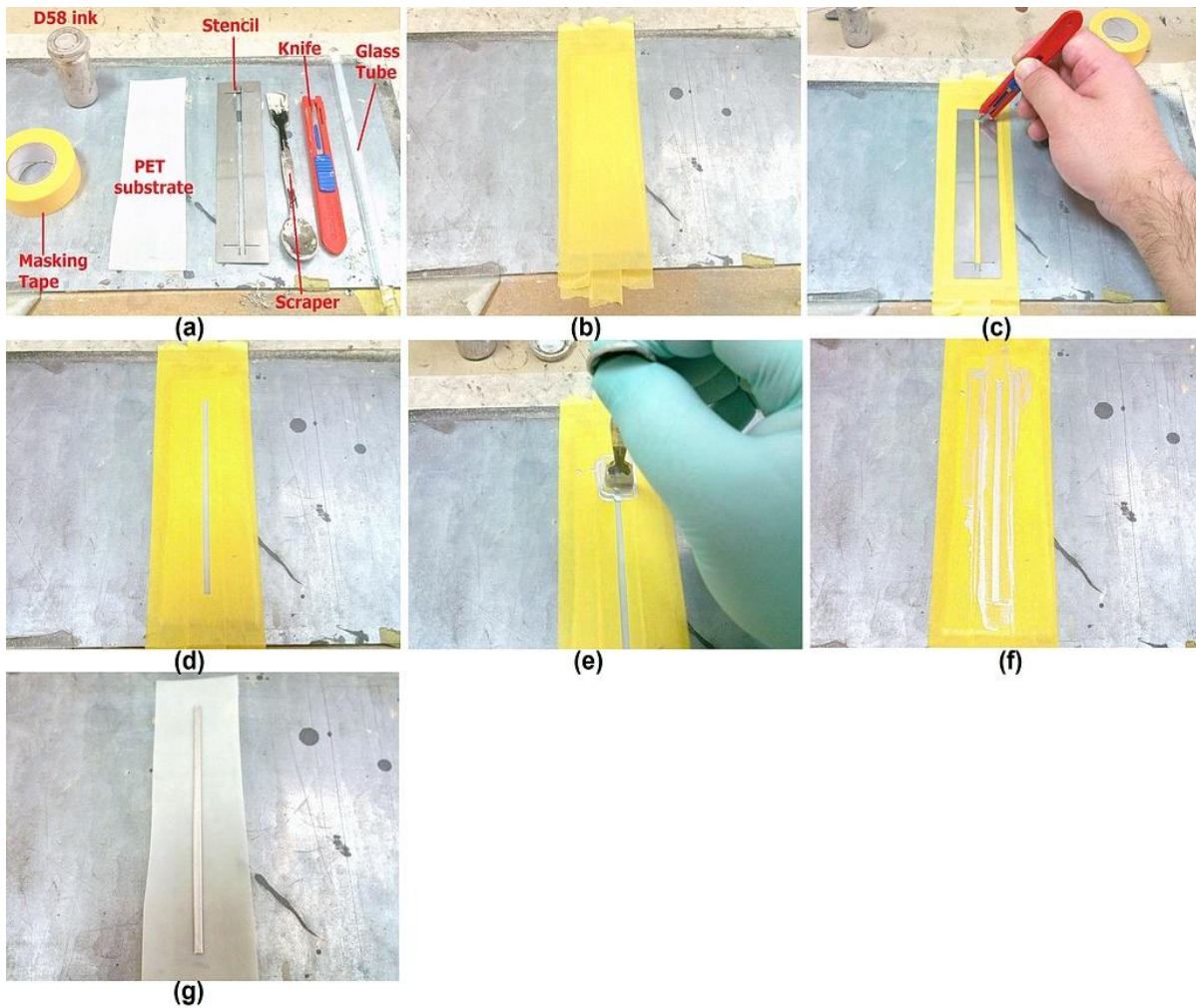


Figure 3.15: Illustration shows the sequence of Liverpool laser group's doctor blading method. (a) Equipment for doctor blading method, (b) PET substrate was covered by two layers of masking tape, (c) A negative track shape image was carved by a knife along internal edges of the stencil, (d) The carved tape was peeled off for followed printing process, (e) A scraper was used for printing epoxy-based conductive silver ink along the negative track shape image, (f) A finished epoxy-based conductive silver ink track, and (g) A finished epoxy-based conductive silver ink track with masking tape removed.

3.3.2 Analysis Equipment

3.3.2.1 Surface Morphology Measurement of Epoxy-based Silver Ink

Surface roughness can result in negative effects on a finished sample, particularly for cured antenna samples used in high frequency telecommunications. A roughened surface on an antenna used in high frequency communication can significantly attenuate its transmitted signal, as found by Coonrod [3.2].

Figure 3.16 shows a Veeco[®]'s WYKO NT1100 white light interferometer used in this investigation for obtaining cross-sectional information of the epoxy-based silver ink track sample. In white light interferometry, the interference fringes are produced by combining light reflected from a mirror and light reflected from the sample [3.6]. This WYKO NT1100 white light interferometer operates in Vertical Scanning Interferometry (VSI) mode based on white light vertical scanning interferometry for measuring the sample's roughness and surface geometry properties.

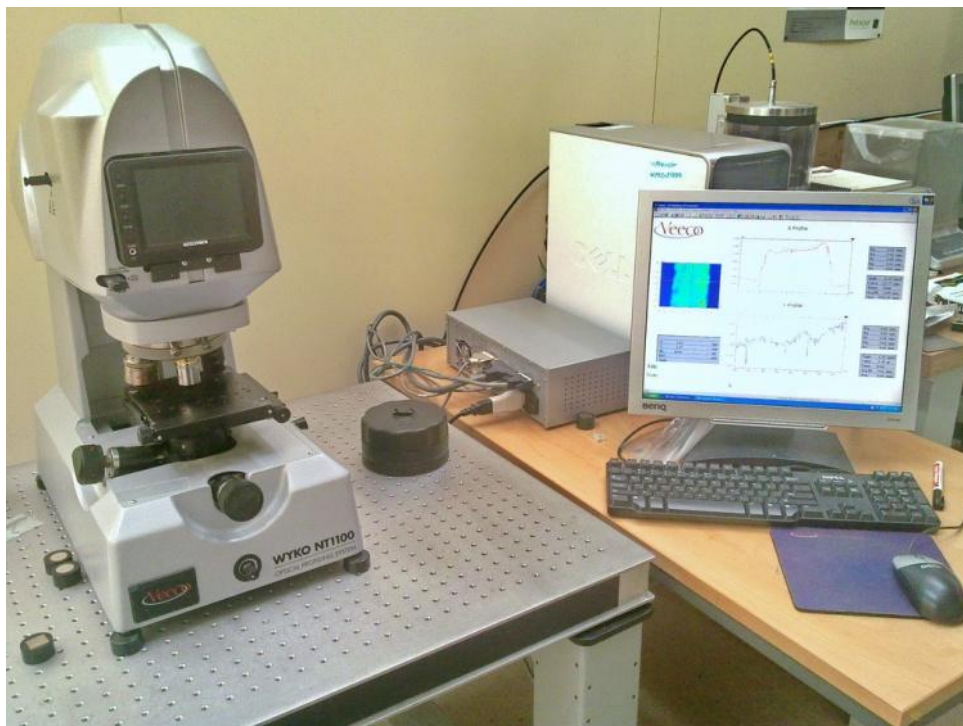


Figure 3.16: The Veeco[®]'s WYKO NT1100 white light interferometer used in this investigation.

Figure 3.17 shows the working principle of a WYKO white light interferometer working in VSI mode. The objective moves downward vertically to form an interference pattern, which contains each point's interference information of the sample surface at various heights [3.10].

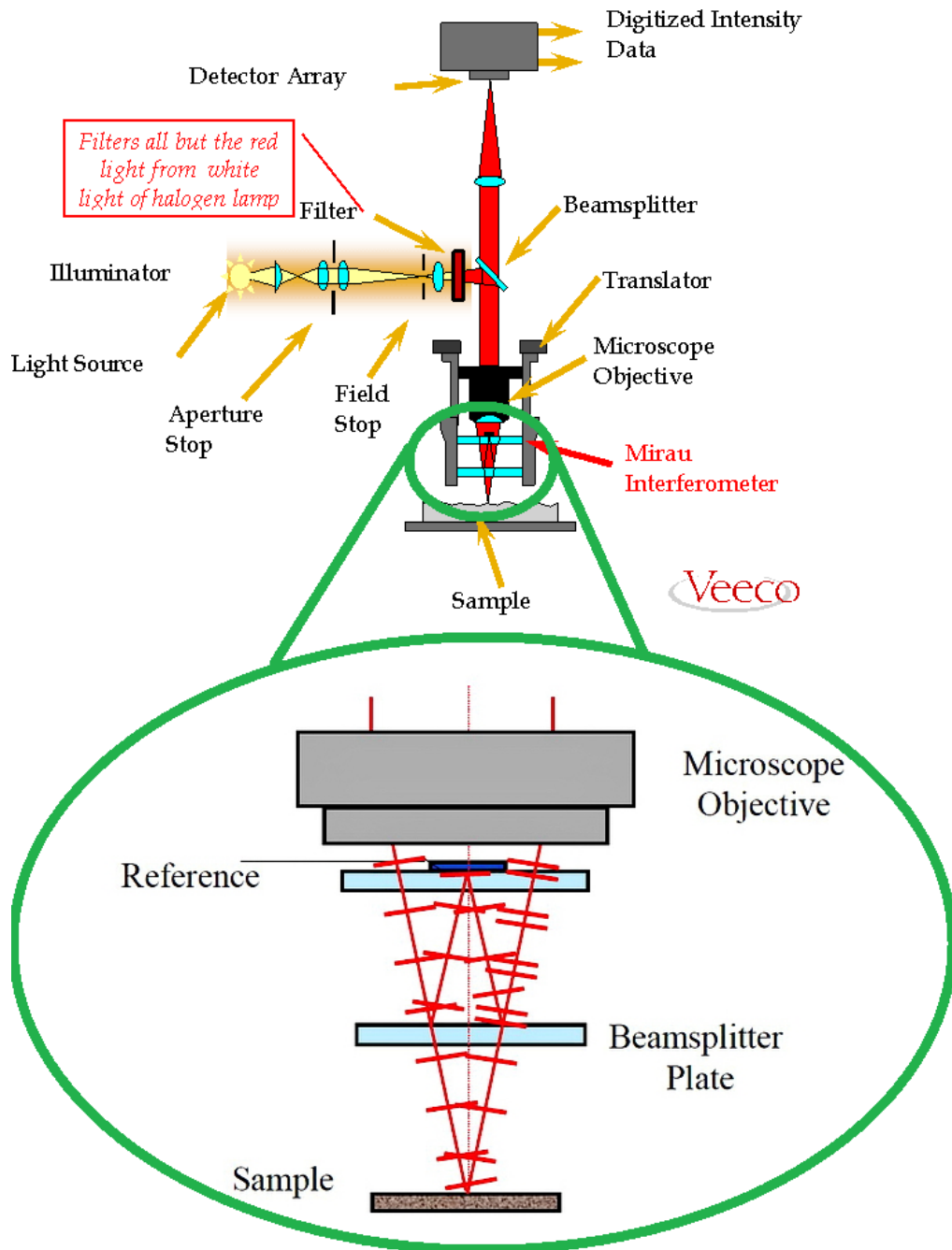


Figure 3.17: The working principle of WYKO white light interferometer working in vertical scanning interferometry (VSI) mode [3.10].

3.3.2.2 Electrical Resistivity Measurement of Epoxy-based Silver Ink

Electrical resistivity is one of a conductor's key physical properties. It reflects the degree of difficulty for the conducting material to conduct electricity. In other words, the electrical resistivity can be used as a measure of conductor's electrical conductivity. The electrical resistivity is mathematically defined as in **(3-1)** [2.52].

$$\rho = \frac{1}{\sigma} = R \frac{A}{\ell} \quad (3-1)$$

Where:

- ρ = electrical resistivity of the ink material (Ohm*m),
- σ = electrical conductivity of the ink material (S/m),
- R = resistance,
- A = the cross-sectional area of the material,
- ℓ = length of the piece of the material.

Four-point probes were used for measuring the sheet resistance which can be used to derive a calculation of the electrical resistivity of cured epoxy-based conductive silver ink. **Figure 3.18** shows the four-point probes used in this investigation. The four-point probes were connected to a data logger for recording the measurement readings of sheet resistance onto a computer. **Figure 3.19** shows four measuring tips with an uniform spacing distance S for a typical four-point probes, the current is added onto two outer tips, the sample's sheet resistance is then measured by a voltmeter which measures the voltage between two inner tips.

Therefore, in this case, equation **(3-1)** can be modified as below in **(3-2)** for calculating the conducting material's electrical resistivity from the measurements provided by the four-point probes [3.5].

$$\rho = \frac{\pi}{\ln 2} \left(\frac{V}{I} \right) t K \quad (3-2)$$

Where:

- ρ = electrical resistivity of the ink material (Ohm*cm),

V = the measured voltage (volts),
 I = the current (amperes),
 t = the thickness of the ink track sample (cm),
 K = correction factor.

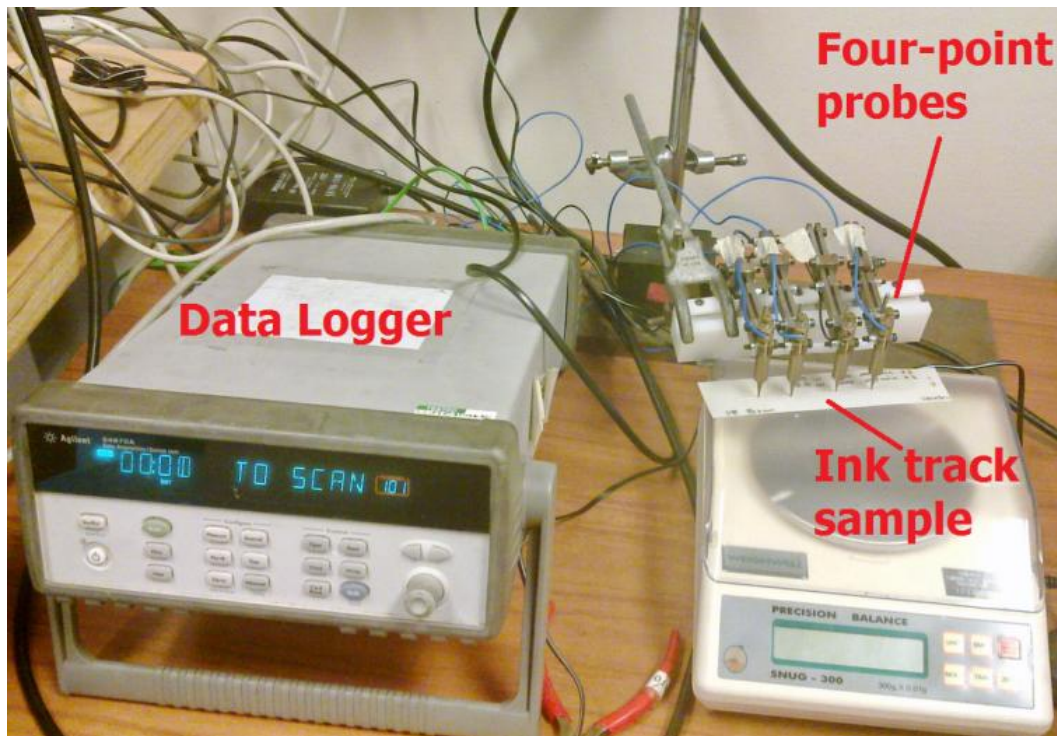


Figure 3.18: The four-point probes configuration in this investigation.

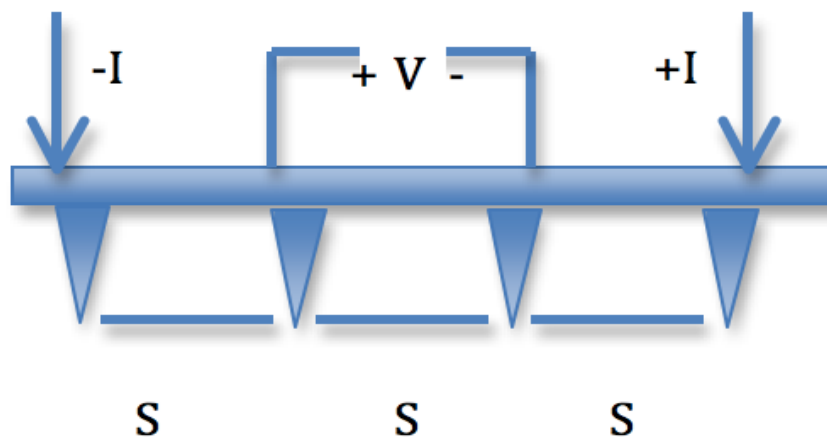


Figure 3.19: Illustration of the working principle of the four-point probe method for measuring resistivity.

As the value measured by four-point probe is the sheet resistance [3.7], the equation (3-2) can be modified below in (3-3) for the calculation of the resistivity of the conducting material from the four point probe measurement.

$$\rho = R_s t K \quad (3-3)$$

Where:

ρ = electrical resistivity of the ink material (Ohm*m),
 R_s = sheet resistance measured by four point probe,
 t = thickness of the material measured by white light interferometer,
 K = correction factor.

The value of sheet resistance R_s can be directly measured from the data logger connecting to a four point probe, while the thickness of the conducting material (epoxy-based conductive silver ink track in this case), can be measured by using a white light interferometer (WYKO).

Equation **(3-3)** shows the calculation of electrical resistivity for conducting material. However due to the shape and geometry of the conducting material (epoxy-based conductive silver ink track) and the relatively small thickness used in this investigation, inaccuracy of the resistivity measurement may occur [3.7]. Therefore two major correction factors are required to compensate the resistivity values of the epoxy-based silver ink track; they are (i) f_1 : the thickness correction factor – this corrects error that occurs when conductive silver ink track's thickness is comparable to the spacing distance S between probes of the four-point probe, and (ii) f_2 : the edge correction factor – this correction factor compensates errors caused by the edge effect, i.e. when the width of the epoxy-based silver ink track is comparable to the spacing distance S between probes [3.8].

Therefore the calculation of resistivity in equation **(3-3)** can be modified as shown in **(3-4)**.

$$\rho' = R_s t f_1 f_2 = \rho f_1 f_2 \quad (3-4)$$

Where:

ρ = initial electrical resistivity calculated based on four point probe reading and results from white light interferometer,
 ρ' = revised electrical resistivity,
 f_1 = the finite thickness correction factor,

f_2 = the finite width correction factor, or the edge correction factor.

3.3.2.2.1 The Thickness Correction Factor, f_1

The mathematical definition of the finite thickness correction factor can be shown in equation **(3-5)** below for an insulating bottom boundary [3.8].

$$f_1 = \frac{\ln(2)}{\ln\left[\frac{\sinh(t/S)}{\sinh(t/2S)}\right]} \quad \text{(3-5)}$$

Where:

t = thickness of the material measured by the white light interferometer,
 S = spacing distance between probes of the four-point probe, in this case the probe spacing distance was measured as 25mm.

As the value of the thickness for silver ink track measured in this thesis t is far less than the value of spacing distance between probes of the four-point probe S , therefore f_1 is approximated to the value of 1 ($f_1 \approx 1$).

3.3.2.2.2 The Edge correction factor, f_2

The finite width correction factor, or the edge correction factor, f_2 , is defined as a function of the width of the material over the probe spacing distance of the four-point probe, or d/S , where d is the width of material, in this case is the width of epoxy-based silver ink track was measured as 3.5mm, and the probe spacing between probes S was measured as 25mm apart. F.M.Smiths investigated the relationship between the width correction factor f_2 and d/S [3.8]. **Figure 3.20** shows a reproduced graph with an extending line that can ease the calculation of f_2 in this thesis with a reasonable assumption that f_2 is a linear function of d/S within the domain $[0, 2]$.

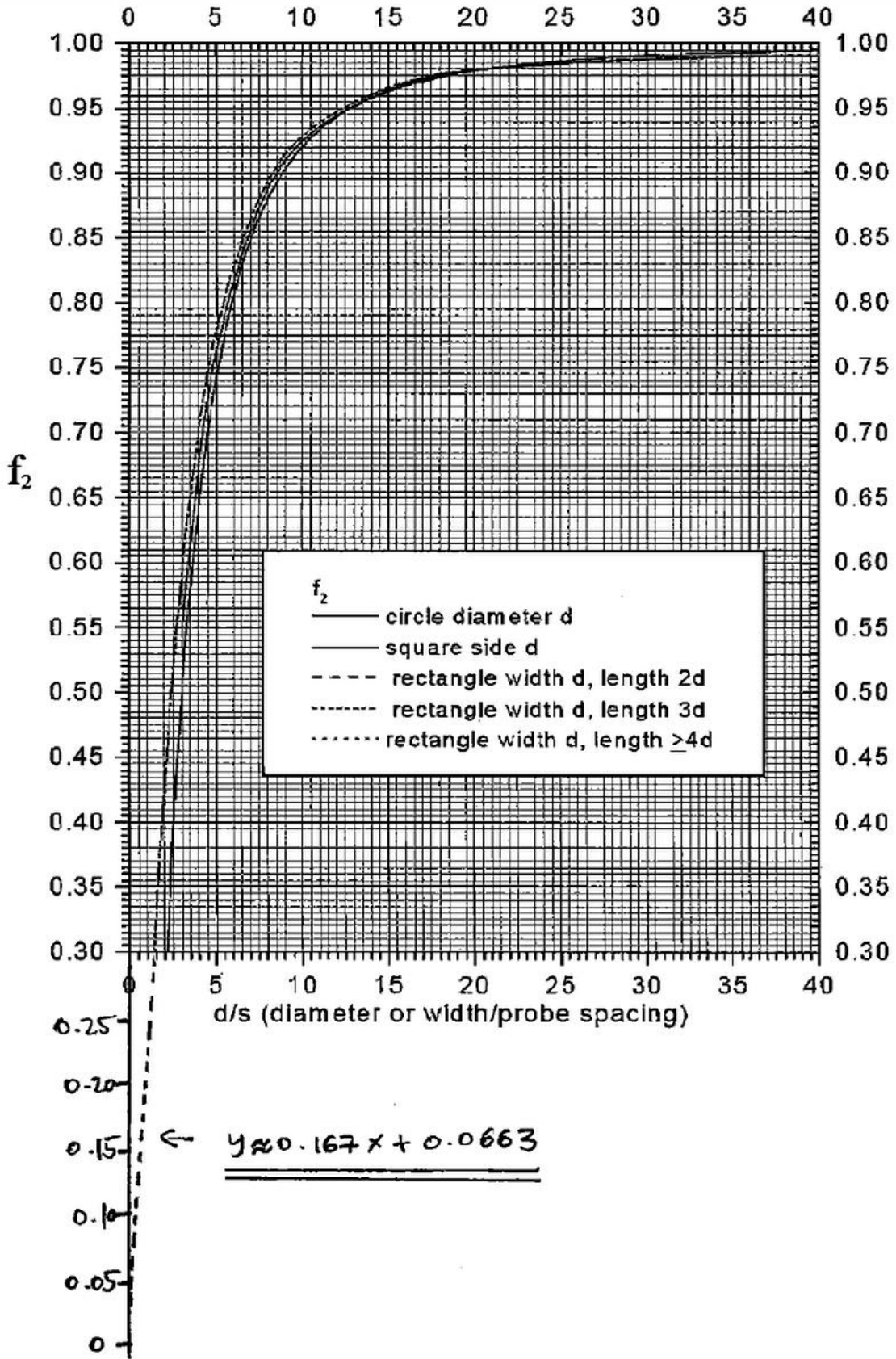


Figure 3.20: The finite width correction factor f_2 as a function of d / S , a linear extension line within the domain $[0, 2]$ is reproduced for the ease of the calculation of f_2 within this domain $[3.8]$.

Therefore as seen from **Figure 3.20**, the function of f_2 within the domain $[0, 2]$ can be approximately represented as the linear equation in **(3-6)** below.

$$f_2 \approx 0.167(d/S) + 0.0663 \quad (3-6)$$

As $d/S = 3.5/25 = 0.14$, therefore equation **(3-6)** can be solved as:

$$f_2 \approx 0.08968 \quad (3-7)$$

Thus the revised calculation of the electrical resistivity in **(3-4)** can be therefore modified as shown in **(3-8)**.

$$\rho' = \rho f_1 f_2 = 0.08968\rho \quad (3-8)$$

Where:

ρ' = revised electrical resistivity,

ρ = initial electrical resistivity calculated based on four point probe reading and data of white light interferometer.

3.3.2.2.3 An Example of Calculating Electrical Resistivity of Epoxy-based Silver Ink

An example is given to demonstrate the calculation of the electrical resistivity for an oven cured D58 epoxy-based conductive silver ink sample (cured in oven at 110°C for 1 hour) investigated in this thesis based on the correction factors given in **section 3.3.2.2**.

Step 1,

The sheet resistance of D58 epoxy-based conductive ink track sample was measured by using the four point probe, the value of sheet resistance was measured as 930.39 milliohms (mOHM).

Therefore,

$$R_s = 930.39 \text{ mOHM} \quad (3-9)$$

Step 2,

The thickness of the D58 epoxy-based silver ink track was measured by using the white light interferometer (WYKO). In this case, the average thickness of the D58 silver ink was measured as 32 micron (μm), as shown in **Figure 3.21**.

Therefore,

$$t = 32 \mu\text{m} \tag{3-10}$$

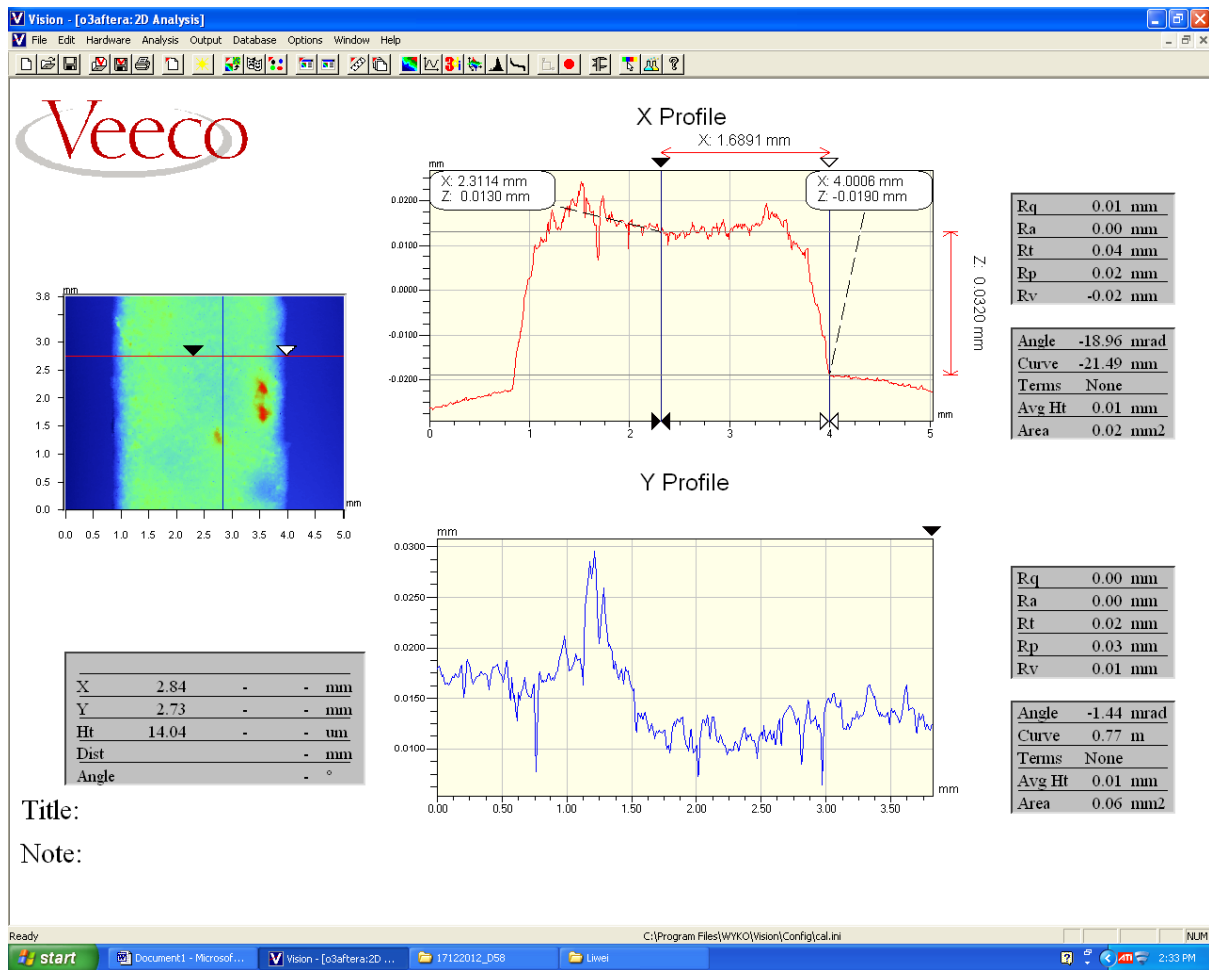


Figure 3.21: A WYKO interferometer measurement shows the thickness of the D58 silver ink track cured in oven at 110°C for 1 hour.

Step 3,

By combining the results (3-9) and (3-10) from **step 1** and **2**, the value of electrical resistivity for this oven cured D58 epoxy-based silver ink track was calculated based on the equations (3-4) and (3-8).

Therefore the revised electrical resistivity can be calculated in **(3-11)**:

$$\rho' = 0.08968R_s t = 2.67E-6 \text{ Ohm*m} \quad \mathbf{(3-11)}$$

3.3.2.3 Hardness Measurement of Epoxy-based Silver Ink

The hardness property of the epoxy-based ink is another characteristic which is useful for determining the degree of cure. In this investigation, the Wolff-Wilborn test was used for its easy set-up and a fast measurement process.

Figure 3.22 shows a typical hardness measurement set-up to a cured epoxy-based conductive silver ink track by Elcometer[®] 501 pencil hardness tester, this Elcometer[®] 501 pencil hardness tester can be used in accordance with international standards: ASTM D 3363, BS 3900-E19, EN 13523-4, ISO 15184, JIS K 5600-5-4 [3.11]. The silver ink track's hardness property can be measured by evaluating the maximum hardness index that the pencil hardness tester can prevent damaging the physical structure of the silver ink track. Ink track's hardness index is represented by the hardness of the graphite pencil used in this pencil hardness test that can damage the physical structure of the ink track, which can be determined by visually examining the ink track surface after pushing the pencil hardness tester horizontally with a graphite pencil fitted across the ink track. The hardness of the graphite pencil is marked with a label from soft (6B) to hard (6H). For the ease of data analysis and comparisons in later Chapters, the hardness index was assigned to values as shown in **Figure 3.23**.



Figure 3.22: A conductive silver ink track was measured by Elcometer[®] 501 pencil hardness tester for Wolff-Wilborn hardness test to measure ink track hardness property.

	Softest Hardest													
Hardness Index	6B	5B	4B	3B	2B	B	HB	F	H	2H	3H	4H	5H	6H
Assigned value in this thesis	1	2	3	4	5	6	7	8	9	10	11	12	13	14

Figure 3.23: Illustration of the hardness index marked on graphite pencils, from the lowest hardness index 6B (1) to the highest hardness index 6H (14).

3.3.2.4 Infrared (IR) Camera

An infrared (IR) camera – FLIR[®] SC 660 developed by FLIR[®] Systems Inc, with an image resolution of 640*480 pixels (**Figure 3.24**) was used as surface temperature measurements in this investigation. The IR camera was also used to record a series of thermal video clips of surface temperatures in Nd:YAG laser curing process at 532nm.

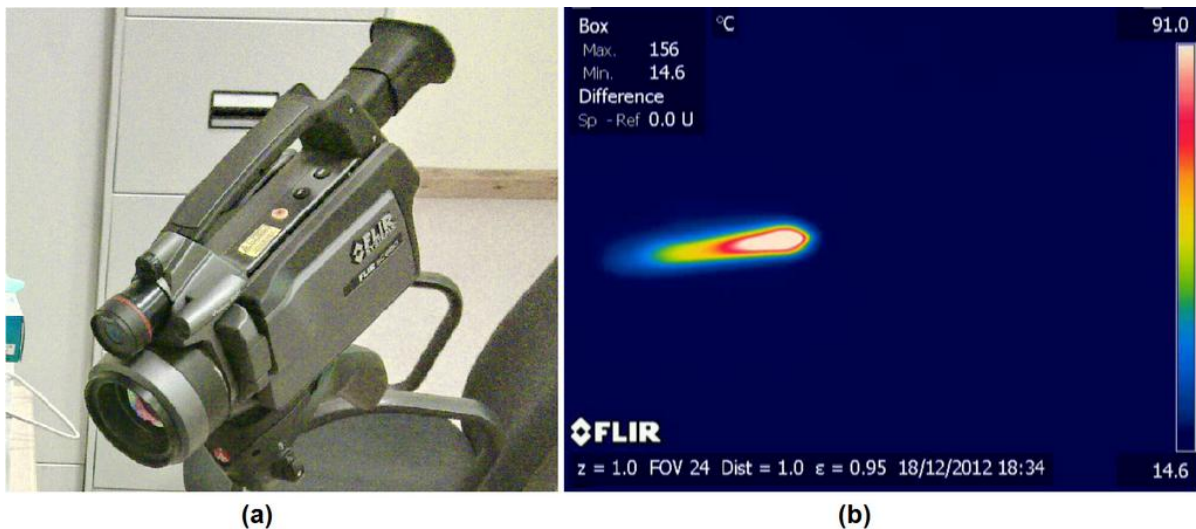


Figure 3.24: FLIR® SC 660 IR camera used in this investigation (a), a typical IR image recorded for curing the D58 conductive silver ink track at the speed of 5mm/s under Nd:YAG laser irradiations with laser output power at 17.94W is shown in (b).

Figure 3.25 shows the working principle of a typical IR camera [3.12], in which the infrared signals were collected through optical components and then transferred for digital processing to generate graphical outputs.

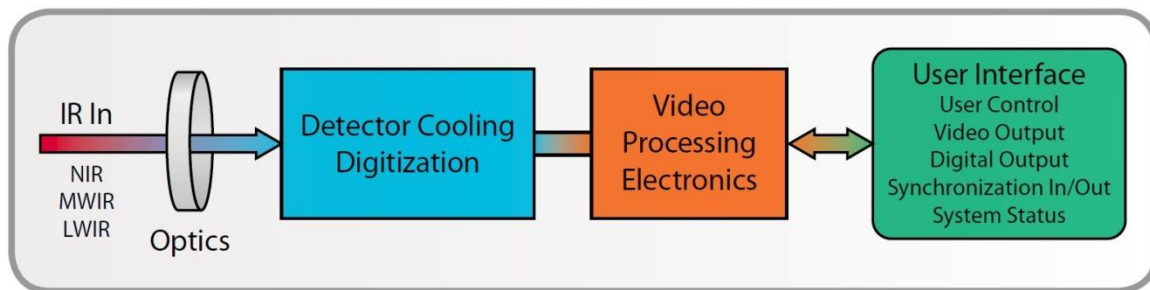


Figure 3.25: Working principle of a typical IR camera [3.12].

Although the surface temperature of the material can be detected and measured by an IR camera, it needs calibration before use. The reflected apparent temperature and emissivity of the material should be predefined before each measurement.

An example of demonstrating how to calibrate the emissivity of the material correctly before measuring its surface temperature by an IR camera is shown in **Figure 3.26**. **Figure 3.26** shows the experimental set-up for calibrating the emissivity of D58 epoxy-based silver ink according to instructional manual of the IR camera (Please see **Appendix 1**). The PET substrate was taped on top of a hot plate, with half of

its surface area masked by 3M Scotch[®] Super 33+ PVC electrical insulation tape (with a known emissivity value of 0.96), another half area of PET surface was coated with a thin layer of D58 epoxy-based silver ink – the material with an unknown emissivity that needs to be measured.



Figure 3.26: Experimental set-up for measuring emissivity of D58 silver ink.

The ambient reflected apparent temperature was measured as 20°C, thus the temperatures of the hot plate were set above the room temperature of 20°C, thermal images were taken and frozen for adjusting the emissivity value of D58 silver ink.

Figure 3.27 shows a frozen thermal image with temperature measurement tools (spot and rectangular measuring cursors) focused on the 3M black tape (with a known emissivity of 0.96), where the temperature was measured as 36.1°C at the spot cursor. This spot measuring cursor was then moved to D58 ink by adjusting the camera setting manually for detection of the surface temperature of D58 epoxy-based silver ink, then the emissivity value was adjusted on IR camera to ensure the surface temperature of D58 silver ink remained at a same temperature reading of the black tape at 36.1°C, then this emissivity value was obtained and recorded as the revised emissivity value of this material (**Figure 3.28**).

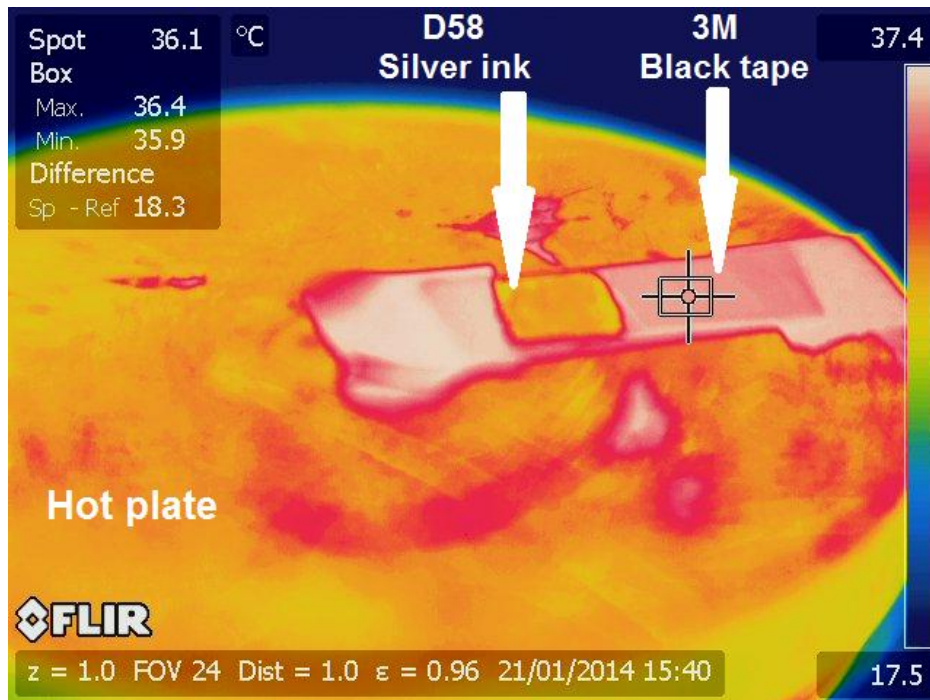


Figure 3.27: Temperature recording of the black tape (°C).

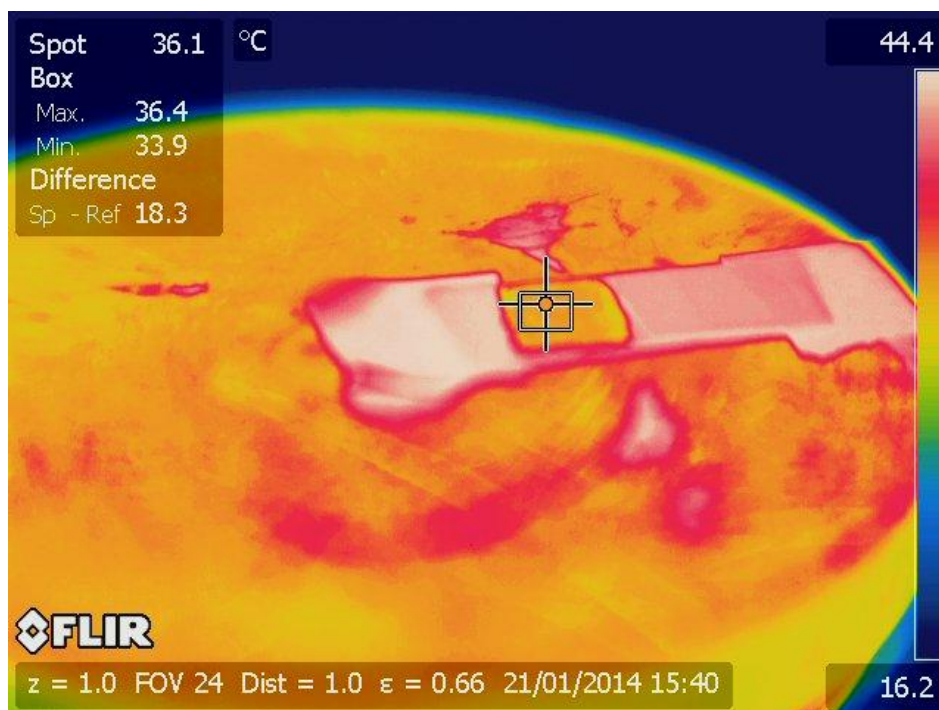


Figure 3.28: Emissivity adjustment and calibration for D58 silver ink, the temperature value (°C) should be kept a same reading of that measured from the black tape in **Figure 3.27**.

In this thesis, D58 epoxy-based silver ink and its ink components were measured by an IR camera for measuring the surface temperature profiles, therefore the emissivities for D58 epoxy-based conductive silver ink, resin complex, solvent, and

silver flakes were pre-defined before the IR temperature measurement. Repeated iterations of the emissivity calibration procedure are shown in **Figures 3.27-3.28**, and the revised emissivity values for different materials used in this thesis are shown in **Table 3.5**.

Table 3.5: Emissivity calibration for different materials used in this thesis.

Material	Emissivity Measurement 1	Emissivity Measurement 2	Emissivity Measurement 3	Mean Emissivity
D58 silver ink	0.66	0.66	0.65	0.66
Resin Complex	0.95	0.97	0.97	0.96
Organic Solvent	1	0.99	1	1
Silver flakes	0.59	0.59	0.59	0.59

As the material's emissivity can be calibrated through the calibration procedure discussed earlier in **section 3.3.2.4**, the corresponding temperature could be therefore correctly measured by IR camera with the revised emissivity data, or can be revised based on the Stefan-Boltzmann law, which is mathematically defined in **(3-12)**.

$$P_r = \varepsilon \sigma A T^4 \quad (3-12)$$

Where:

P_r = Power irradiated;

ε = emissivity of the radiating surface between 0 and 1;

σ = Stefan's constant ($5.6703 \times 10^{-8} \text{ W}/(\text{m}^2 \cdot \text{K}^4)$);

A = radiating surface area;

T = Temperature;

For the same object under the same irradiation, the irradiation power and irradiation surface area are constant, the correction of temperature can be therefore calculated based on equation **(3-12)**, this can be mathematically defined in **(3-13)**.

$$\varepsilon_1 T_1^4 = \varepsilon_2 T_2^4 \quad (3-13)$$

Therefore the revised temperature reading T_2 can be calculated in **(3-14)**,

$$T_2 = \sqrt[4]{\frac{\varepsilon_1}{\varepsilon_2}} T_1 \quad (3-14)$$

Where:

ε_1 = emissivity value of initial setting (default value);

T_1 = inaccurate temperature reading based on default emissivity value ε_1 ;

ε_2 = calibrated emissivity value after IR camera emissivity calibration;

T_2 = revised temperature reading.

Due to the high sensitivity of the infrared sensor used in IR camera, the use of the IR camera was restricted to measuring temperature profiles of the laser curing process at visible wavelengths, this was to avoid damaging the camera sensor at high infrared intensities. Therefore an alternative of temperature measurement to epoxy-based silver inks cured by an infrared CO₂ laser is required and was achieved by using a Type-K thermocouple to replace the IR camera measurements at these wavelengths.

Figure 3.29 shows the temperature comparison of a cooling down stage of 3M Scotch[®] Super 33+ PVC electrical insulation tape on a PET substrate placed on top of a hot plate measured by both an IR camera and the Type-K thermocouple. As seen from the **Figure 3.29**, the surface temperature measured by the Type-K thermocouple fitted well to that by the IR camera with the revised emissivity of the material.

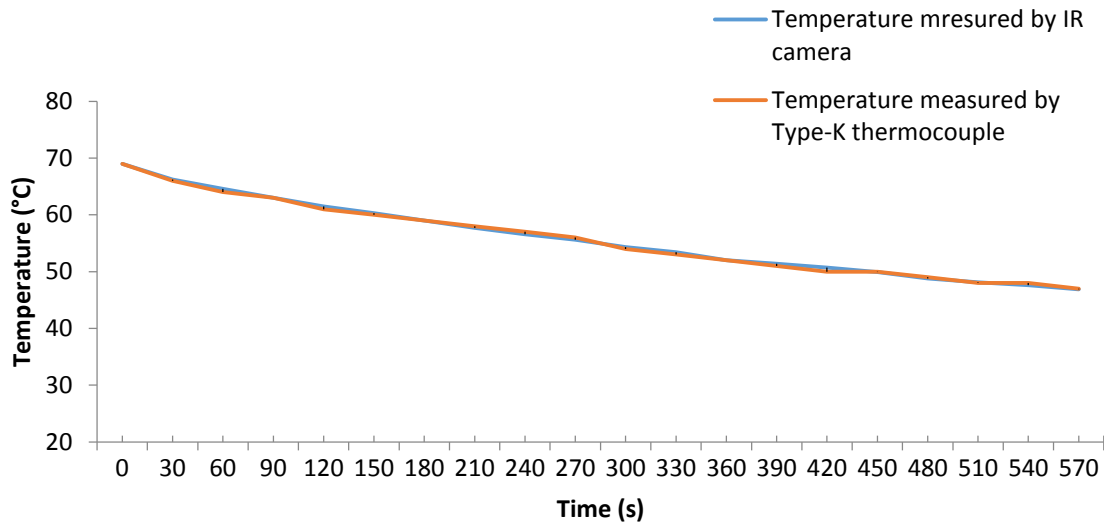


Figure 3.29: Dynamic temperature (°C) comparisons between temperature measured by an IR camera and temperature measured by a Type-K thermocouple.

In this thesis, IR surface temperature profiles for Nd:YAG laser curing the epoxy-based silver ink were compared with those measured by the type-K thermocouple for CO₂ laser and oven curing processes in **Chapter 4**, also the Nd:YAG laser curing mechanism theory were developed in **Chapter 5** based on these temperature profiles recorded by the IR camera. In addition, the thermal data recorded by IR camera were used to validate the finite-element (FE) model for model verification in **Chapter 6**.

3.3.2.5 Scanning Electron Microscope (SEM) and Energy Dispersive X-ray Spectroscopy (EDX) Measurement to Epoxy-based Silver Inks

Scanning Electron Microscope (SEM) can provide morphological information of internal structures with a high degree of resolution down to micron or even nanometre scale, therefore space arrangement information for silver micro-sized flakes of the epoxy-based silver ink can be directly observed and analysed using a SEM.

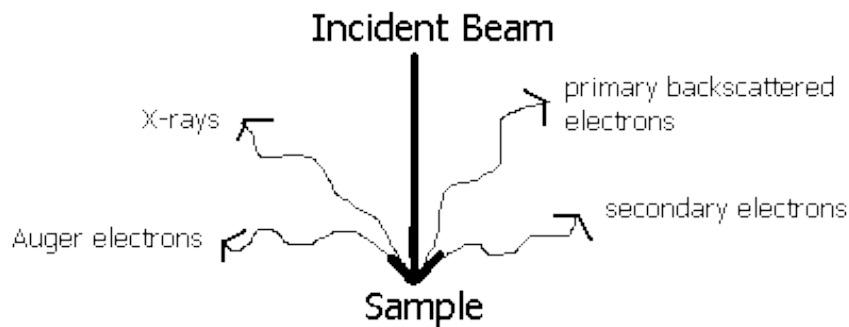


Figure 3.30: Working principle for SEM based on electron secondary irradiation [3.13].

Electrons are accelerated inside the vacuum chamber of the SEM, which contain significant amounts of kinetic energy. These electrons interact with the sample material which was placed inside the vacuum chamber, resulting in the secondary electrons that can be collected by the SEM to generate graphical SEM image [3.13]. This electron-material interaction can also result in x-ray emission, as shown in **Figure 3.30** [3.13]. These x-rays are specific to elements within the sample and can be collected and compared with each other in a proportional ratio to determine relative proportions of the elements within the sample by a silicon drifted detector (SDD) fitted in SEM for elemental composition analysis, or energy dispersive x-ray spectroscopy (EDX) analysis [3.14].

Figure 3.31 shows the SEM used in this investigation - FEI's Phenom™ desktop SEM system (FEI's Phenom production line has now been acquired by NTS Group B.V. [3.3]). As in a standard SEM, the Phenom SEM scans the sample with a focused electrons beam, and the electrons beam interacts with the sample to generate secondary electrons that can be detected by the SEM.



Figure 3.31: A FEI Phenom™ desktop SEM system used in this investigation.

Figure 3.32 shows another SEM facility in Nanoinvestigation centre at Liverpool (NiCaL) in the main campus of the University of Liverpool - JEOL's JSM-6610 Scanned Electron Microscope (SEM) fitted with an Oxford Instruments' x-act 10mm² silicon drift detector (SDD), this offers an ultra high resolution down to 3 nm and it also offers the capability of x-ray elemental analysis to the sample material.

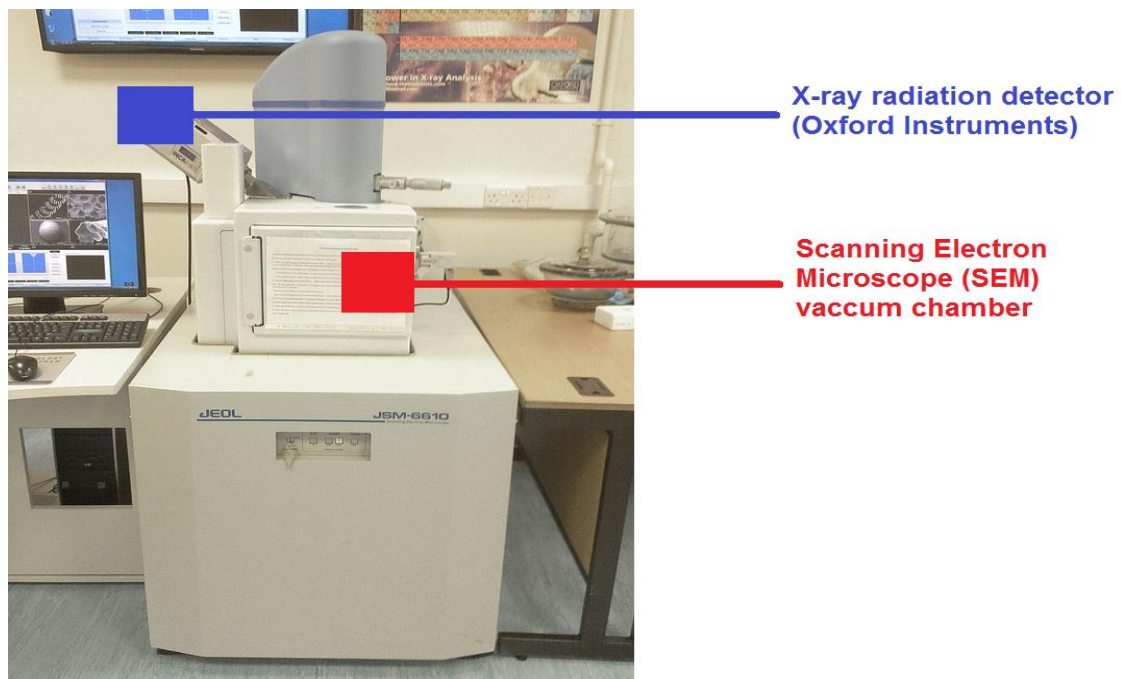


Figure 3.32: JEOL's JSM-6610 SEM with x-ray detector fitted in Liverpool's NiCaL.

3.3.2.6 Fourier Transform Infrared (FTIR) Spectroscopy Examination

Fourier Transform Infrared Spectroscopy (FTIR) examination was used to compare chemical compound information of the epoxy-based silver ink and its components to help in developing the resin cross-linking theory in **Chapter 5**.

FTIR spectroscopy provides a fast analysis technique based on the Michelson interferometer by using the interferogram signals to detect a sample's molecular vibrations and stretches. The sample material is placed on top of the diamond stage of the Attenuated Total Reflectance (ATR) and exposed by infrared signals (**Figure 3.33**). These signals are combined in the interferogram over time, then this interferogram is interpreted by the Fourier transform from the time domain to the frequency domain to generate an IR spectrum [3.15].

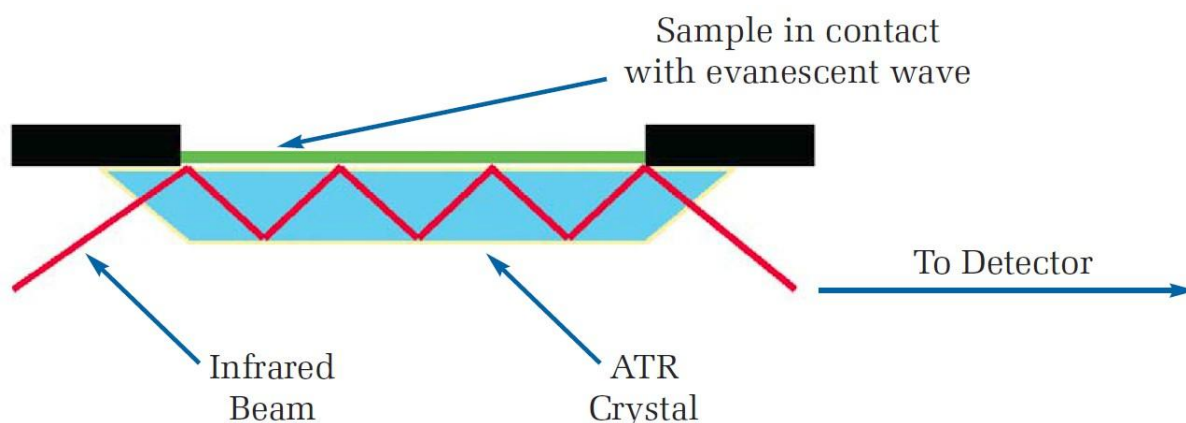


Figure 3.33: Sample can be exposed to infrared beam due to Attenuated Total Reflectance (ATR) for a FTIR measurement [3.15].

Figure 3.34 shows a PerkinElmer®'s Spectrum 100 Spectrometer used in this investigation, and a typical FTIR analysis procedure is shown in **Figure 3.35** [3.4].

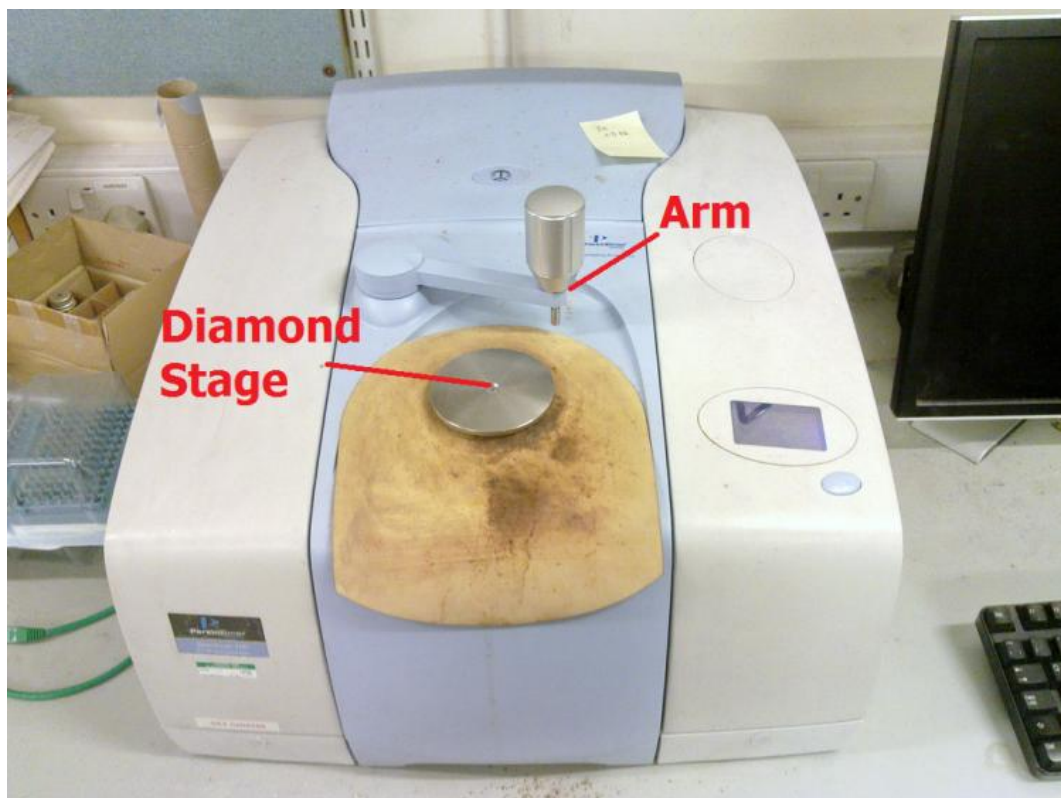


Figure 3.34: PerkinElmer® Spectrum 100 Spectrometer used in samples' FTIR measurement (The FTIR measurements were carried out in Department of Chemistry, the University of Liverpool).

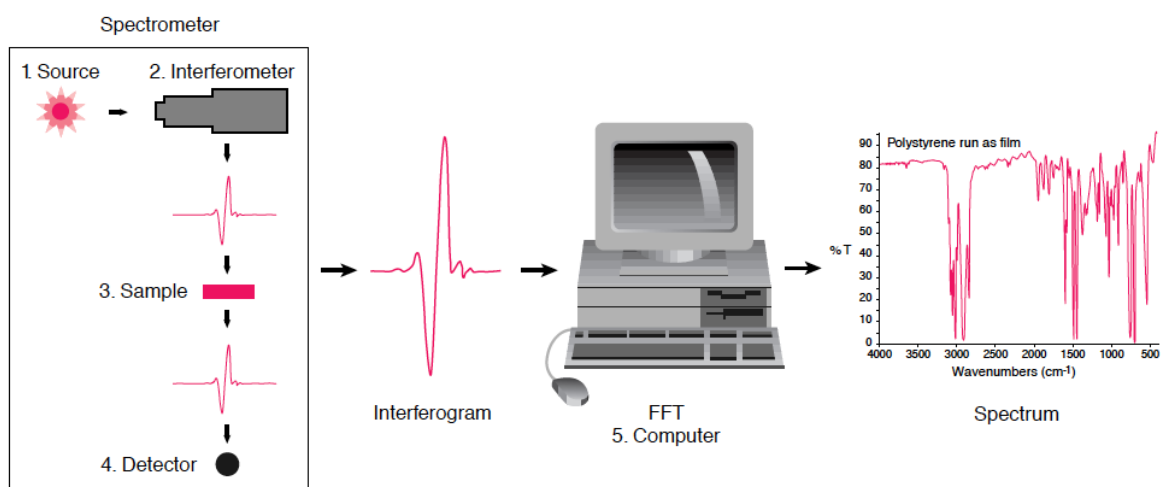


Figure 3.35: A typical FTIR sample analysis procedure [3.4].

3.4 Chapter Summary

In this Chapter the materials, apparatus and experimental methods used have been discussed. PET film is chosen as the substrate material in this investigation for its structure flexibility and good chemical and gas resistance as a potential material to replace conventional plastic substrates used in PCB industries. D58 epoxy-based conductive silver ink and its components are also discussed in the context of a general understanding of ink compositions. The equipment used in the experiments include an oven and lasers (CO₂ laser marker at 10.6μm and Nd:YAG frequency doubled DPSS laser system at 532nm) for sample curing investigation and comparison. And a selection of analysis equipment including four-point probes for calculating material's electrical resistivity, pencil hardness tester for measuring material's hardness property, white light interferometer for measuring material's roughness and thickness after treatment, SEM and EDX for investigating epoxy-based silver ink composition and structure after cure, and FTIR spectroscopy for investigating material's chemical compound information are described.

4. RESULTS: CURING OF EPOXY-BASED CONDUCTIVE SILVER LOADED INKS

This Chapter discusses experimental results of curing D58 epoxy-based silver ink and other epoxy-based silver inks with various ink compositions by using a CO₂ laser at 10.6 μ m, Nd:YAG laser at 532nm, and a conventional heating oven. The inks' curing results are measured and curing properties are compared in terms of the material's physical and electrical properties, for different curing processes. As discussed in **Chapter 3**, epoxy-based conductive silver inks were printed manually on a flexible PET polymer substrate by using the doctor blading method, these ink samples then underwent curing treatments with different processing parameters before a comparison to find out the most suitable processing method and processing window for curing a particulate epoxy-based conductive silver ink.

4.1 Curing Results of D58 Epoxy-based Silver Ink Cured by Lasers and by Oven

As discussed in **Chapter 3**, epoxy-based conductive silver inks with various ink compositions were selected in this investigation, as shown in **Table 3.2**. The epoxy-based conductive silver inks were supplied by Gwent Electronic Materials, Ltd. (GEM).

Table 3.2: Approximated compositions for silver inks used in this investigation (Data from GEM).

Ink Name	Approximated composition	Silver content (wt%)
Silver Ink D58	Silver flakes, Epoxy resin, Blocked Isocyanates, Solvent	59%
Laser Curable Silver Ink D5	Silver flakes, Epoxy resin, Blocked Isocyanates, Solvent	78%
Graphite Doped Silver Ink D5	0.5wt% Graphite, Silver flakes, Epoxy resin, Blocked Isocyanates, Solvent	61%
Silver Ink D2	Silver particles (micro- and nano-size), Epoxy resin, Blocked Isocyanates, Solvent	45%

The initial investigation used D58 epoxy-based silver ink with silver content of 59wt% for comparison of curing results carried out by three different curing processes - CO₂ laser curing process at the wavelength of 10.6μm (**Table 4.1**), Nd:YAG laser curing process at the wavelength of 532nm (**Table 4.2**), and an oven curing process (**Table 4.3**). Ink track samples were processed using different processing parameters to create an approximated process window to investigate the suitable curing parameters for curing the ink sample for each treatment. Surface temperatures were measured by using a Type-K thermocouple for ink track samples cured by CO₂ laser and an IR thermal camera for ink track samples cured by 532nm Nd:YAG laser. In this experiment, ink track samples' electrical resistivity, hardness and surface temperature properties were compared.

Table 4.1: D58 epoxy-based conductive silver ink track samples cured by CO₂ laser at 10.6μm.

Scanning Power (W)	Scanning speed (mm/s)	Number of Scanning passes	Curing Temperature (°C)	Sample condition	Hardness of samples	Resistivity (Ohm*m)
4.25	4	10	N/A	Good	H	7.21E-07
6.25	5.5	5	N/A	Good	3H	7.60E-07
5	5	10	N/A	Good	H	1.28E-06
4.25	4.5	10	N/A	Good	2H	8.33E-07
3.75	5	10	N/A	Good	6B	5.35E-06
4.5	5	10	N/A	Good	3B	1.20E-06
5	4	12	123	Good	3H	2.22E-06
13	4	12	432	Burnt	N/A	N/A
18	4	12	630	Burnt	N/A	N/A
13	8	12	275	Burnt	N/A	N/A
18	8	12	570	Burnt	N/A	N/A
5	14	12	60	Uncured	3B	N/A
13	14	12	125	Good	5H	3.19E-06
18	14	12	180	Burnt	N/A	N/A

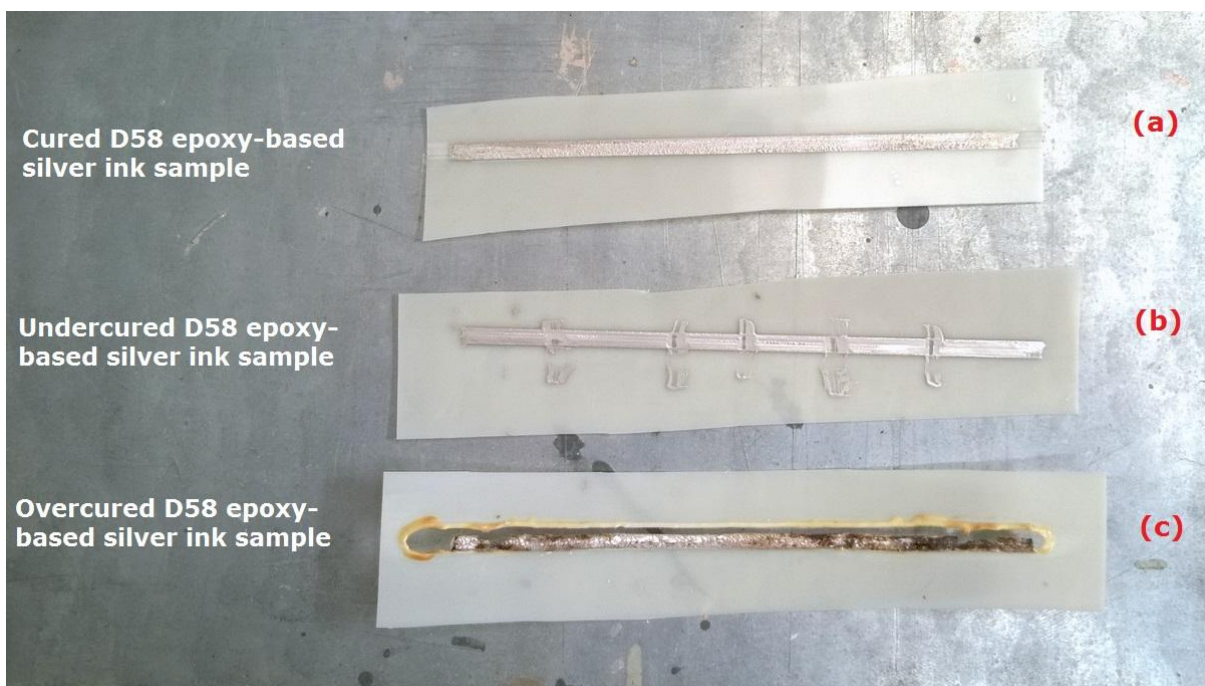
Table 4.2: D58 epoxy-based conductive silver ink track samples cured by Nd:YAG laser at 532nm.

Scanning Power (W)	Scanning speed (mm/s)	Number of Scanning passes	Curing Temperature (°C)	Sample condition	Hardness of samples	Resistivity (Ohm*m)
5.06	4	12	93	Uncured	5B	N/A
12.972	4	12	120	Good	6H	5.19E-07
17.94	4	12	153	Good	6H	1.55E-06
5.06	8	12	73	Uncured	2B	N/A
12.972	8	12	106	Good	6B	4.19E-06
17.94	8	12	115	Good	H	7.93E-07
5.06	14	12	55	Uncured	2B	N/A
12.972	14	12	82	Uncured	5B	N/A
17.94	14	12	104	Good	2B	5.33E-06
17.94	8.33	30	129	Good	HB	3.55E-07
17.94	5	30	134	Good	H	3.55E-07

Table 4.3: D58 epoxy-based conductive silver ink track samples cured by Oven.

Curing Temperature (°C)	Curing time (s)	Sample condition	Hardness of samples	Resistivity (Ohm*m)
67	2400	Uncured	6B	6.33E-06
67	2400	Uncured	6B	5.52E-06
59/60/65	300/900/600	Good	HB	6.35E-06
150	2700	Good	6H	6.72E-07
150	2700	Good	6H	7.87E-07
90	3600	Good	5H	4.16E-06
110	3600	Good	5H	2.67E-06
130	3600	Good	5H	1.49E-06
140	3600	Good	5H	1.56E-06

As seen from **Tables 4.1-4.3**, the condition of the D58 epoxy-based silver ink after different curing processes were categorized to three curing conditions by visually examining the physical structure of the silver ink, as well as investigating whether the ink was solid using a smearing process by hand. An example of showing these three different curing conditions can be seen in **Figure 4.1**, in which **Figure 4.1(c)** shows the overcured or burnt condition as the physical structure of the silver ink and the polymer substrate were damaged; **Figure 4.1(b)** shows the undercured condition as the silver ink was still wet, and can be smeared or wiped off; **Figure 4.1(a)** shows the cured or good curing condition indicated by undamaged material structure of both ink and substrate, and a dry ink that would not smear.

**Figure 4.1:** D58 epoxy-based silver ink can be cured (a), undercured (b), or overcured (c).

From these initial experiments, an approximated range of the processing window of curing the D58 epoxy-based silver ink can be concluded from the **Tables 4.1-4.3**, in which (i) for the CO₂ laser curing process the laser power is within the range from 5 to 13 Watts, and the laser traverse speed is within the range from 4 to 8 mm/s, (ii) for the 532nm laser curing process the laser power is within the range from 5.06 to 17.94 Watts, and the laser traverse speed is within the range from 4 to 14 mm/s. And (iii) for an Oven curing process, the temperature for optimized curing result is suggested above 90°C.

4.2 D58 Epoxy-based Silver Ink Curing Results At 532nm with Multiple Scanning Passes

In **Chapter 2**, a difficulty in curing a silver ink track in just one laser scanning pass for Liverpool's Laser Assisted Direct Write (LA-DW) process in previous investigations was discussed. Hence, an alternative laser curing process with multiple-pass laser curing method is suggested to improve the laser curing quality by gradually cross-linking the resin complex pass by pass (Please refer to **Chapter 5** for 532nm Laser curing mechanism theories). The aim of this approach is to improve the final electrical conductivity and prevent burn damage to the ink track sample due to excessive heating in a single pass.

Three D58 epoxy-based conductive silver ink samples were cured by 532nm Nd:YAG laser with laser working parameters within the approximated range of the process window for the 532nm laser curing process. As shown in **Table 4.4**, these three D58 epoxy-based silver inks were cured at different laser output powers (13.984W, 14.7W and 17.94W) with a constant laser scanning speed at 15mm/s. Each ink's electrical resistance values were measured by using a multimeter immediately after each laser scanning pass, this illustrated the relationship between the ink's curing result against curing time.

Table 4.4: Electrical resistance measured for 532nm Nd:YAG laser curing D58 epoxy-based silver ink track samples at 15mm/s with multiple laser scanning passes.

Laser Power: 13.984W		Laser Power: 14.7W		Laser Power: 17.94W	
Pass Number	Electrical Resistance (Ohm)	Pass Number	Electrical Resistance (Ohm)	Pass Number	Electrical Resistance (Ohm)
80	13.7	80	6.2	42	4.2
60	17.8	60	8.7	30	5.4
40	29.1	40	15.9	18	8.3
30	46.6	30	26.4	14	10.8
28	56.7	20	75.8	12	29.6
27	59.2	18	112	10	39
26	59.6	17	170	9	94
25	64.3	16	1.20E+05	8	1015
24	74.8	-	-	7	6.00E+06
23	85.6	-	-	6	1.20E+07
22	89.5	-	-	-	-
21	105.2	-	-	-	-
20	125	-	-	-	-
19	129	-	-	-	-
18	229.7	-	-	-	-
17	910	-	-	-	-
16	1312	-	-	-	-
15	1.37E+06	-	-	-	-
14	4.51E+06	-	-	-	-

As seen from the **Table 4.4**, the higher the laser output power used in laser curing process, the more laser energy coupled into the ink, and therefore the less time for epoxy-based D58 silver ink to become electrically conductive (**Figure 4.2**). Repeating the curing process for multiple passes can cross-link the resin complex gradually and/or remove the remaining solvent with a greater degree of control (Please refer to **Chapter 5** for 532nm laser curing mechanism theories). This can prevent thermal damage to both ink track and the polymer substrate materials due to excessive heating in a single pass (Thermal damage of the ink track and substrate materials will be discussed in **section 4.7**).

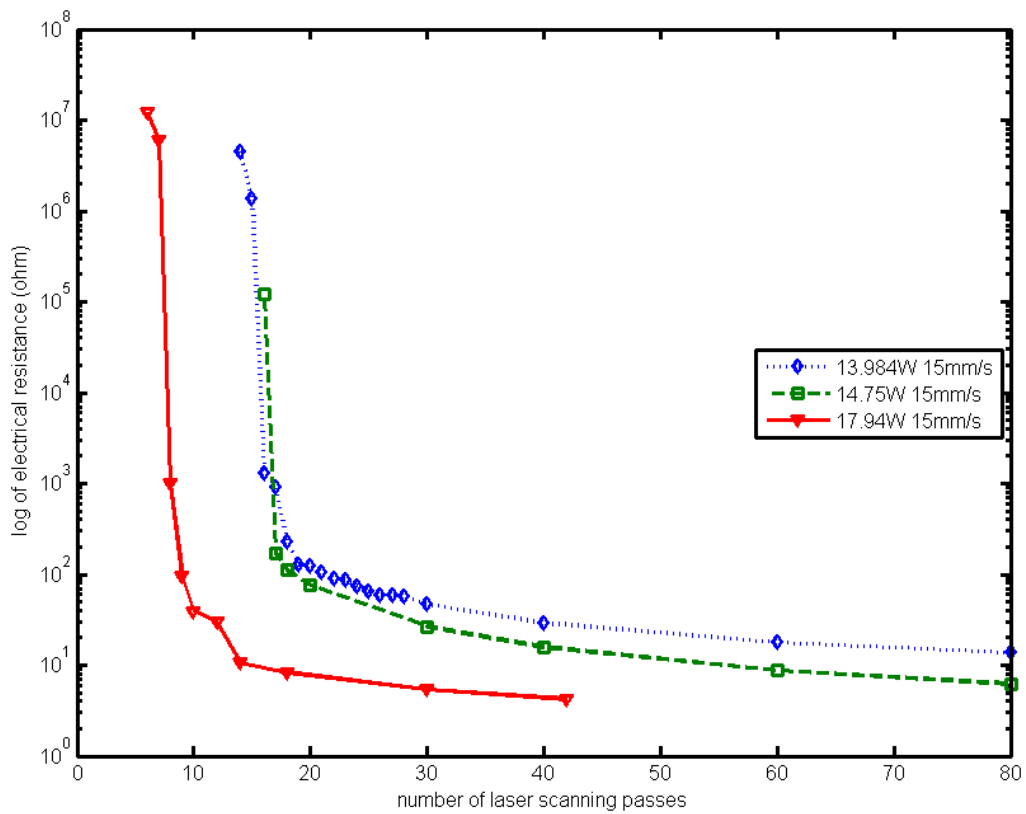


Figure 4.2: The electrical resistance of the ink track as a function of laser working parameters and the laser scanning pass, showing how the multiple-pass scanning method can significantly reduce the electrical resistance pass by pass.

4.3 Electrical Resistivity Results

Table 4.1: D58 epoxy-based conductive silver ink track samples cured by CO₂ laser at 10.6μm.

Scanning Power (W)	Scanning speed (mm/s)	Number of Scanning passes	Curing Temperature (°C)	Sample condition	Hardness of samples	Resistivity (Ohm*m)
4.25	4	10	N/A	Good	H	7.21E-07
6.25	5.5	5	N/A	Good	3H	7.60E-07
5	5	10	N/A	Good	H	1.28E-06
4.25	4.5	10	N/A	Good	2H	8.33E-07
3.75	5	10	N/A	Good	6B	5.35E-06
4.5	5	10	N/A	Good	3B	1.20E-06
5	4	12	123	Good	3H	2.22E-06
13	4	12	432	Burnt	N/A	N/A
18	4	12	630	Burnt	N/A	N/A
13	8	12	275	Burnt	N/A	N/A
18	8	12	570	Burnt	N/A	N/A
5	14	12	60	Uncured	3B	N/A
13	14	12	125	Good	5H	3.19E-06
18	14	12	180	Burnt	N/A	N/A

Table 4.2: D58 epoxy-based conductive silver ink track samples cured by Nd:YAG laser at 532nm.

Scanning Power (W)	Scanning speed (mm/s)	Number of Scanning passes	Curing Temperature (°C)	Sample condition	Hardness of samples	Resistivity (Ohm*m)
5.06	4	12	93	Uncured	5B	N/A
12.972	4	12	120	Good	6H	5.19E-07
17.94	4	12	153	Good	6H	1.55E-06
5.06	8	12	73	Uncured	2B	N/A
12.972	8	12	106	Good	6B	4.19E-06
17.94	8	12	115	Good	H	7.93E-07
5.06	14	12	55	Uncured	2B	N/A
12.972	14	12	82	Uncured	5B	N/A
17.94	14	12	104	Good	2B	5.33E-06
17.94	8.33	30	129	Good	HB	3.55E-07
17.94	5	30	134	Good	H	3.55E-07

Table 4.3: D58 epoxy-based conductive silver ink track samples cured by Oven.

Curing Temperature (°C)	Curing time (s)	Sample condition	Hardness of samples	Resistivity (Ohm*m)
67	2400	Uncured	6B	6.33E-06
67	2400	Uncured	6B	5.52E-06
59/60/65	300/900/600	Good	HB	6.35E-06
150	2700	Good	6H	6.72E-07
150	2700	Good	6H	7.87E-07
90	3600	Good	5H	4.16E-06
110	3600	Good	5H	2.67E-06
130	3600	Good	5H	1.49E-06
140	3600	Good	5H	1.56E-06

As seen from **Table 4.1-4.3**, the electrical resistivity values for some ink track samples could not be measured due to overcure or undercure of the ink track caused by selection of inappropriate working parameters used to cure the ink (this will be discussed in **section 4.5**). Thus, only cured samples were measured and compared for electrical resistivity comparison. **Figure 4.3** compares laser cured D58 epoxy-based silver inks and indicates that a reduced electrical resistivity could be achieved by using a combination of lower laser scanning speed and higher laser output power. However increased resistivities were observed in some of these cured tracks due to thermal damage to the ink caused by either too high the laser output power or too slow the laser scanning speed selected. **Figure 4.3** also shows lower electrical resistivities were achieved for ink track samples cured by 532nm Nd:YAG than those cured by CO₂ laser at 10.6μm, a particular example is the ink track cured by 532nm Nd:YAG laser that achieved an electrical resistivity of 3.55×10^{-7} Ohm*m, which is ~22 times of that of bulk silver (equal to 1.59×10^{-8} Ohm*m). This resistivity value is better than the lowest electrical resistivity of the ink track sample achievable by CO₂ laser (7.21×10^{-7} Ohm*m, ~45 times of the bulk silver) and the ink track sample cured by Oven (6.72×10^{-7} Ohm*m, ~42 times of the bulk silver). These results indicate that a lower electrical resistivity with a quicker processing time could be achieved for ink track samples cured by 532nm Nd:YAG laser than those cured by CO₂ laser and Oven (**Table 4.5**). According to equation **(3-1)** defined in **Chapter 3**, a higher electrical conductivity can therefore be achieved for ink track samples cured by Nd:YAG laser at 532nm than cured by CO₂ laser and oven.

$$\rho = \frac{1}{\sigma} = R \frac{A}{\ell} \quad (3-1)$$

Where:

ρ = electrical resistivity of the ink material (Ohm*m),

σ = electrical conductivity of the ink material (S/m),

R = resistance,

A = the cross-sectional area of the material,

ℓ = length of the piece of the material.

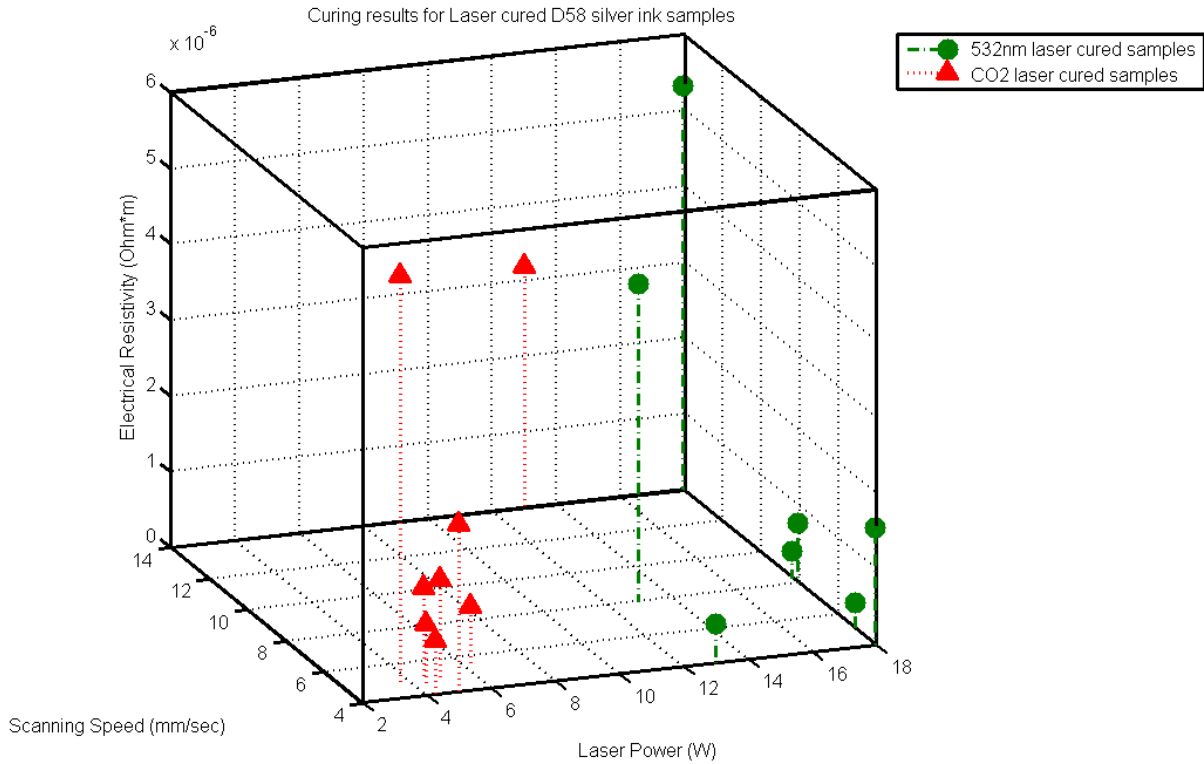


Figure 4.3: Electrical resistivity comparisons for ink track samples cured by CO₂ laser (red triangles) at 10.6μm and Nd:YAG laser (green dots) at 532nm

Table 4.5: Electrical resistivity comparison of D58 epoxy-based silver microparticle ink after cure.

	Curing method	Lowest resistivity (Ohm*m)	resistivity of bulk silver (Ohm*m)	Times of bulk silver (resistivity)
D58 silver ink	Oven	6.72E-07	1.59E-08	42
D58 silver ink	CO ₂ laser	7.21E-07	1.59E-08	45
D58 silver ink	532nm laser	3.55E-07	1.59E-08	22

Another parameter can be used to directly compare the laser curing results - the laser coupling energy density per each laser scanning pass, or effective laser energy density per laser scanning pass. Equation (4-1) shows the mathematical definition of the effective laser energy density per unit scanning pass.

$$U = \frac{\eta E}{Sj} = \frac{\eta Pt}{Sj} \tag{4-1}$$

Where:

- U = effective laser energy density per each scanning pass (J/mm²),
- η = laser energy coupling efficiency,
- E = laser energy (J),
- S = laser beam spot size (mm²),
- j = the number of laser beam scanning pass,

P = laser power (W),
 t = the total laser scanning time (s).

The laser energy coupling efficiency η has been investigated in previous researches by Sato and Shang [2.52, 4.1], in which the laser energy coupling efficiency η of CO₂ laser at 10.6 μ m is found as 0.87, and 0.22 for that of Nd:YAG laser at 532nm. Therefore the corresponding laser energy density per scanning pass can be shown in **Table 4.6-4.7**.

Table 4.6: D58 conductive silver ink track samples cured by CO₂ laser at 10.6 μ m.

Scanning Power (W)	Scanning speed (mm/s)	Number of Scanning passes	Sample condition	Effective laser energy density per scanning pass (J/mm ²)	Resistivity (Ohm*m)
4.25	4	10	Bubbled	5.65	7.21E-07
6.25	5.5	5	Good	6.05	7.60E-07
5	5	10	Good	5.32	1.28E-06
4.25	4.5	10	Good	5.02	8.33E-07
3.75	5	10	Good	3.99	5.35E-06
4.5	5	10	Good	4.79	1.20E-06
5	4	12	Good	6.65	2.22E-06
13	4	12	Burnt	17.29	N/A
18	4	12	Burnt	23.94	N/A
13	8	12	Burnt	8.64	N/A
18	8	12	Burnt	11.97	N/A
5	14	12	Uncured	1.90	N/A
13	14	12	Good	4.94	3.19E-06
18	14	12	Burnt	6.84	N/A

Table 4.7: D58 conductive silver ink track samples cured by Nd:YAG laser at 532nm.

Scanning Power (W)	Scanning speed (mm/s)	Number of Scanning passes	Sample condition	Effective laser energy density per scanning pass (J/mm ²)	Resistivity (Ohm*m)
5.06	4	12	Uncured	1.70	N/A
12.972	4	12	Good	4.36	5.19E-07
17.94	4	12	Good	6.03	1.55E-06
5.06	8	12	Uncured	0.85	N/A
12.972	8	12	Good	2.18	4.19E-06
17.94	8	12	Good	3.02	7.93E-07
5.06	14	12	Uncured	0.49	N/A
12.972	14	12	Uncured	1.25	N/A
17.94	14	12	Good	1.72	5.33E-06
17.94	8.33	30	Good	2.90	3.55E-07
17.94	5	30	Good	4.83	3.55E-07

The electrical resistivity of the epoxy-based silver ink track can also be affected by laser working parameters. As shown in **Figure 4.3**, where a lower laser scanning speed and a higher laser output power can lead to a lower electrical resistivity value

of the ink track sample. This can be further explained by effective laser energy density coupled into the epoxy-based silver ink per unit laser scanning pass, as seen in **Figure 4.4**, where lower electrical resistivities were achieved by 532nm laser curing process with a reduced laser energy density coupled into the silver ink per unit scanning pass compared to samples cured by CO₂ laser. **Figure 4.4** also shows that the electrical resistivity reduces in line with an increased laser energy density per unit scanning pass (this can be caused by increasing the laser output power, or reducing the laser scanning speed). However too high a value of the effective laser energy density per scanning pass can causes potential damage to materials, leading to an increased electrical resistivity (This will be discussed in **section 4.7.1**), as shown in **Figure 4.4**.

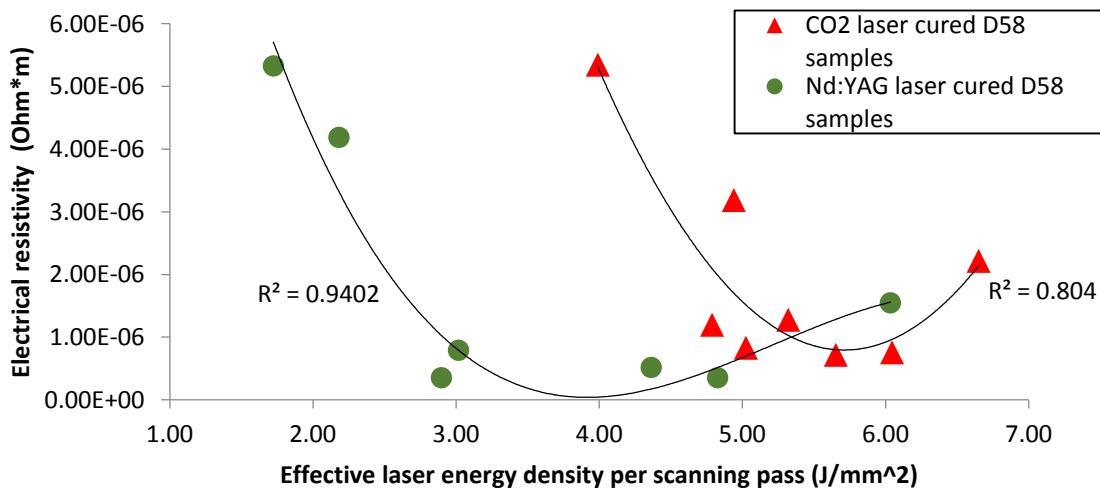


Figure 4.4: Electrical resistivity of laser cured D58 silver ink track samples as a function of effective laser energy density per unit scanning pass.

For oven cured D58 epoxy-based silver inks, **Figure 4.5** shows a lower value of electrical resistivity could be achieved by curing the ink track sample at a higher curing temperature in an Oven, the curing mechanism will be discussed in **Chapter 5**.

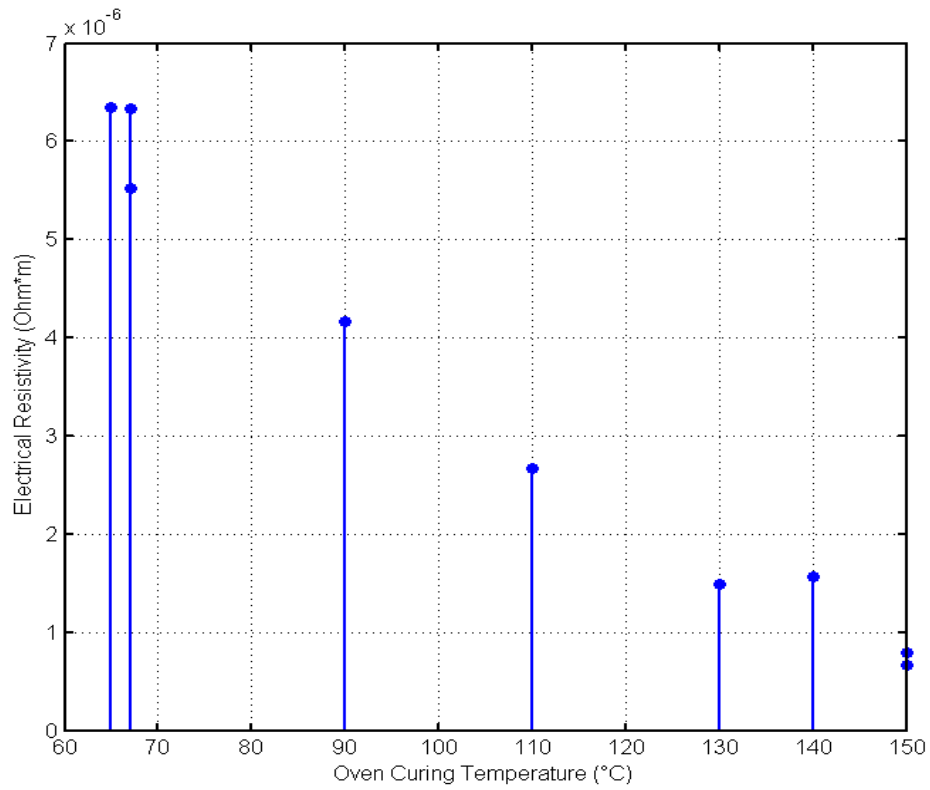


Figure 4.5: Electrical resistivities for oven cured D58 ink track samples.

4.4 Hardness Results

Ink track samples' hardness indexes were measured by using the Elcometer 501 pencil hardness tester and the results are shown in **Figure 4.6** and **4.7**. With a lower laser scanning speed and a higher laser output power (**Figure 4.6**), or a higher oven curing temperature (**Figure 4.7**), a higher hardness index could be achieved.

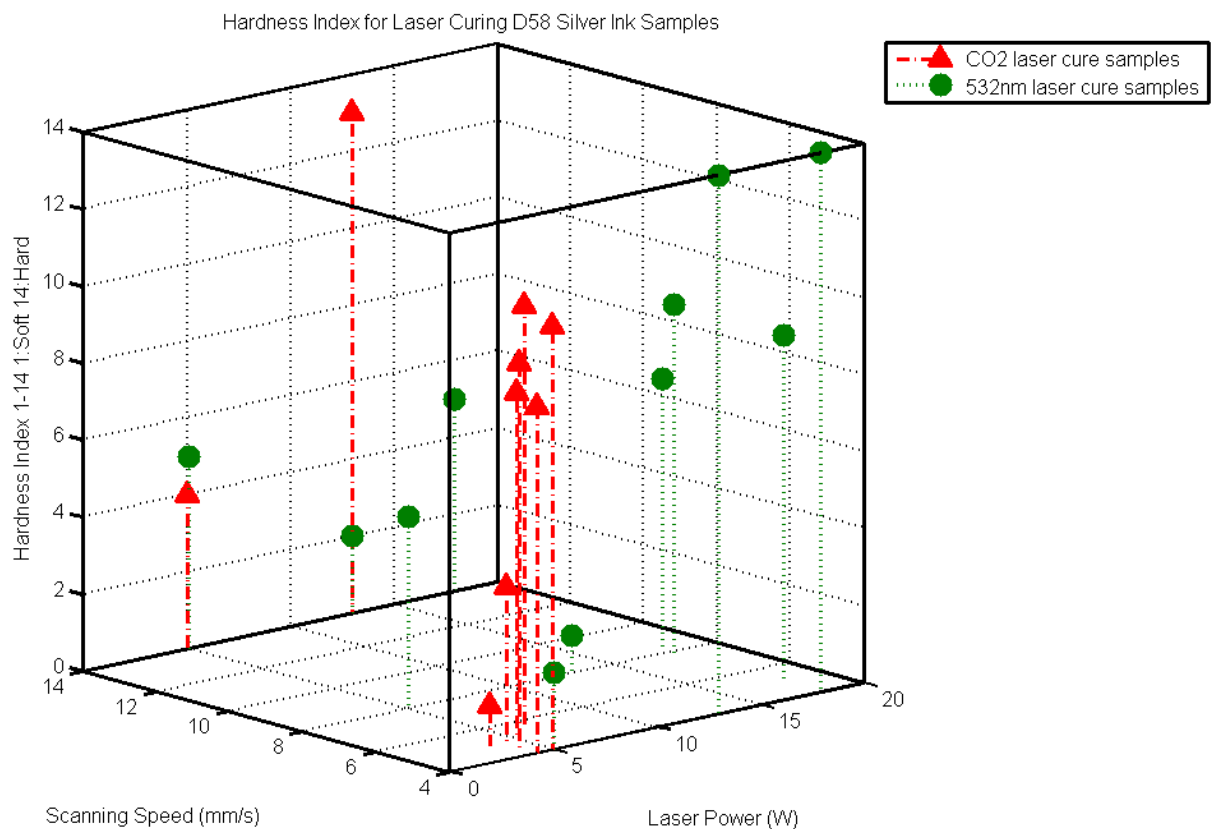


Figure 4.6: Hardness Index comparisons for ink track samples cured by CO₂ laser (red triangles), and 532nm Nd:YAG laser (green dots).

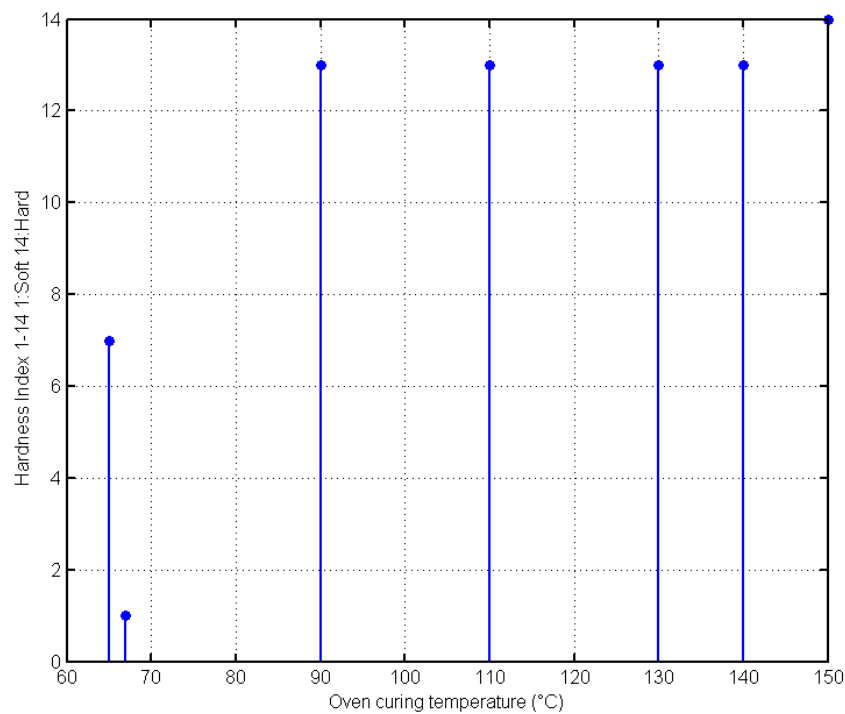


Figure 4.7: Hardness Index comparisons for oven cured D58 ink track samples.

As laser power increases, and the laser scanning speed reduces, or the oven curing temperature increases, the hardness of the ink track sample is also increased. The highest hardness index values of cured D58 epoxy-based silver ink were measured as 6H, this is better than that (5H) of ENTHONE 60 - a commercial ink containing a typical two-part resin system, which is similar to that in D58 epoxy-based silver ink as discussed in **Chapter 3** [4.2]. Oven cured D58 epoxy-based silver ink shows good hardness properties, however the whole processing time was much longer (cured for 1 hour in oven) compared to inks cured by laser for a couple of minutes.

4.5 Scanning Electron Microscope (SEM) and Energy-dispersive X-ray spectroscopy (EDX) analysis for Cured D58 Epoxy-based Silver Inks

Cured D58 epoxy-based silver inks were examined by Scanning Electron Microscope (SEM) and Energy-dispersive X-ray spectroscopy (EDX) after treatments by lasers and oven in order to investigate the microstructure and elemental composition properties. Cross-sectional SEM images were taken for a CO₂ laser cured sample (cured at 13W with scanning speed at 14mm/s), a 532nm Nd:YAG laser cured sample (cured at 12.972W with scanning speed at 4mm/s), these D58 epoxy based silver ink samples were cured at an equivalent temperature of ~125°C (as discussed in **section 4.1**) and can be compared to an oven cured sample (cured at 140°C for 1 hour), as shown in **Figure 4.8**.

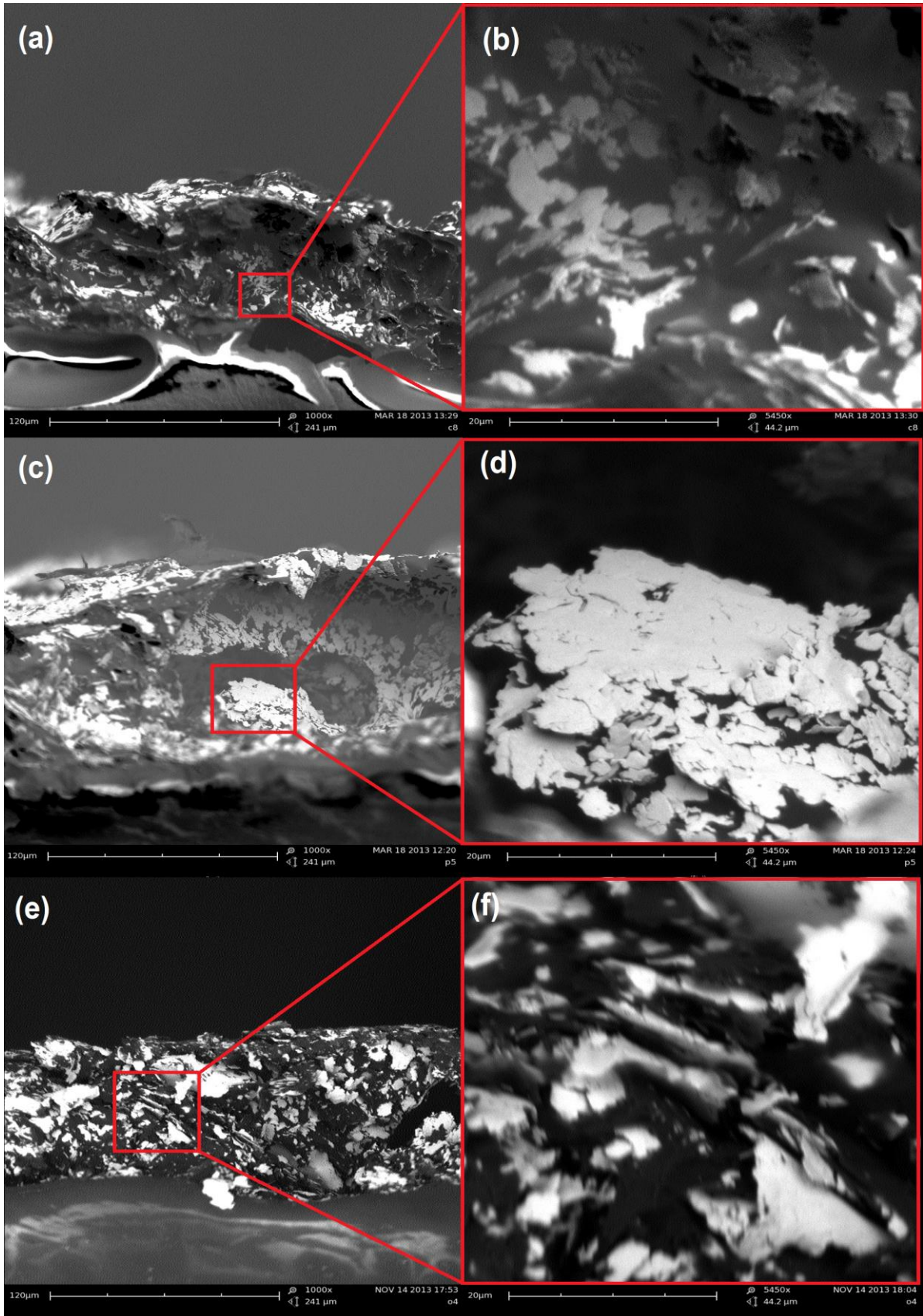


Figure 4.8: SEM cross-sectional images with 1000x magnification on the left, and 5450x magnification on the right for: CO₂ laser cured ink track sample (a), (b); 532nm Nd:YAG laser cured sample (c), (d); and oven cured sample (e), (f), respectively.

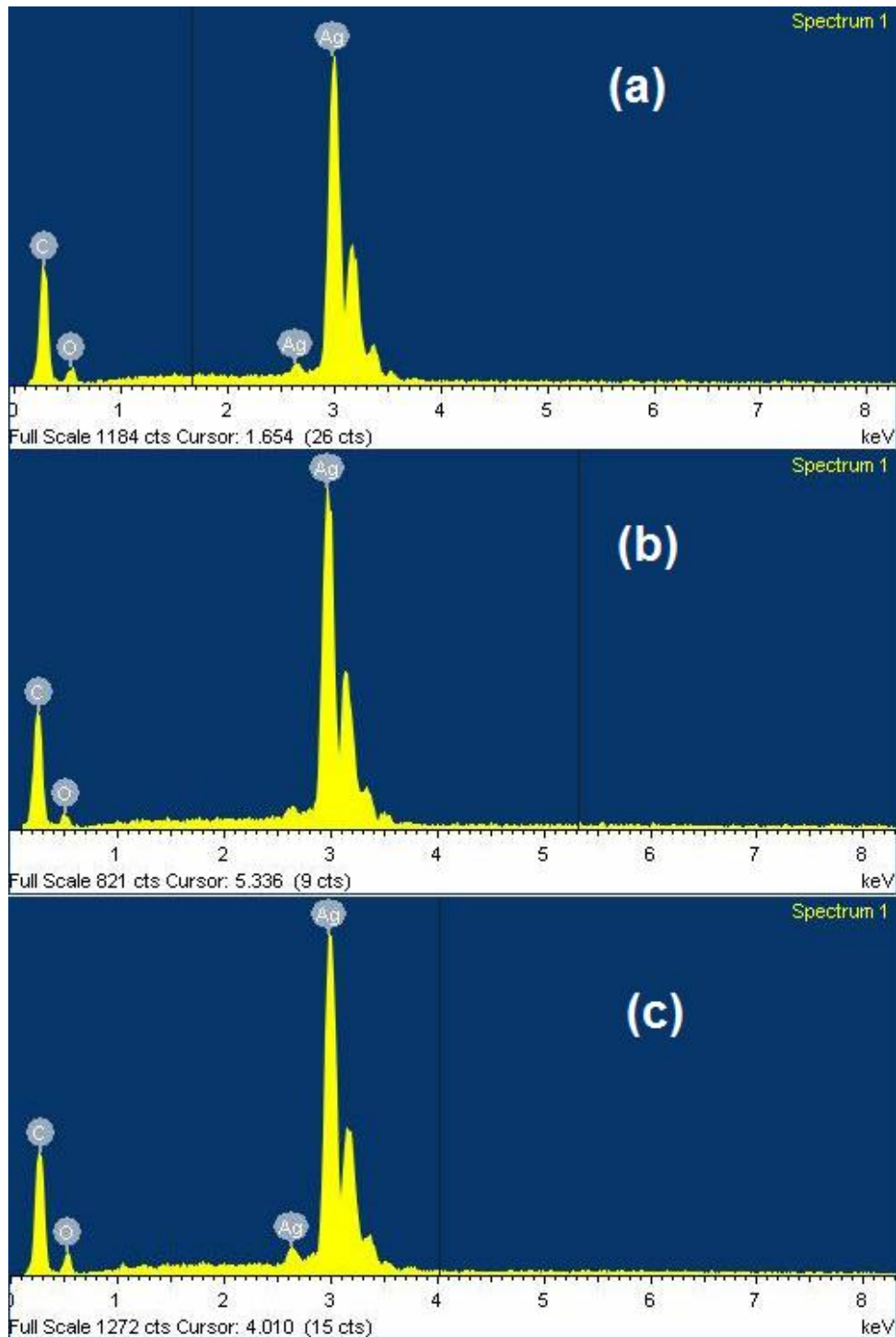


Figure 4.9: EDX spectrums for D58 silver ink track samples cured by CO₂ laser at 10.6 μm (a), Nd:YAG laser at 532 nm (b), and oven (c).

Figure 4.9 shows the spectrum of energy-dispersive x-ray analysis (EDX, or EDXA) carried out at the Nanoinvestigation Centre at Liverpool (NiCaL), all three ink samples contain silver, oxygen, and carbon elements, as shown in **Table 4.8**.

Table 4.8: Elemental analysis in D58 ink.

	Silver (wt%)	Carbon and Oxygen (wt%)
Oven Cured D58 Ag Ink	64.06	35.94
CO ₂ Laser Cured D58 Ag Ink	65.58	34.41
532nm Laser Cured D58 Ag Ink	68.89	31.11

As shown in **Table 4.8**, all three curing processes results in a cured epoxy-based silver ink containing silver, oxygen, and carbon elements, the oxygen and carbon within the D58 epoxy-based silver ink were considered as elements whose presence is due to the resin and solvent components of the ink, this will be discussed in **Chapter 5** with more details.

SEM/EDX analysis for wet samples were unable to be obtained due to liquid material evaporation in vacuum, therefore proportional ratio of elemental components in D58 silver ink before cure were unable to be obtained directly from the EDX analysis. However as specified in the approximated ink composition of D58 silver ink provided by Gwent Electronic Materials, Ltd. (GEM), the proportional ratio of mass percent for silver, carbon and oxygen elements in D58 silver before cure can be calculated and are shown in **Appendix 2** to this Thesis. Therefore, the EDX values measured for each process and the proportional mass percent of carbon and oxygen of uncured D58 epoxy-based silver ink can be compared to an ideal curing result in which the solvent is assumed to be removed completely from the ink system as also calculated in **Appendix 2** (this comparison of values is shown in **Table 4.9**).

Table 4.9: Elemental composition in D58 silver ink

	Mass Percent of Silver in Ink (wt%)	Mass Percent of Carbon and Oxygen in Ink (wt%)	Normalized Proportional Mass Percent in Ink	
			Normalized Silver Proportional Mass Percent in Ink (wt%)	Normalized Carbon and Oxygen Proportional Mass Percent in Ink (wt%)
D58 ink before cure	62.73	37.27	62.73	37.27
Oven cured D58 ink	64.06	35.94	62.73	35.19
CO ₂ laser cured D58 ink	65.58	34.41	62.73	32.91
532nm laser cured D58 ink	68.89	31.11	62.73	28.33
Ideal D58 ink after cure	71.86	28.14	62.73	24.56

Using the normalized carbon and oxygen proportional mass percent in D58 ink as calculated in **Table 4.9** with a constant silver content 62.73wt%, the relative efficiency of each process in reducing the amount of carbon and oxygen in the ink can be compared, as shown in **Figure 4.10**.

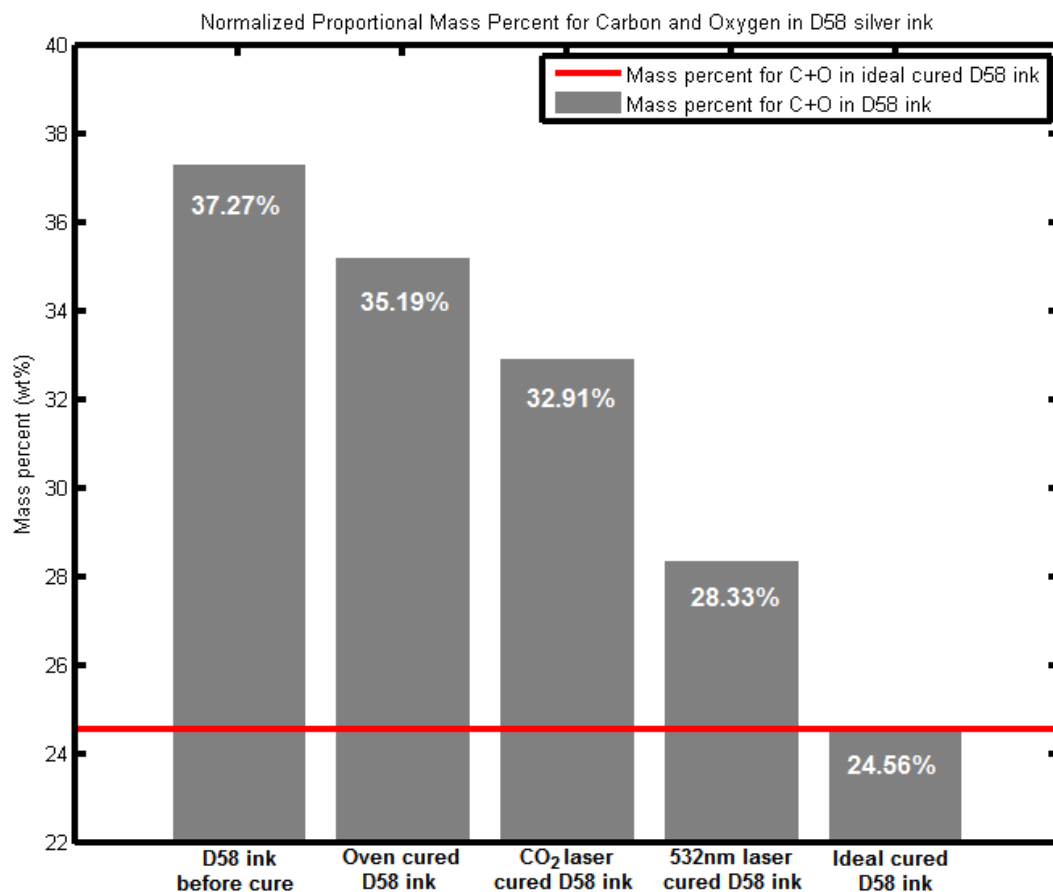


Figure 4.10: Carbon and Oxygen content in D58 silver ink for different curing processes.

As seen from **Figure 4.10**, the proportional mass percent of carbon and oxygen remaining in the D58 ink is affected by the curing process used. The carbon and oxygen are elements included both the resin complex and solvent. As the resin is retained in the chemical crosslinking process, the primary reduction in weight of carbon and oxygen in epoxy-based silver ink is as the result of the solvent removal. The 532nm laser curing process caused the greatest reduction of weight of carbon and oxygen in the ink out of the three different curing processes (532nm Nd:YAG laser, CO₂ laser, and oven). The carbon and oxygen content indicates the solvent

removal in D58 epoxy-based silver ink cured by 532nm laser is much more efficient when compared to both CO₂ and Oven curing. **Figure 4.10** also shows the carbon and oxygen content in D58 epoxy-based silver ink cured by 532nm laser is close to (~3% higher) that in a perfectly cured D58 ink with no solvent assumed as an ideal case.

Sato has investigated the mass loss with variant curing temperature in a thermogravimetric analysis (TGA) for uncured D58 epoxy-based silver ink [2.52]. In his research, the overall mass loss for D58 ink cured in oven at 140°C can be measured roughly at around 5% (**Figure 4.11**), this fits well to ~5% weight reduction of carbon and oxygen cured by Oven measured by EDX and shown in **Figure 4.10**.

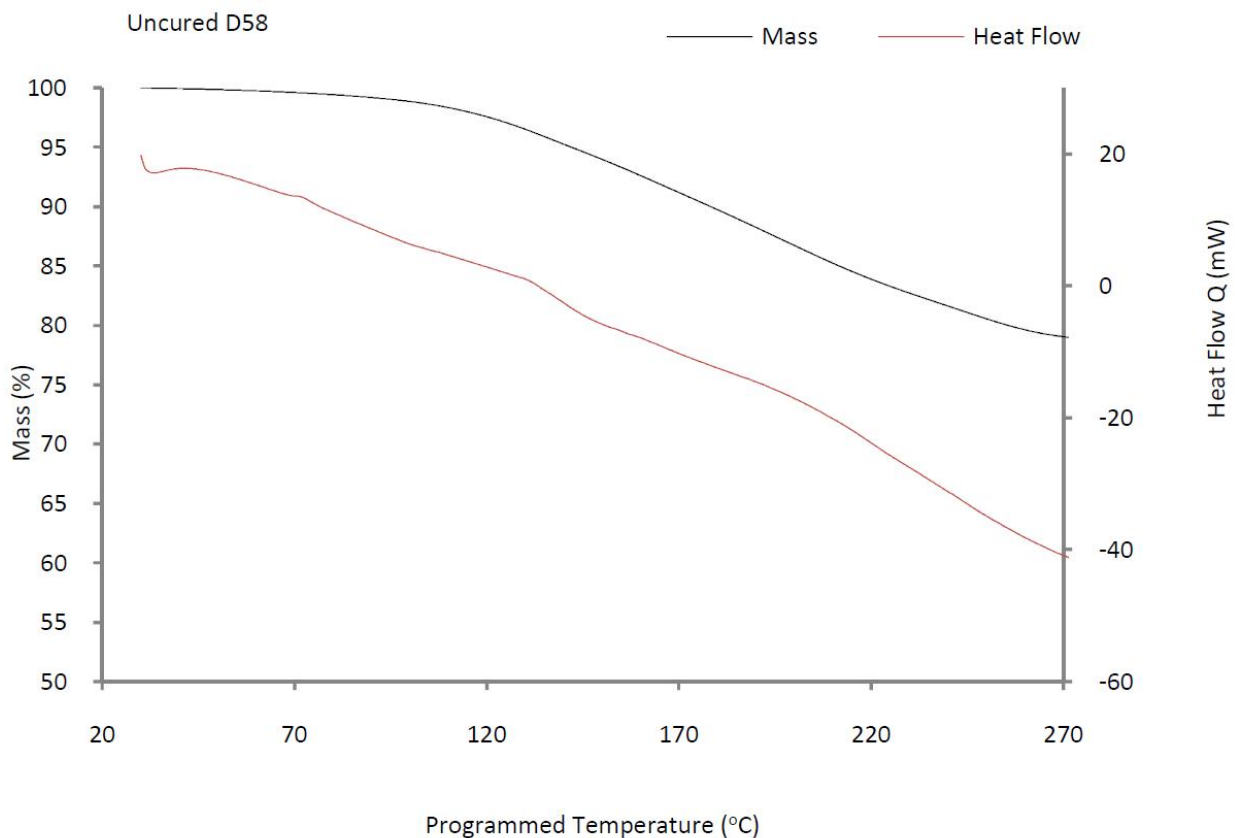


Figure 4.11: Thermogravimetric analysis (TGA) graph of uncured D58 silver ink shows the mass loss as a function of curing temperature, investigated by Sato [2.52].

Figure 4.12 shows the proportional mass percent of silver in D58 epoxy-based silver ink for the different curing processes. The proportional silver content of

68.89% in ink cured by 532nm laser is considered as the highest proportional mass percent of the silver in ink cured by the different curing techniques ($\sim 3.31\%$ more overall than from the CO₂ laser curing process, $\sim 4.83\%$ more than the oven curing process, and $\sim 6.16\%$ more than uncured D58 silver ink).

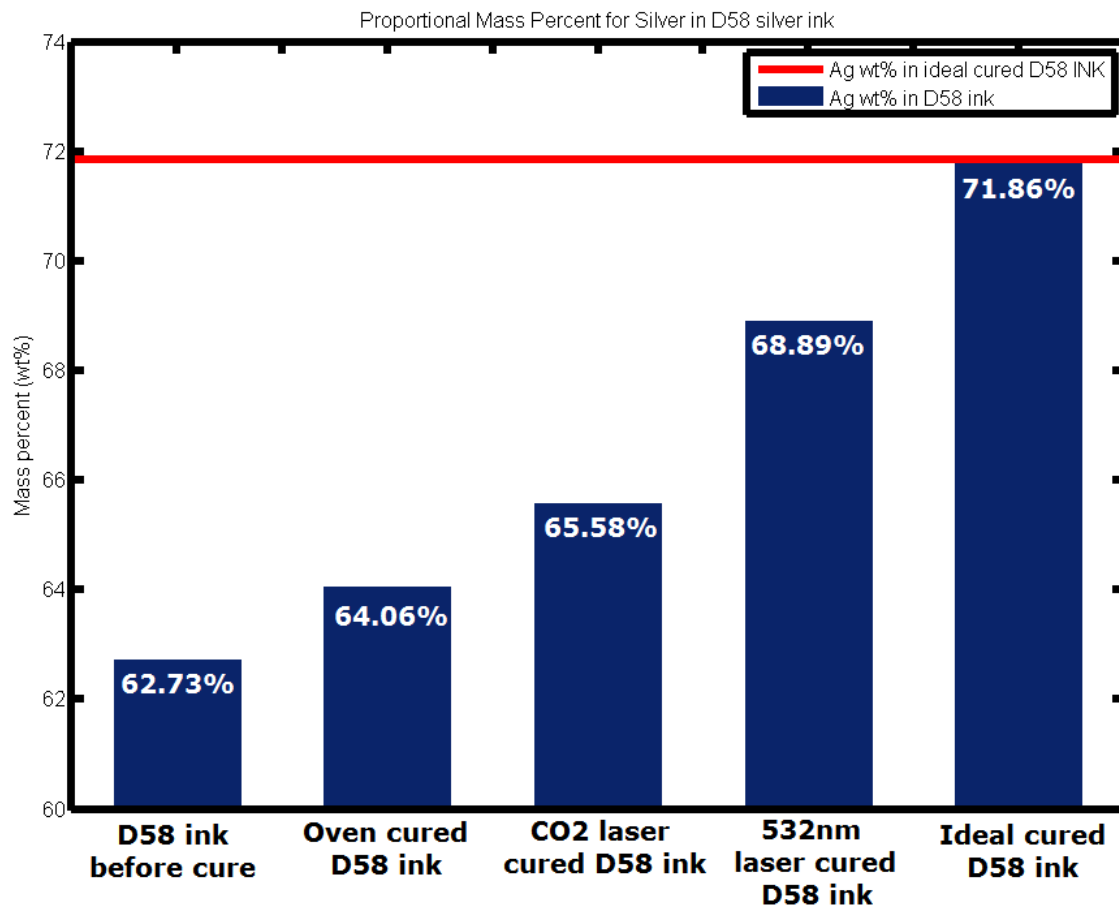


Figure 4.12: Silver content in D58 silver ink for different curing processes.

Therefore the D58 epoxy-based silver ink cured by 532nm laser curing process can be considered as a more fully cured silver ink with higher proportional silver-to-carbon and oxygen ratio than that cured by CO₂ laser and an Oven. This higher proportional silver to carbon and oxygen ratio in D58 ink cured by 532nm laser is partially caused by a more efficient solvent transport mechanism due to the Marangoni effect (the 532nm laser curing mechanism theories will be discussed in **Chapter 5**). This can result in a spatial arrangement of silver flakes stacked together with less gaps. As shown in **Figure 4.8 (c), (d)**, if the silver micro-sized flakes in 532nm Nd:YAG laser curing process are stacked with less gaps, this space

arrangement results in a tighter packaging of silver flakes, and therefore a lower electrical resistivity of the epoxy-based silver ink as discussed in **Chapter 2**.

4.6 Curing Window for Laser Curing D58 Silver Ink

As discussed in **Chapter 2**, due to the nature of wavelength selected in laser curing processes, the curing mechanism when treating with either infrared or 532nm wavelengths is dominated by thermal effects caused by the laser beam (**Chapter 5** discusses laser curing mechanisms at 532nm in more depth). Here, therefore, the surface temperature distribution during the laser curing of the D58 epoxy-based silver ink track is investigated. Different laser process parameters (e.g. laser output power, beam scanning speed) will result in a different local temperature rise at the interface where the laser beam interacts with the top surface of the ink material, it is important to determine the effect of this localised temperature on the final curing result.

Figure 4.13 shows surface temperature comparisons for D58 silver inks cured by CO₂ laser at 10.6 μ m and Nd:YAG laser at 532nm. Red triangles are surface temperatures recorded by a Type-K thermocouple for CO₂ laser cured inks, and green dots are surface temperatures recorded by an IR camera for 532nm Nd:YAG laser cured inks. As seen from the **Figure 4.13**, the lower the laser scanning speed used in laser curing process, or the higher the laser output power, then the higher surface temperature can be resulted.

As discussed in **Chapter 3**, the polymer substrate material - PET's melting point is $\sim 260^{\circ}\text{C}$ [3.9], any temperature excesses 260°C can damage the PET substrate material and can also damage the ink track sample (*Overcure*). The minimum temperature for resin to cross-link is roughly at 90°C [4.3] (please refer to **Chapter 5** for resin crosslinking theory), thus any temperature below 90°C will unable to cross-link the resin complex of the epoxy-based conductive silver ink system, and hence fail to make the ink electrically conductive (*Undercure*).

These results show that a process window for laser curing the D58 epoxy-based conductive silver ink can be more easily obtained using a Nd:YAG laser operating at 532nm compared to D58 epoxy-based silver inks cured by CO₂ laser at 10.6μm which have a markedly reduced process window within the temperature boundaries.

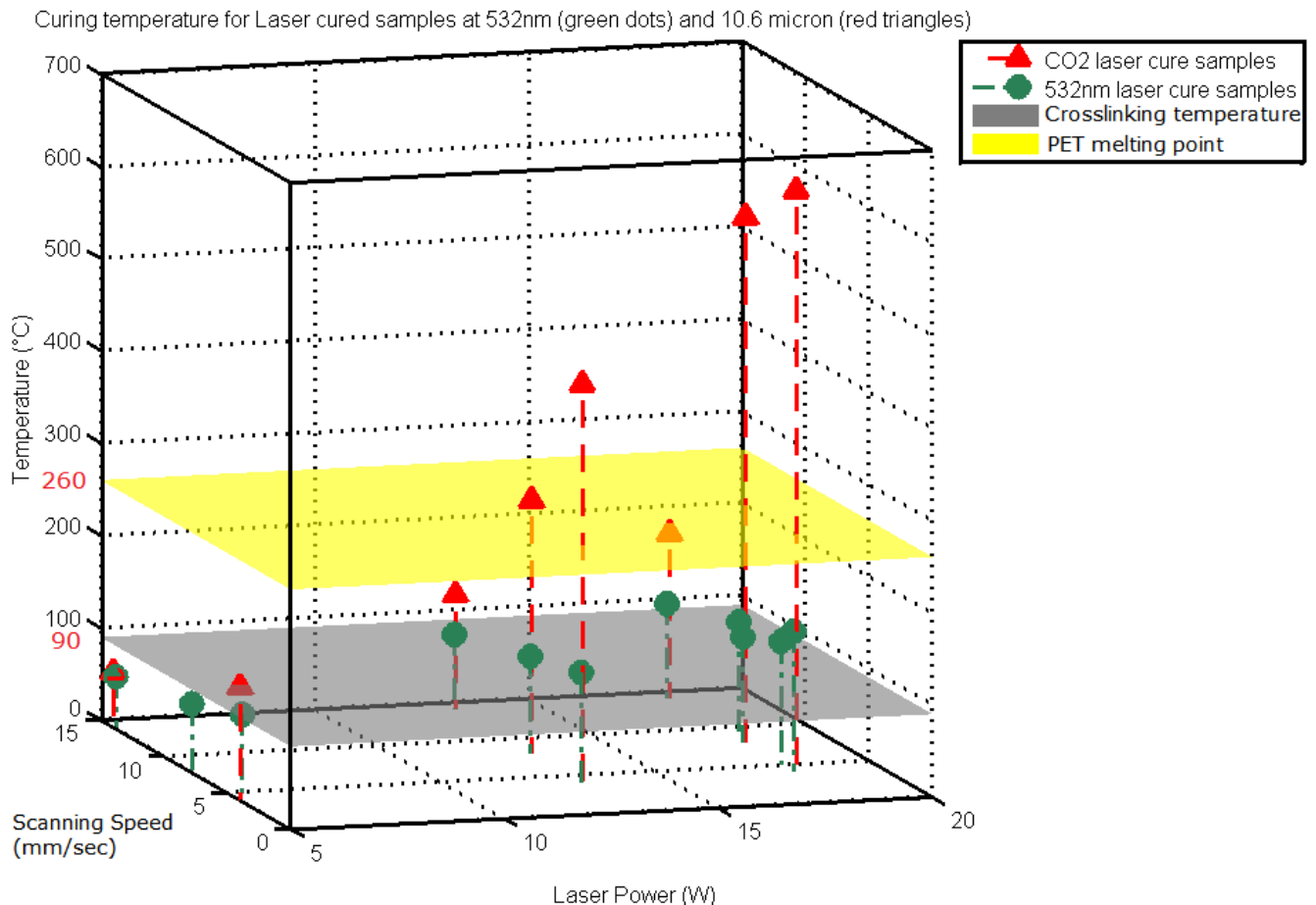


Figure 4.13: Temperature profiles (°C) for D58 conductive silver ink track samples irradiated by CO₂ (red triangles) laser at 10.6μm and Nd:YAG (green dots) laser at 532nm. A window for suitable working parameters is given between resin cross-linking temperature at around 90°C (gray) and the PET melting temperature at 260°C (yellow).

The results of curing of the epoxy-based conductive ink material can be determined by the condition of material's physical structure as well as the value of electrical resistivity of the ink after curing process. For the purpose of this Thesis the following definitions will be used, in which the cured conductive ink can be defined as the ink with an electrical resistivity close (<500 times) to that of bulk conductive material (in this case, silver) after the curing process and the physical structure of the ink has

not been damaged, the undercured ink is defined as having an undamaged (i.e. neither burned or bubbled) structure and an ink with an electrical resistivity significant larger (>500 times) than that of the bulk silver material, and the overcured ink is defined as an ink with its physical structure damaged due to excessive heat. **Figure 4.14** shows the curing process window for curing D58 epoxy-based silver ink by lasers, the cured ink samples are grouped into these three curing conditions – overcured, cured, and undercured according to their electrical resistivity values and condition of the ink physical structures. The 532nm laser offers a wider window for laser processing parameters than that of CO₂ laser at 10.6 μ m, indicating that the D58 epoxy-based silver ink can be cured at a lower electrical resistivity by 532nm laser on the PET substrate with a lower risk of damaging the both ink and substrate materials.

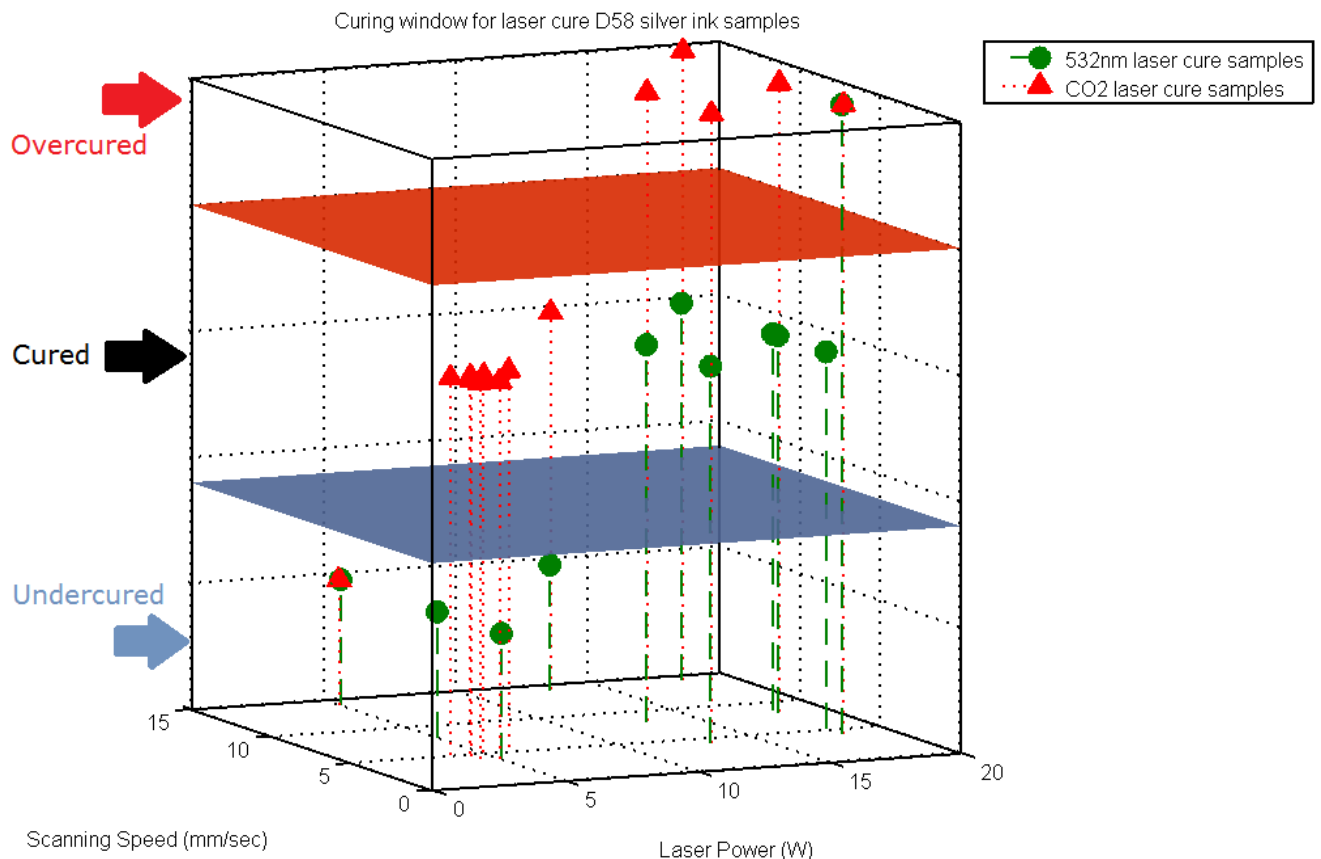


Figure 4.14: Curing window for curing D58 silver ink.

4.7 Thermal Damage to Epoxy-based Silver Ink and Polymer Substrate Material

As discussed in **section 4.5**, the epoxy-based conductive silver ink can easily be overcured with (i) thermal damage to the silver ink; and (ii) thermal damage to the PET polymer substrate material. This is a particular risk when irradiated by CO₂ laser at an infrared wavelength of 10.6 μ m.

4.7.1 Thermal Damage to Epoxy-based Silver Ink Material

As shown in **Figure 4.4**, the electrical resistivity of the epoxy-based silver ink is a function of the effective laser energy density per unit laser scanning pass, in that, the electrical resistivity value decreases with an increasing effective laser energy density per scanning pass. However too high an effective laser energy density per scanning pass (as a result of either a too high laser power or a too slow laser traverse speed), can damage the resin complex of the silver ink, which will reduce the electrical conductivity of the silver ink and/or cause the dissociation of the ink from the polymer substrate, (this has been previously investigated by Shang, Sato, and Merad *et al.* [2.51, 2.52, 4.4]). As seen in **Figure 4.4**, the increased electrical resistivities for D58 epoxy-based silver inks cured by 532nm laser with effective laser energy density per pass greater than 4 J/mm² and silver inks cured by CO₂ laser with effective laser energy density per pass greater than \sim 6 J/mm² can indicate the thermal damage caused by excessive laser energy coupled into the silver ink.

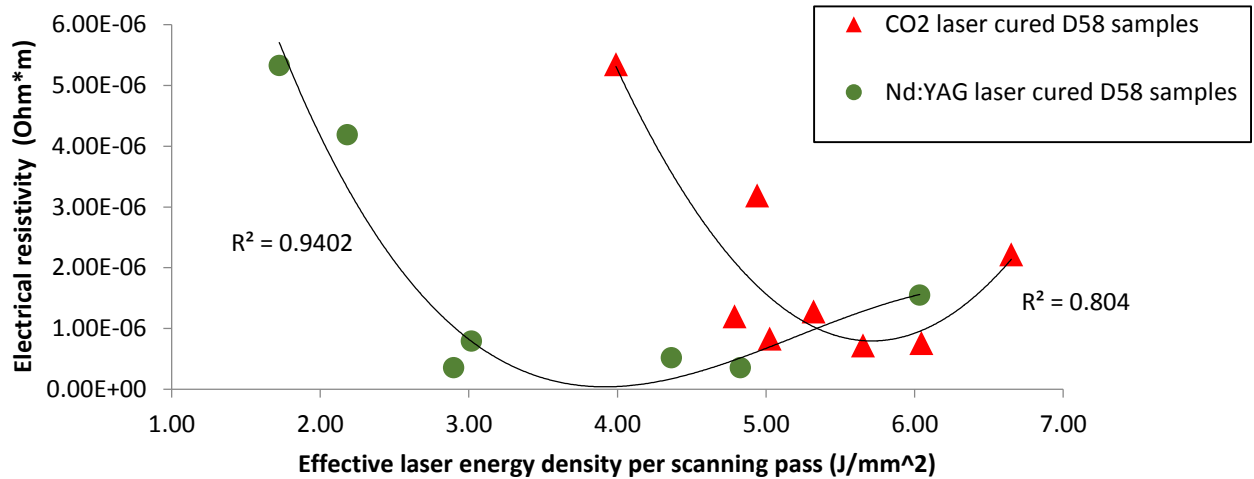


Figure 4.4: Electrical resistivity of laser cured D58 silver ink track samples as a function of effective laser energy density per unit scanning pass.

A more shallow gradient either side of the inflexion point on the curved trendline for D58 epoxy-based silver inks cured by laser at 532nm as observed in **Figure 4.4**, suggesting that a wider window for laser working parameters could be selected to cure the ink at the laser wavelength of 532nm without the risk of damaging the silver ink, compared to that for CO₂ laser at an infrared wavelength at 10.6 μ m.

4.7.2 Thermal Damage to PET Substrate Material at an Infrared Wavelength

As discussed in **Chapter 2**, the PET polymer substrate is highly transparent ($\sim 87\%$ transmission) at the wavelength of 532nm (**Figure 2.48**), however the PET polymer substrate can be damaged at a 10.6 μ m infrared wavelength due to photothermal absorption, therefore the surface morphology of the PET polymer substrate can be changed due to heating by infrared laser irradiation (**Figure 2.49**).

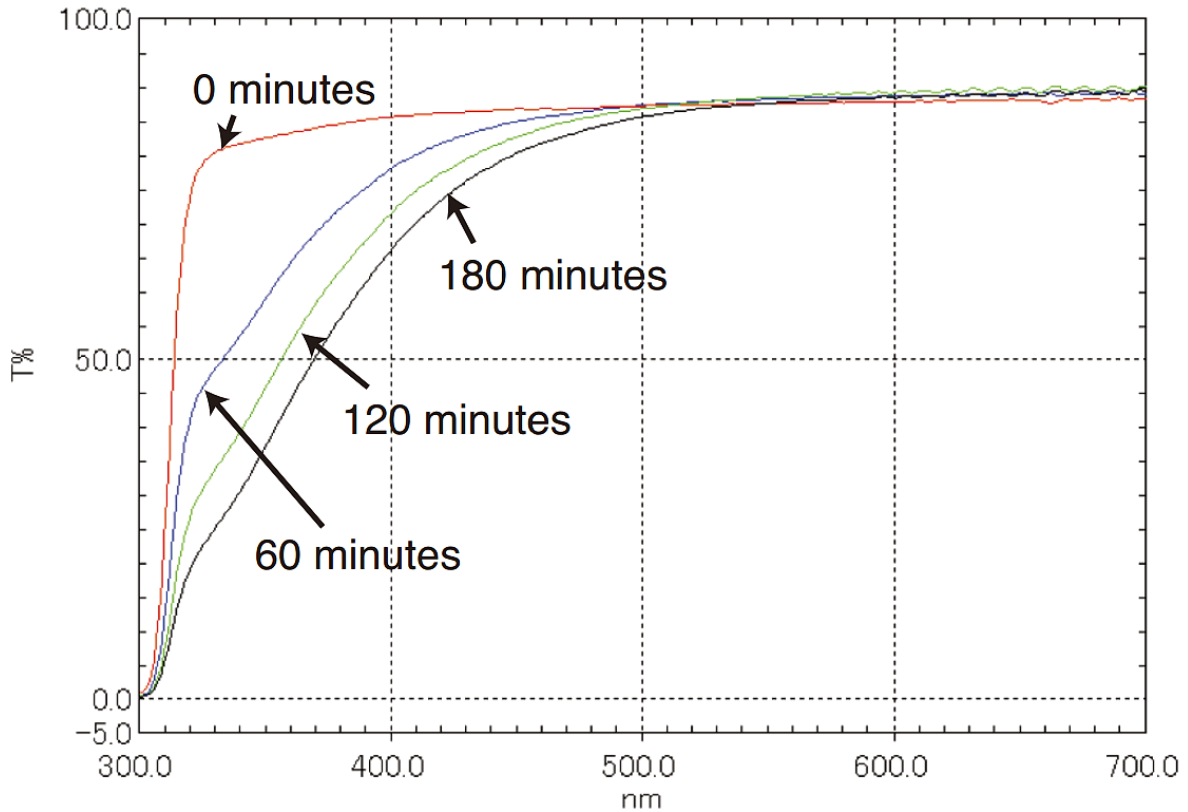


Figure 2.48: Absorbance spectrum of PET polymer substrate, the red curve labelled '0 minutes' can be treated as a clean PET substrate as it has not been irradiated by UV irradiations [2.55].

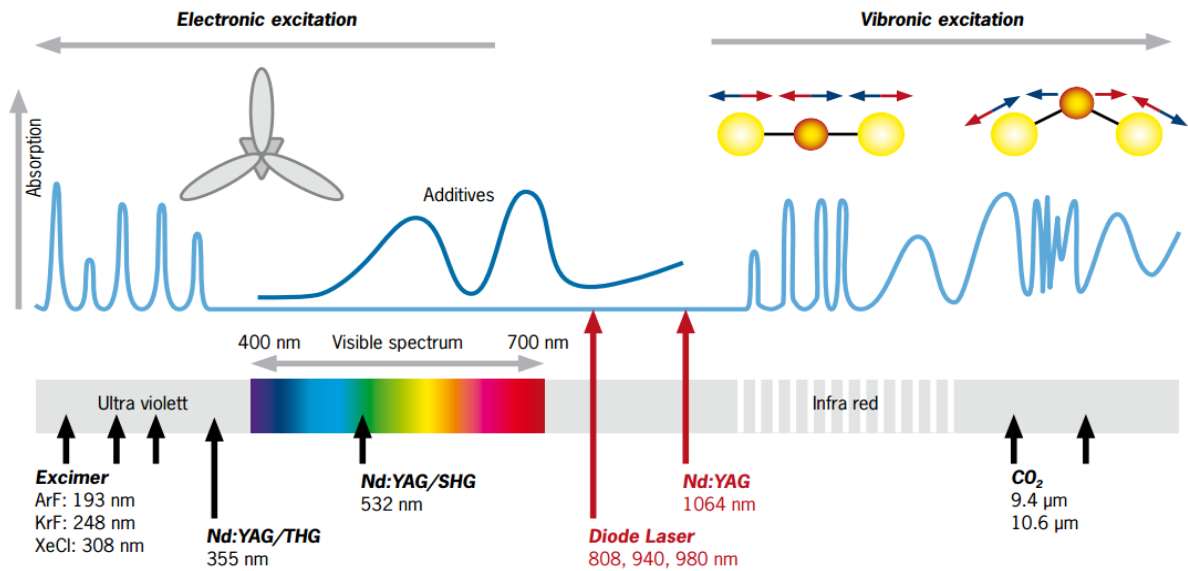


Figure 2.49: Both UV and infrared wavelengths can cause damage to polymer substrate, leaving the visible wavelength as a suitable range for curing functional materials on polymer substrate [2.58].

An investigation has been carried out to quantify the damage caused on the PET polymer substrate material at a 10.6μm infrared laser irradiation wavelength, this

can be measured visually and by a WYKO white light interferometer measurement. As shown in **Table 4.10**, the PET substrate samples were exposed to CO₂ laser irradiations with variant laser working parameters.

Table 4.10: Investigation of damage caused to the PET substrate at infrared wavelength by CO₂ laser at 10.6 μ m.

Laser Power (W)	Scanning Speed (mm/s)	Scanning Pass	PET Substrate Condition
5	4	1	Damaged
13	4	1	Burnt
18	4	1	Burnt
5	8	1	Damaged
13	8	1	Burnt
18	8	1	Burnt
5	14	1	No Damage
13	14	1	Burnt
18	14	1	Burnt
5	3.5	1	Damaged
5	5	1	Damaged
5	6	1	Damaged
5	7	1	Damaged

As seen in **Table 4.10**, PET substrate materials were easily damaged or burnt through due to strong infrared interaction with the CO₂ laser, **Figure 4.15** shows the graphical representation of PET samples which were not entirely burnt through, their widths of damage caused by infrared wavelength were measured by a WYKO white light interferometer. The width of damage caused by infrared laser beam at 10.6 μ m is inversely proportional to laser scanning speed at a constant laser output power, this can be seen in **Figure 4.16**.

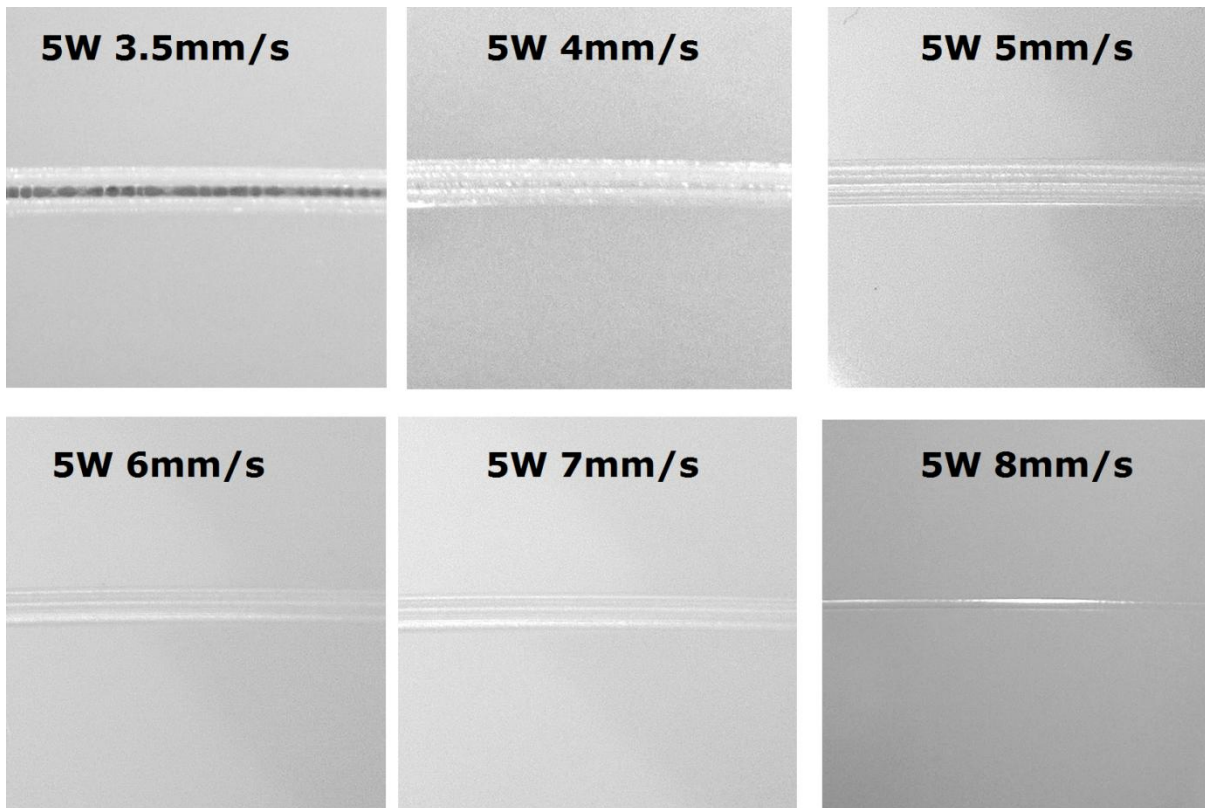


Figure 4.15: Demonstration of the PET substrate materials which were not entirely burnt through by infrared wavelength by CO₂ laser at 10.6 μ m (pictures were not taken with the same scale).

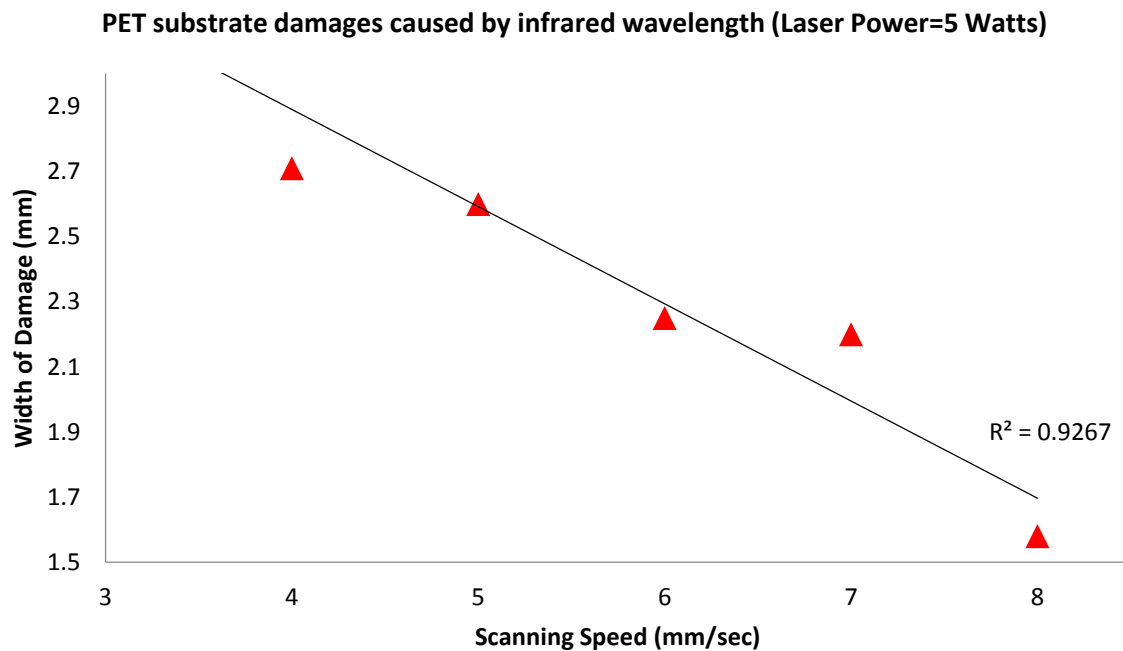


Figure 4.16: the width of damage on PET substrate as a function of CO₂ laser working parameters, measured by a WYKO measurement.

As both epoxy-based silver ink and the PET polymer substrate materials can be easily damaged at the infrared wavelength, this makes the visible wavelength at 532nm a suitable wavelength that could be used to cure the epoxy-based conductive silver ink while reducing risks of damaging both ink and polymer substrate materials.

4.8 Results of Curing Epoxy-based Silver Inks with Variant Ink Compositions

As discussed in **Chapter 3**, D58 epoxy-based silver ink was chosen as the primary ink in this investigation for its basic ink composition (Silver micro-sized flakes, Resin complex, and Organic solvent) to simplify the investigation into the theory of a 532nm laser curing mechanism in **Chapter 5**. Other epoxy-based silver ink materials with variant ink compositions were also studied in this experimental-based investigation. **Table 3.2** shows the approximated ink composition for silver inks used in this thesis.

Table 3.2: Approximate compositions for silver inks used in this investigation (Data from GEM).

Ink Name	Approximate composition	Silver content (wt%)
Silver Ink D58	Silver flakes, Epoxy resin, Blocked Isocyanates, Solvent	59%
Laser Curable Silver Ink D5	Silver flakes, Epoxy resin, Blocked Isocyanates, Solvent	78%
Graphite Doped Silver Ink D5	0.5wt% Graphite, Silver flakes, Epoxy resin, Blocked Isocyanates, Solvent	61%
Silver Ink D2	Silver particles (micro- and nano-size), Epoxy resin, Blocked Isocyanates, Solvent	45%

In this section, two types of epoxy-based silver inks with different ink compositions were used to investigate benefits that brought by a change in ink compositions (Laser curable silver ink D5, and Graphite doped silver ink D5). For example, the laser coupling efficiency of the silver ink can be increased by adjusting the ink composition in either of the following methods:

- 1) Increasing the concentration of silver particles in ink system,
- 2) Adding optically absorbing agent to laser wavelength, or dopant to ink system, such as carbon or graphite particles.

4.8.1 Increasing Laser Coupling Efficiency by an Increased Silver Concentration

A specific epoxy-based silver ink (*Laser curable silver ink D5*) was supplied by Gwent Electronic Materials, Ltd. (GEM) with a high concentration of silver micro-flakes in ink system (78wt% of Ag). Such a high level concentration of silver flakes (19% more than that in D58 silver ink) increased the curing efficiency with improved curing results, **Table 4.11** shows curing results of laser curable silver ink D5 on a PET substrate cured by Nd:YAG laser beam irradiations at 532nm. Due to an increased concentration of silver flakes in ink, the curing time was significantly reduced from ~7 minutes in a D58 curing process as shown in **Table 4.2** down to ~20 seconds for the Laser curable D5 ink as shown in **Table 4.11**.

Table 4.11: Laser curable D5 silver ink track samples cured by Nd:YAG laser at 532nm.

Laser Output Power (W)	Scanning speed (mm/s)	Number of Scanning Passes	Effective laser energy density per scanning pass (J/mm ²)	Electrical Resistivity (Ohm*m)
12.972	12	2	1.45	2.72E-07
13.984	12	2	1.57	2.84E-07
13.984	16.67	2	1.13	2.31E-07
17.94	16.67	1	1.45	2.64E-07
12.972	16.67	2	1.05	3.93E-07
12.972	10	1	1.75	1.91E-07
12.972	16.67	5	1.05	5.00E-07
12.972	10	2	1.75	1.99E-07
15.456	16.67	5	1.25	2.38E-07
16.48	16.67	5	1.33	1.46E-07
16.48	16.67	5	1.33	2.62E-07
16.48	16.67	5	1.33	2.23E-07
17.296	16.67	4	1.40	1.82E-07
17.296	16.67	4	1.40	2.41E-07
17.296	20.83	5	1.12	2.47E-07
17.296	20.83	5	1.12	2.72E-07
17.94	20.83	5	1.16	2.61E-07
17.94	20.83	5	1.16	2.11E-07

The lowest electrical resistivity was achieved for silver ink D5 at 1.46×10^{-7} Ohm*m, which is only 9 times of the bulk silver. This low resistivity value of 1.46×10^{-7} Ohm*m is less than a half of that for D58 ink cured at the same wavelength of 532nm (3.55×10^{-7} Ohm*m). In addition, as seen from **Table 4.11**, the curing time of the laser curable silver ink D5 is reduced due to an increased curing efficiency resulted from a higher degree of silver concentration in ink. This helped energy absorption to laser irradiation at 532nm (please refer to **Chapter 5** for laser curing mechanism). Therefore a reduced electrical resistivity can be achieved at a lower value of effective laser energy density per scanning pass (**Figure 4.17**), in which the laser curable D5 silver ink requires less energy density per laser scanning pass (nearly a half of that required for curing D58 epoxy-based silver ink) to become highly electrical conductive.

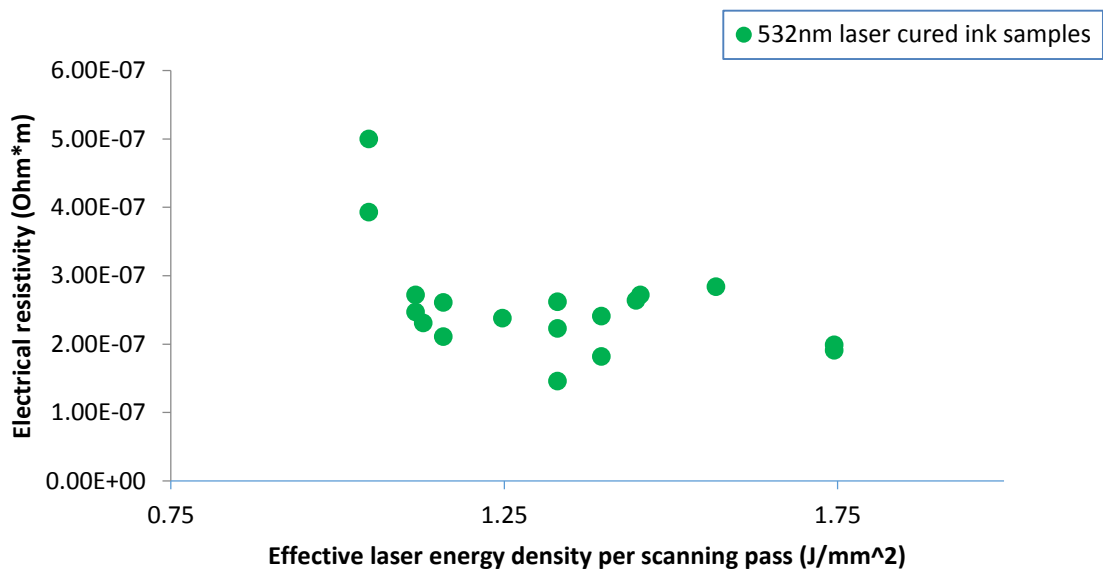


Figure 4.17: Electrical resistivity of laser cured laser curable D5 silver ink track samples as a function of effective laser energy density per unit scanning pass.

4.8.2 Increasing Laser Coupling Efficiency by an Added-in Optically Absorbing Agent to Laser Wavelength, or Dopant

The curing efficiency of the epoxy-based silver ink system could also be increased by adding optically absorbing agent to laser wavelength, i.e. a dopant to the ink system, such as graphite or carbon particles. This helps to increase the coupling efficiency of the laser radiation into the inks due to the higher optical absorption coefficient of carbon and graphite, as investigated by Sato [1.6]. When the laser beam is irradiating the ink, carbon or graphite absorbs the laser energy efficiently and transfers the absorbed energy as heat into the rest of the ink to assist the thermal curing process. Both carbon and graphite have been observed to be sublimated off after the laser curing processes. In this section, a specified epoxy-based silver ink (*Graphite doped silver ink D5 with 0.5wt% graphite content*) was provided by Gwent Electronic Materials, Ltd. (GEM) for this investigation.

Table 4.12: Graphite doped D5 silver ink track samples cured by Nd:YAG laser at 532nm.

Laser Output Power (W)	Scanning speed (mm/s)	Number of Scanning Passes	Effective laser energy density per scanning pass (J/mm ²)	Electrical Resistivity (Ohm*m)
17.296	20.83	5	1.12	3.86E-07
17.296	16.67	5	1.40	2.26E-07
17.296	20.83	5	1.12	3.24E-07
17.296	20.83	5	1.12	2.34E-07
17.94	20	8	1.21	2.61E-07
17.94	20	10	1.21	2.34E-07
17.94	20	10	1.21	2.47E-07
17.94	20	10	1.21	2.51E-07

Table 4.12 shows curing results of graphite doped epoxy-based silver inks D5 cured on the PET substrate by Nd:YAG laser at 532nm. The lowest electrical resistivity value for graphite doped D5 silver ink was achieved at 2.26×10^{-7} Ohm*m (**Table 4.12**), which is ~ 14 times of the bulk silver (this is better than that of the D58 epoxy-based silver ink cured at the same wavelength of 532nm (3.55×10^{-7} Ohm*m)). In 532nm laser curing of graphite doped D5 silver inks, the ink became highly electrically conductive with a reduced laser energy density per unit scanning pass compared to that required to cure D58 silver ink, as shown in **Figure 4.18**. This

helped to increase the curing efficiency by graphite absorption to laser beam energy. In addition, as seen in **Figure 4.18**, a reduction in effective laser energy density can result in a greater variation in electrical resistivities. This increased variation in resistivity (e.g. resistivity values for graphite doped D5 silver inks with effective laser density at 1.12) is considered as a result of not using optimum curing parameters in a 532nm laser curing process.

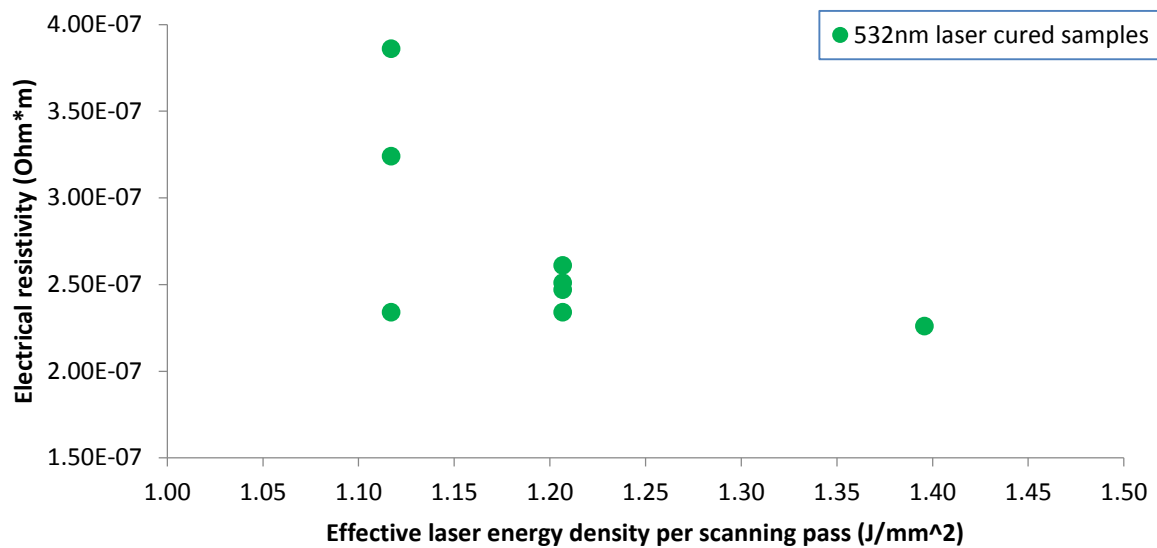


Figure 4.18: Electrical resistivity of laser cured graphite doped D5 silver ink track samples as a function of effective laser energy density per unit scanning pass.

4.9 Chapter Summary

This Chapter discussed experimental results for curing epoxy-based conductive silver inks. These inks were cured by CO₂ laser, 532nm Nd:YAG laser, and oven. Electrical resistivity, hardness, curing temperature, silver ink's internal structure and elemental analysis were measured and compared. As result of these comparisons, epoxy-based conductive silver ink cured by Nd:YAG laser at 532nm with multiple laser scanning passes showed the best curing quality in terms of having a lowest electrical resistivity and the widest set of parameters for curing. In addition, the 532nm laser curing efficiency of curing the epoxy-based silver ink can be increased by either an increased silver concentration or an added-in optically absorbing agent, or dopant.

5. RESULTS FROM THE STUDY OF LASER CURING MECHANISMS AT THE LASER WAVELENGTH OF 532NM

This Chapter discusses the development of mechanism theories for curing an epoxy-based silver particulate ink with successive laser beam irradiations at 532nm. The experimental-based investigations start with the analysis of the epoxy-based silver ink components irradiated by Nd:YAG laser beam at 532nm, including factors causing a temperature rise in the overall ink system during the laser curing process, solvent transport theory, and resin complex cross-linking theory.

5.1 Analysis of Epoxy-based Silver Ink Components

The strategy used to develop a mechanism theory for laser curing an epoxy-based silver ink system was to investigate the effect of the laser irradiation on each ink component individually (those being the silver flakes, resin complex, and organic solvent). Then, the theory of laser curing mechanism could be developed by combining these ink component results together.

In this Chapter, the epoxy-based conductive silver ink D58 was chosen for its basic ink composition of silver micro flakes, resin complex, and solvent. As shown in **Figure 3.2**, this basic ink composition helped to develop the laser curing mechanism theory.

D58 silver ink composition (wt%)

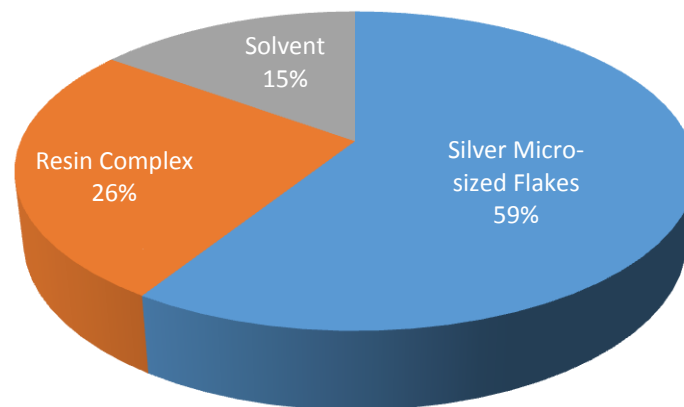


Figure 3.2: Illustration shows D58 silver ink composition by weight percentage (Data from Gwent Electronic Materials, Ltd. (GEM)).

5.1.1 Temperature Rise in Epoxy-based Silver Ink Due To Laser Energy Primary Absorption by Silver Flakes

Experiments using an Nd:YAG laser beam at 532nm to irradiate D58 epoxy-based silver ink components including silver micro-sized flakes, resin complex, and organic solvent were carried out. **Table 5.1** lists laser working parameters used to irradiate these ink components, while their surface temperature was monitored and recorded by using an IR camera.

Table 5.1: Temperature profiles of D58 epoxy based silver ink components (silver flakes, resin complex, and organic solvent) irradiated under Nd:YAG laser beam irradiation at 532nm.

Material	Laser Output Power (W)	Laser Scanning Speed (mm/s)	Surface Temperature (°C)
Silver flakes	3.864	5	32
	10.948	5	68
	17.94	5	90
	3.864	3.33	34
	10.948	3.33	81
	17.94	3.33	169
	3.864	2.5	51
	10.948	2.5	141
	17.94	2.5	237
Resin complex	3.864	1.5	32
	10.948	1.5	55
	17.94	1.5	82
	3.864	1.167	38
	10.948	1.167	65
	17.94	1.167	102
	3.864	0.83	42
	10.948	0.83	79
	17.94	0.83	120
Organic solvent	3.864	12	20
	10.948	12	28
	17.94	12	39
	3.864	20	18
	10.948	20	24
	17.94	20	31
	3.864	30	17
	10.948	30	21
	17.94	30	25
	3.864	5	29
	10.948	5	41
	17.94	5	59
	3.864	0.83	69
	10.948	0.83	84
	17.94	0.83	128

The experimental results indicated a relationship between laser working parameters and their corresponding surface temperatures. As seen from the **Tables 5.1** and **Figures 5.1-5.3**, the surface temperature of ink components increased with a decreasing laser scanning speed or an increasing laser power. Silver flakes are more sensitive to laser working parameters than the other two ink components (**Figure 5.4**), which suggests that silver flakes absorb the laser energy much more strongly to raise the temperature more rapidly than the other ink components.

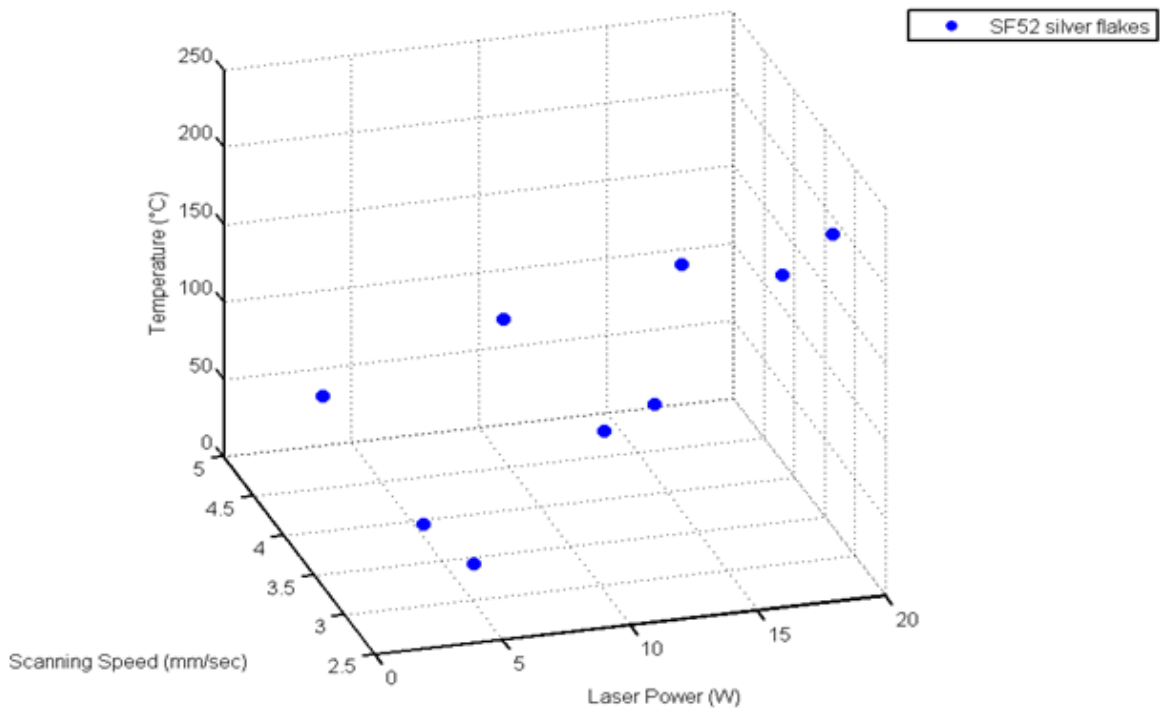


Figure 5.1: Surface temperature (°C) comparisons for D58 silver ink components - silver flakes.

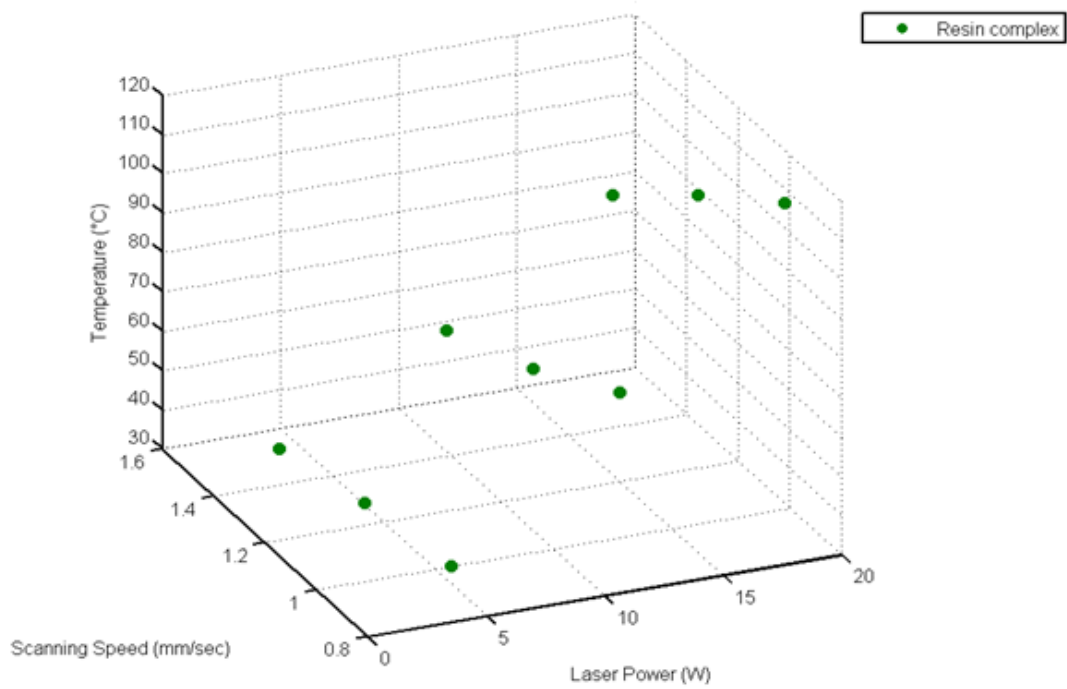


Figure 5.2: Surface temperature (°C) comparisons for D58 silver ink components - resin complex.

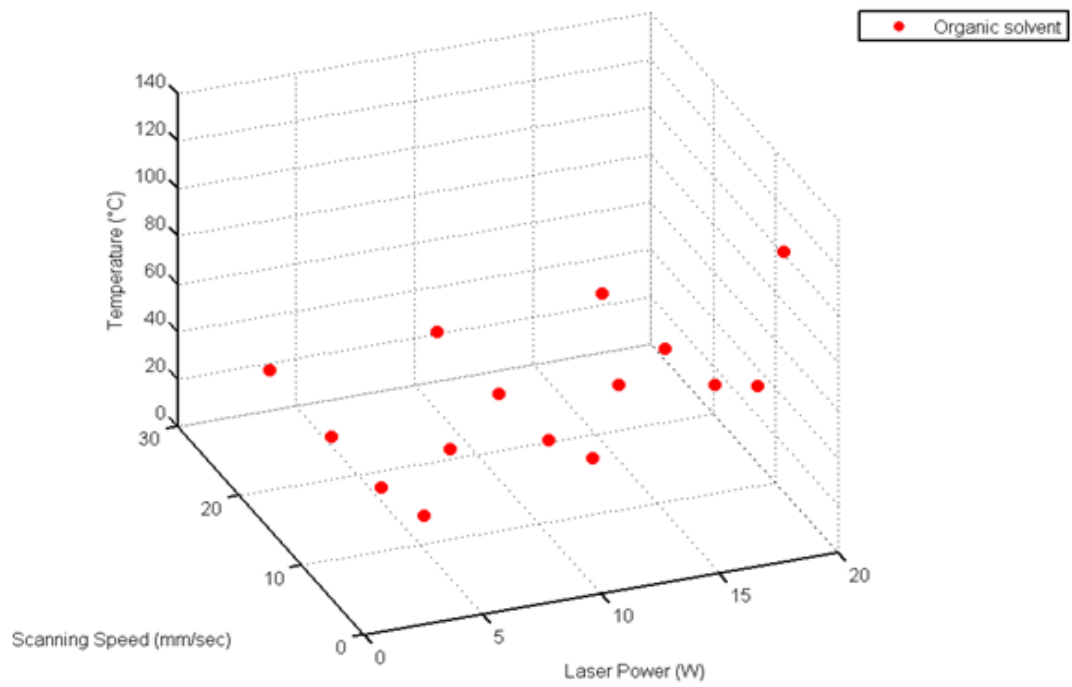


Figure 5.3: Surface temperature (°C) comparisons for D58 silver ink components - organic solvent.

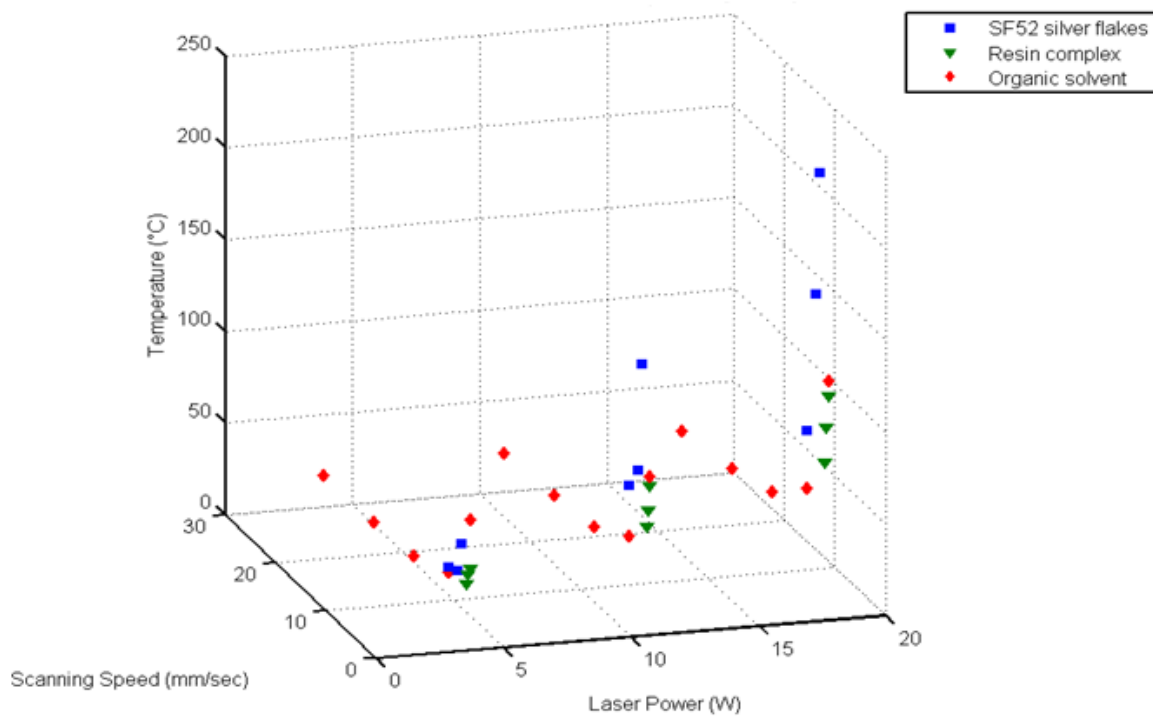


Figure 5.4: Surface temperature (°C) comparisons for D58 silver ink components - silver flakes (blue), resin complex (green), and organic solvent (red).

As discussed in **Chapter 3**, a typical flake size of silver flakes ranges from a few to tens of microns. When the laser beam is scanned over the D58 epoxy-based conductive silver ink, part of the laser beam is being reflected away, and the remaining part of the laser beam is being transmitted into the ink (**Figure 5.6**), in the latter case, Geometric scattering and multiple internal reflections (the reflectance of silver at 532nm is $\sim 95\%$, as can be seen in **Figure 5.5** [5.11]) are taking place among silver flakes inside the ink system [5.3], the $\sim 5\%$ laser beam energy per laser incident is absorbed by silver flakes, this leads to a photothermal effect causing a localized temperature rise [5.4], resulting in an overall temperature increase of the ink system.

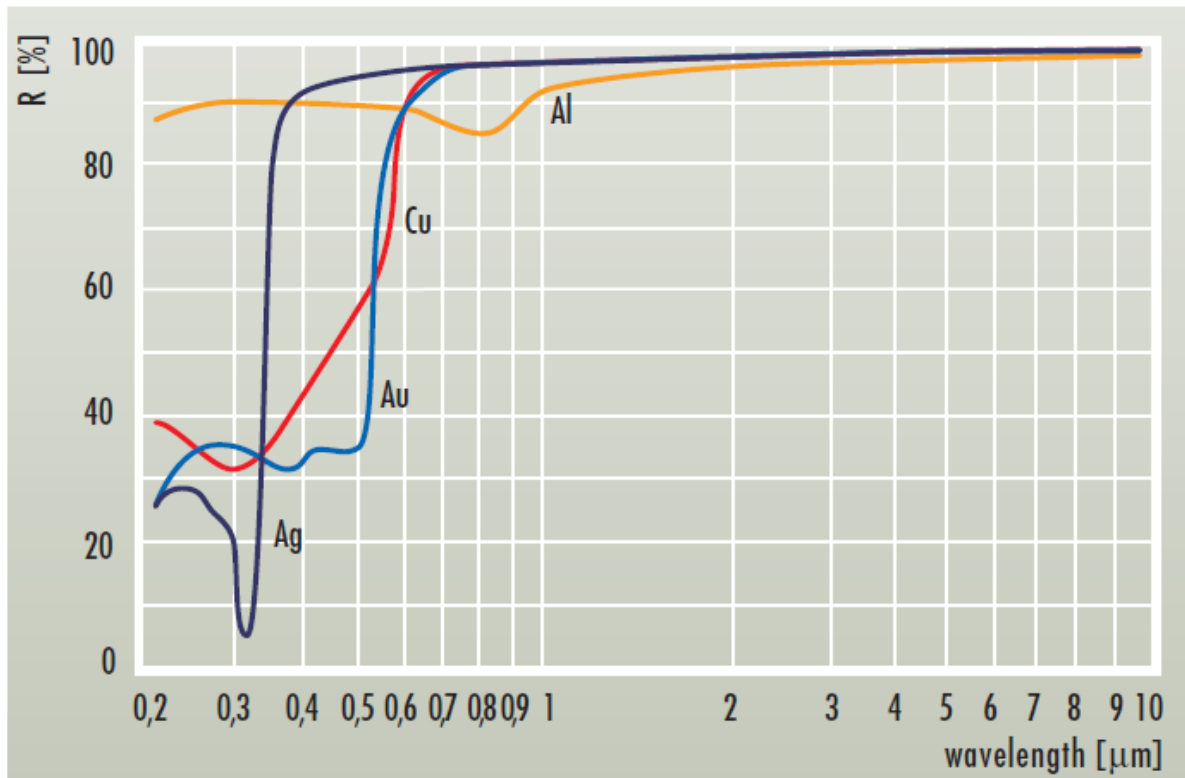


Figure 5.5: The reflectance of silver, for laser irradiation at 532nm, the reflectance of silver is at ~95% [5.11].

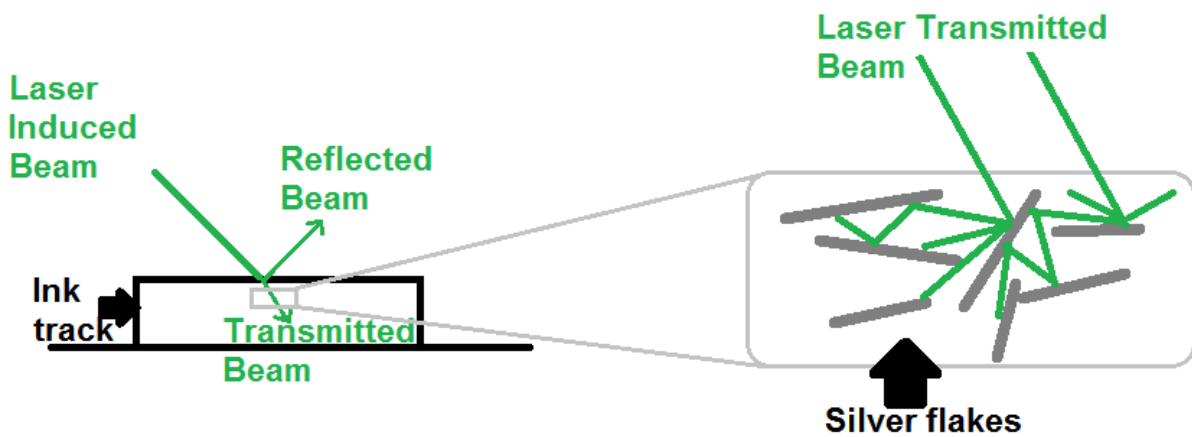


Figure 5.6: Illustration for silver flakes rising up temperature during the laser curing process due to Geometric scattering and laser beam multiple reflections among silver flakes within the D58 ink.

5.1.2 Solvent Transport Theory

As discussed in **section 5.1.1**, the laser energy is primarily absorbed by silver flakes inside the ink due to scattering and reflections, this leads to a photothermal effect, which causes a temperature rise of the whole ink system. In this section, a series of experiments were carried out to investigate how solvent viscosity is being affected with a rising temperature, followed by the development of solvent transport theories.

Due to fluorescence caused by the laser beam at the wavelength of 532nm, the change in viscosity and surface area of the solvent under the laser irradiation is difficult to measure directly. As the laser curing process at the wavelength at 532nm is mainly dominated by the thermal effects, which has discussed in **Chapter 2** and **4**, an alternative experiment was suggested for a better observation and measurement.

Figure 5.7 shows an illustration of the experimental set-up, where a piece of the PET substrate was placed on top of the heating plate, with a white paper softening the backlight at behind, a DSLR camera with a macro lens was placed at the same horizontal level with the PET substrate, and the syringe injector was fixed vertically between the camera and the backlight. An IR camera was lifted beside the DSLR camera at the same horizontal level for monitoring and recording the surface temperature of the solvent in experiment.

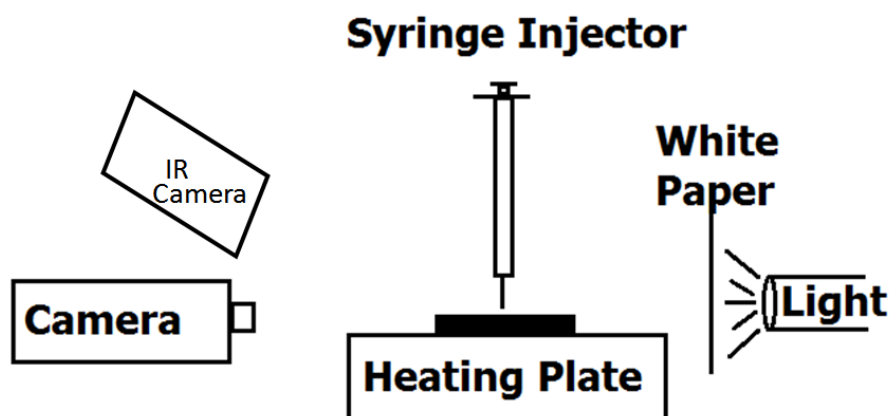


Figure 5.7: Illustration of the experimental set-up to investigate solvent removal theory.

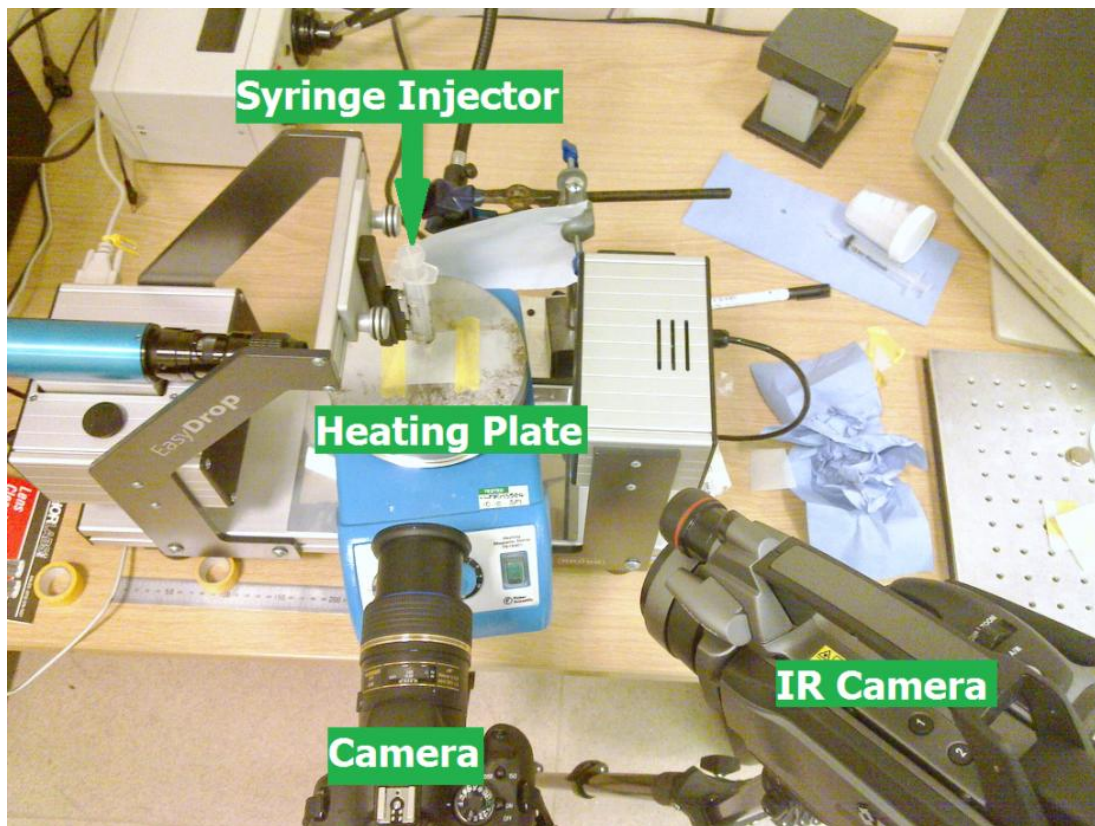


Figure 5.8: Experimental set-up for solvent removal investigation, which can represent the conditions by which the solvent removal mechanism in D58 silver ink system during thermal-based laser curing process at the wavelength of 532nm.

As shown in **Figure 5.8**, the DSLR camera was used to record video clips while the IR camera was recording the temperature profile of solvent on the PET substrate at the same time (the data obtained from experiment is shown in **Figure 5.9-5.12**). Images were snapped from the raw video clip at second 0, 1, 3, 5, 10, 20, 40, 60, 120, 240, 300, and at each time interval the width of the solvent expansion were measured (scale bar: 1mm).

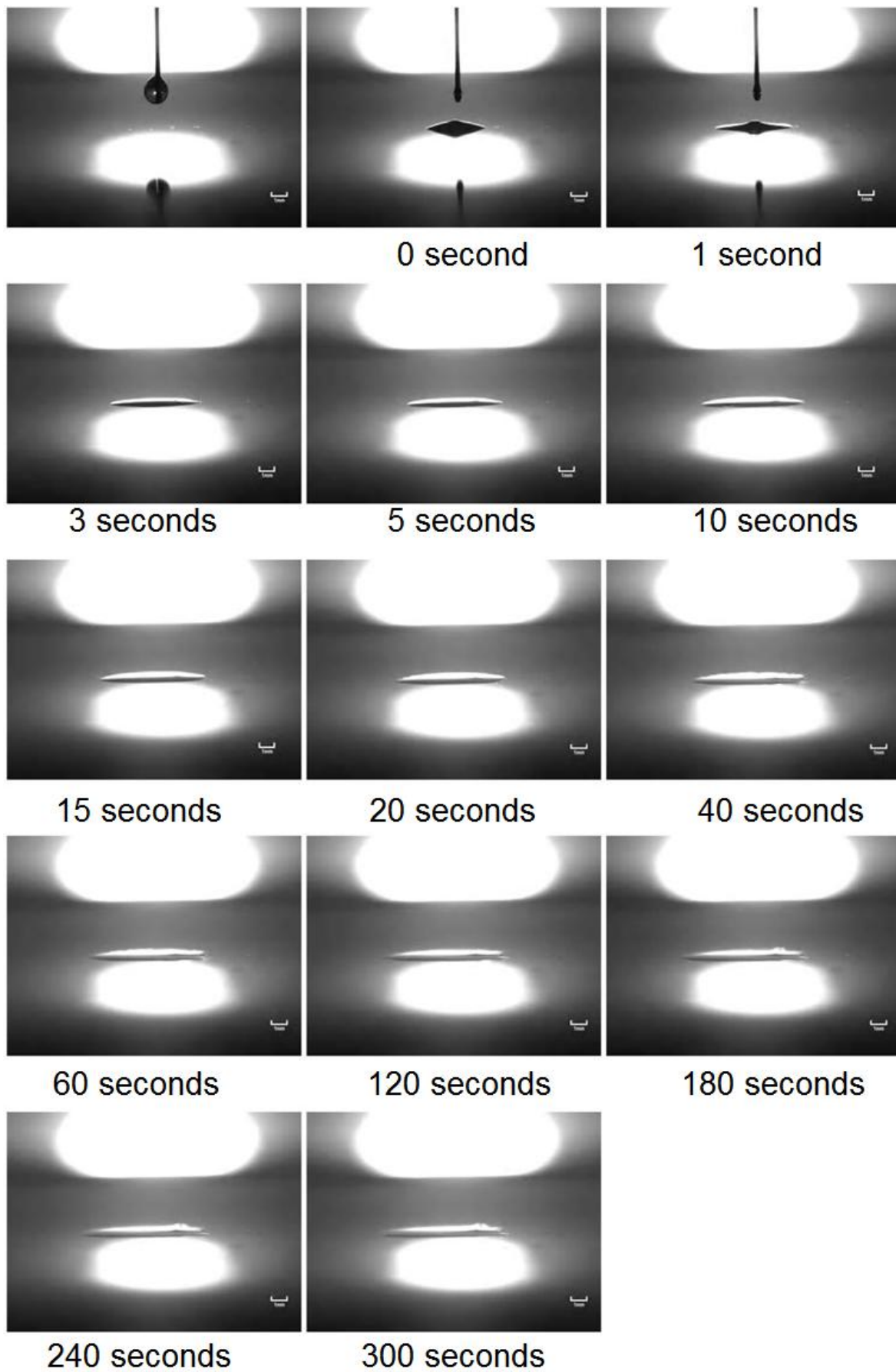


Figure 5.9: Sequence of captured images showing the evolution of solvent transport at 40°C.

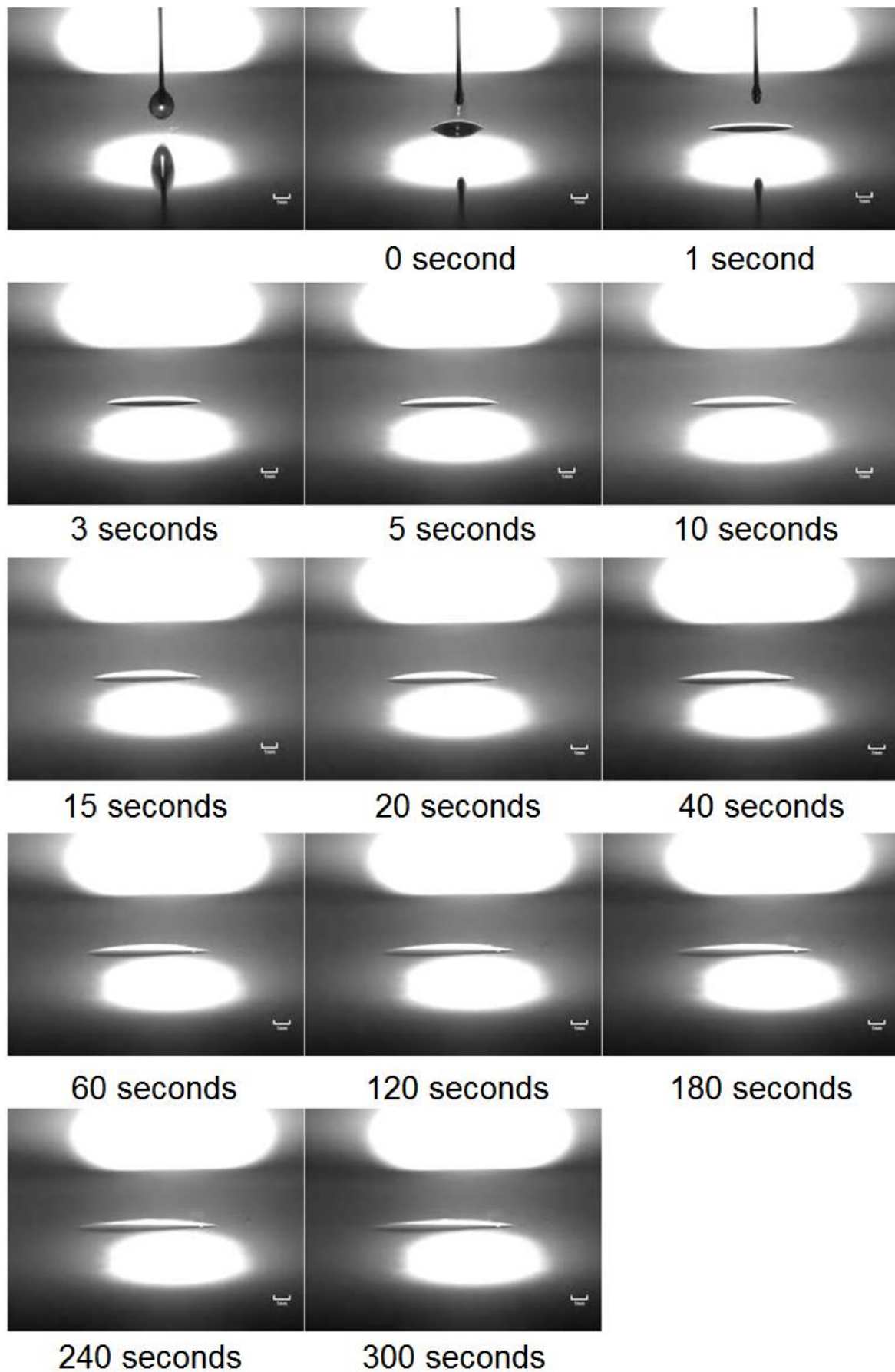


Figure 5.10: Sequence of captured images showing the evolution of solvent transport at 50°C.

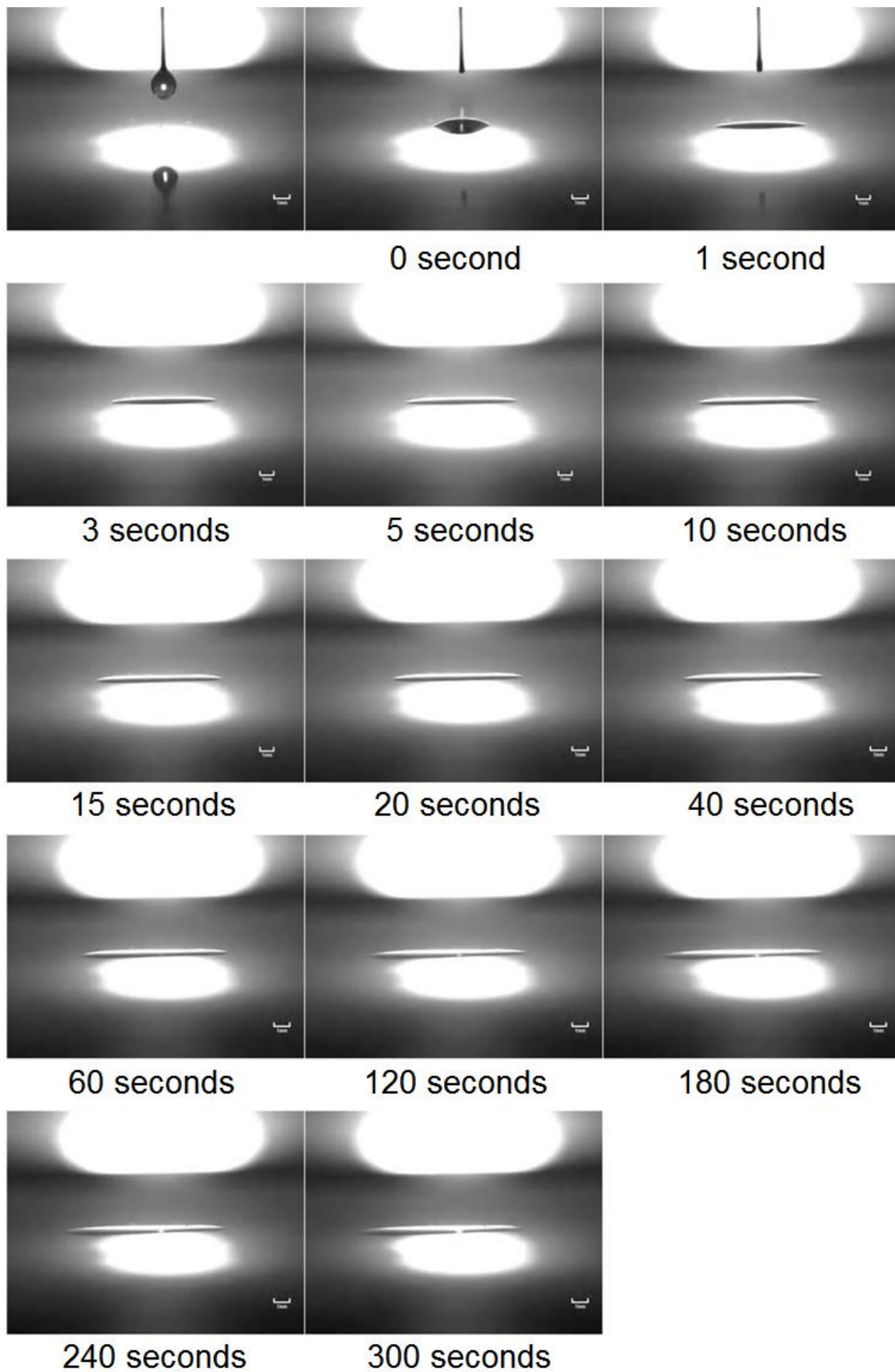


Figure 5.11: Sequence of captured images showing the evolution of solvent transport at 60°C.

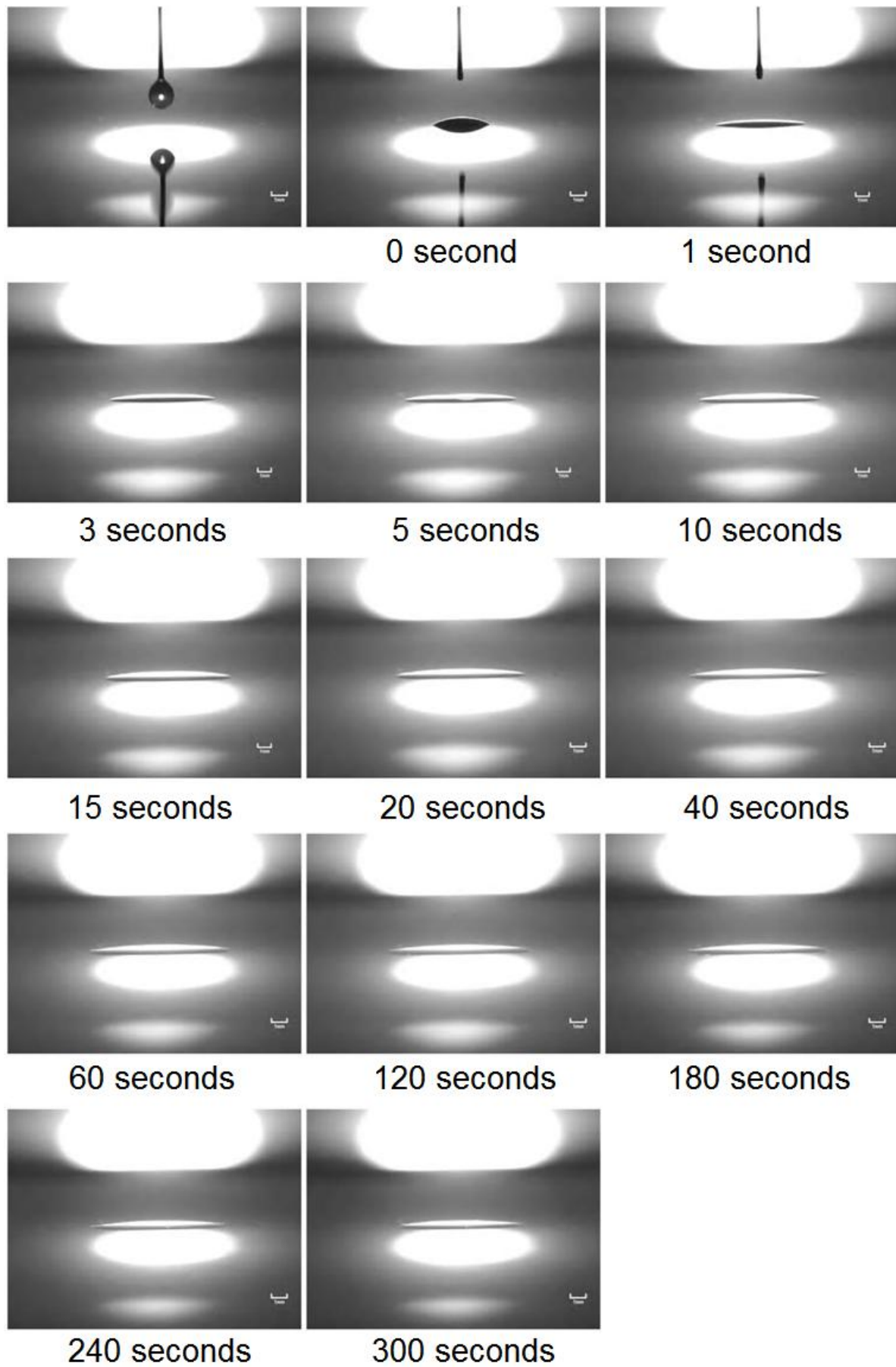


Figure 5.12: Sequence of captured images showing the evolution of solvent transport at 70°C.

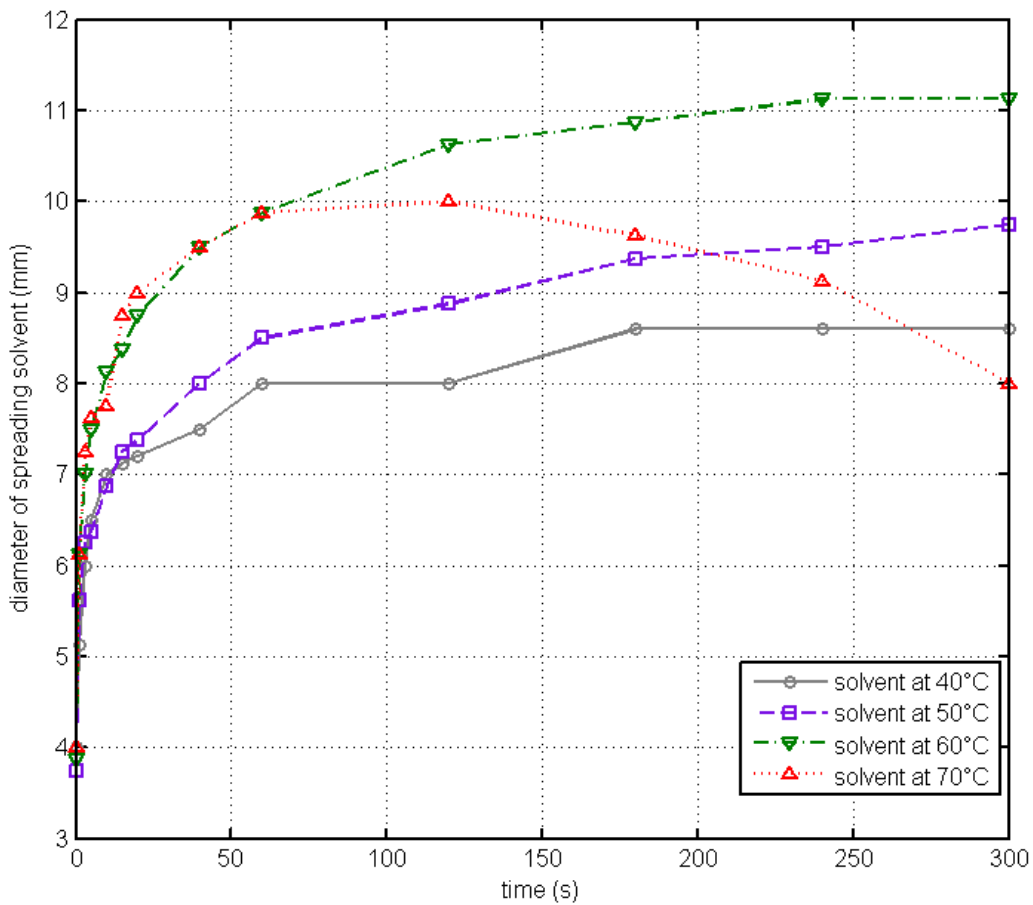


Figure 5.13: The rate of solvent expansion against temperature and duration of heating.

As seen in **Figure 5.13**, the rate of solvent expansion is proportional to the heating temperature (a steeper curve indicates a higher rate of solvent expansion at high temperature than that at low temperature). However when temperature reaches the solvent evaporation point at around 70°C [5.1], the solvent is being evaporated directly from the PET substrate at or above 70°C rather than being expelled away at a lower temperature below 70°C shown in **Figure 5.13**.

A repeat of the experimental procedure was applied to epoxy resin and blocked isocyanates (BI) components, **Figure 5.14** shows the comparison of rate of expansions for different components in the first 60 seconds, during which the solvent liquid flows quicker than other two components.

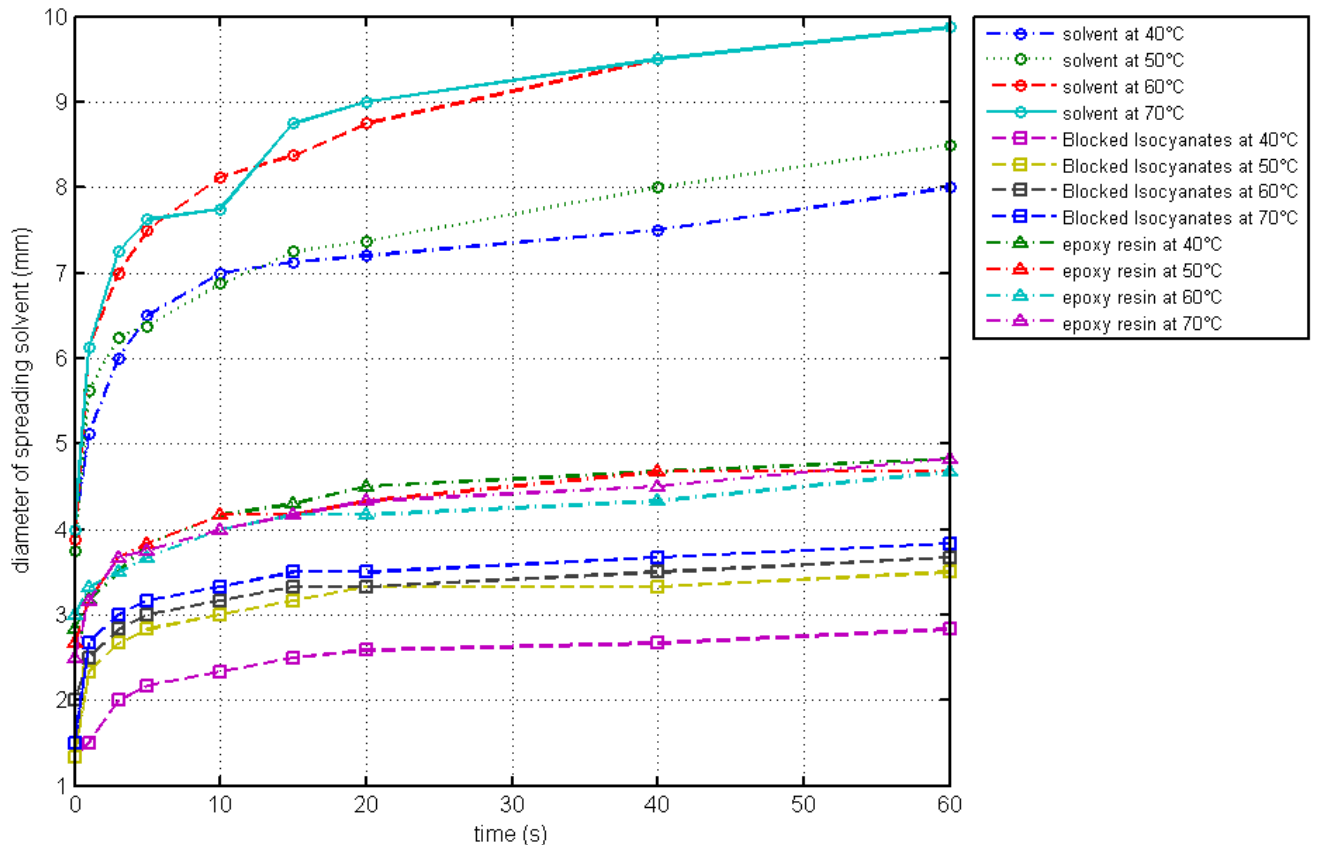


Figure 5.14: The rate of expansion against temperature and time for solvent, BI, and epoxy resin components.

5.1.2.1 Solvent Transport Mechanism

The rate of expansion experiments in previous **section 5.1.2** simulates the thermal process by which the laser beam interacts with the solvent component of the ink, therefore a theory which includes two stages can be developed for explaining the solvent transport mechanism in the epoxy-based D58 silver ink system at the laser beam irradiations of 532nm.

5.1.2.1.1 Solvent Molecular Excitation

When 532nm laser beam is irradiating the top surface of the epoxy-based conductive silver ink, absorption of the laser energy by the silver flakes results in a local temperature rise of the whole ink system, and such a localized temperature rise leads to relatively violent molecular movements of the solvent along the liquid-to-air

interface at the contact area covered by the laser beam (**Figure 5.15**). Further temperature rise leads to more violent solvent molecular movements which can motivate the solvent liquid expansion, causing the solvent to be transported from the central area to both edges due to the Marangoni effect (the Marangoni effect will be discussed in **section 5.1.2.1.2**).

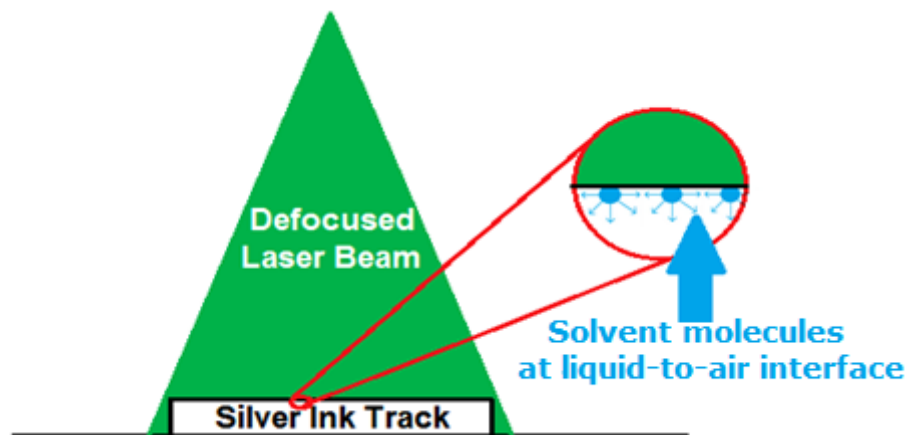


Figure 5.15: Illustration of how the laser beam energy excites solvent molecular movements within a D58 silver ink during the laser curing process at the wavelength of 532nm.

This theory is supported by the experimental results of rate of expansion for solvent, in which the solvent is expelled away from the ink system much quicker with a higher heating temperature. This solvent molecule excitation stage is also supported by a dynamic viscosity change of organic solvent. **Figure 5.16** shows a dynamic viscosity change for solvent - Butyl Carbitol which shows that with an increasing temperature, the solvent's viscosity decreases [5.1]. **Figure 5.17** shows a dynamic viscosity change for a typical two part resin, which could be used as the approximation for representing the resin complex used in epoxy-based conductive D58 silver ink of this experiment as it has a similar composition that containing resin and hardener to form a resin system [5.2]. As seen in **Figure 5.16-5.17**, the dynamic viscosity for solvent is significantly lower (~ 90 times lower) than that for the resin complex, showing that the solvent component tends to be much more mobile than any other components in the ink system.

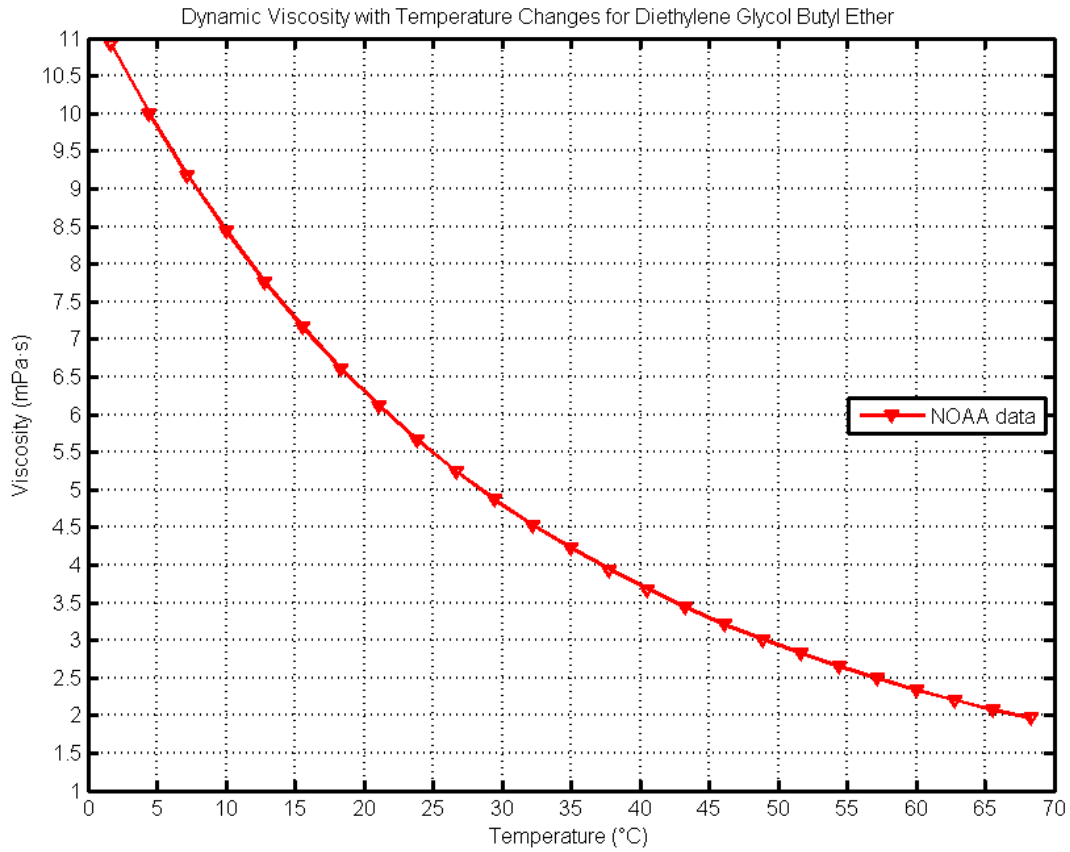


Figure 5.16: Variation in dynamic viscosity of solvent with temperature (graph reproduced based on NOAA data) [5.1].

Viscosity Profiles

Dynamic Viscosity Curve

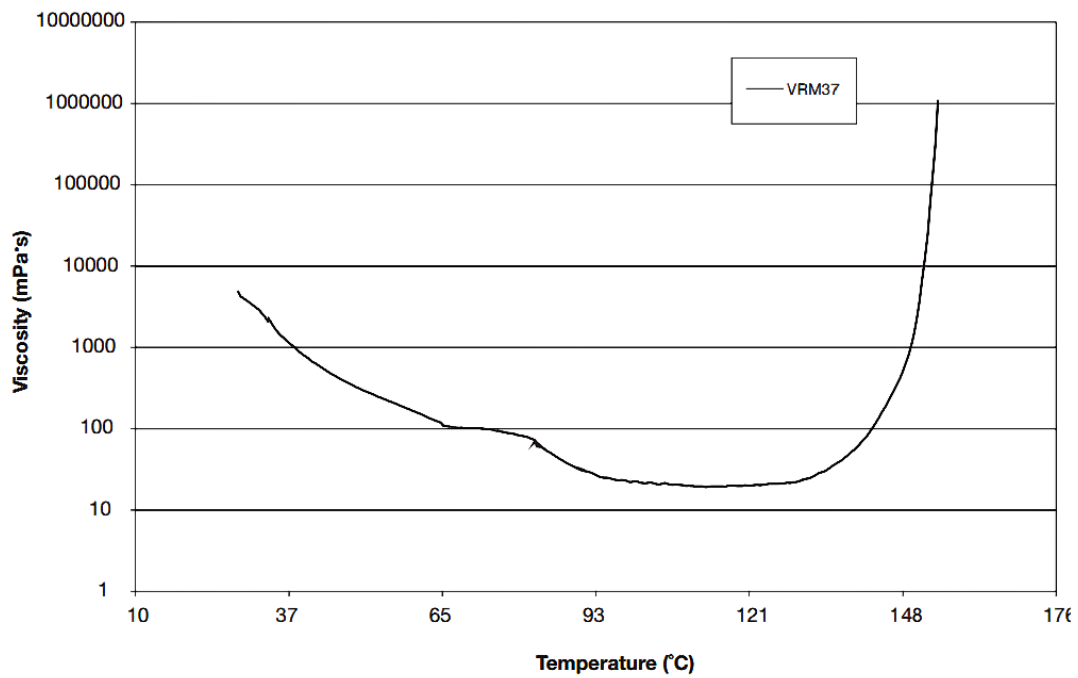
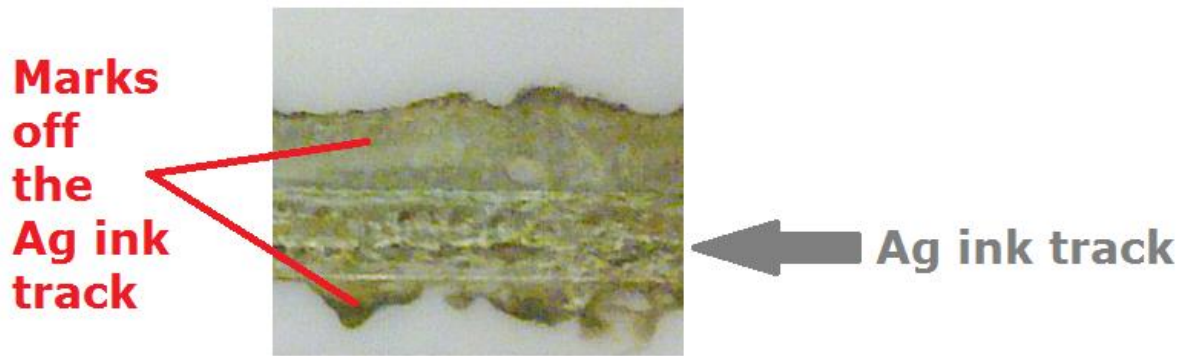


Figure 5.17: Variation in dynamic viscosity of a typical two part epoxy resin with temperature [5.2].

5.1.2.1.2 Solvent Transport Due To The Marangoni Effect

In previous **section 5.1.2.1.1**, solvent was experimentally found to be the most likely ink component to flow in D58 silver ink with a decreased viscosity due to the solvent molecule excitation at a higher temperature. This phenomenon of solvent flow therefore, can be explained by the Marangoni effect, in which the fluid movement is associated to the surface tension gradient, or the gradient in composition and temperature [5.5, 5.6]. When the 532nm laser beam irradiates the top surface of the silver ink track, silver flakes at the ink-air interface absorbed the laser beam energy, increasing the local temperature in the ink. This rise in temperature then preferentially reduces the surface tension of the solvent at the interface area being irradiated [5.7, 5.8, 5.9]. Therefore as a result of the Marangoni effect, the solvent can be transported from a lower surface tension area (the area of irradiated by the laser beam) towards to a higher surface tension area (ahead and around of the laser beam irradiation area). This has been previously investigated and reported by Bieri *et al.* and Chung *et al.* in their investigations [2.84, 5.10].

Figure 5.18 shows an example indicating that the Marangoni effect has been observed in laser cured D2 silver ink by Nd:YAG laser at 532nm. As seen in **Figure 5.18**, silver ink D2 (with ~45wt% silver content) containing both micro- and nano-sized silver particles, was cured by 532nm laser at 7 watts, with a traverse speed at 10mm/s for 4 scanning passes. Tide marks have been observed at both sides of the silver ink tracks.



Ink Name	Approximate composition	Silver content (wt%)
Silver Ink D2	Silver particles (micro- and nano-size), Epoxy resin, Blocked Isocyanates, Solvent	45%

Figure 5.18: Tide marks have been observed at both sides of the D2 ink, cured by 532nm laser at 7 Watts, with a curing speed at 10 mm/s for 4 scanning passes.

Figure 5.19 shows SEM images of silver micro- and nano-sized particles in 532nm laser cured D2 silver ink. As evidenced by EDX elemental analysis to areas on and off the silver ink track of the 532nm laser cured D2 silver ink, both areas on and off the silver ink track contain silver, carbon and oxygen elements (**Table 5.2** and **Figure 5.21**). The area "Spectrum 2" is the area on the ink track of the 532nm laser cured D2 silver ink, whereas the area "Spectrum 1" is the area off the ink track – the area where tide marks have been found in **Figure 5.18**. As seen in **Figure 5.19-5.20**, the average particle size for particles on-track is roughly 2-3 times larger than that for off-track, this indicates only silver particles with small size and mass (such as nano-sized particles, as shown in **Figure 5.20**) can be moved out of the ink track with the fluid movement of solvent transport.

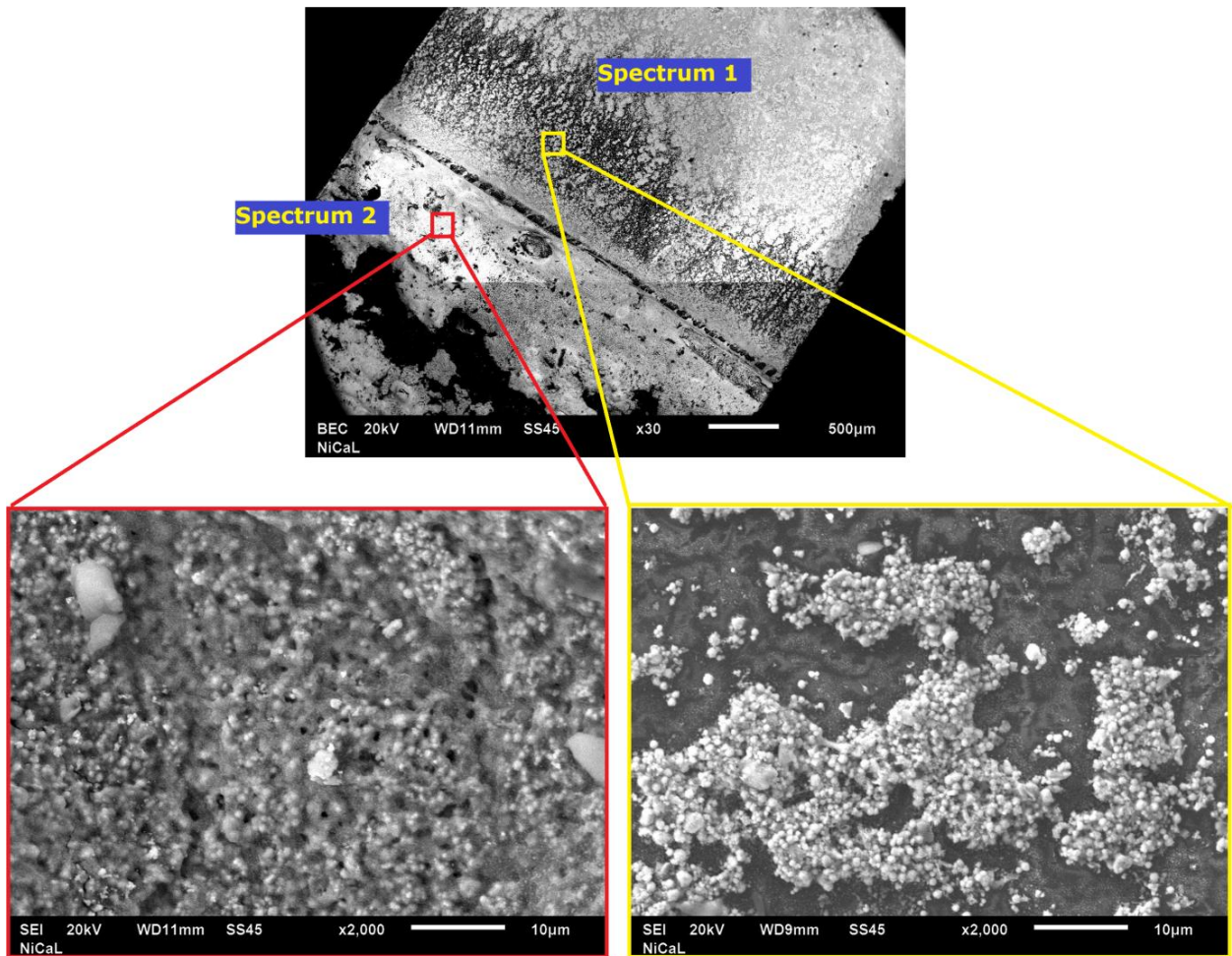


Figure 5.19: SEM images for silver ink D2 (Spectrum 2 – on track; Spectrum 1 – off track).

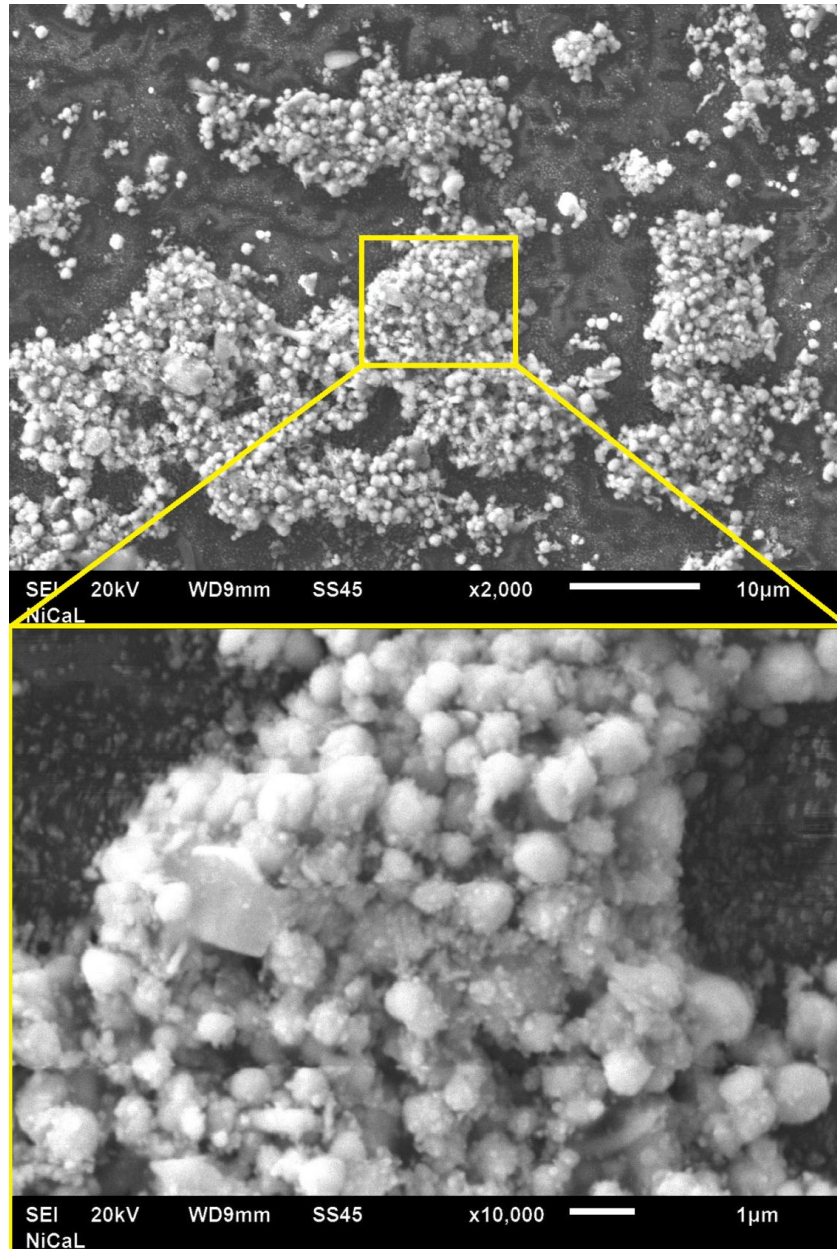


Figure 5.20: SEM images of nanoparticles carried off the track of D2 silver ink.

Table 5.2: Elemental analysis to element content in silver ink D2

Spectrum	Carbon (wt%)	Oxygen (wt%)	Silver (wt%)
Spectrum 1 (Off track)	15.33	11.67	73.00
Spectrum 2 (On track)	16.34	17.84	65.83

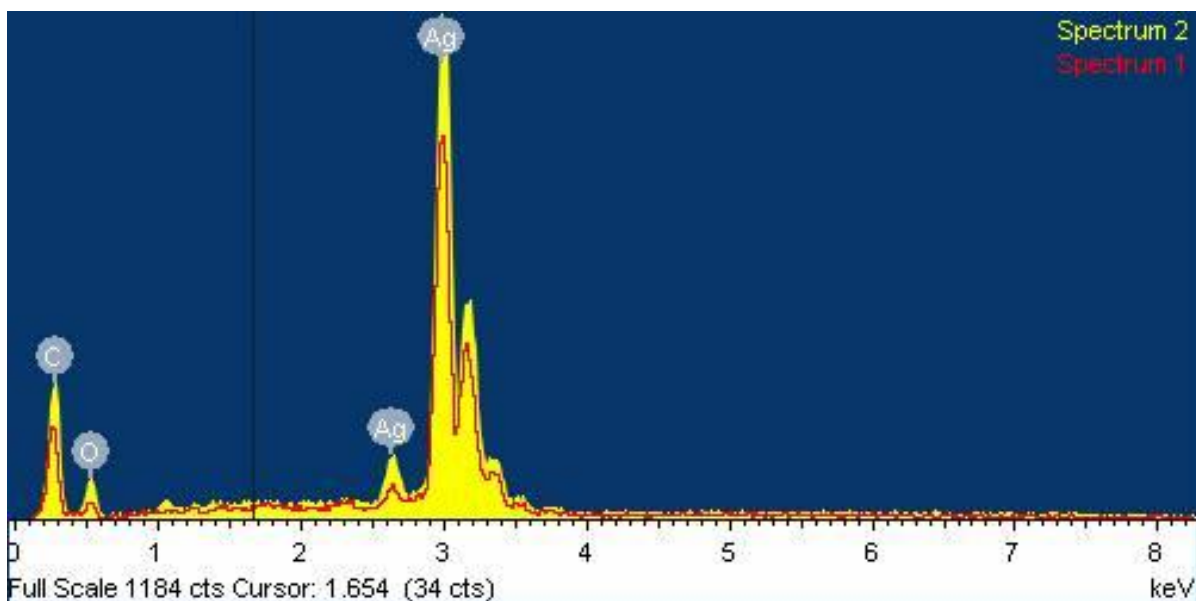


Figure 5.21: EDX Spectrum for silver ink D2 on ink track (Spectrum 2) and off track (Spectrum 1).

The Marangoni effect on D58 epoxy-based silver ink which contains micro-sized silver flakes in 532nm laser curing process is illustrated in **Figures 5.22-5.23**. When a moving laser beam irradiates the top of the silver ink track, silver flakes absorb the induced laser beam energy in a photothermal effect promoted by Geometric scattering and multiple reflections among silver flakes, as discussed in **section 5.1.1**, which increases the local temperature in the ink system. This rise in temperature causes the Marangoni effect, which promotes flow of the liquid solvent component (due to its greater reduction in viscosity compared to the other liquid components in the ink) from a lower surface tension area to a higher surface tension area. The silver micro-sized flakes are not carried with the solvent due to their relatively large size and mass, and the resin complex also remains in the main body of the track due to its higher viscosity at temperature compared to the solvent viscosity. The Marangoni effect thus causes the solvent to flow from the centre of the ink track to areas ahead of the laser beam (**Figure 5.22**) and to both sides of the ink track (**Figure 5.23**), preferentially removing the liquid solvent from the ink system in the area of the 532nm laser. This mechanism is to be contrasted with the direct solvent evaporation at the top surface of the ink system which was observed and discussed in the corresponding infrared CO₂ laser curing process of the same type of ink previously investigated by Sato and Shang [4.1].

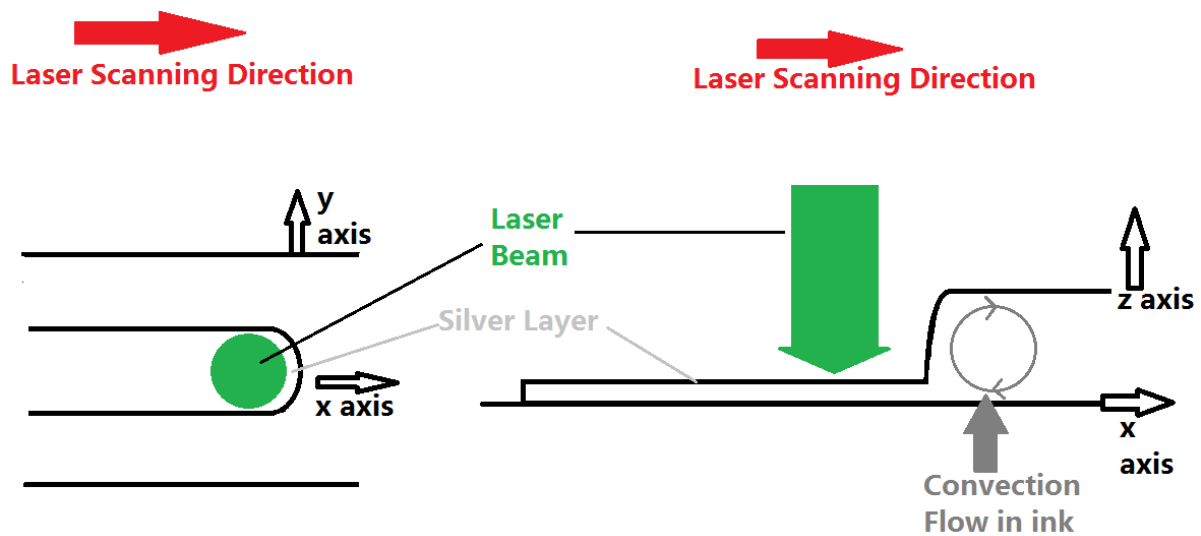


Figure 5.22: Illustration of the Marangoni effect during the 532nm laser curing process shows how solvent is being transported from the centre of the ink track towards to area ahead of the laser beam.

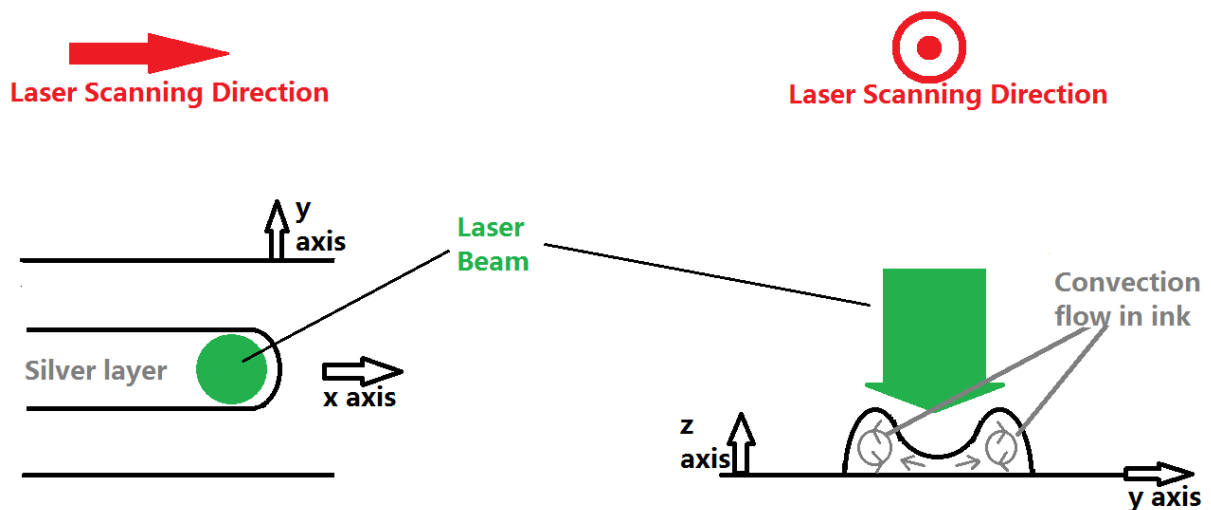


Figure 5.23: Illustration of the Marangoni effect during the 532nm laser curing process shows how solvent is being transported from the centre of the ink track towards to area at both sides of the laser beam.

In addition, as shown in **Figures 5.22-5.23**, a reduction of the specific heat of the overall epoxy-based silver ink material can be predicted as a result of this solvent removal due to the Marangoni effect. This reduction in specific heat capacity of the ink system therefore results in an increased temperature that can be coupled into the ink. This has been observed experimentally in the investigation of the D58 epoxy-based silver ink laser curing process at 532nm. In **Figure 5.24**, a D58 epoxy-based silver ink was irradiated with a laser working parameter within the

approximated process window for a 532nm laser curing process found in **section 4.5** (Laser output power=20W, Laser traverse speed=15mm/s). **Figure 5.24** shows the temperature within the D58 epoxy-based silver ink measured at the middle position of the ink track for the first 3 scanning passes by a Type-K thermocouple. The peak temperature in the first pass was measured at 125°C, with no plateau indicating the evaporation of solvent. This temperature profile was similar in the second and the third pass. This is because the liquid solvent component was transported out of the ink system to both sides (**Figure 5.23**) and ahead (**Figure 5.22**) instead of evaporating from the surface of the silver ink. This reduced the ink's overall specific heat capacity and allowed a higher temperature rise in silver ink in the first laser scanning pass.

Temperature measured for D58 epoxy-based silver ink by a Type-K thermocouple for the first 3 scanning passes

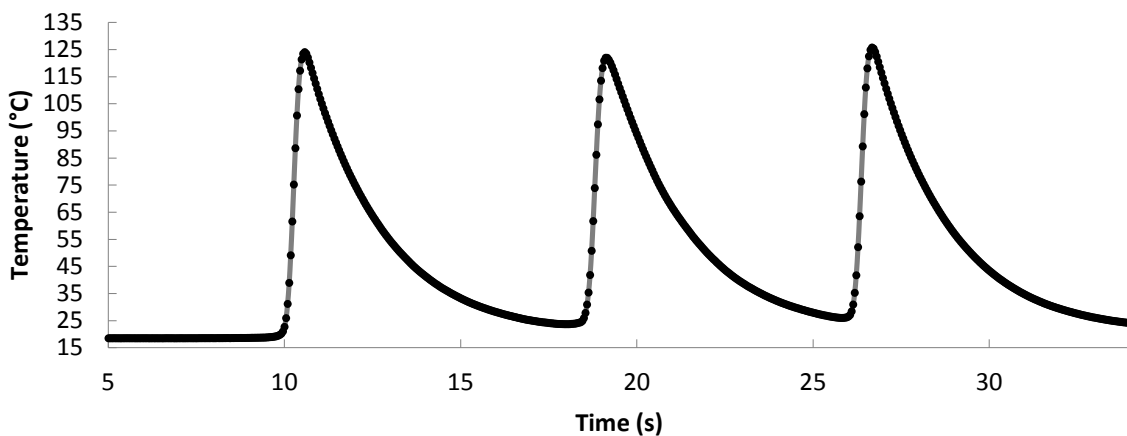


Figure 5.24: Temperature (°C) within the silver ink measurement for 532nm laser curing a D58 epoxy-based silver ink (Laser Power=20W, traverse speed=15mm/s) at the middle position of the ink track by a Type-K thermocouple for the first 3 scanning passes. The high temperature measured in the first pass was observed, this was caused by a reduction in specific heat capacity of the ink due to solvent removal in area of the laser irradiation due to the Marangoni effect ahead of the laser beam irradiation.

Additional evidence to support the theory of Marangoni effect in curing D58 epoxy-based conductive silver ink by Nd:YAG laser at 532nm is shown in **Figure 5.25**, where liquid solvent can be observed at the edges of a freshly cured D58 epoxy-based silver ink, providing further evidence to support the solvent transport theory (N.B. the greater amount of expelled solvent liquid seen on one side is thought to be

caused by the operation of the fume extractor system during the laser curing process).



Figure 5.25: Solvent watermark observed at the edge of D58 silver ink track immediately after the laser cure process – the greater amount of expelled solvent liquid seen on one side is assumed to be as a result of the operation of the fume extractor system during the laser curing process.

5.1.3 Resin Complex Crosslink Due To Chemical Reactions

5.1.3.1 Crosslinking Theory

As discussed in **Chapter 3**, the resin complex is a mixture of epoxy resin and blocked isocyanates (BI), where the epoxy resin is used as an adhesion base for silver flakes, and BI is used as a hardener. Blocked Isocyanates (BI) can be unblocked by heating the BI up to de-blocking temperature at around 90°C, and the products as a result of chemical reaction are isocyanates (R-NCO) and blocking agent (BL) (**Figure 5.26**) [5.12].

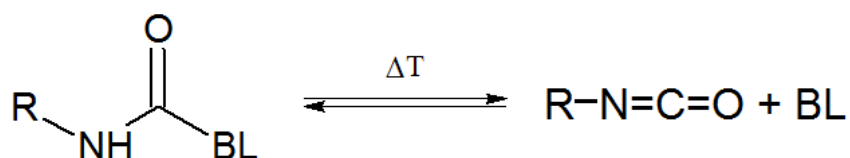


Figure 5.26: The unblocking reaction process for Blocked Isocyanates (BI).

The unblocked isocyanates (R-NCO) remain active above the de-blocking temperature and can form poly(isocyanurate)s with isocyanates itself through the trimerization process (**Figure 5.27**) and poly(2-oxazolidone)s with epoxy resin (**Figure 5.28**). Further rise in temperature can result in a chemical reaction between isocyanurate and epoxy resin, in which poly(2-oxazolidone)s can also be formed (**Figure 5.29**).

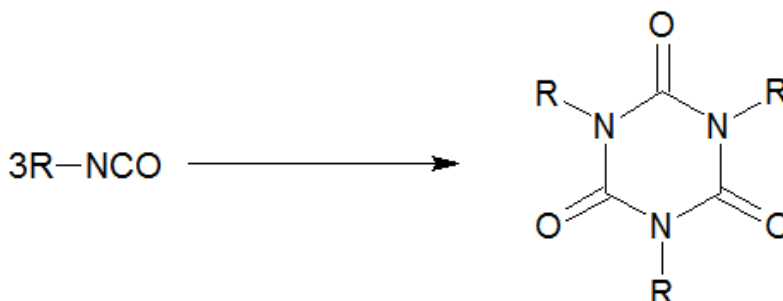


Figure 5.27: Trimerization of Isocyanates to generate Isocyanurate.

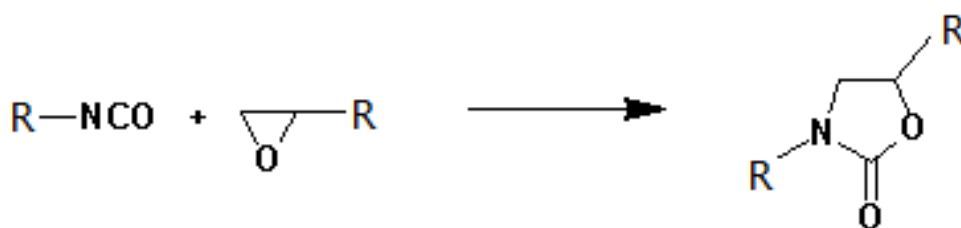


Figure 5.28: Resin cross-linking process between Isocyanates and Epoxy resin.

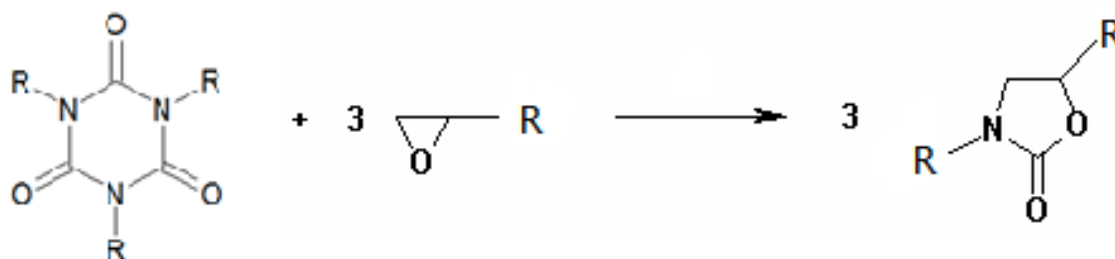


Figure 5.29: Resin cross-linking process between Isocyanurate and Epoxy resin.

5.1.3.2 Results of Fourier Transform Infrared Spectroscopy Examination

As discussed in **Chapter 2**, Fourier Transform Infrared Spectroscopy (FTIR) can provide chemical bonding information for cured ink samples. In this section, five FTIR spectrums for epoxy-BI mixture samples cured by Nd:YAG laser at 532nm with variant curing temperatures were compared. These FTIR spectrums were labelled with different colours and compared in a sequence from low curing temperature to high curing temperature (**Figure 5.30–5.34**). All temperature measurements in the laser curing process were recorded by an IR camera.

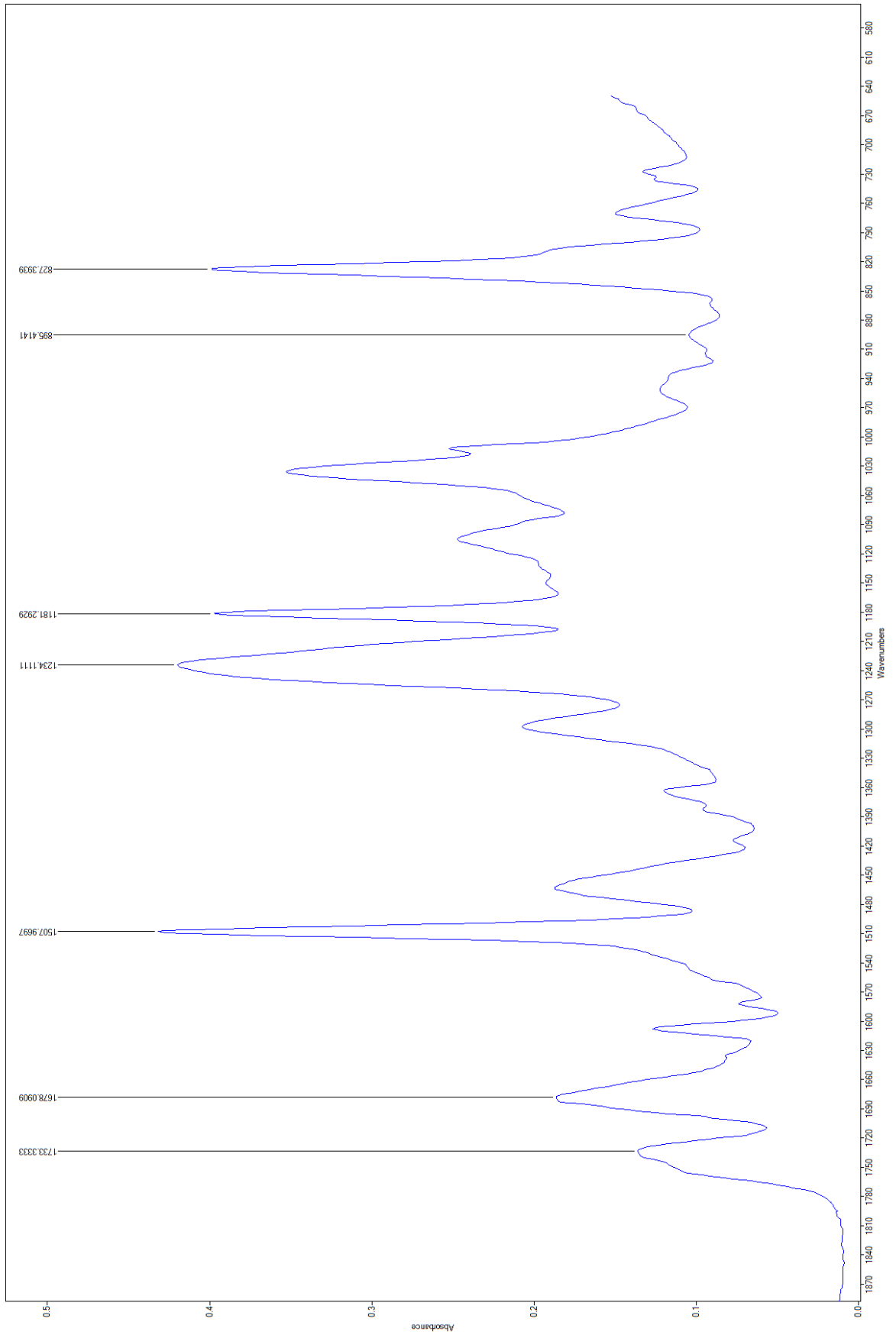


Figure 5.30: FTIR spectrum of resin complex with curing temperature recorded at 35°C.

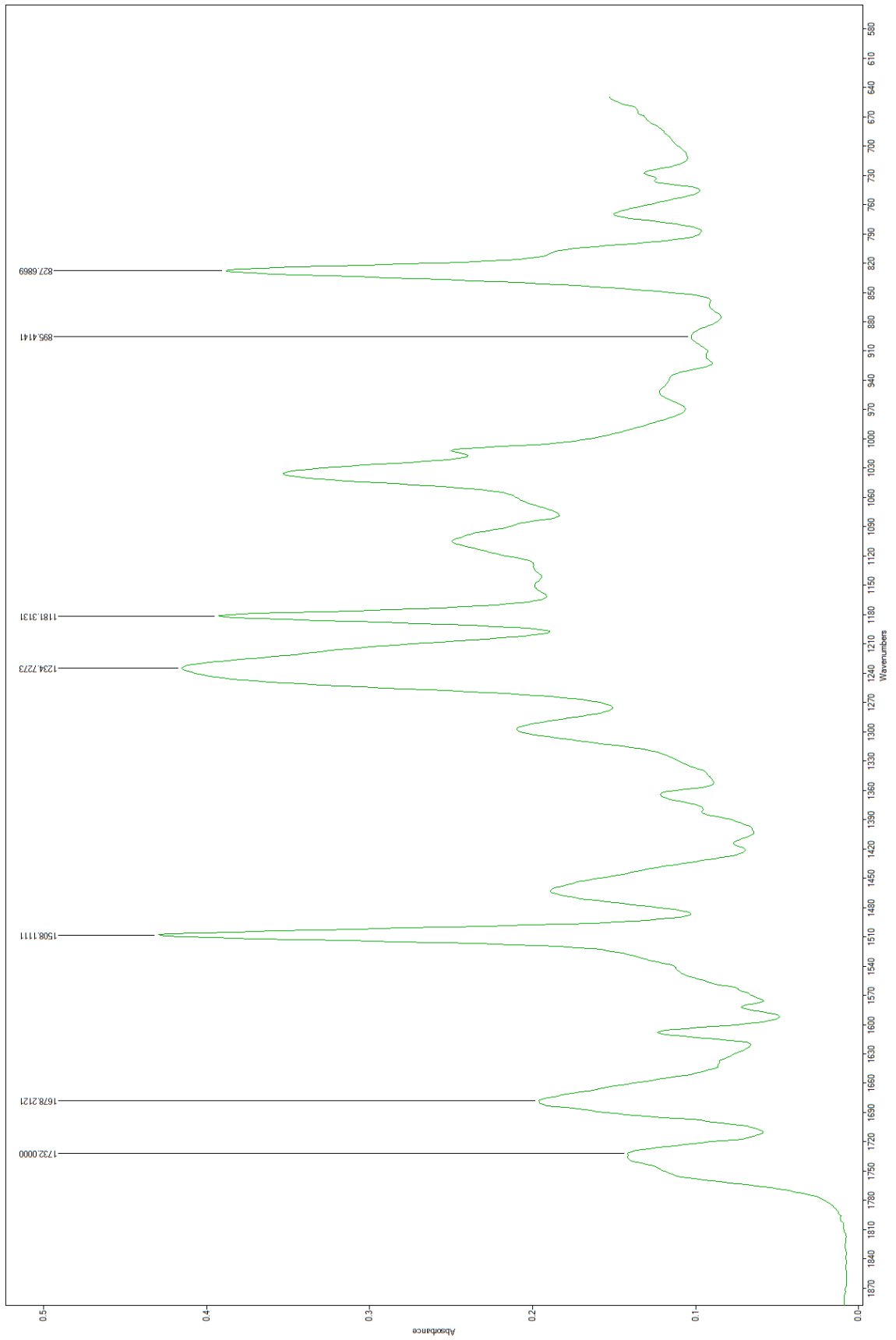


Figure 5.31: FTIR spectrum of resin complex with curing temperature recorded at 70°C.

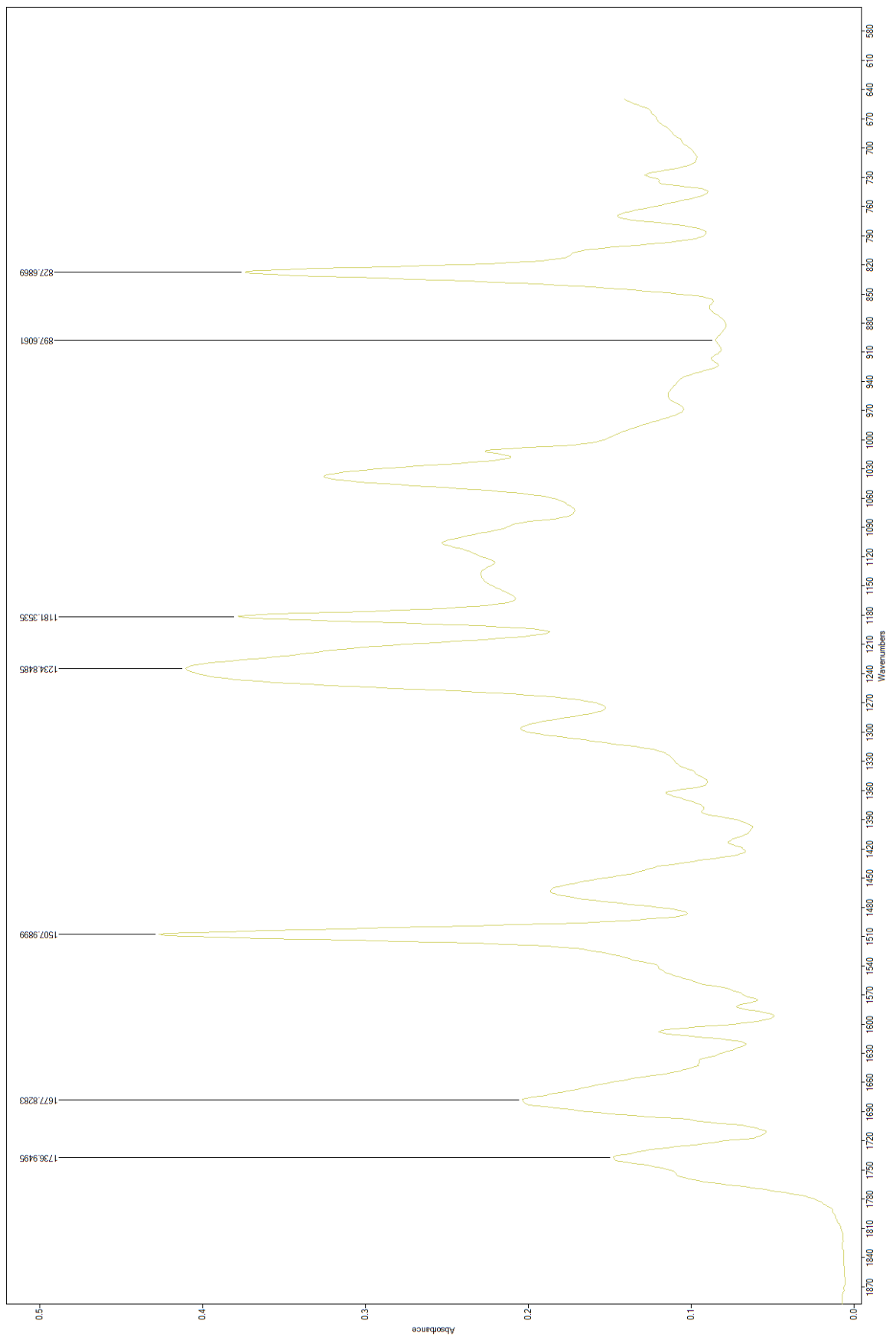


Figure 5.32: FTIR spectrum of resin complex with curing temperature recorded at 105°C.

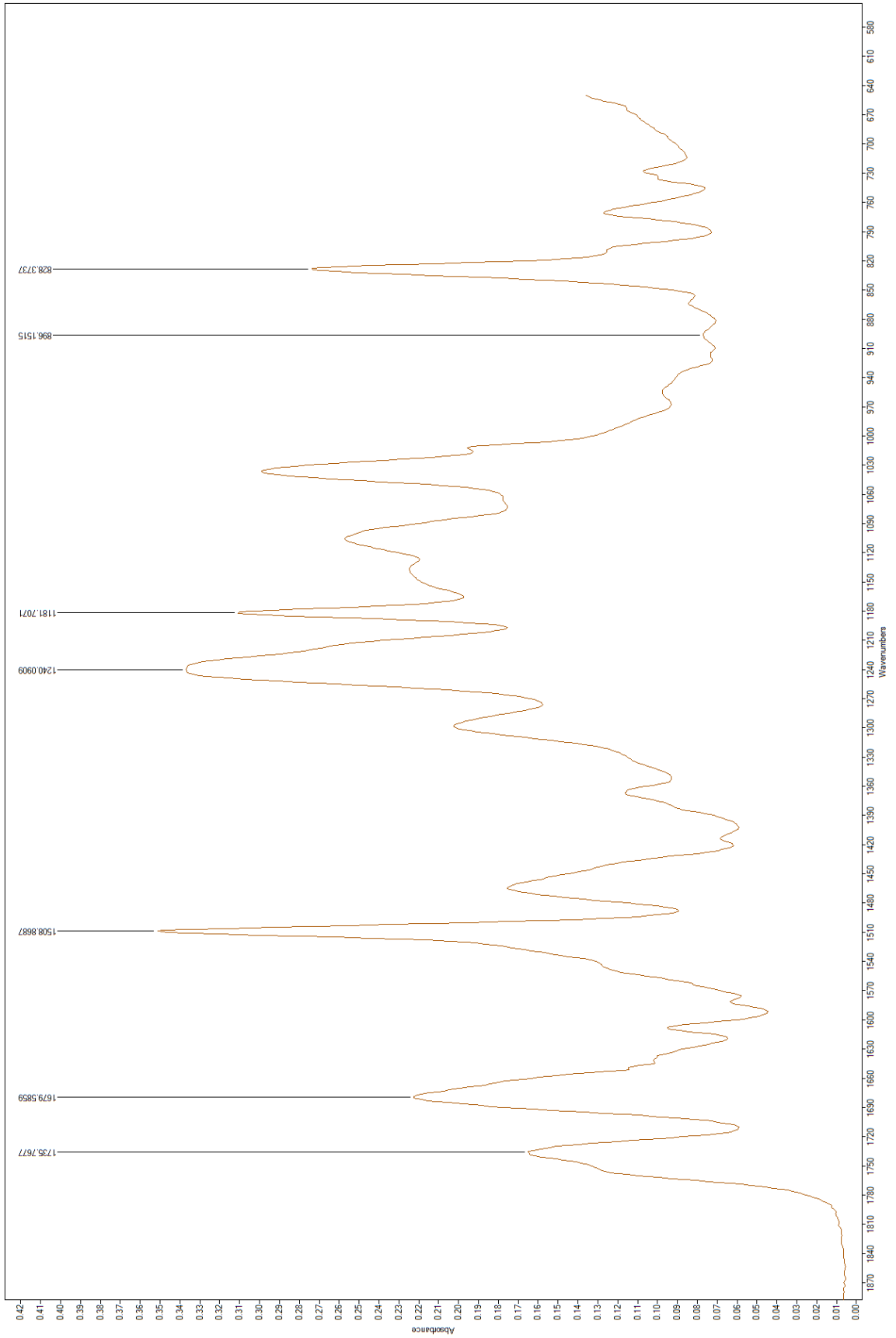


Figure 5.33: FTIR spectrum of resin complex with curing temperature recorded at 160°C.

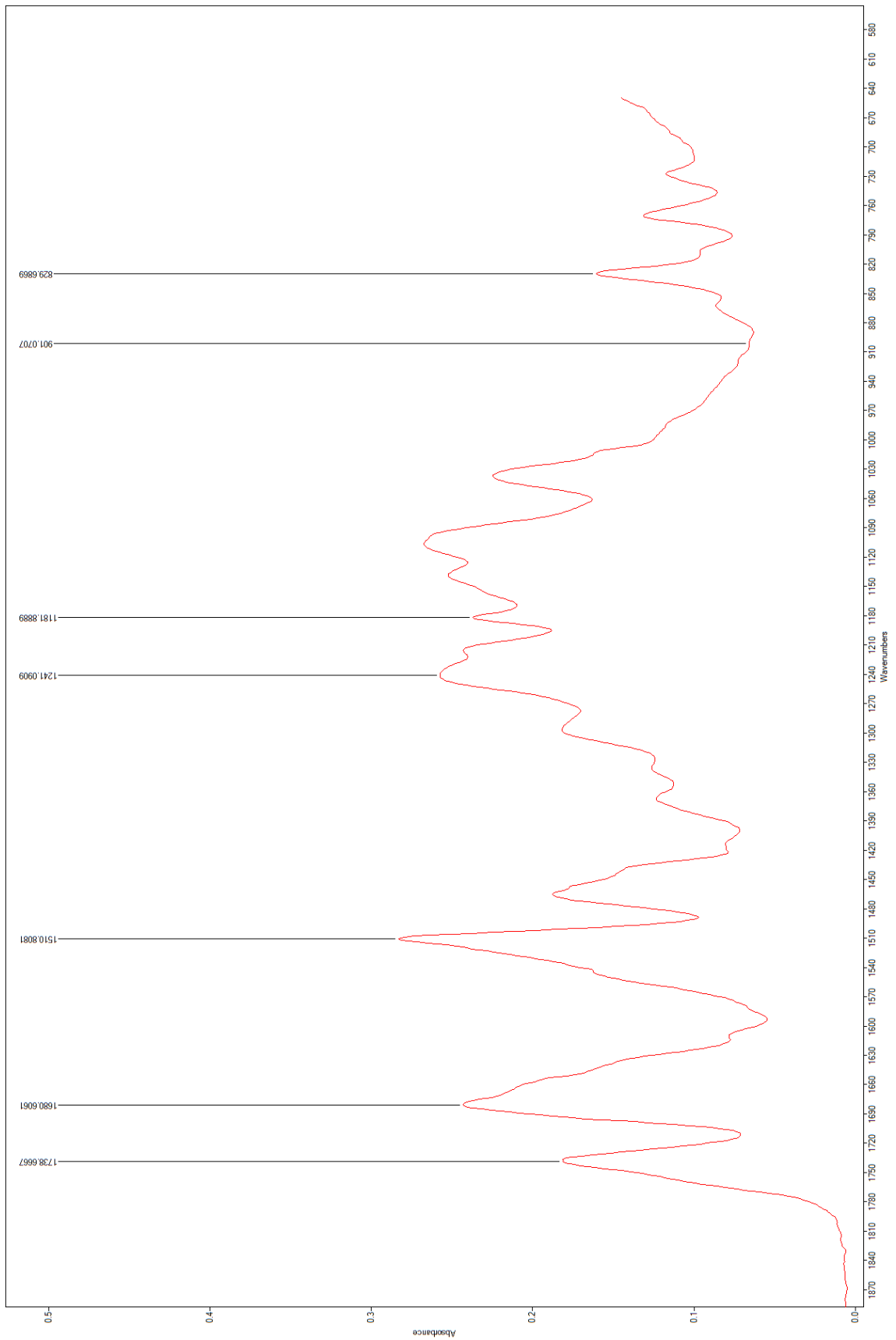


Figure 5.34: FTIR spectrum of resin complex with curing temperature recorded at 180°C.

Figure 5.35 shows the isocyanurate (1681cm^{-1}) and 2-oxazolidone (1739cm^{-1}) formed as results of trimerization and chemical reaction between epoxy resin and isocyanurate/isocyanurate. The higher the curing temperature, the more amount of isocyanurate and 2-oxazolidone formed (**Table 5.3**), and the denser cross-link it forms.

Table 5.3: FTIR spectrum absorbance of resin complex at the wavenumber 1681cm^{-1} and 1739cm^{-1} .

Wave Number (cm^{-1})	Curing temperature recorded ($^{\circ}\text{C}$)	Absorbance (%)
1681	35	18.7
1681	70	19.7
1681	105	20.4
1681	160	22.25
1681	180	24.25
1739	35	13.5
1739	70	14
1739	105	14.75
1739	160	16.5
1739	180	18.25

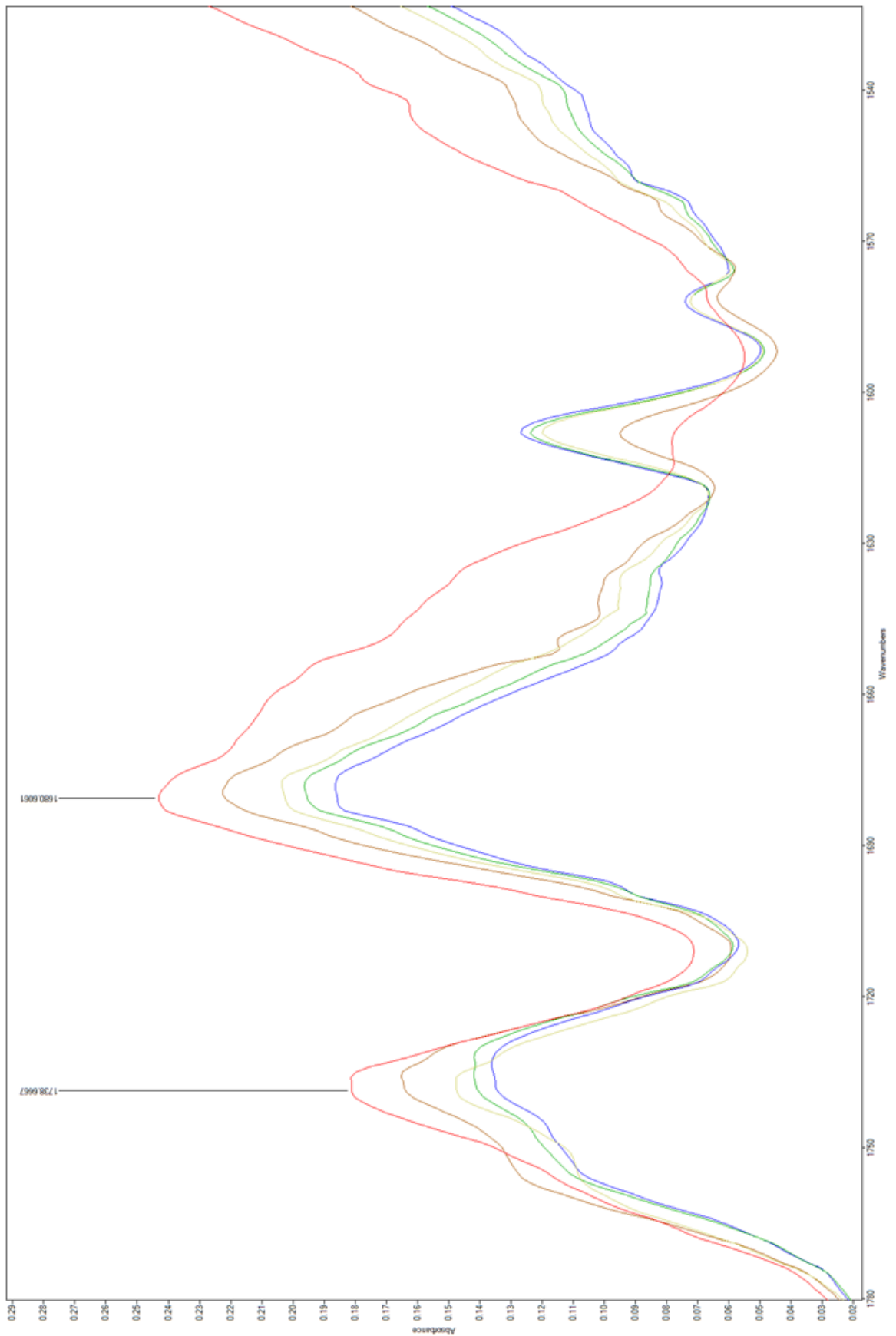


Figure 5.35: FTIR spectrum of resin complexes shows two increasing peaks at 1681cm^{-1} and 1739cm^{-1} are observed for samples with increased curing temperatures (blue:35°C green:70°C light yellow:105°C brown:160°C red:180°C).

Figure 5.36 shows epoxy resin (Epikote) peaks were diminished as a result of chemical reaction (901cm^{-1} and 1241cm^{-1}), and BIs were diminished as a result of the trimerization process (830cm^{-1} , 1241cm^{-1} , 1182cm^{-1} and 1510cm^{-1}) (**Table 5.4**).

Table 5.4: FTIR spectrum absorbance of resin complex at the wavenumber 830cm^{-1} , 901cm^{-1} , 1182cm^{-1} , 1241cm^{-1} and 1510cm^{-1} .

Wave Number (cm^{-1})	Curing temperature recorded ($^{\circ}\text{C}$)	Absorbance (%)
830	35	39.75
830	70	38.75
830	105	37
830	160	27
830	180	15.9
901	35	10.4
901	70	10.2
901	105	8.25
901	160	7.5
901	180	6
1182	35	39.5
1182	70	39.45
1182	105	37.75
1182	160	30.9
1182	180	23.5
1241	35	42.5
1241	70	41.5
1241	105	41
1241	160	33.5
1241	180	25.7
1510	35	43.25
1510	70	43
1510	105	42.6
1510	160	35
1510	180	28.25

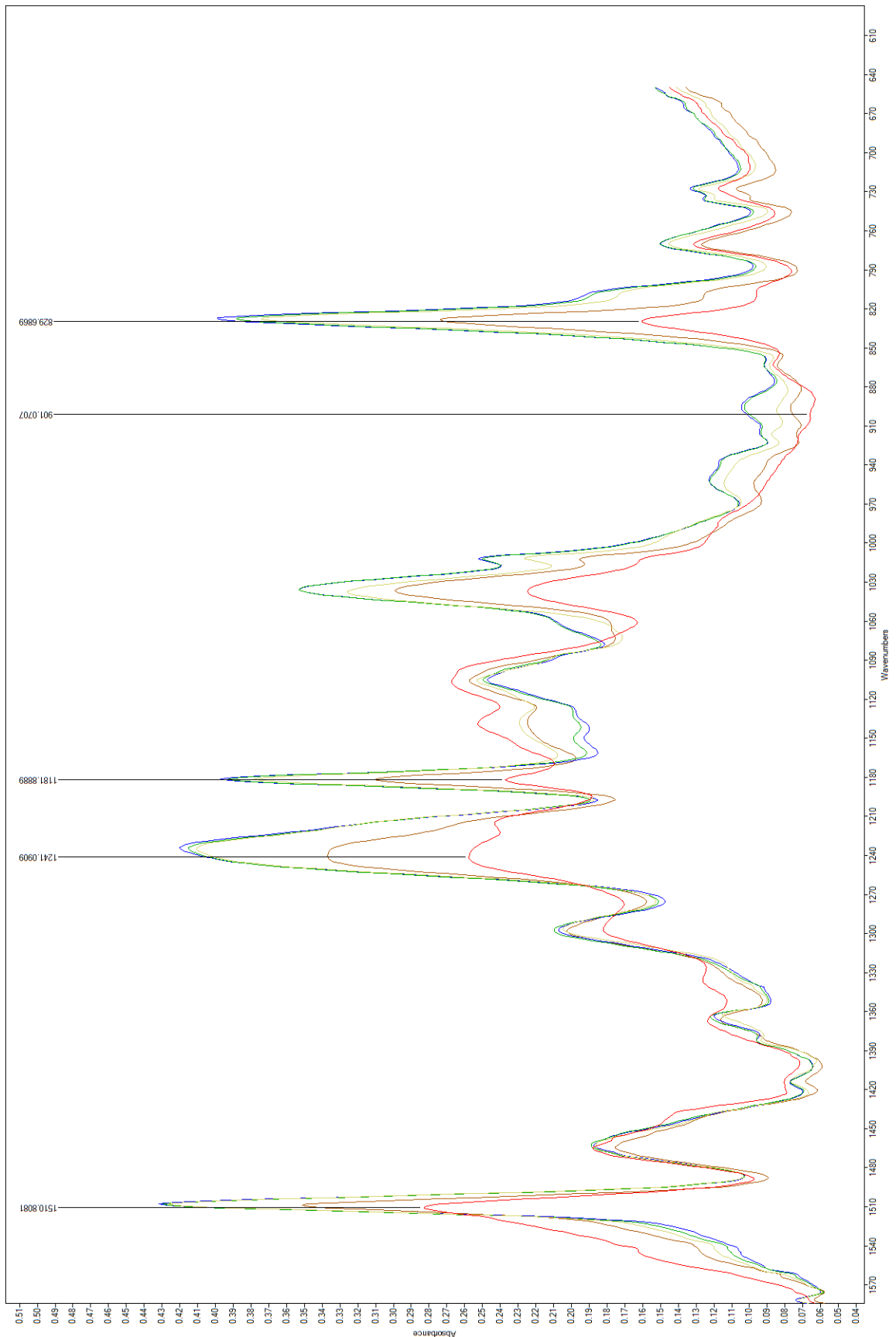


Figure 5.36: FTIR spectrum of resin complexes shows five decreasing peaks at 830cm^{-1} , 901cm^{-1} , 1182cm^{-1} , 1241cm^{-1} and 1510cm^{-1} are observed for samples with increased curing temperatures (blue:35°C green:70°C light yellow:105°C brown:160°C red:180°C).

5.1.4 Nd:YAG Laser Curing Mechanism Theory At The Laser Wavelength Of 532nm

The described theory of rise in epoxy-based silver ink's temperature due to silver flakes primary absorption; transport of solvent due to molecular excitation followed by the Marangoni effect; and the resin complex chemical cross-linking process, is supported by the observations gathered from experimental results. The mechanism proposed for thermally curing the D58 epoxy-based conductive silver ink by Nd:YAG laser at the wavelength of 532nm is expanded below.

1. Silver flakes are the primary absorber of laser energy at 532nm, this causes a localized temperature rise due to the photothermal effect with absorption coefficient enhanced by Geometric scattering and laser beam multiple reflections among silver flakes inside the epoxy-based conductive silver ink system.
2. The local rise in temperature expels the solvent towards the edges of the ink track, as well as ahead of the laser beam in the area of the laser irradiation due to the Marangoni effect.
3. Further temperature increase unblocks the hardener of the resin complex causing resin cross-linking process as a result of chemical reactions.
4. The epoxy-based conductive silver ink is thus cured as a result of resin cross-linking and the corresponding reduction in ink track volume causing the formation of a cluster with multiple conducting paths throughout the epoxy-based conductive silver ink, resulting in an electrically conducting solid.

5.2 Chapter summary

In this Chapter, experiments in irradiating D58 epoxy-based conductive silver ink components including silver flakes, resin complex and solvent using Nd:YAG frequency doubled nanosecond laser at 532nm and their experimental results are discussed. Silver flakes were found to be the major component to absorb laser energy, causing a localized temperature rise enhanced due to Geometric scattering and multiple reflections between flakes. Such absorption promoted an overall temperature rise of the local ink system, as evidenced by experimental results. The solvent was transported out of the ink by expulsion from the ink track towards the edges and ahead of the ink system in the area of the laser irradiation by the Marangoni effect. The further rise in ink temperature caused resin complex to cross link due to chemical reactions, as evidenced by FTIR spectrums. These observations strongly support the curing mechanism proposed in this thesis.

6. FINITE ELEMENT MODELLING OF EPOXY-BASED SILVER INK CURING PROCESS BY REPEATING LASER BEAM IRRADIATIONS AT 532NM

This Chapter discusses a finite element (FE) model that was developed to simulate a multiple-pass scanning process for Nd:YAG frequency doubled laser curing of a D58 epoxy-based silver ink track at a wavelength of 532nm. This modelling of thermal field will be compared with thermal profiles recorded by an IR camera for the FE model validation, and then compared with previous experimental results to validating curing mechanisms developed in **Chapter 5**, followed by suggestions to improve laser curing efficiency based on the simulation of the FE model.

6.1 Overview

Finite element method (FEM) as a discretization method, helps the engineer and scientist to solve complicated engineering and scientific problems by simplifying degrees of freedom and providing solutions using partial differential equations (PDEs) as well as ordinary differential equations (ODEs) [6.1]. COMSOL 4.3b, as an up-to-date version of the COMSOL Multiphysics software, is developed by Swedish company - COMSOL AB. It provides a user friendly graphical user interface (GUI) and a powerful tool that enables a precise and smooth multiphysics simulation, as well as integrating various applications such as MATLAB programming software.

COMSOL Multiphysics contains various modules for users to select for solving different engineering and scientific problems (**Figure 6.1**). Curing an epoxy-based particulate silver ink track under a repeating laser energy beam irradiation at 532 nm is considered as a thermal process, which has been discussed in **Chapter 5**, therefore a heat transfer module is selected for building a thermal field to simulate a laser-based curing process.

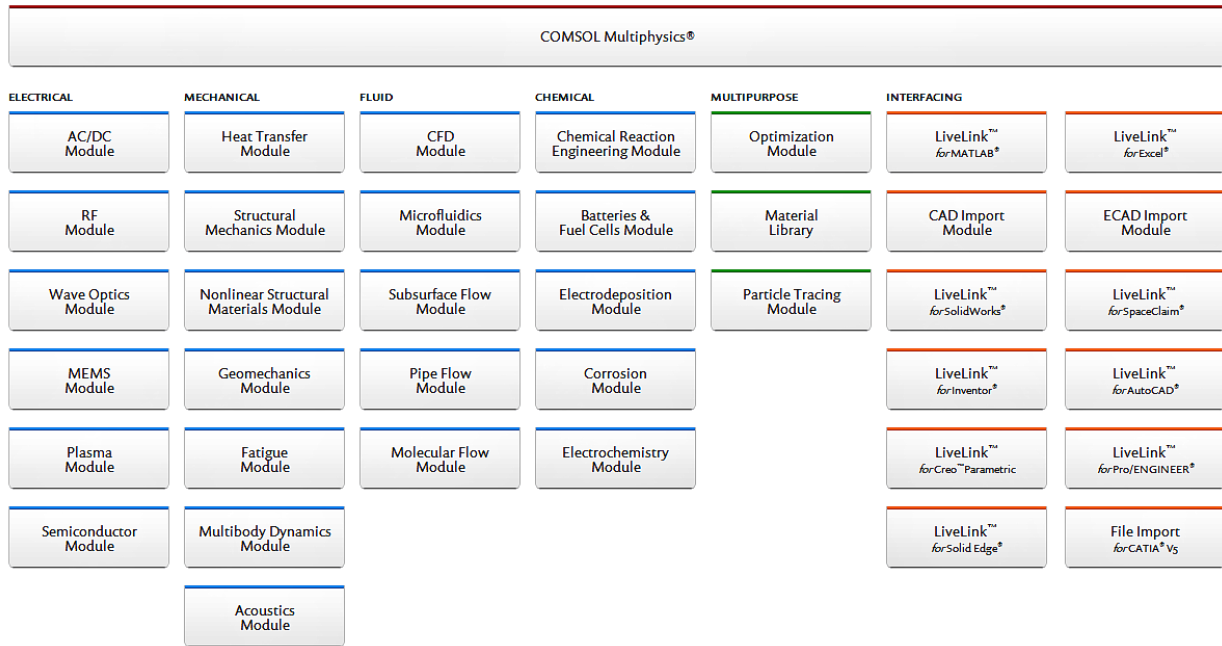


Figure 6.1: The structure of modules in COMSOL Multiphysics FE modelling software [6.2].

The modelling strategy is shown in **Figure 6.2** [6.3], for which an understanding of the physical processes is essential, followed by mathematically defining physical parameters and boundary conditions to the model, in which PDEs and ODEs will be solved by the FE modelling software. The simulated results will then be compared to the experimental data for model verification and enhancement.

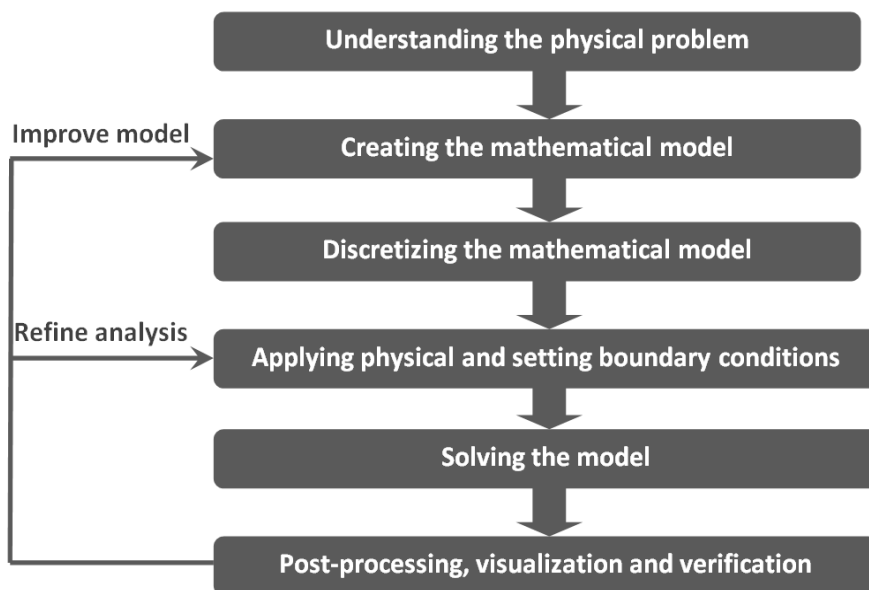


Figure 6.2: FE Modelling strategy [6.3].

6.2 Temperature Evolution for Modelling

As discussed in **Chapter 2**, Shang *et al.* developed a FE model to predict the temperature variation as a function of total heat input for CO₂ based laser curing of a conductive silver ink track at 10.6 μ m. This included a latent heating process due to a direct solvent evaporation from the ink and resin cross-linking [2.51]. In **Chapter 4** and **5** however, presented experimental results have suggested a different curing mechanism for an epoxy-based silver ink track being cured by laser beam irradiations at the wavelength of 532nm. This is without solvent evaporation as the solvent is entirely transported out of the ink system by solvent molecule excitation followed by the Marangoni effect (please refer to **Chapter 5** for the laser based curing mechanism proposed with more details).

A new temperature evolution model is therefore required FEM analysis of the curing of a D58 epoxy-based conductive silver ink track by repeating laser beam irradiations at 532nm. This will be based on mechanism theories developed in **Chapter 5**. **Figure 6.3** shows a drawing of the new temperature evolution model for curing a D58 epoxy-based silver ink track at 532nm through 3 different stages:

- 1) In the *first stage* [ΔQ_1], the solvent transport due to the Marangoni effect below 70°C leads to a gradual reduction in the D58 epoxy-based silver ink's specific heat capacity. As in reality, the dynamic change in material's physical properties upon thermal interaction is a nonlinear process, therefore a curve is predicted here due to the nonlinear rate of solvent loss and an increasing temperature (for solvent transport theory please refer to **Chapter 5**).
- 2) In *stage 2* [ΔQ_2], as the solvent has been fully expelled from the ink system before the solvent evaporation point at around 70°C, further heating does not affect the specific heat of the remaining ink (at this point, the ink system only contains silver flakes and resin complex). As the ink composition does not

change in this stage, a greater temperature gradient is predicted due to the overall reduction of specific heat capacity of the ink.

- 3) In *stage 3* [ΔQ_3], a chemical cross-linking process is taking place when the temperature exceeds the resin hardener unblocking temperature at around 90°C. This leads to a further decrease of the ink's specific heat capacity, and an increased temperature gradient is therefore predicted due to an overall loss of solvent in first stage and an overall loss of resin component in the cross-linking process (for resin cross-linking theory please refer to **Chapter 5**).

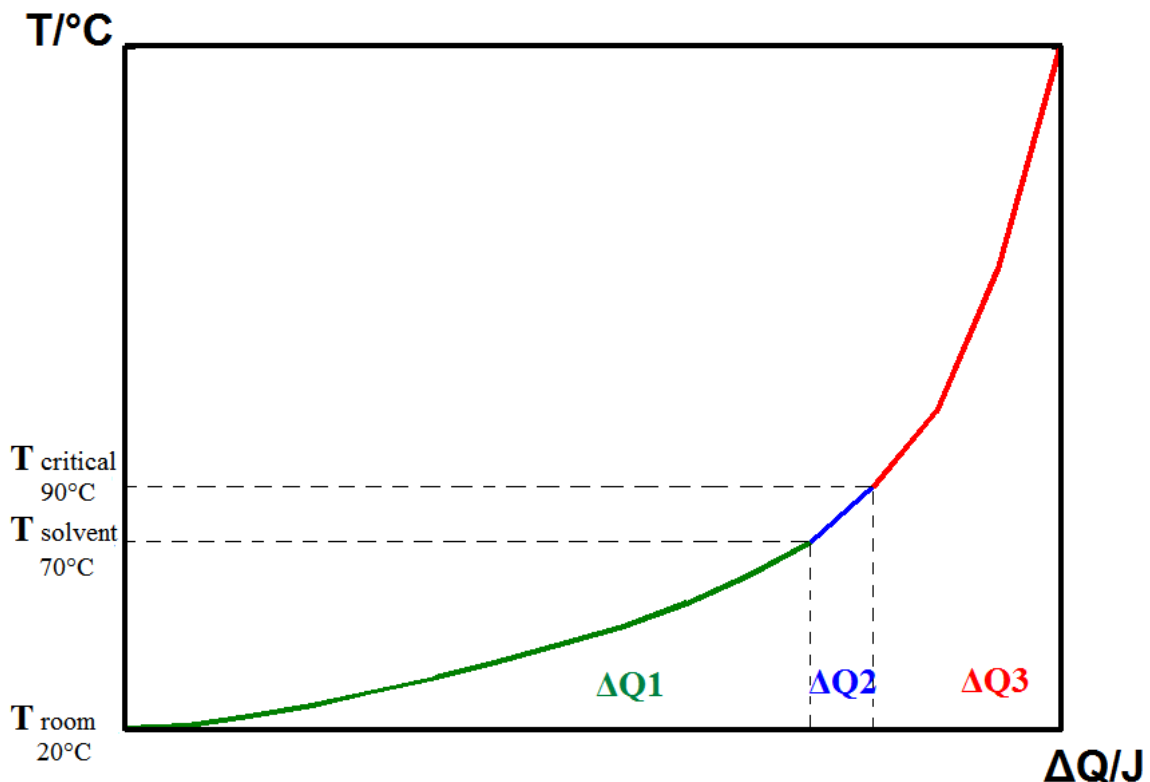


Figure 6.3: Drawing of the temperature evolution as a function of overall heat input for Nd:YAG laser curing a D58 silver ink track at the laser irradiation wavelength of 532nm.

As there is no solvent evaporation in the laser curing process at 532nm, the mathematical equation for the energy balance (2-1) in **Chapter 2** could be rewritten as follows in (6-1).

$$A \cdot P_{laser} = \Delta Q = \sum \Delta Q_i = \Delta Q_1 + \Delta Q_2 + \Delta Q_3 \quad (6-1)$$

Where:

A = absorbance of D58 conductive silver ink,

P_{laser} = laser output power,

ΔQ = total amount of heat absorbed,

ΔQ_i = amount of heat absorbed in different stage.

For *stage 1* shown in **Figure 6.3**,

$$\sum \Delta Q_1 = \sum \Delta T_j V_{ink_j} \rho_{ink_j} c_{ink_j} \quad (6-2)$$

$$\rho_{ink_j} = Ag\% \rho_{Ag} + r\% \rho_r + s\% \rho_s \quad (6-3)$$

$$\begin{aligned} c_{ink_j} &= \frac{C_{ink}}{m_{ink}} = \frac{V[Ag\% \rho_{Ag} c_{Ag} + r\% \rho_r c_r + s\% \rho_s c_s]}{V \rho_{ink}} \\ &= \frac{Ag\% \rho_{Ag} c_{Ag} + r\% \rho_r c_r + s\% \rho_s c_s}{Ag\% \rho_{Ag} + r\% \rho_r + s\% \rho_s} \end{aligned} \quad (6-4)$$

For *stage 2* shown in **Figure 6.3**,

$$\Delta Q_2 = \Delta T_2 V [Ag\% \rho_{Ag} c_{Ag} + r\% \rho_r c_r] \quad (6-5)$$

For *stage 3* shown in **Figure 6.3**,

$$\sum \Delta Q_3 = \sum \Delta T_k V_{ink_k} \rho_{ink_k} c_{ink_k} \quad (6-6)$$

$$\rho_{ink_k} = Ag\% \rho_{Ag} + r\% \rho_r \quad (6-7)$$

$$c_{ink_k} = \frac{C_{ink}}{m_{ink}} = \frac{V[Ag\% \rho_{Ag} c_{Ag} + r\% \rho_r c_r]}{V \rho_{ink}} = \frac{Ag\% \rho_{Ag} c_{Ag} + r\% \rho_r c_r}{Ag\% \rho_{Ag} + r\% \rho_r} \quad (6-8)$$

Where:

ΔT = the temperature change in each stage,

V = volume of the ink,

$A_g\%, r\%, s\%$ = volume percentages for silver flakes, resin and solvent,

$\rho_{Ag}, \rho_r, \rho_s$ = densities of silver flakes, resin and solvent,

c_{Ag}, c_r, c_s = the specific heat capacities of silver flakes, resin and solvent,

c_{ink} = the specific heat capacity of the D58 silver ink,

C_{ink} = heat capacity of the D58 silver ink,

m_{ink} = the mass of the D58 silver ink,

ρ_{ink} = the density of the D58 silver ink.

6.3 Definition for Parameters and Variables

The mechanism of laser curing will result in physical properties of the epoxy-based silver ink track changing dynamically during the laser curing process at 532nm. This occurs due to a change from liquid to solid and an associated change in composition of the ink. These dynamic physical properties of epoxy-based particulate silver inks considered are thermal conductivity, specific heat capacity, density and laser intensity absorbance, etc. and are subject to the change with increasing temperature as a result of coupling the laser induced energy into the silver ink material. Therefore having these key dynamic physical properties such as thermal conductivity, specific heat capacity, etc. mathematically defined will increase the accuracy of the finite element (FE) model.

6.3.1 Material Physical Parameters Definition

As calculating the material's physical properties with a dynamic change in temperature is complex and time-consuming, therefore an assumption can be made to simplify the modelling for approximating dynamic change in the material's physical parameters.

An assumption for D58 epoxy-based silver ink material composition with an increasing temperature can be made based on **Figure 6.3** in **section 6.2** before a finite element (FE) model can be constructed, which simplifies the mathematical modelling by making the assumptions as follows.

Table 6.1 shows the ink's dynamic composition in the solvent transport stage below 70°C, and **Table 6.2** shows the ink's dynamic composition in the resin cross-linking stage. A further temperature rise beyond 150°C will not change the ink's composition as the ink is considered as fully cured.

Table 6.1: Assumption to change-in-ink's composition below 70°C.

	20°C	30°C	40°C	47°C	50°C	53°C	55°C	59°C	62°C	67°C	70°C
Silver	100%	100%	100%	100%	100%	100%	100%	100%	100%	100%	100%
Resin	100%	100%	100%	100%	100%	100%	100%	100%	100%	100%	100%
Solvent	100%	90%	80%	70%	60%	50%	40%	30%	20%	10%	0%

Table 6.2: Assumption to change-in-ink's composition above 70°C.

	90°C	95°C	103°C	120°C	150°C
Silver flakes	100%	100%	100%	100%	100%
Resin	100%	90%	80%	70%	60%
Solvent	0%	0%	0%	0%	0%

Such composition changes to the ink system are irreversible, therefore the associated physical properties of a D58 silver ink such as the laser energy absorbance, thermal conductivity, density, specific heat capacity are also irreversible in this case. Temperature drops will not then affect the ink's physical parameters as they only change with an increasing temperature. This function of locking material's physical property within the model and preventing it being changed back during the cool down stage after the laser beam is moving away can be achieved by defining a command within the COMSOL model based on the equation in **(6-16)**.

$$M_{property} = \begin{cases} M_{t-1} & \text{if } (T_t < T_{t-1}) \\ M_t & \text{if } (T_t \geq T_{t-1}) \end{cases} \quad (6-16)$$

Where:

$M_{property}$ = Material's physical property, such as density, specific heat capacity, thermal conductivity, laser energy absorbance, etc.,

M_{t-1} = Material's physical property at time of t-1,

M_t = Material's physical property at time t,

T = Temperature,

t = Processing time.

6.3.1.1 Laser Energy Absorbance of D58 Epoxy-based Silver Ink

Shang *et al.* concluded and mathematically defined the absorbance to laser induced energy for D58 conductive silver ink as below in **(6-9)** [6.4].

$$A = \begin{cases} (1-A_g\%)[A_s+(1-A_s)A_r] & (\text{before solvent removal}) \\ (1-A_g\%)A_r & (\text{after solvent removal}) \end{cases} \quad (6-9)$$

Where A_s and A_r refer to the absorbance of solvent and epoxy resin in ink system, respectively, and can be calculated using the Beer-Lambert law [2.51, 2.52]. $A_g\%$ refers to the volume percentage of silver flakes within the ink. In the laser curing process, the composition of the ink will change, and the change in ink's composition will further affect the thermal absorbance and the overall volume of the ink.

Based on the assumption made in **section 6.3.1**, a dynamic change for D58 silver ink's absorbance with an increasing temperature could be plotted in **Figure 6.4** below.

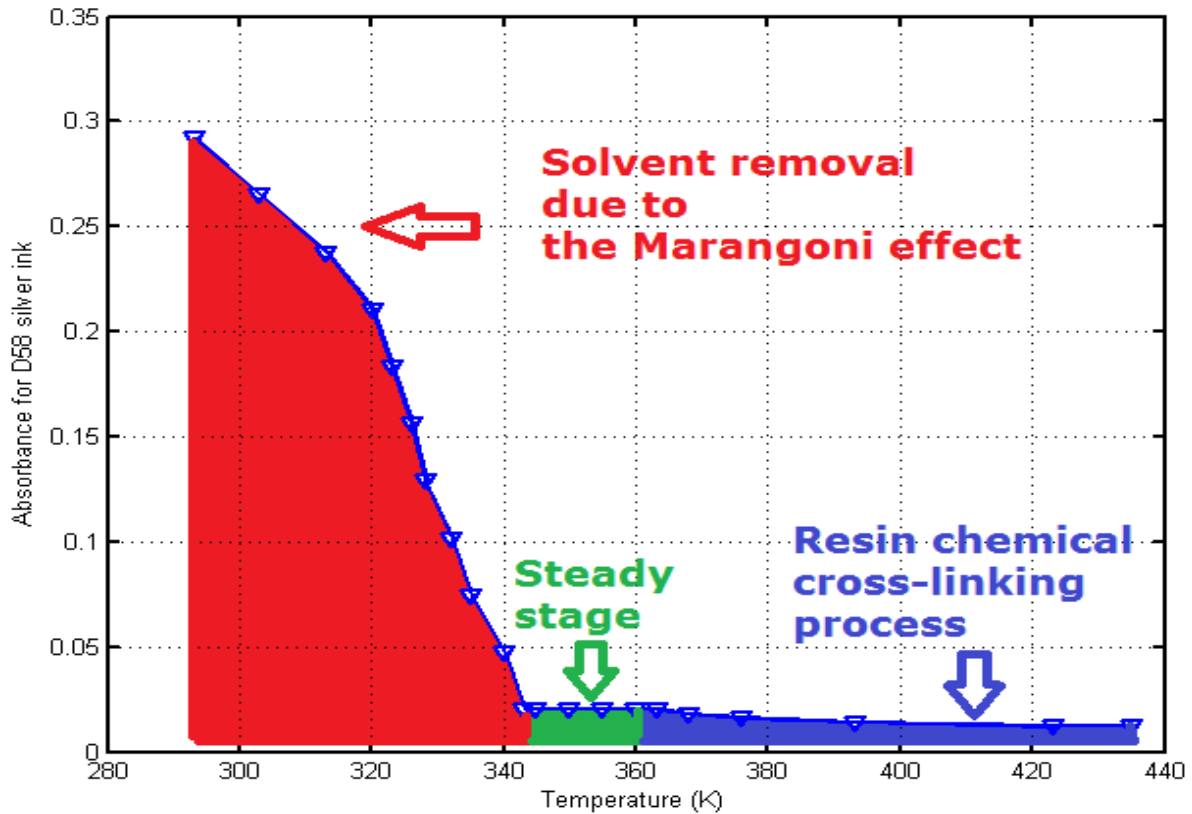


Figure 6.4: Dynamic absorbance of D58 silver ink is a function of an increasing temperature.

6.3.1.2 Dynamic Density of D58 Epoxy-based Silver Ink

The overall density of D58 conductive silver ink also changes with an increasing temperature due to the dynamic change in composition of the components inside the D58 ink system, this is given by:

$$\rho_{ink_j} = Ag\% \rho_{Ag} + r\% \rho_r + s\% \rho_s \tag{6-3}$$

$$\rho_{ink_k} = Ag\% \rho_{Ag} + r\% \rho_r \tag{6-7}$$

Where:

ρ_{ink_j} = the density of D58 silver ink in *stage 1* of **Figure 6.3**,

ρ_{ink_k} = the density of D58 silver ink in *stage 2* and *3* of **Figure 6.3**.

Based on the ink composition assumption made in **section 6.3.1**, the dynamic density of D58 ink can be plotted as below in **Figure 6.5**.

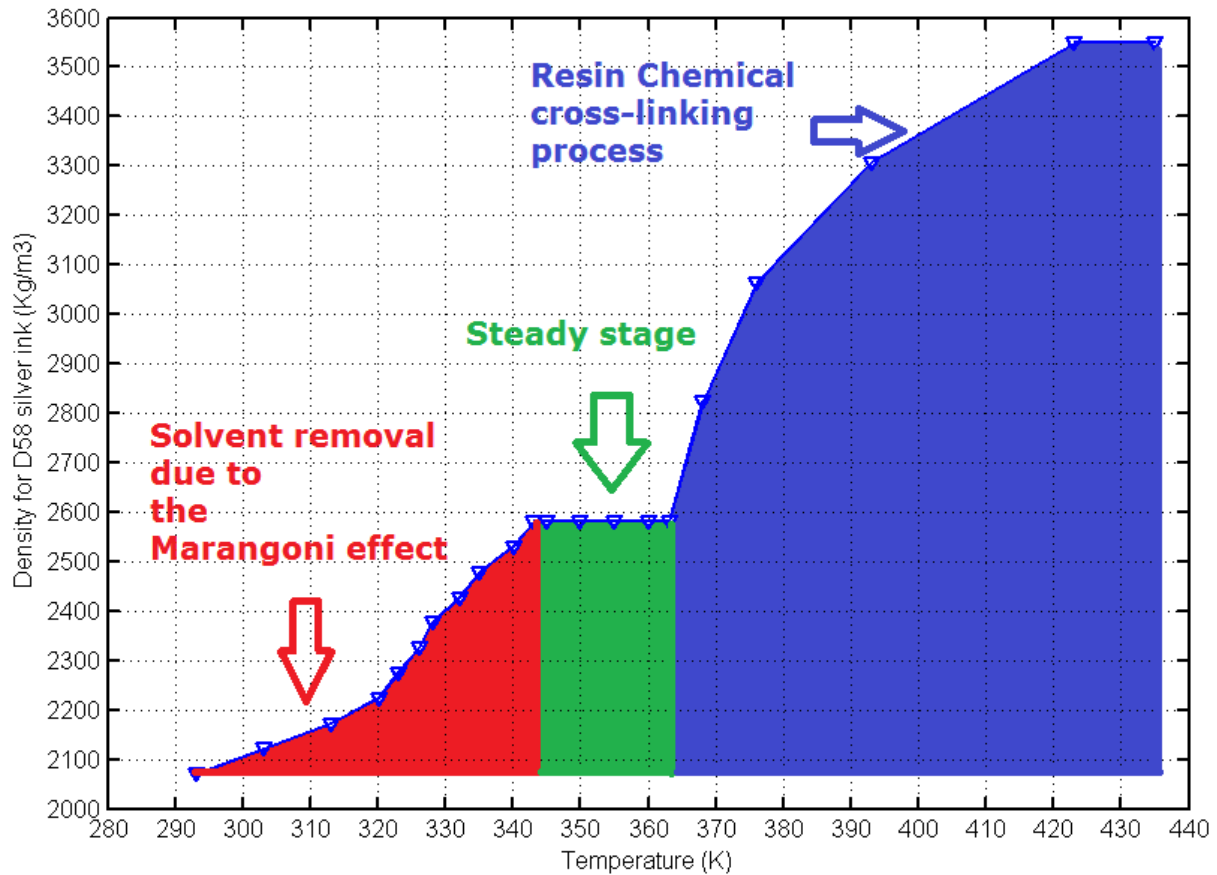


Figure 6.5: Dynamic density of D58 silver ink is a function of an increasing temperature.

6.3.1.3 Dynamic Specific Heat Capacity of D58 Epoxy-based Silver Ink

Another key physical parameter of the ink that needs to be defined is the ink's specific heat capacity. The specific heat capacity changes dynamically in the laser curing process with the dynamic change in ink composition (**Figure 6.6**). This can be represented by:

$$c_{ink_j} = \frac{C_{ink}}{m_{ink}} = \frac{V[Ag\% \rho_{Ag} c_{Ag} + r\% \rho_r c_r + s\% \rho_s c_s]}{V \rho_{ink}}$$

$$= \frac{Ag\% \rho_{Ag} c_{Ag} + r\% \rho_r c_r + s\% \rho_s c_s}{Ag\% \rho_{Ag} + r\% \rho_r + s\% \rho_s}$$

(6-4)

$$c_{ink_k} = \frac{Ag\% \rho_{Ag} c_{Ag} + r\% \rho_r c_r}{Ag\% \rho_{Ag} + r\% \rho_r}$$

(6-8)

Where:

c_{ink_j} = the specific heat capacity of D58 silver ink in *stage 1* of **Figure 6.3**,

c_{ink_k} = the specific heat capacity of D58 silver ink in *stage 2* and *3* of **Figure 6.3**.

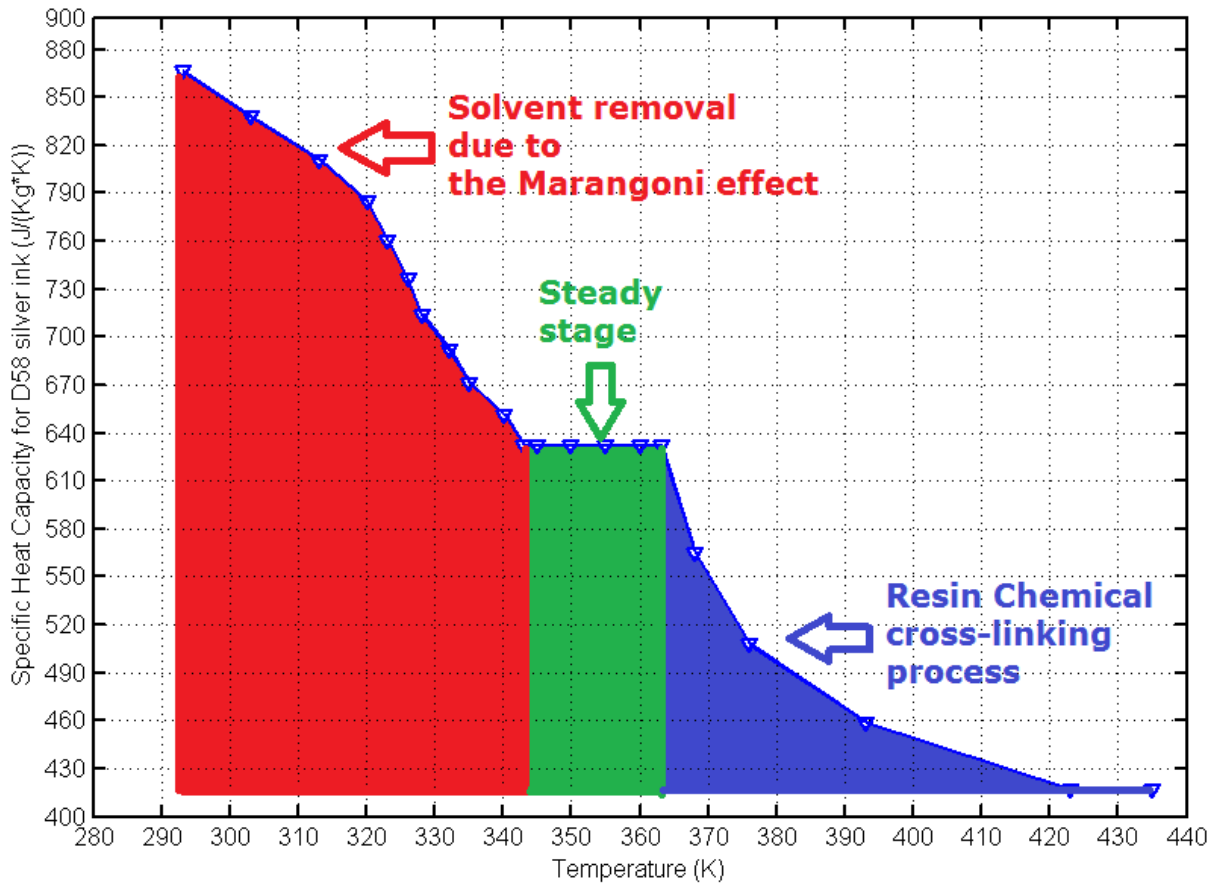


Figure 6.6: Dynamic specific heat capacity of D58 silver ink is a function of an increasing temperature.

6.3.1.4 Dynamic Thermal Conductivity of D58 Epoxy-based Silver Ink

Thermal conductivity of D58 epoxy-based conductive silver ink is extremely low at the beginning of the laser curing process due to its liquid phase. Once the dominant heat transfer mechanism changes from convection to conduction, at the de-blocking temperature of 90°C (where Blocked Isocyanates (BI) are unblocked and poly(isocyanate)s are formed for resin chemical cross-linking reactions, as discussed in **Chapter 5**), the thermal conductivity of the ink is a function of the electrical resistivity, as mathematically defined in **(6-10)** by Wiedemann-Franz law [6.4]. The silver ink's thermal conductivity is inversely proportional to its electrical resistivity, as shown in **(6-11)**.

$$\sigma = \frac{1}{\rho} = \frac{\ell}{RA} \quad (3-1)$$

$$\frac{\kappa_{ink}}{\sigma_{ink}} = \frac{\kappa_{bulkAg}}{\sigma_{bulkAg}} = L \cdot T \quad (6-10)$$

$$\kappa_{ink} = \frac{\kappa_{bulkAg} \sigma_{ink}}{\sigma_{bulkAg}} = \frac{\kappa_{bulkAg} \rho_{bulkAg}}{\rho_{ink}} \quad (6-11)$$

Where:

σ = electrical conductivity of the material,

ρ = electrical resistivity of the material,

R = resistance,

A = the cross-sectional area of the material,

ℓ = the length of the material,

κ = material's thermal conductivity,

L = Lorenz number,

T = temperature,

ρ_{bulkAg} = electrical resistivity of the bulk silver, which is $\sim 1.59 \cdot 10^{-8} \Omega m$ [2.75],

κ_{bulkAg} = thermal conductivity of the bulk silver, which is $\sim 430 \text{ W/mK}$ at 20°C [6.5].

Therefore, the approximated values of dynamic thermal conductivity can be calculated based on equation **(6-11)** using the electrical resistivity results from

532nm laser curing D58 epoxy-based silver ink as discussed in experimental result Chapter (**Chapter 4**) and the assumption made in **section 6.3.1**. The dynamic thermal conductivity of D58 ink can therefore be plotted with an increasing temperature as shown in **Figure 6.7**.

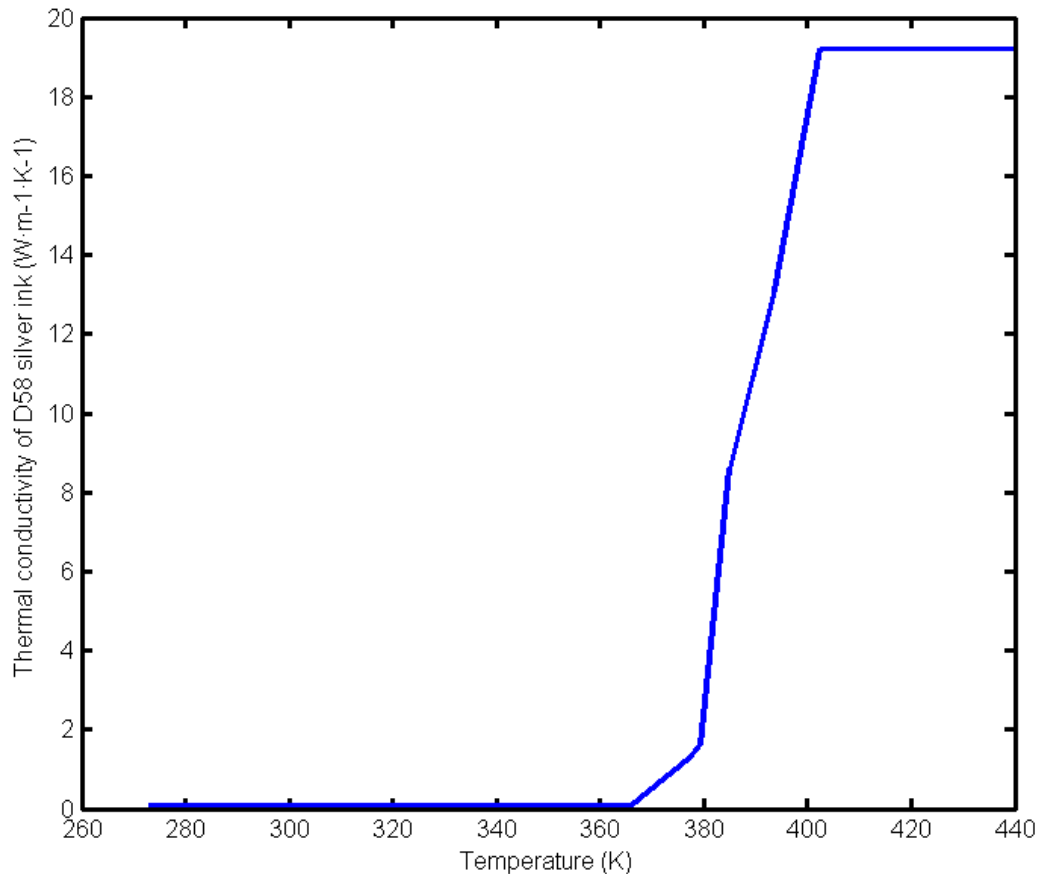


Figure 6.7: Dynamic thermal conductivity of D58 silver ink as a function of temperature.

6.3.2 Laser Working Parameters Definition

As the heating source used in this investigation is a frequency doubled Nd:YAG laser with a top-hat beam shape, the laser working parameters can be defined as below (**Table 6.3** and **Table 6.4**) for better accuracy in the FE model.

Table 6.3: Laser working parameters used as the input to the FE model.

Parameter	Value	Name
P	P	laser beam output power
v0	v0	laser beam traverse speed
w0	5 mm	laser beam radius
I0	$(P)/((\pi)*(w0^2))$	laser beam Intensity

Table 6.4: Laser working variables used as the input to the FE model.

Variable	Value	Name
y1	y1	Y starting point
x1	x1	X starting point
r1	$\text{sqrt}((x-x1)^2+(y-y1)^2)$	definition of top-hat beam shape
q_laser	$I0*(r1 \leq w0)$	laser power with a top-hat beam shape

6.4 Boundary Conditions for FE Modelling

The top surfaces of both the silver ink track and the PET substrate will absorb the laser beam during the laser curing process. The absorbance to laser radiation at 532nm for the PET substrate is approximately at 0.12 [2.55], and the absorbance for silver ink track is a predefined variable parameter – A. Both materials are subjected to convective cooling with ambient air and the laser inward heat flux, which is described as below in **(6-12)** and **(6-13)**.

$$-\vec{n} \cdot (-k \nabla T) = h_0 (T_{ext} - T) + q_0 \quad (6-12)$$

$$q_0 = A \cdot I_{laser} \quad (6-13)$$

Also the base of the PET substrate is subjected to thermal insulation with the equation as below in **(6-14)**.

$$-\vec{n} \cdot (-k \nabla T) = 0 \quad (6-14)$$

Where:

\vec{n} = the normal vector of the boundary,

q_0 = the inward flux heat,

h_0 = the heat transfer coefficient,

A = the absorbance,

I_{laser} = laser power intensity,

k = material's thermal conductivity,

T_{ext} = the ambient temperature,

T = the initial temperature which is defined here as 293.15K.

6.5 Finite Element (FE) Model Construction

The finite element (FE) model in this study is constructed with COMSOL Multiphysics 4.3b, **Figure 6.8** shows the main graphical user interface (GUI) of building a FE model. Model definition including the global parameter setting, model geometry setting, material definition, etc. can be operated in the Model Builder section. The settings section in the middle offers the capability for users of defining a specific parameter, and the change in parameters can be viewed in the graphic section.

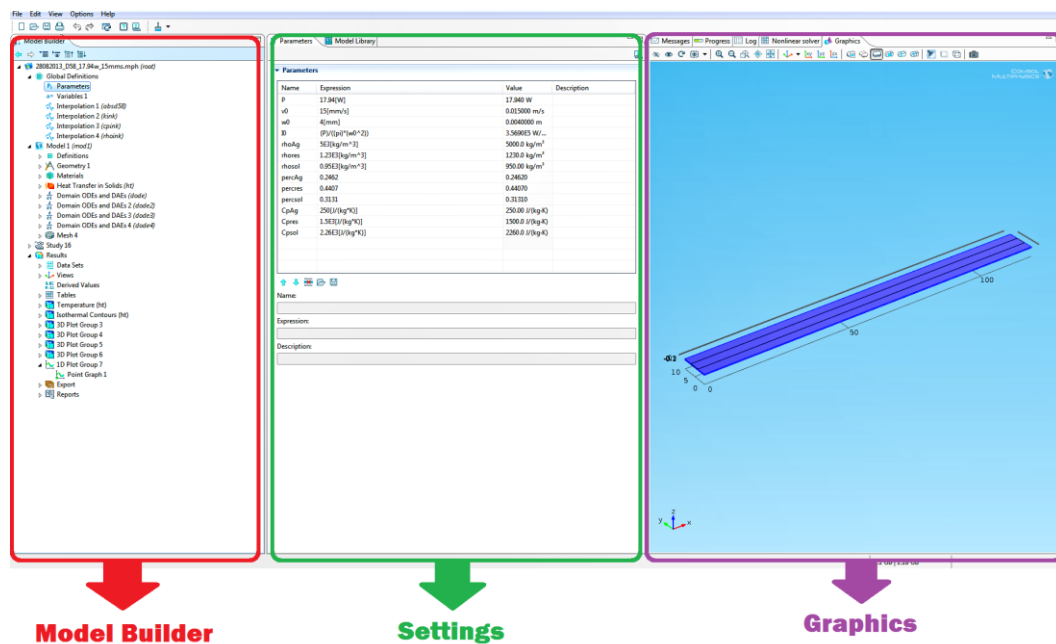


Figure 6.8: Interface of COMSOL Multiphysics 4.3b.

The geometry of the PET substrate is 135mm long, 10mm wide, and with a thickness of 0.35mm, and the D58 epoxy-based silver ink track is geographically defined on top of the PET surface with an ink track 120mm long, 3.5mm wide, and with the initial thickness of the ink at 50 μ m, based on experimental measurements (**Figure 6.9**). A steel plate with dimensions 150mm long, 50mm wide and 10mm deep is placed underneath the PET substrate material. Key physical properties such

as thermal conductivity, density, specific heat capacity, and laser power absorbance of the silver ink can be defined in COMSOL Multiphysics 4.3b based on mathematical equations in **section 6.3**.

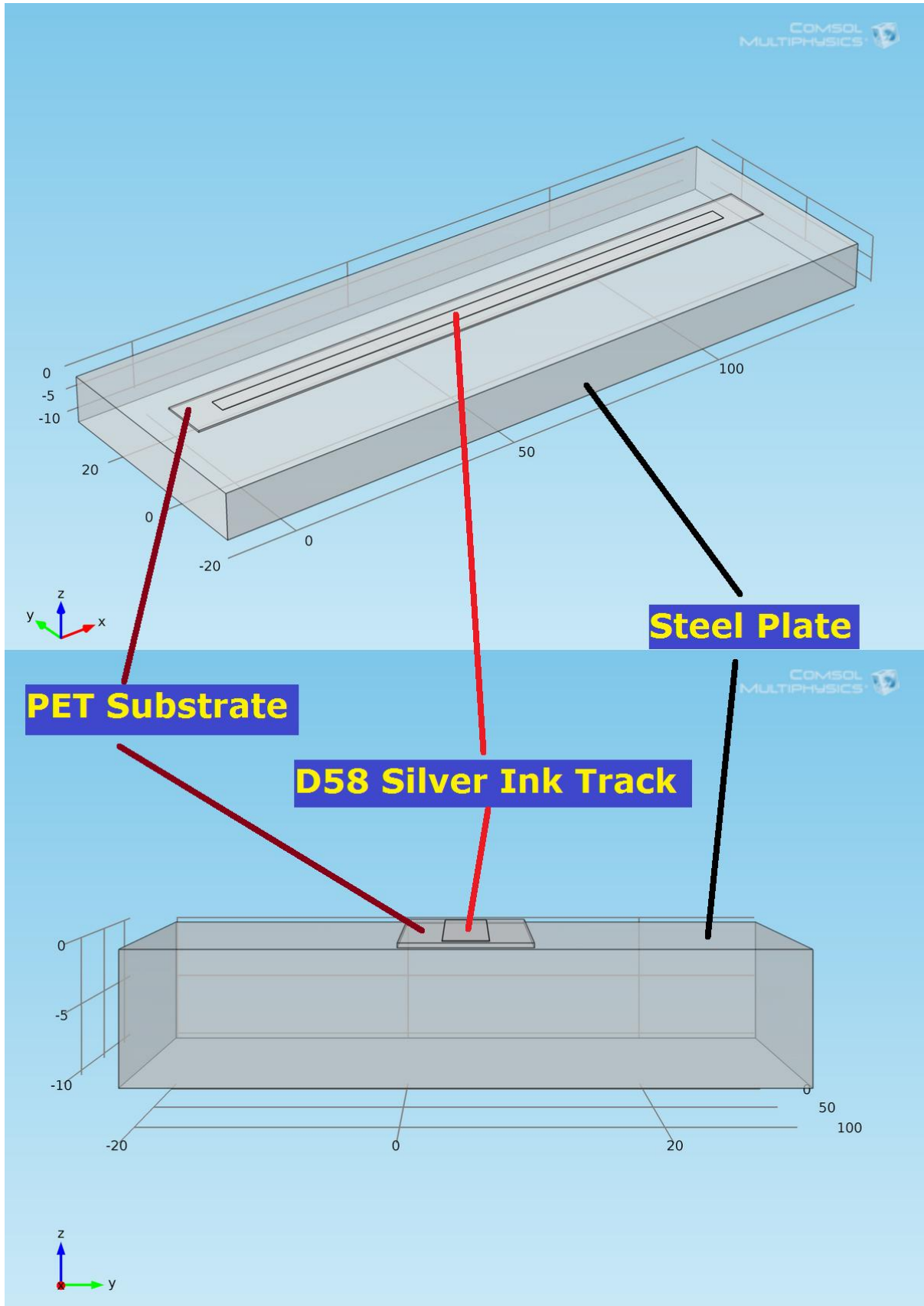


Figure 6.9: FE model construction for laser curing a D58 silver ink track.

Figure 6.10 shows the meshing of the FE model, the meshing enables the discretization of the model into small elements, and endpoints of the mesh elements, (or nodes) are points that basic functions need to be solved.

In this modelling study, the weak form of the governing differential equation of the heat equation needs to be solved. **Table 6.5** shows meshing data of the FE model. Tetrahedron (3D) and triangle (2D) are the simplest type of common shapes for small elements, or cells in the mesh generation, both are generated automatically in most cases.

Table 6.5: Mesh data of the FE model.

Property	Value
Tetrahedral elements	1090975
Triangular elements	250648
Edge elements	6122
Vertex elements	24
Maximum element size (mm)	5
Minimum element size (mm)	1E-01
Maximum element growth rate	1.45
Predefined size	Extremely coarse

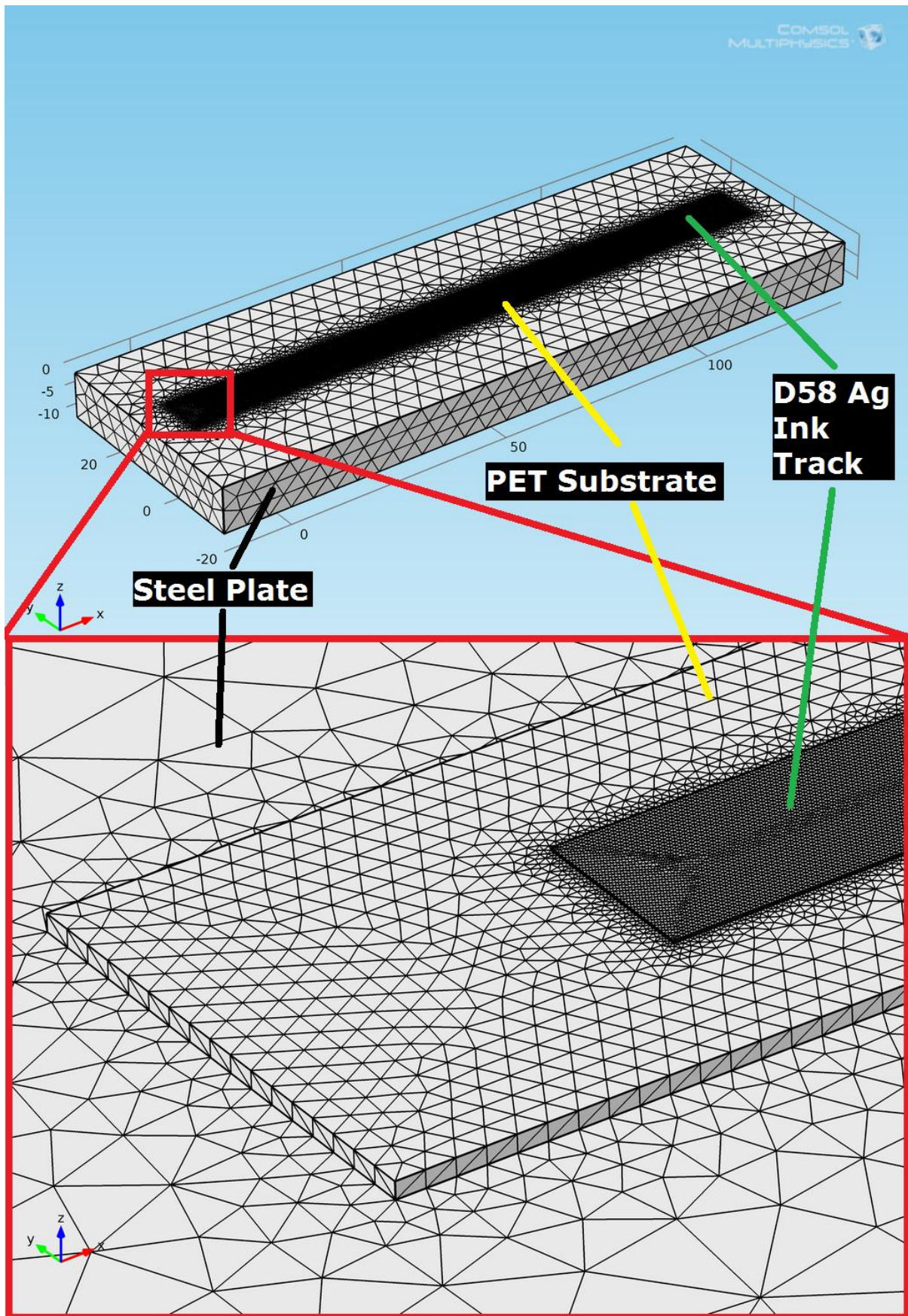


Figure 6.10: The meshing of the model, more nodes on the ink track than PET substrate material ensures smooth and accurate mathematical solutions can be achieved.

6.6 Results of Finite Element (FE) Modelling

6.6.1 Finite Element (FE) Model Validation

As this FE model is constructed for modelling the thermal field of epoxy-based silver ink track system at the laser irradiations of 532nm, this FE model needs to be compared to thermal images taken by an IR camera in experiment for FE model validation.

532nm Laser curing of D58 epoxy-based silver inks with variant laser working parameters as listed in **Table 6.6** are compared. **Figures 6.11-6.16** show the comparisons to the thermal field of D58 silver ink track as modelled from the FE model (top, in Kelvin - K) and thermal images captured by an IR camera (bottom, in degree Celsius - °C). **Figures 6.17-6.18** show the temperature evolution graph of the silver ink in the middle of the ink track in a repeating 532nm laser curing process for 4 passes.

Table 6.6: Laser working parameters as the input into the FE model.

Laser Power (W)	Scanning Speed (mm/s)
3.86	5.00
3.86	12.00
10.95	12.00
17.94	5.00
17.94	8.33
17.94	12.00

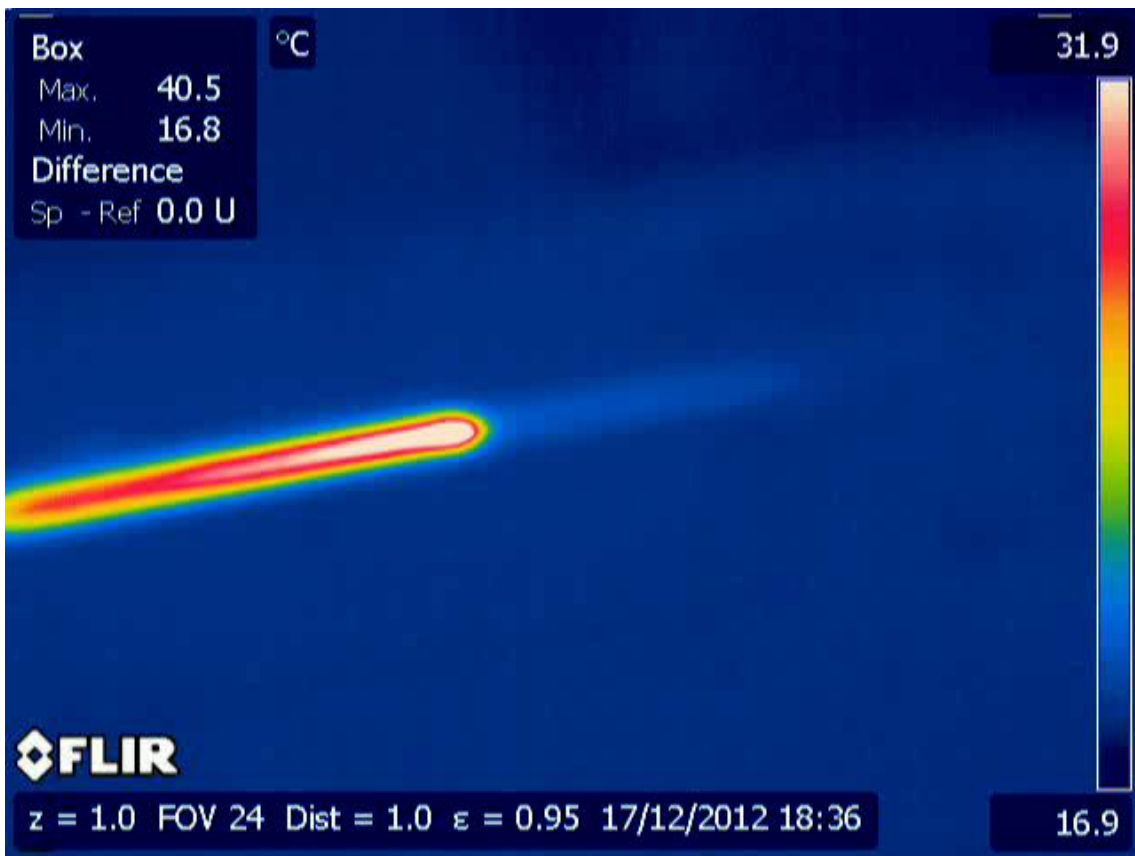
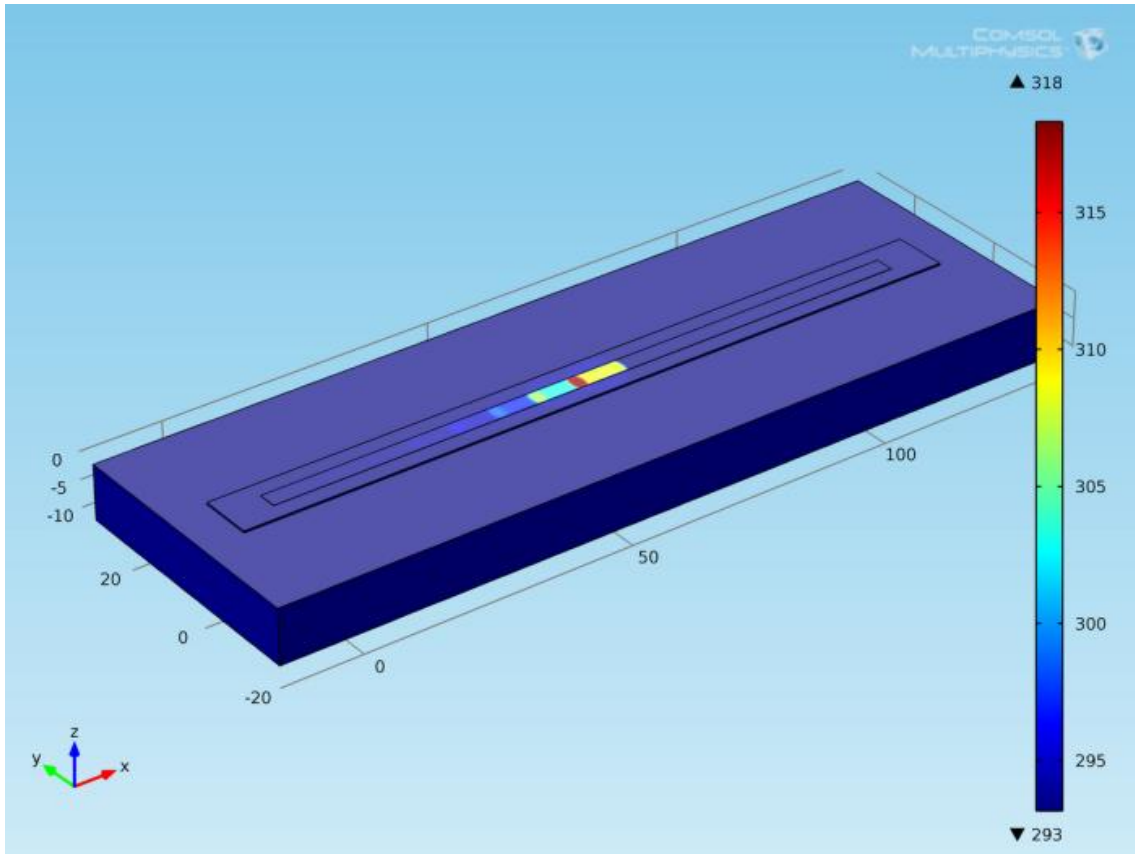


Figure 6.11: The comparison of thermal field constructed and simulated from FE modelling results (top, in Kelvin - K) and the thermal data recorded by an IR camera in experiment (bottom, in degree Celsius - °C) for D58 silver ink track in 532nm laser curing process at 3.86W, 12mm/s.

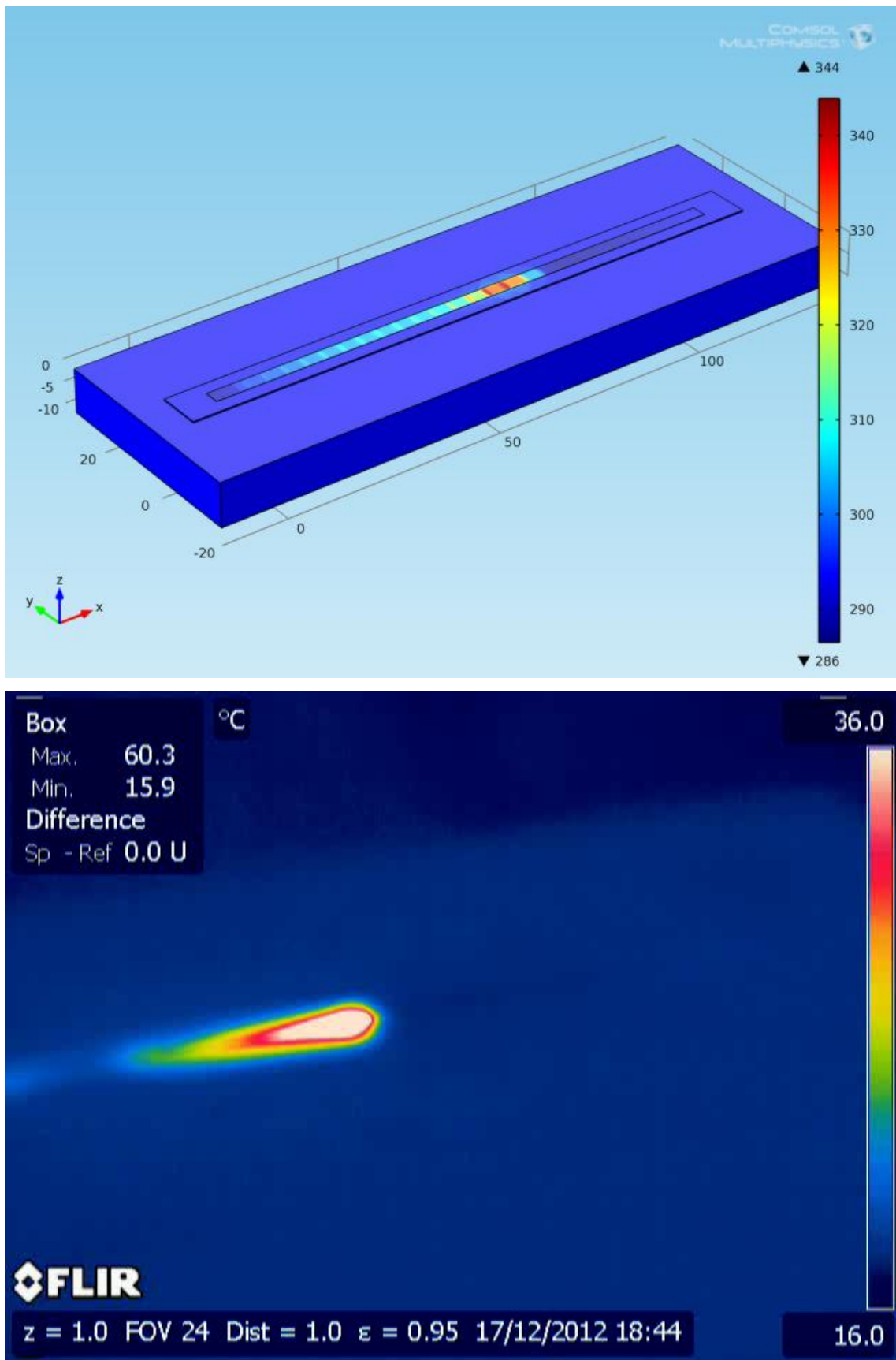


Figure 6.12: The comparison of thermal field constructed and simulated from FE modelling results (top, in Kelvin - K) and the thermal data recorded by an IR camera in experiment (bottom, in degree Celsius - °C) for D58 silver ink track in 532nm laser curing process at 10.95W, 12mm/s.

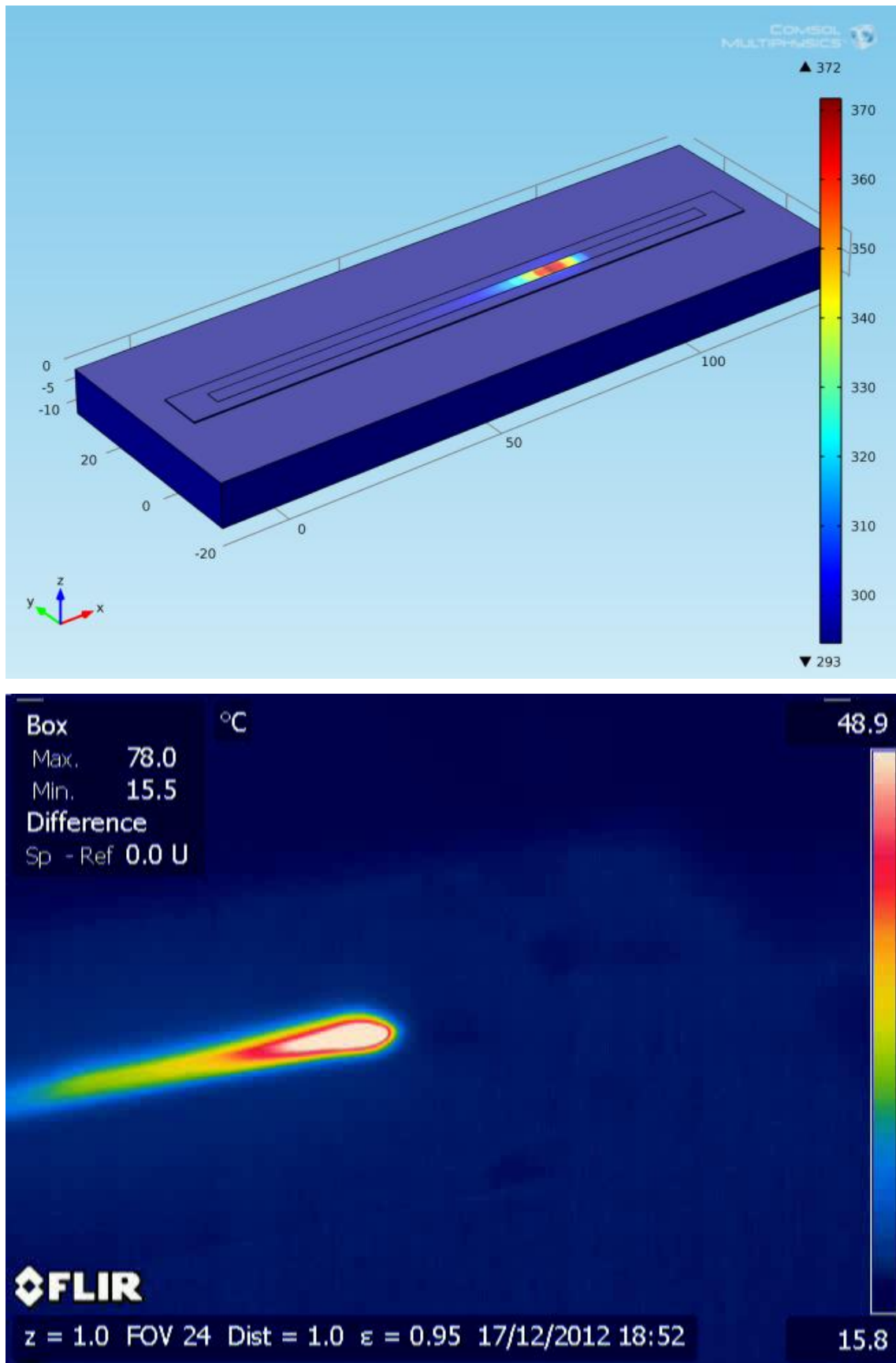


Figure 6.13: The comparison of thermal field constructed and simulated from FE modelling results (top, in Kelvin - K) and the thermal data recorded by an IR camera in experiment (bottom, in degree Celsius - °C) for D58 silver ink track in 532nm laser curing process at 17.94W, 12mm/s.

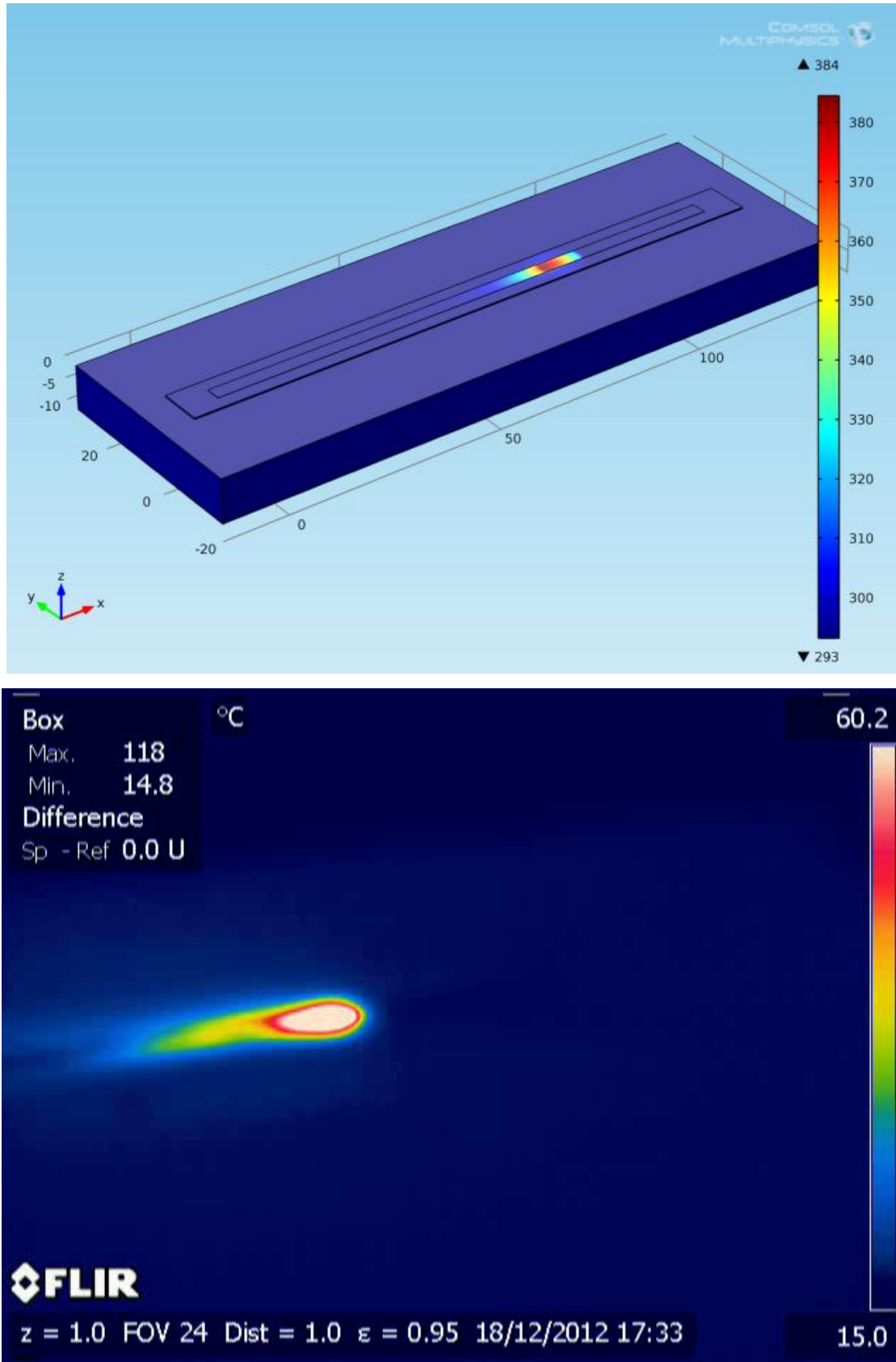


Figure 6.14: The comparison of thermal field constructed and simulated from FE modelling results (top, in Kelvin - K) and the thermal data recorded by an IR camera in experiment (bottom, in degree Celsius - °C) for D58 silver ink track in 532nm laser curing process at 17.94W, 8.33mm/s.

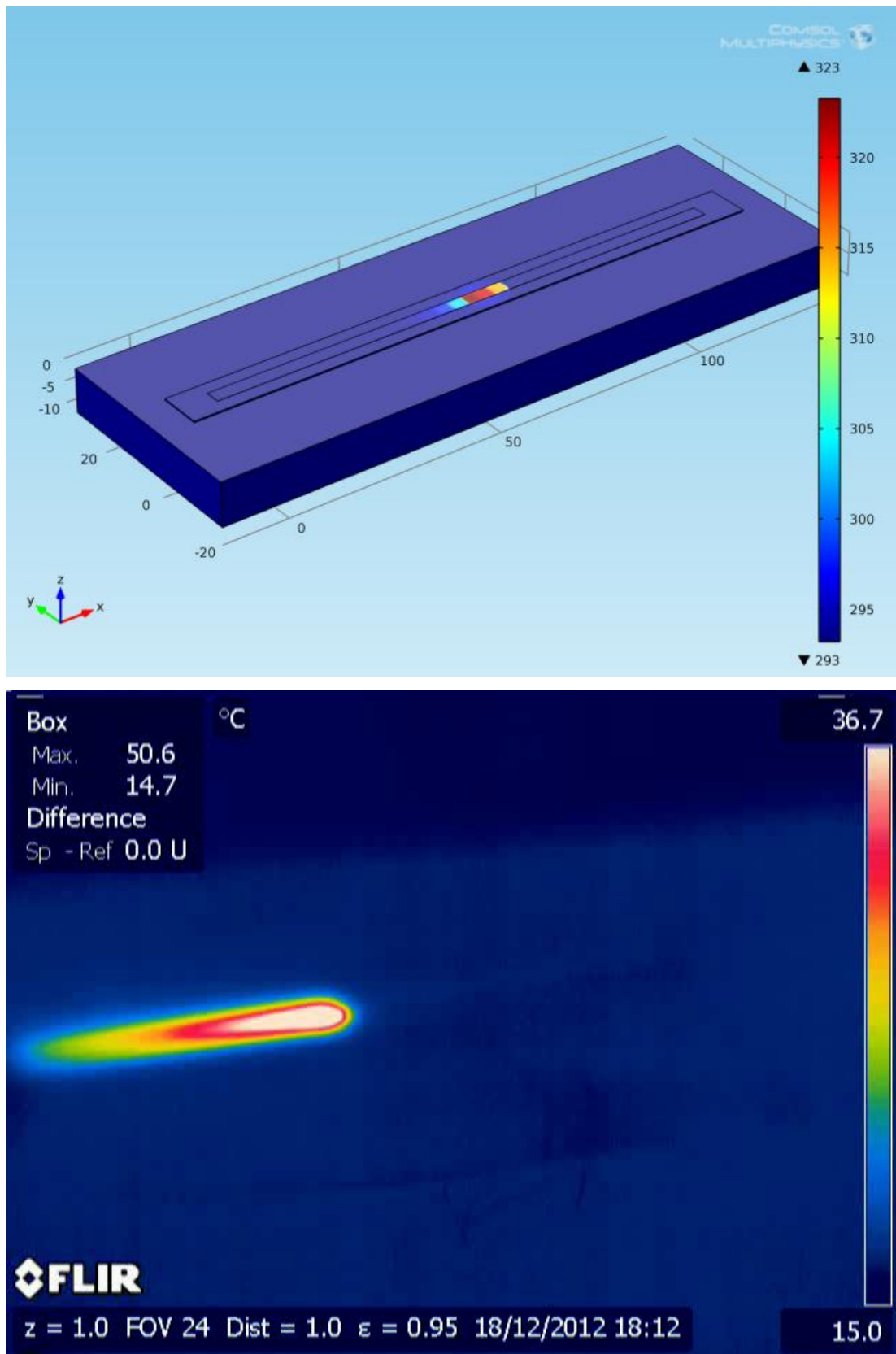


Figure 6.15: The comparison of thermal field constructed and simulated from FE modelling results (top, in Kelvin - K) and the thermal data recorded by an IR camera in experiment (bottom, in degree Celsius - °C) for D58 silver ink track in 532nm laser curing process at 3.86W, 5mm/s.

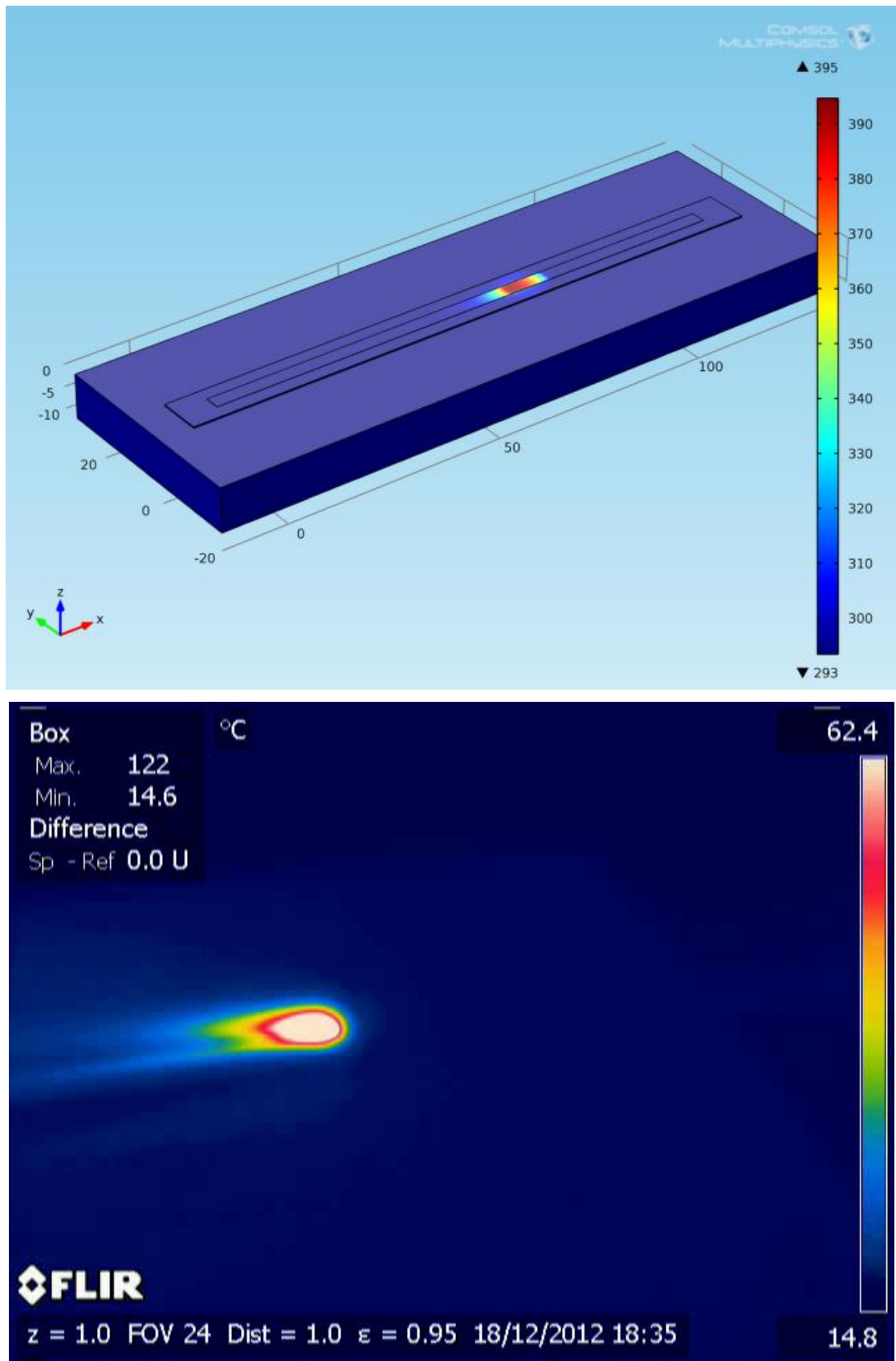
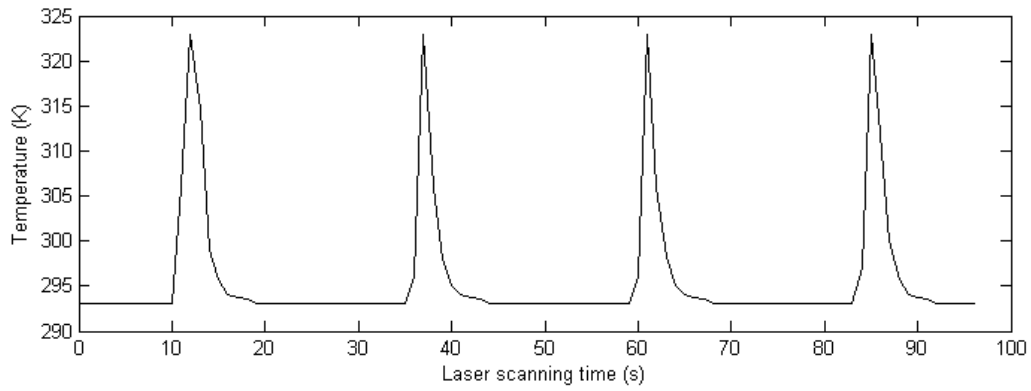
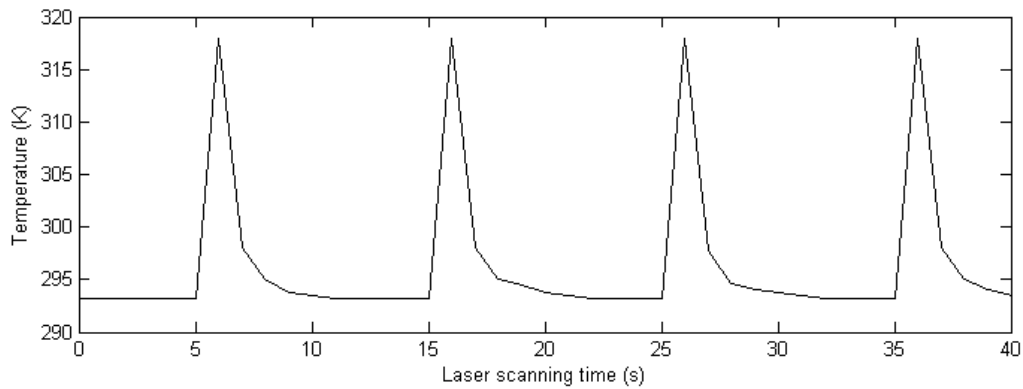


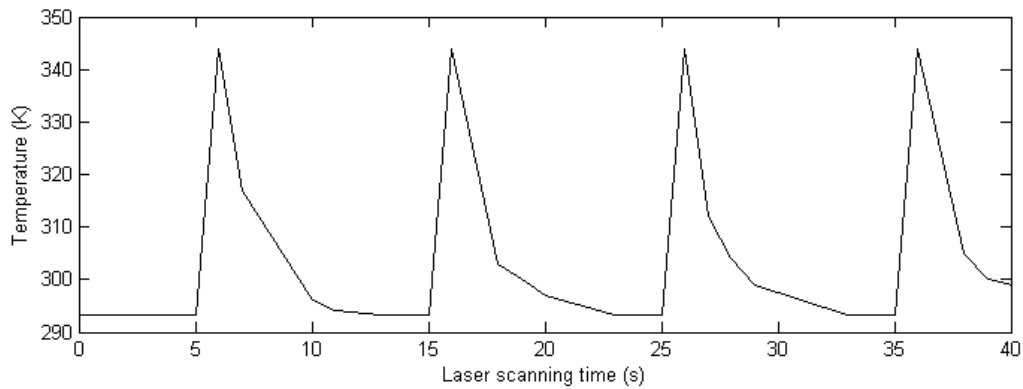
Figure 6.16: The comparison of thermal field constructed and simulated from FE modelling results (top, in Kelvin - K) and the thermal data recorded by an IR camera in experiment (bottom, in degree Celsius - °C) for D58 silver ink track in 532nm laser curing process at 17.94W, 5mm/s.



$P=3.86\text{ W } V=5\text{ mm/s}$

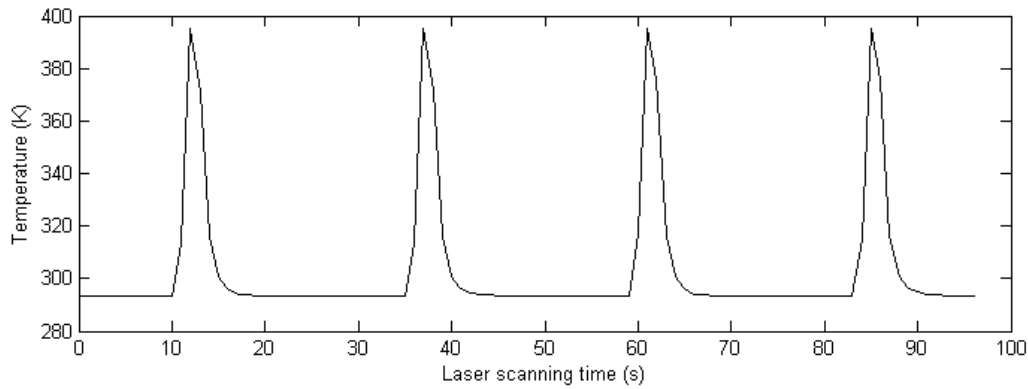


$P=3.86\text{ W } V=12\text{ mm/s}$

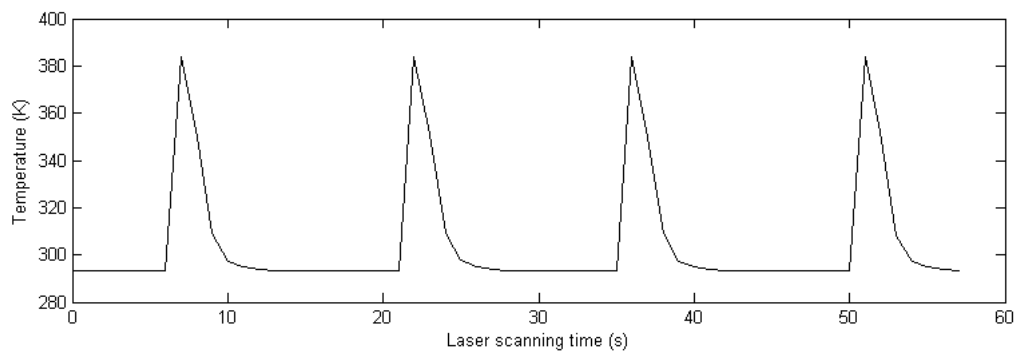


$P=10.95\text{ W } V=12\text{ mm/s}$

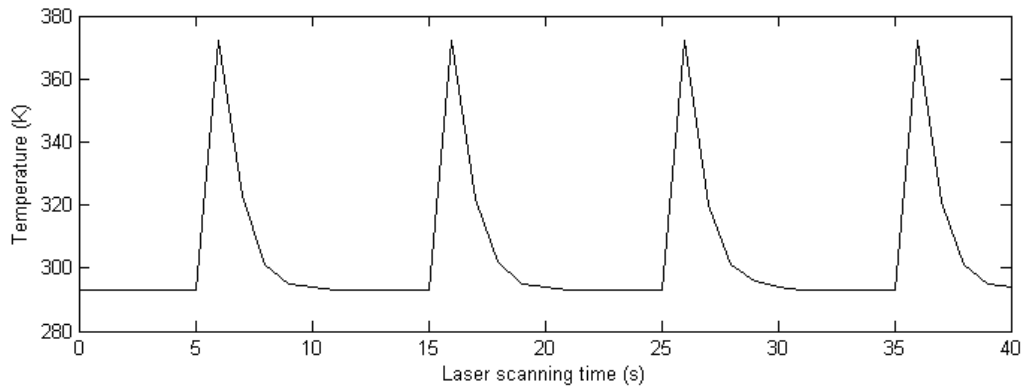
Figure 6.17: Temperature (in Kelvin - K) evolution result in the middle position of the ink track from the FE model for 532nm laser curing the D58 epoxy-based silver ink over the processing time of 4 passes.



P=17.94 W V=5 mm/s



P=3.86 W V=8.33 mm/s



P=17.94 W V=12 mm/s

Figure 6.18: Temperature (in Kelvin - K) evolution result in the middle position of the ink track from the FE model for 532nm laser curing the D58 epoxy-based silver ink over the processing time of 4 passes.

The thermal images from an IR camera as shown in **Figures 6.11-6.16** were taken without the calibration to the emissivity of D58 epoxy-based silver ink, therefore the temperature readings from thermal images need to be corrected. The procedure of correcting the temperature reading has previously discussed in **Chapter 3**, and the revised temperature T_2 has been mathematically defined in **(3-14)**.

$$T_2 = \sqrt[4]{\frac{\varepsilon_1}{\varepsilon_2}} T_1 \quad (3-14)$$

Where:

ε_1 = emissivity value of initial setting (default value, here $\varepsilon_1 = 0.95$);

T_1 = inaccurate temperature reading based on fault value of ε_1 ;

ε_2 = calibrated emissivity value after IR camera emissivity calibration (here, for D58 silver ink, $\varepsilon_2 = 0.66$);

T_2 = revised temperature reading.

The revised temperatures of thermal images can therefore be compared to thermal fields modelled by a FE model, as seen in **Table 6.7**. The curing temperatures modelled from the FE model fit well to the experimental results (**Figure 6.19**). In addition, for temperature fields modelled from the FE model, as shown in **Figure 6.19**, the change in laser working parameters can result in different corresponding curing temperature, this fits well with the experimental result as previously discussed in **Chapter 4**, indicating a good level of FE model validation.

Table 6.7: Curing temperature comparison between modelling results and experimental data.

Laser Power (W)	Scanning Speed (mm/s)	Temperature Recorded by IR Camera (°C)	Temperature Recorded by IR Camera (°C) [with revised emissivity]	Peak Temperature Simulated from FE Model (°C)
3.86	5.00	50.60	55.42	49.85
3.86	12.00	40.50	44.36	44.85
10.95	12.00	60.30	66.05	70.85
17.94	5.00	122.00	133.63	121.85
17.94	8.33	118.00	129.25	110.85
17.94	12.00	78.00	85.44	98.85

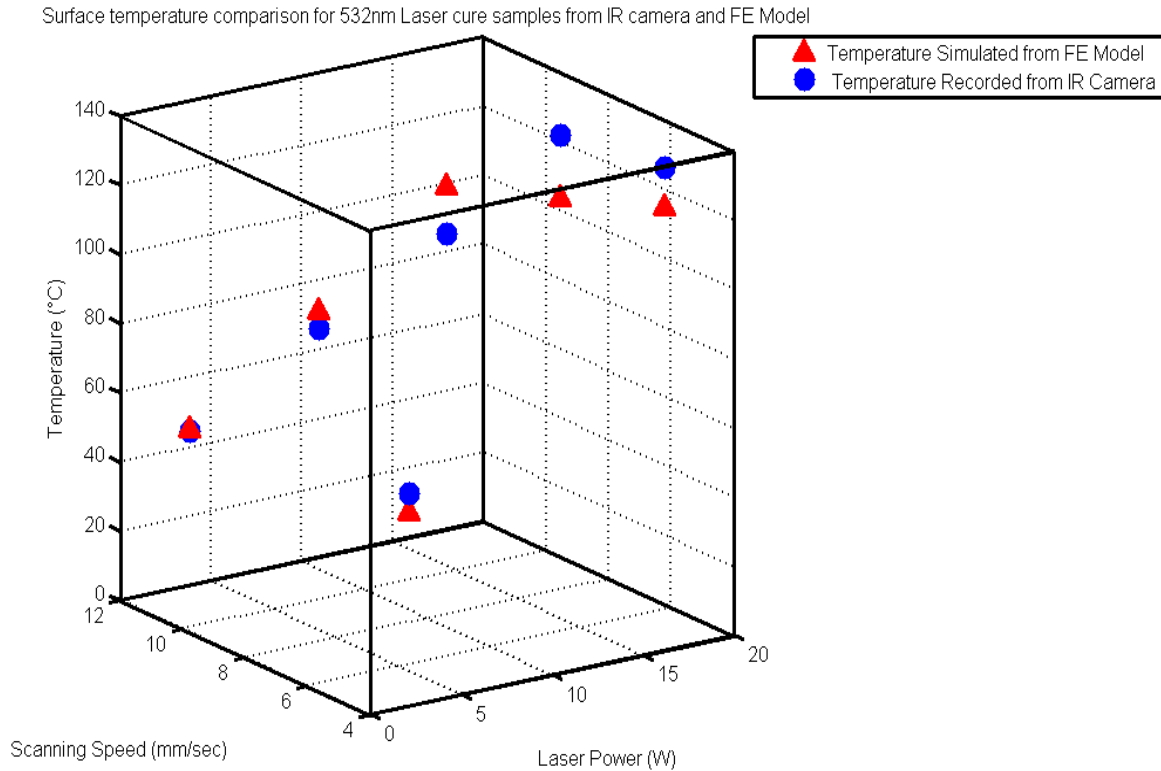


Figure 6.19: Curing temperature (°C) comparison between modelling results and experimental data.

6.6.2 Experiment and Mechanism Theory Verification

The FE model outputs can also be checked against previous experimental results and mechanism theories once the model has been validated in **section 6.6.1**, to see how well the theory and assumptions behind the FE model compare to the real laser processing environment. This can be achieved by comparing the material's physical properties such as the silver ink's electrical resistivity, etc. As discussed in **section 6.3** of this Chapter, the material's electrical resistivity can be derived from the FE model with the thermal field constructed.

Table 6.8: Laser working parameters as the input into the FE model.

Laser Power (W)	Scanning Speed (mm/s)
17.94	4.00
17.94	5.00
17.94	8.00
17.94	8.33
17.94	14.00

For the purpose of comparing electrical resistivity values of the epoxy-based silver ink, variant laser working parameters from the experimental data listed in **Chapter 4** are used as the input in modelling the 532nm laser curing process of D58 epoxy-based conductive silver ink (**Table 6.8**). **Figure 6.20-6.21** shows the temperature distribution for each laser scanning pass at the same position of the D58 epoxy-based silver ink track cured by a multiple pass laser curing process at 532nm. In the FE model, the ink's physical properties can be derived based on the temperature field modelled from the FE model. In this section, the electrical resistivity of D58 epoxy-based silver ink can be derived from thermal conductivity with equations (**3-1**), (**6-11**), and (**6-15**) based on the Wiedemann-Franz law (this has been discussed in **section 6.3.1.4**).

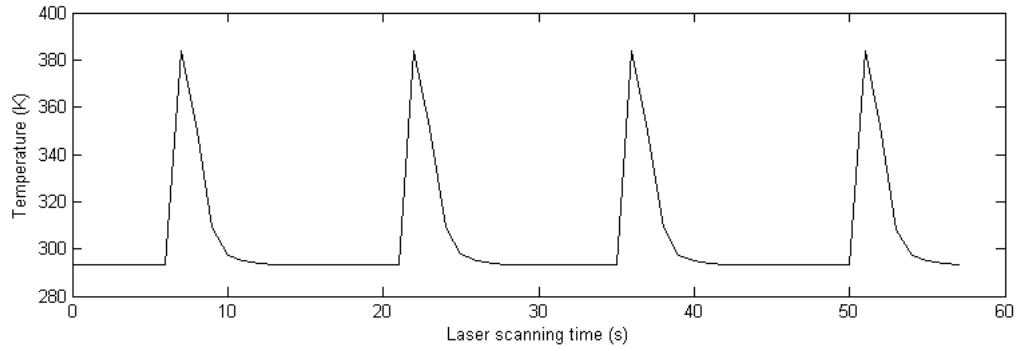
$$\sigma = \frac{1}{\rho} = \frac{\ell}{RA} \quad (3-1)$$

$$\frac{\kappa_{ink}}{\sigma_{ink}} = \frac{\kappa_{bulkAg}}{\sigma_{bulkAg}} = L \cdot T \quad (6-11)$$

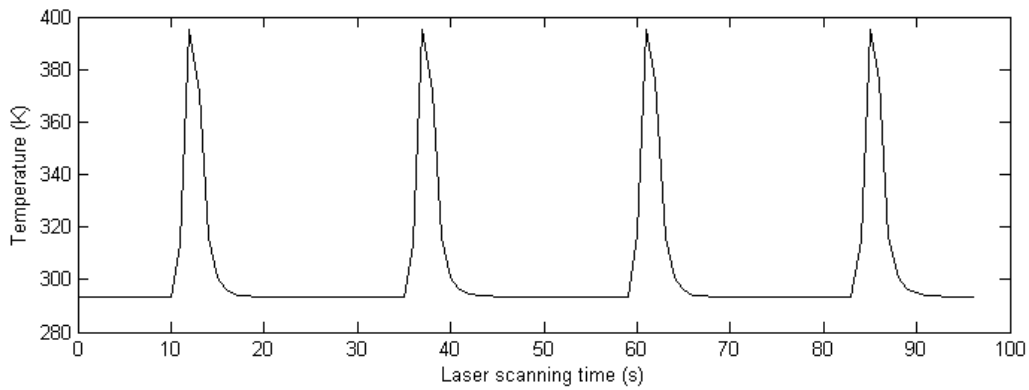
$$\rho_{ink} = \frac{\kappa_{bulkAg} \rho_{bulkAg}}{\kappa_{ink}} \quad (6-15)$$

Where:

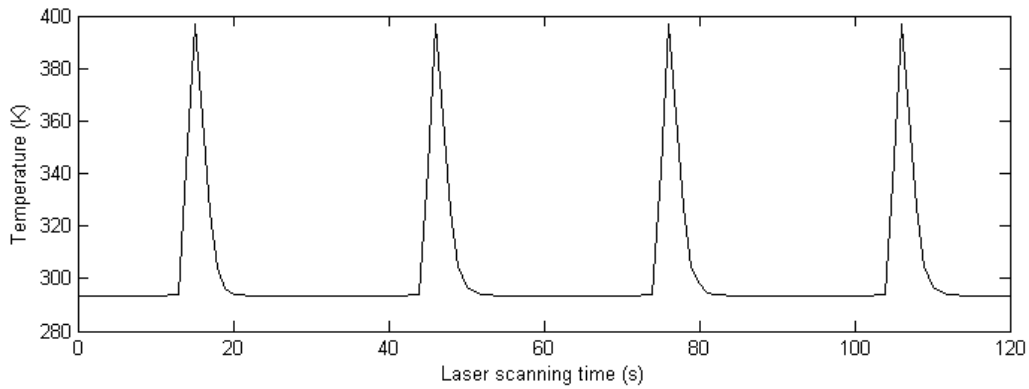
- σ = electrical conductivity of the material,
- ρ = electrical resistivity of the material,
- R = resistance,
- A = the cross-sectional area of the material,
- ℓ = the length of the material,
- κ = material's thermal conductivity,
- L = Lorenz number,
- T = temperature.



$P=17.94\text{ W } V=8.33\text{ mm/s}$

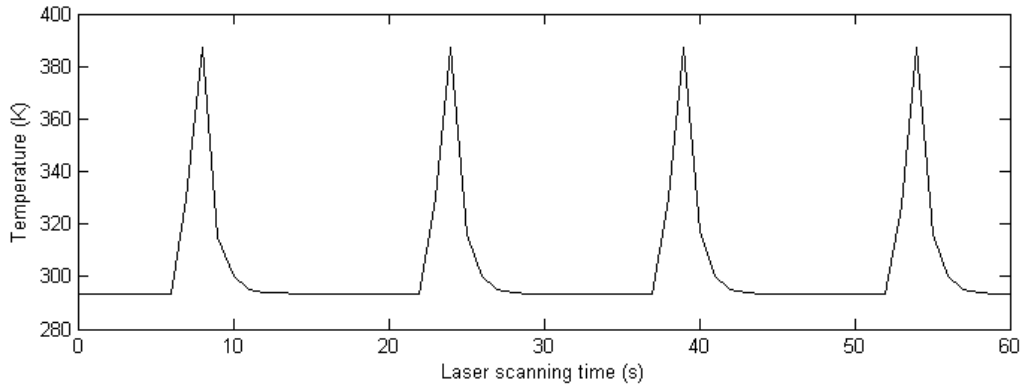


$P=17.94\text{ W } V=5\text{ mm/s}$

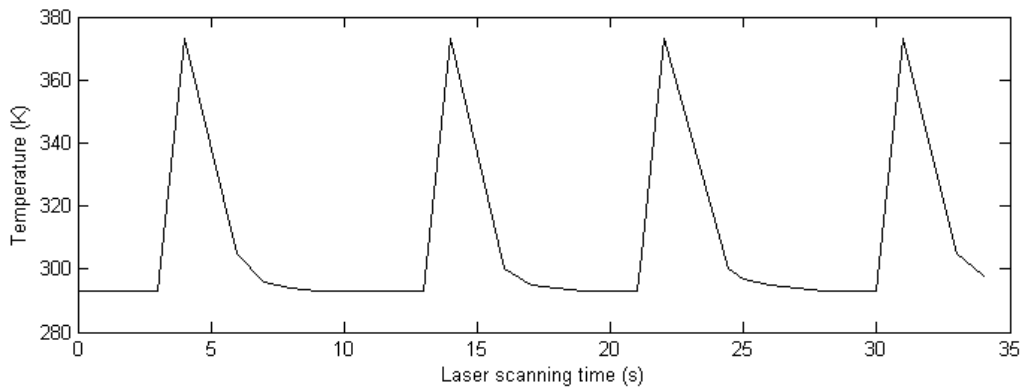


$P=17.94\text{ W } V=4\text{ mm/s}$

Figure 6.20: Modelling results of temperature (K) evolution in the middle of the ink track of the D58 epoxy-based silver ink over the laser scanning time for four scanning passes.



P=17.94 W V=8 mm/s



P=17.94 W V=14 mm/s

Figure 6.21: Modelling results of temperature (K) evolution in the middle of the ink track of the D58 epoxy-based silver ink over the laser scanning time for four scanning passes.

The electrical resistivity of D58 epoxy-based silver ink can be calculated based on equation (6.15), therefore the FE thermal conductivity modelling results with the associated derived electrical resistivity can be shown in **Table 6.9**.

Table 6.9: Derived electrical resistivity compares to experimental measurement.

Laser Power (W)	Scanning Speed (mm/s)	Peak Temperature Simulated from FE Model (°C)	Thermal Conductivity Simulated from FE Model (W/m*K)	Electrical Resistivity Converted from Simulated Thermal Conductivity (Ohm*m)	Electrical Resistivity Measured in Experiment (Ohm*m)
17.94	8.33	110.85	7.4	9.22E-07	3.55E-07
17.94	5	121.85	14.1	4.84E-07	3.55E-07
17.94	4	123.85	15.5	4.40E-07	1.55E-06
17.94	8	113.85	9.7	7.03E-07	7.93E-07
17.94	14	99.85	0.8	8.53E-06	5.33E-06

As shown in **Figure 6.22**, with a constant laser output power at 17.94 Watts, the electrical resistivities derived from the FE model (red triangles) decreased with a

reducing laser scanning speed, this fits well with the experiment result (blue squares). However in a real laser curing experiment, as discussed in **Chapter 4**, a too slow laser scanning speed can result in potential damage to the ink track, which would therefore increase the value of electrical resistivity (the blue square with laser scanning speed at 4mm/s).

Electrical resistivity comparison for 532nm Laser cure samples from experimental result and from FE Modelling (Power=17.94 Watts)

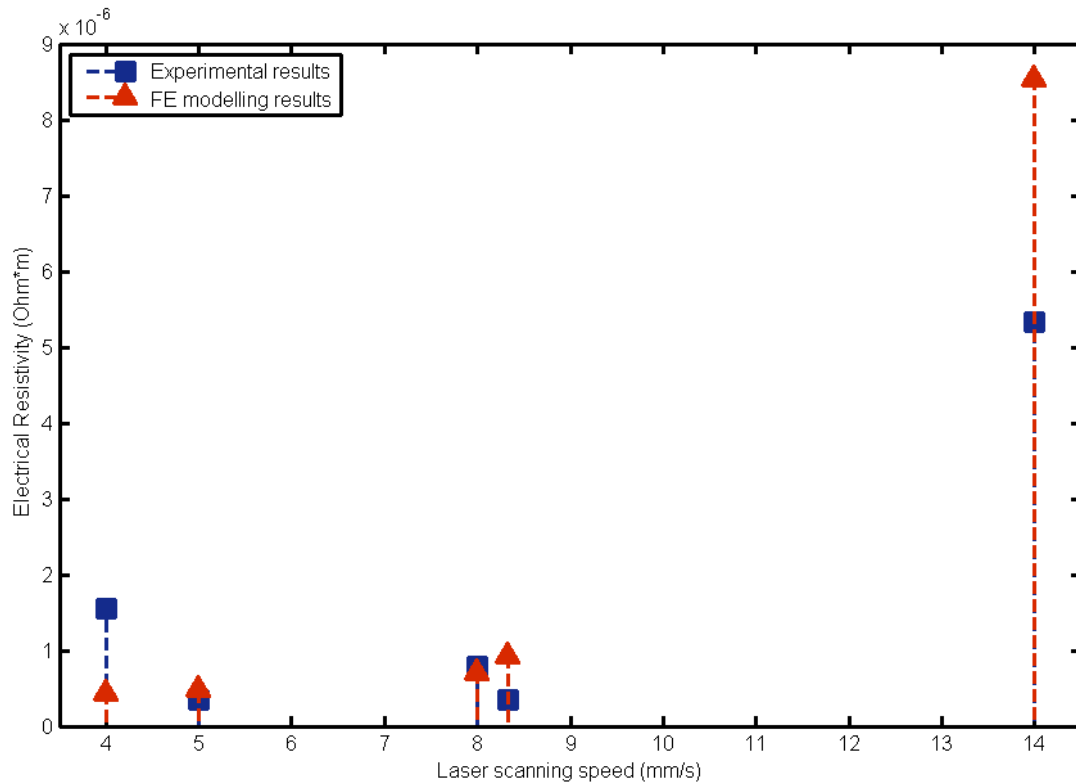


Figure 6.22: Electrical resistivity comparison between derived data from the FE model and the experimental measurement.

In addition, **Figures 6.20-6.21** agreed with the 532nm laser curing mechanism theory discussed in **Chapter 5**. The liquid solvent component within the ink system is removed from the ink in directions towards to both sides of the ink track and ahead of the laser beam in area of the laser irradiation due to the Marangoni effect leading the laser beam irradiation. This can cause a reduction in the overall ink's specific heat capacity, and increasing the coupled temperature. This can be observed in FE modelling results, as shown in **Figures 6.20-6.21**, where the peak temperature of the temperature distribution in the first pass has already reached to the same level of that in following passes, due to the reduction in overall specific

heat of the ink system as solvent was removed due to the Marangoni effect in the first pass. **Figure 6.23** shows an example of thermal field modelling of 532nm laser curing D58 epoxy-based ink from the FE model. The area that surrounds the laser beam is cooler than the central area of the laser beam, causing the Marangoni effect in the area of the laser irradiation (ahead and at both sides of the ink track), wherein the liquid solvent component is removed towards to edges of the ink track as well as ahead of the laser beam in the area of laser irradiation. This fits well to the 532nm laser curing mechanism theory as discussed in **Chapter 5**.

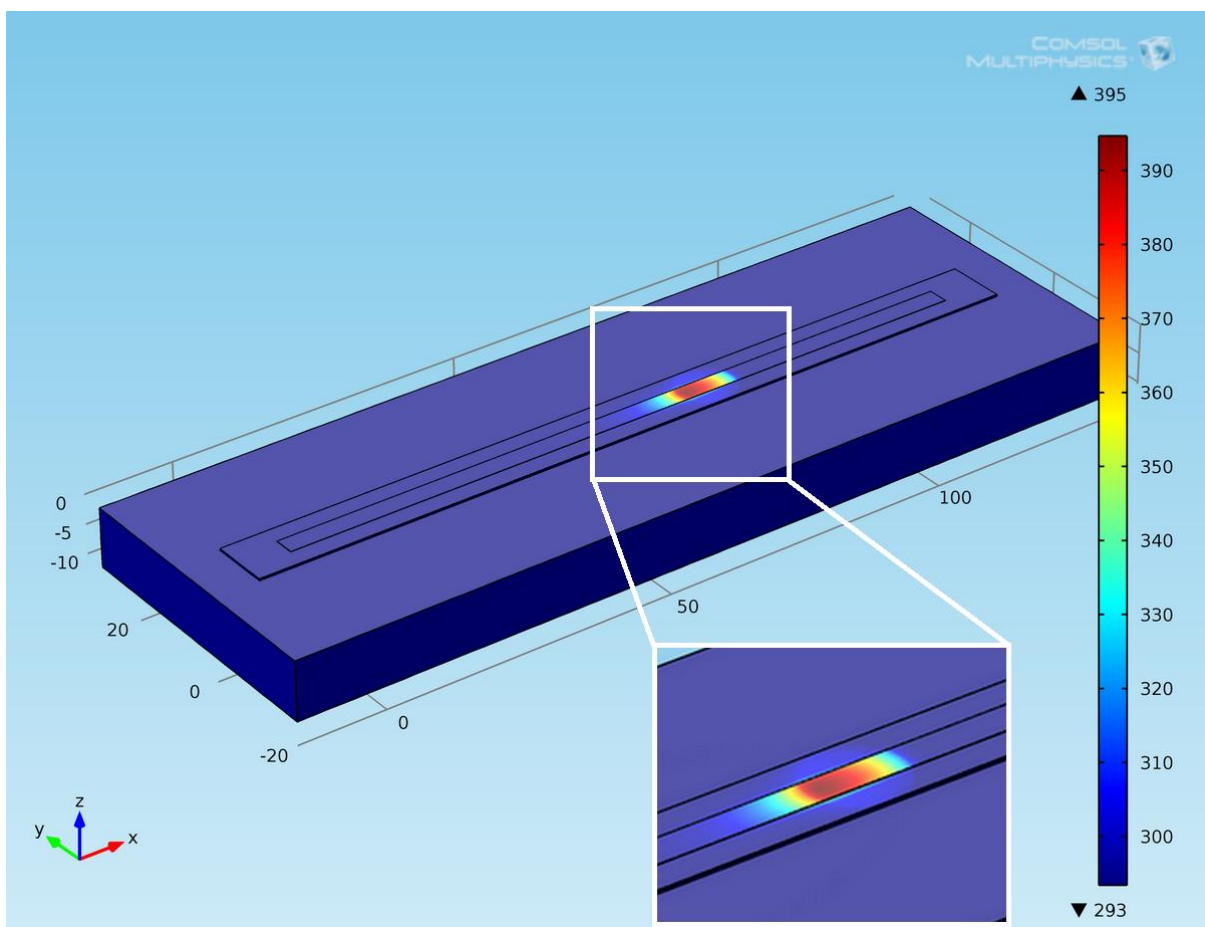
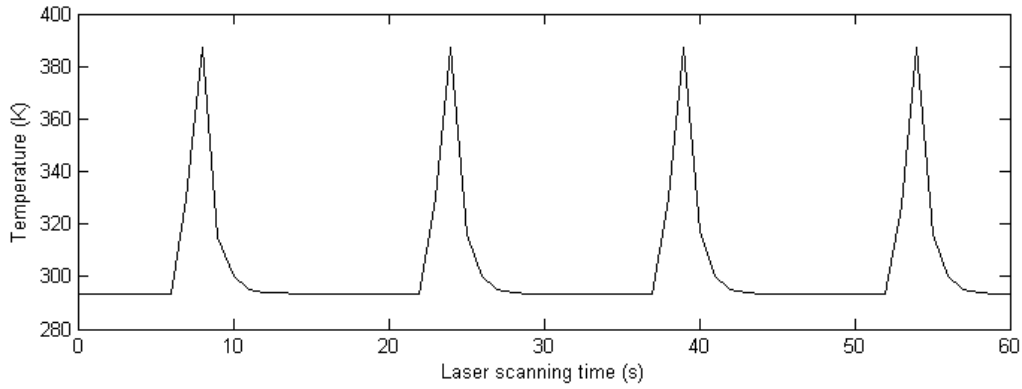


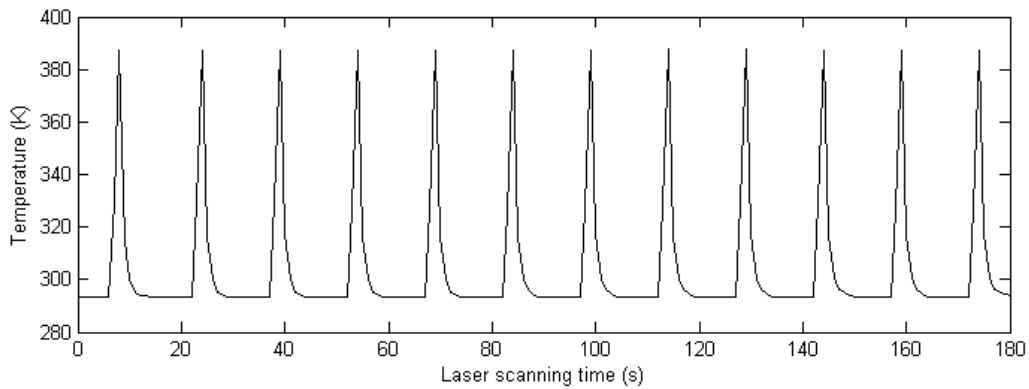
Figure 6.23: An example of the thermal field (in Kelvin) modelled from the FE model of 532nm laser curing of a D58 epoxy-based silver ink track with the laser output power at 17.94W, and the laser traverse speed at 5mm/s. This shows the temperature distribution surrounding the laser beam. The cooler temperature surrounding the laser beam can result in the Marangoni effect removing the liquid solvent component out of the ink system towards both sides of the ink track and ahead of the laser beam prior to the laser beam irradiation, which fits well to the mechanism theories discussed in **Chapter 5**.

Despite the fact that the FE model can successfully predict the thermal field associated with D58 epoxy-based silver ink in a laser curing process at the

wavelength of 532nm, this FE model has a limitation. To review, in a 532nm laser curing process, the selection of the laser power and laser traverse speed results in an associated curing temperature. This associated curing temperature can help to remove the solvent in area of laser beam irradiation due to the Marangoni effect leading the laser beam irradiation area. When the associated temperature heats up the silver ink to above the BI unblocking temperature at $\sim 90^{\circ}\text{C}$, the resin chemical cross-linking process takes place. Repeating the laser beam irradiation process pass by pass, cross-links the resin more gradually allowing the silver flakes to bind closely to each other, a process which makes the silver ink electrically conductive. As seen in **Figure 6.24**, the thermal field and associated temperature evolution can be successfully predicted from the FE model for curing a D58 epoxy-based silver ink with laser power at 17.94 W, and the laser traverse speed at 8 mm/s. However, in a real curing environment (as discussed in **Chapter 4**), curing a D58 epoxy-based silver ink of these laser processing parameters needs 12 passes to obtain an optimized curing result. Therefore despite the FE model's successful prediction of the thermal field, further improvements of this FE model are needed to predict the optimized number of scanning passes in a repeating pass laser curing process.



P=17.94 W V=8 mm/s for 4 scanning passes



P=17.94 W V=8 mm/s for 12 scanning passes

Figure 6.24: Temperature (K) evolution graphs in the middle of the ink track for a repeating 532nm laser curing process in this FE model can only predict the thermal field property, it needs improvement to predict the optimized number of scanning passes to suggest a fully cured situation.

6.6.3 How Curing Results Are Affected by A Change in Laser Absorbance of the Epoxy-based Silver Ink

The study of laser curing mechanisms has been limited here to the investigation of D58 epoxy-based conductive silver ink - this ink has three fundamental components: silver flakes, resin complex, and organic solvent (for silver ink composition please refer to **Chapter 3**). There is an increasing demand in printed electronic applications for inks with an increased electrical conductivity, therefore the ink physical properties could in principle be modified and optimised in the FE study.

In **Chapter 5**, an increased curing efficiency was shown by increasing the silver flakes' concentration in the ink system, or by adding an optically absorbing dopant such as carbon or graphite particles to the ink. To simulate the effects of this, the overall absorbance of the ink to laser induced energy can be simulated in this FE study.

FE modelling can assist this type of investigation by changing the laser induced energy absorbance of the silver ink in model settings. As an example, two assumptions are made and compared to the existing curing result with initial absorbance set at 0.29 to 532nm laser energy for standard D58 epoxy-based silver ink (**Table 6.10**).

Table 6.10: Assumptions for different ink compositions as the input to the FE model.

Initial absorbance of D58 silver ink to laser energy at 532nm (293.15K)	0.29
Assumption 1 (absorbance at 293.15K)	0.52
Assumption 2 (absorbance at 293.15K)	0.61

Figure 6.25 shows the thermal field modelled for 532nm laser curing the original D58 epoxy-based ink with initial absorbance to laser irradiation at 0.29, this D58 silver ink was cured with laser output power at 12.972 Watts, and with a traverse speed at 8mm/s. The surface temperature was modelled as at around 368K (~95 °C).

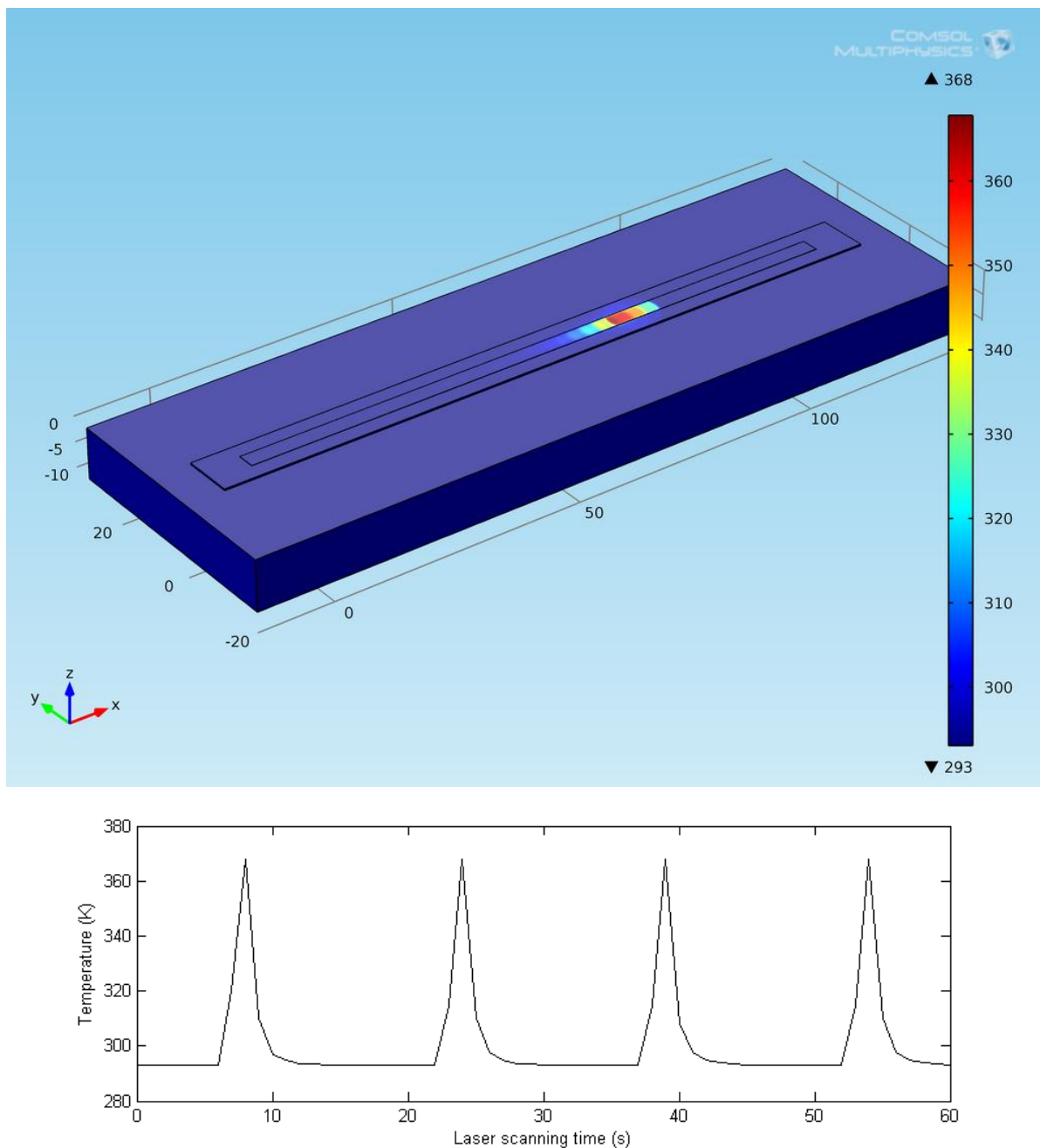


Figure 6.25: Thermal field modelled (top, in Kelvin - K) and the temperature evolution graph in the middle of the ink track of the laser curing process (bottom, in Kelvin - K) for 4 passes from the FE model for initial D58 silver ink (Laser power=12.972W, scanning speed=8mm/s).

For *Assumption 1* defined in **Table 6.10**, by increasing the absorption of the ink, the curing temperature can be significantly increased ($\sim 130^{\circ}\text{C}$), so that more thermal energy from laser irradiation could be coupled into the ink to assist the resin chemical cross-linking process in ink (**Figure 6.26**). Further increase in absorbance to laser energy, as defined in *Assumption 2*, can also therefore further increase the

curing temperature ($\sim 150^{\circ}\text{C}$), which can speed up the resin cross-linking more quickly, as shown in **Figure 6.27**.

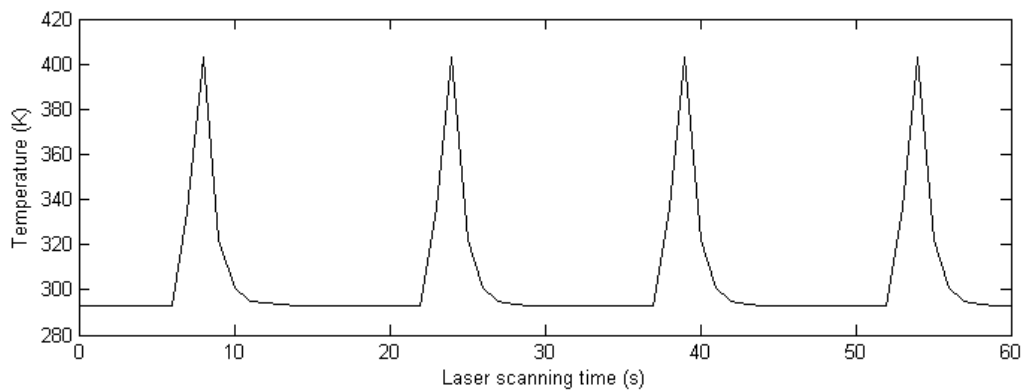
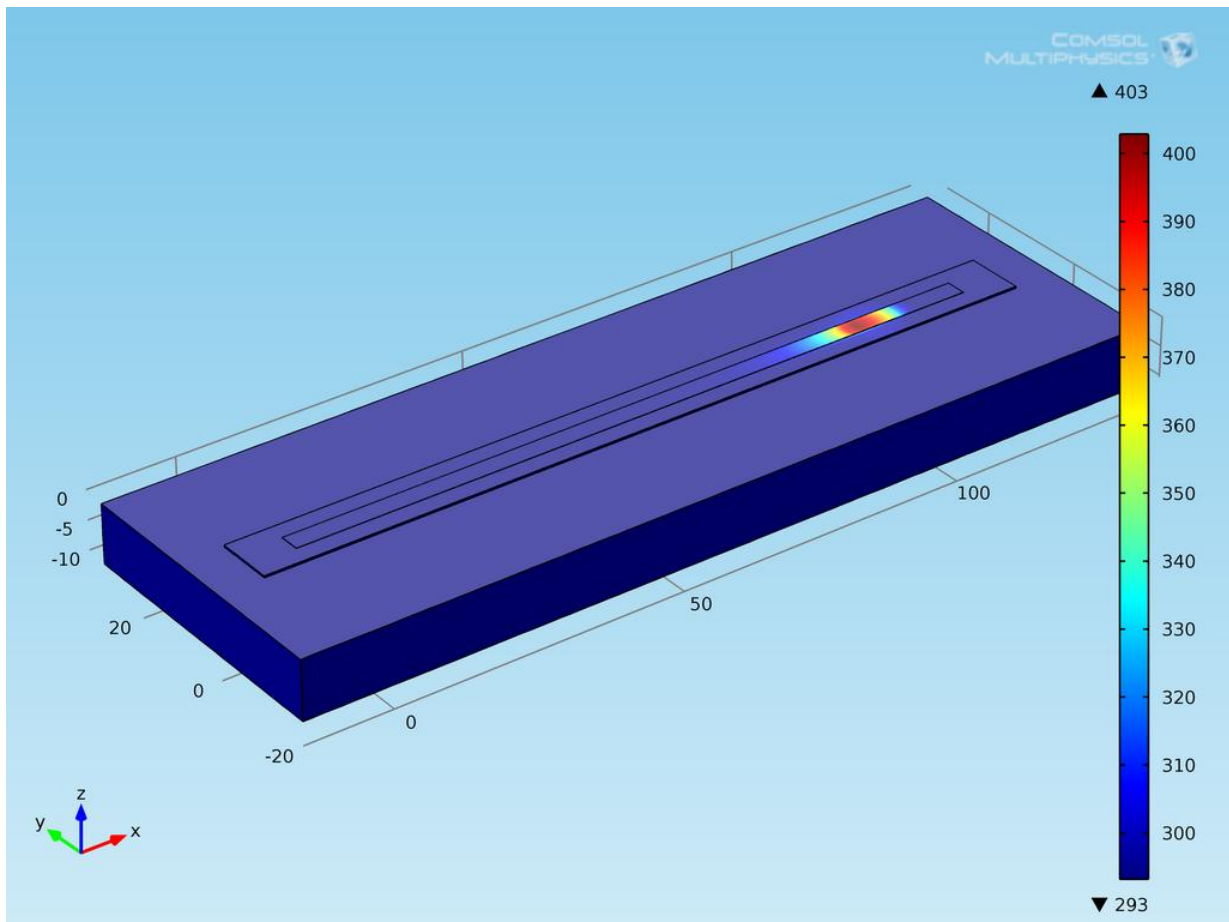


Figure 6.26: Thermal field (top, in Kelvin - K) and the temperature evolution graph in the middle of the ink track of the laser curing process (bottom, in Kelvin - K) for 4 passes modelled from the FE model for silver ink with absorbance to laser energy at 0.52.

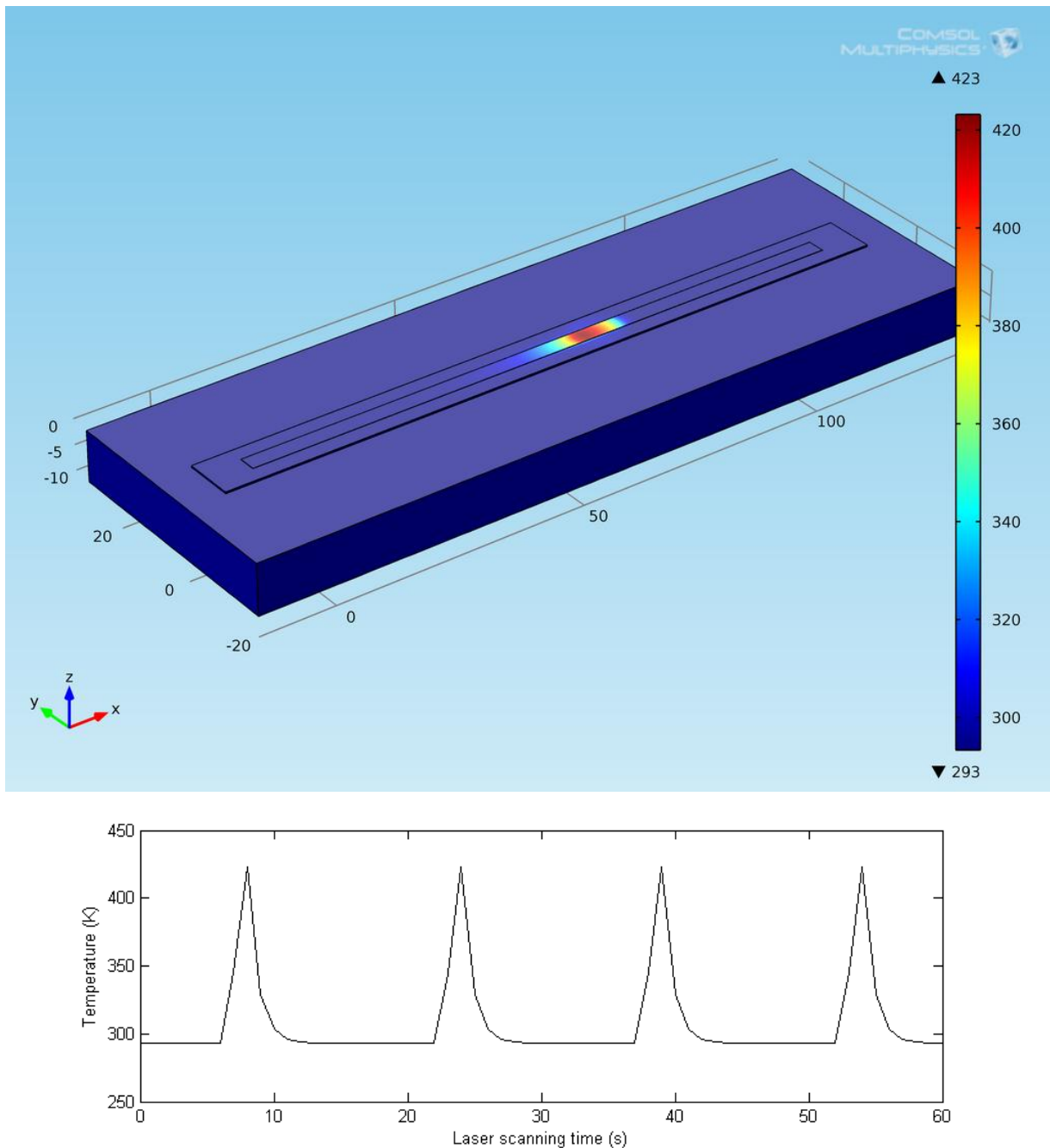


Figure 6.27: Thermal field (top, in Kelvin - K) and the temperature evolution graph in the middle of the ink track of the laser curing process (bottom, in Kelvin - K) for 4 passes modelled from the FE model for silver ink with absorbance to laser energy at 0.61.

The electrical resistivity predicted by the FE model can be derived from equations **(3.10-3.12)**. As shown in **Table 6.11**, where the electrical resistivities derived from the FE model have significantly reduced with increased absorbance to laser energy at 532nm. In this FE modelling result, the electrical resistivity of the silver ink has reduced from $1.71\text{E-}5 \text{ Ohm}\cdot\text{m}$ to $3.55\text{E-}7 \text{ Ohm}\cdot\text{m}$.

Table 6.11: Electrical resistivity comparison for modelled results with different absorbance to laser energy.

	Laser Power (W)	Scanning Speed (mm/s)	Temperature Simulated from FE Model (°C)	Thermal Conductivity Simulated from FE Model (W/m*K)	Electrical Resistivity Converted from Simulated Thermal Conductivity (Ohm*m)
D58 default	12.97	8	94.85	0.40	1.71E-05
Assumption 1	12.97	8	129.85	19.20	3.55E-07
Assumption 2	12.97	8	149.85	19.20	3.55E-07

Therefore increasing the overall absorption of the silver ink by increasing the concentration of silver content, or by adding carbon or graphite particles to the ink composition, can significantly improve the curing quality with reduced electrical resistivity and reduced processing time.

An example of showing improved curing qualities by increasing the curing efficiency can be seen in **Figure 6.28**. As seen in **Figure 6.28**, an increased electrical conductivity of the epoxy based silver ink with a significantly reduced laser energy input that to cure the ink can be achieved by (i) increasing the silver content, or (ii) adding the optical absorbing agent or dopant, or (iii) increasing the overall laser energy absorption of the ink system.

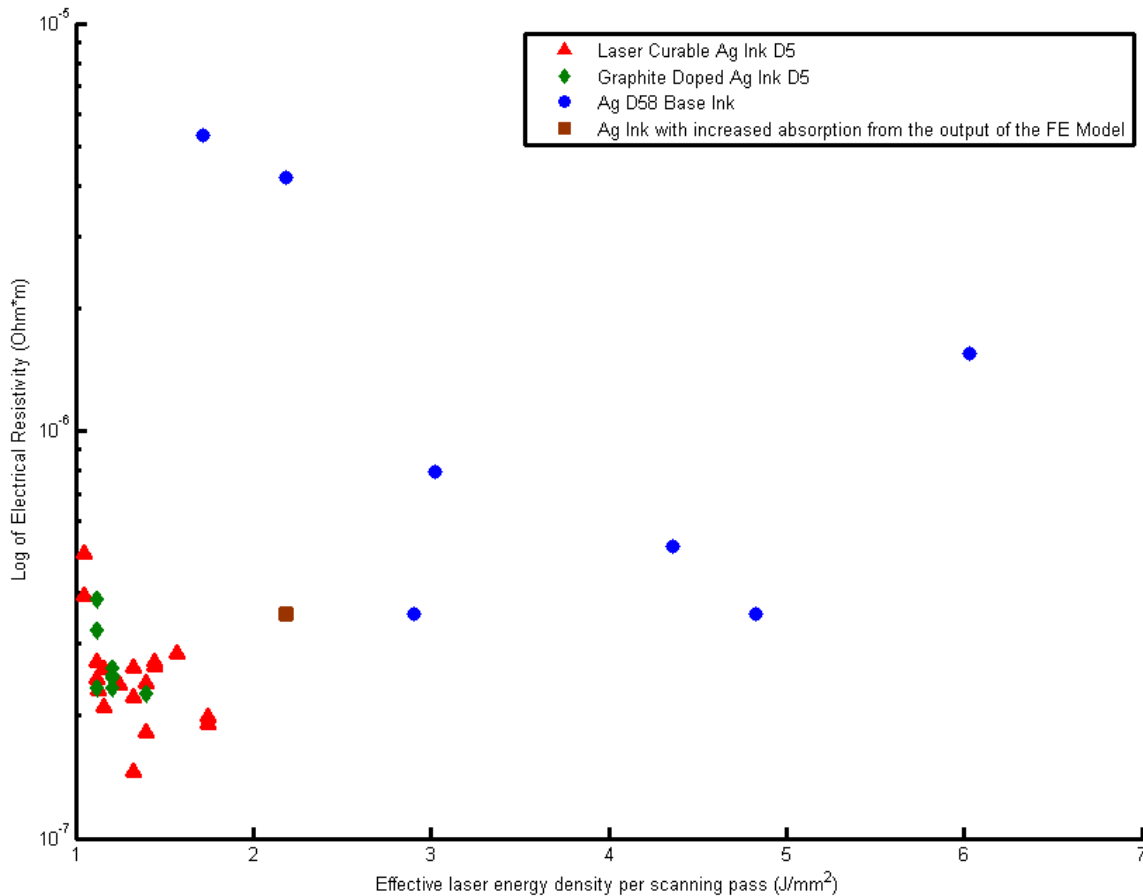


Figure 6.28: Comparison of electrical resistivities of epoxy based silver inks discussed in this thesis to the output from the FE model (this graph is reproduced based on experimental results presented in **Chapter 4**). As can be seen from this figure, the curing efficiency of the epoxy based silver ink can be significantly increased by (i) increasing the silver content (*Laser curable Ag ink D5*), or (ii) adding the optical absorbing agent (*Graphite doped Ag ink D5*), or (iii) increasing the overall absorption to laser energy (*Ag ink modelled in the FE model*).

6.7 Chapter Summary

In this Chapter, mathematical equations were developed representing temperature-dependent physical properties of an industrially relevant silver ink, including thermal conductivity, density, laser energy absorbance, and specific heat capacity. These were built into a finite element (FE) model for simulations, the results of which were used to predict the thermal fields associated with 532nm laser irradiation. Modelling and experimental results were compared and discussed, the FE model was validated and tested against assumptions that the inks' overall absorption changes dynamically during the curing process. It is hoped that these results will benefit further developments to improve laser-based curing technology.

7. CONCLUSIONS AND RECOMMENDATIONS

7.1 Summary of Results of the Investigation and Contributions of New Knowledge

This thesis is motivated by the rapid developments of printed electronics applications in recent years and for which new process technologies are needed that are greener, quicker and better than the the chemical etching process currently used in the PCB industry. This research is also motivated by the progress in research of processes that cure and/or sinter metal particulate inks worldwide, as well as previous laser based direct write research carried out at the University of Liverpool. The aim of this research is to develop new laser based curing methods and to improve knowledge of key mechanisms to enable a quicker ink curing process without damaging the substrate material.

In this research, a commercial electronics printing material – the D58 epoxy-based conductive silver microparticle ink - was chosen and used in this investigation as an industry standard material for a high electrical conductivity after cure. Various compositions of the silver flake, resin complex and organic solvent components were used in order to simplify the approach to understanding the key process mechanisms and identifying a suitable process parameter operating window. Other silver inks with various ink compositions were also investigated, including epoxy-based silver ink with higher silver concentration, and epoxy-based silver ink with optically absorbing agent doped in such as the graphite doped epoxy-based silver ink described.

Curing results for curing epoxy-based silver inks on a PET substrate in three different curing processes were compared (they are: a conventional oven curing process, a 10.6 μm CO₂ laser curing process, and a 532nm frequency doubled Nd:YAG laser curing process). The result showed the best curing quality were achieved by using a frequency doubled Nd:YAG laser at 532nm with multiple laser scanning passes. The

532nm laser based localized heating process resulted in an increased electrical conductivity of silver inks and a reduced thermal impact to the polymer substrate material.

A new curing mechanism for Nd:YAG laser curing of the epoxy-based conductive silver ink at the laser wavelength of 532nm was developed. Based on experimental results, the mechanism proposed comprised steps where the laser induced energy was absorbed primarily by silver flakes as a result of the photothermal effect (enhanced by the Geometric scattering and multiple internal reflections of the laser beam among silver flakes within the ink), causing a temperature rise in the local volume of the ink track. This controllable rise in local temperature assisted solvent transport ahead and aside of the ink in the area of the laser irradiation through the Marangoni effect. The loss of solvent caused an overall change in the ink's composition, leading to a reduction in the specific heat capacity of the ink. Further temperature rise then unblocked the Blocked Isocyanate (BI) components of the ink which promoted the chemical cross-linking reactions with the epoxy resin. Once the resin was cross-linked, a silver cluster was formed which caused the cured ink to be electrically conductive.

A new thermal model as a function of total energy input in Nd:YAG laser curing of the epoxy-based silver ink at 532nm with multiple laser scanning passes was constructed based on the study of laser curing mechanism theories. The latent heat for solvent evaporation could be ignored, since liquid solvents were removed from the ink in area of the laser irradiation due to the Marangoni effect in advance of the laser beam irradiation. The overall energy equation for the epoxy-based silver ink were rewritten based on this new thermal process, and physical properties of the epoxy-based silver ink were mathematically defined based on the predicted changes in ink compositions as a result of this process.

A finite element (FE) method was employed to model the thermal field of a 532nm laser curing process with multiple passes used to cure an epoxy-based silver ink (D58) printed on a PET polymer substrate. Temperature dependent parameters of

D58 epoxy-based silver ink were mathematically defined and used as the input of the model, and the thermal field of the modelling results were compared to those recorded by an IR camera during experiment. The FE model was well validated as modelling results showed a good fit to the experimental measurement; and a relationship between laser energy coupled into the ink material, and the curing quality was formulated. Electrical resistivities of D58 epoxy-based conductive silver ink made in experiment were also predicted by the FE model. The results from the FE model agreed well with the experiment and supported the proposed mechanism theory of 532nm laser curing process. A further investigation of the FE model was then carried out indicating that by adjusting the laser energy absorption in the epoxy-based silver ink, improved curing qualities could be obtained. It is hoped that this could benefit the electronic printing industry by opening up the developing of new 'laser-ready' silver inks with an improved composition ratio or silver inks with appropriate dopants to increase the overall energy absorption efficiency for a better and quicker curing result.

7.2 Recommendations for Further Investigation

- This investigation developed and studied a new laser-based curing technology; however, further development in knowledge on the mathematical approximation to dynamically change-in-silver ink's composition with induced laser energy is still needed for an accurate and smooth approximation to replace the assumptions made in **Chapter 6**.
- The FE model discussed in **Chapter 6** has a high level of agreement with experiment in predicting the thermal field properties of the epoxy-based silver ink in a repeating 532nm laser curing process; however, further improvements are needed to predict the optimal number of laser scanning passes in this FE model to achieve a fully cured situation based on the 532nm laser curing mechanism theories discussed in **Chapter 5**.

- This investigation has solely concentrated on thermal curing an epoxy-based silver ink with silver micro-sized flakes. There is a great potential for further investigations to understand how silver flake/particle size and morphology affects the laser curing result.
- Further investigations into laser curing the epoxy-based conductive silver ink could extend to laser beam irradiations with wavelength at around 450nm, where the results indicate silver will absorb the laser radiation more strongly without interacting with the PET polymer substrate (in **Figure 2.47-2.49**). Also, based on the studies carried out and results obtained, laser curing the epoxy-based silver ink at 450nm should significantly increase the overall curing efficiency. However, the process benefits that might accrue from using 450nm light may be offset by the technical challenges and costs of producing lasers with an output at this wavelength.
- This method developed in this thesis for curing epoxy-based silver ink offers a more environmentally friendly alternative to existing etching processes and a quicker method than oven curing to produce electrical circuitry, but further investigation into raising the technology readiness level of this process to commercially viable throughput rates would be needed to realise these environmental and energy benefits.

References

- [1.1] Pique, A. and Chrisey, D.B. (2002) *Direct-Write Technologies for Rapid Prototyping Applications: Sensors, Electronics, and Integrated Power Sources*, San Diego: Academic Press.
- [1.2] Hon, K.K.B., Li, L. and Hutchings, I.M. (2008) 'Direct writing technology-Advances and developments', *CIRP Annals – Manufacturing Technology*, 57(2), pp. 601-620.
- [1.3] Fearon, E., Sato, T., Wellburn, D., Watkins, K.G. and Dearden, G. (2007) 'Thermal effects of substrate materials used in the laser curing of particulate silver inks', *Proceedings of the International Conference on Laser Assisted Net Shape Engineering 5*, Meisenbach Bamberg, Germany pp. 379-390
- [1.4] Khandpur, R.S. (2006) *Printed Circuit Boards: Design, Fabrication and Assembly* : The McGraw-Hill Companies, Inc.
- [1.5] United States Environmental Protection Agency. (1990) *Guides to Pollution Prevention: The Printed Circuit Board Manufacturing Industry*: EPA.
- [1.6] Sato, T., Fearon, E., Curran, C., Watkins, K.G., Dearden, G. and Eckford, D. (2009) 'Laser-assisted Direct Write for aerospace applications', *Proc. IMechE Part G: Journal of Aerospace Engineering*, 224(4), pp. 519-526.
- [1.7] Bass, M., and Van Stryland, E. W. (1994) *Handbook of Optics*, 2nd edn., New York: McGraw-Hill.
- [2.1] Vaezi, M., Chianrabutra, S., Mellor, B., Yang, S. (2013) 'Multiple Material Additive Manufacturing -Part1: A review', *Virtual and Physical Prototyping*, 8(1), pp. 19-50.
- [2.2] Pique, A., Pratap, B., Mathews, S., Karns., B., Auyeung, R.C., Kasser, M., Ollinger, M., Kim, H., Lakeou, S and Arnold, C.B. (2005) 'Laser Direct-Write of Embedded Electronic Components and Circuits', *Proc. SPIE 5713, Photon Processing in Microelectronics and Photonics IV*, 223.
- [2.3] Rida, A., Yang, L., Vyas, R., Nasay, S., Bhattacharya, S.K. and Tentzeris, M.M. (2007) 'Novel Manufacturing Processes for Ultra-Low-Cost Paper-based RFID Tags with enhanced "wireless intelligence"', *Proceedings in 57th Electronic Components and Technology Conference*, Sparks, Nevada, pp.773-776.
- [2.4] Shah, V., Hayes, D., Wallace, D. (2007) 'Ink-jet as direct-write technology for fuel cell packaging and manufacturing', in *Fuel Cell Electronics Packaging*. : Springer, pp. 205-237.
- [2.5] Cummins, G., Desmulliez, M P.Y. (2012) 'Inkjet printing of conductive materials: a review', in *Circuit World*. : Vol38, pp.193-213.
- [2.6] Perelaer, J., Schubert, U. (2010) 'Inkjet Printing and Alternative Sintering of Narrow Conductive Tracks on Flexible Substrates for Plastic Electronic Applications', in Turcu, C. (ed.) *Radio Frequency Identification Fundamentals and Applications, Design Methods and Solutions*. : InTech, pp. 265-282.
- [2.7] Thompson, J. Funding breakthrough technology - case summary: inkjet printing case report, Available at: <http://www.cbr.cam.ac.uk/pdf/Inkjet%20printing%20case%20report.pdf> (Accessed: 1st September 2013).
- [2.8] Nanyang Technological University, Singapore. Online resource in *Computer Peripherals: Chapter 15. Ink Jet Printing*, Available at: <http://www.lintech.org/comp-per/> (Accessed: 1st September 2013).
- [2.9] Eastman Kodak Company. Meet Stream Inkjet Technology, Available at: http://graphics.kodak.com/KodakGCG/uploadedFiles/kodak_stream_pto_v12.pdf (Accessed: 1st September 2013).
- [2.10] Shar, V., Wallace, D. (2004) 'Low-cost Solar Cell Fabrication by Drop-on-Demand Ink-jet Printing', *Proc. IMAPS 37th Annual International Symposium on Microelectronics*, Long Beach, California, pp. 14-18.
- [2.11] Ho, C., Murata, K., Steingart, D., Evans, J., Wright, P. (2008) 'A super ink jet printed zinc-silver 3d microbattery', *Proceedings of PowerMEMS 2008+microEMS 2008*, Sendai, Japan, pp. 93-96.
- [2.12] Silversheen Inks & Coatings Pvt. Ltd. Introduction to Inkjet Technology, Available at: <http://www.silversheen.com/pdf/Introduction%20to%20Inkjet%20Technology.pdf> (Accessed: 1st September 2013).

- [2.13] Damle, N. (2012) Aerosol Jet Deposition of Samarium-doped Ceria Films. MSc Dissertation, Rochester Institute of Technology.
- [2.14] Paulsen, J., Renn, M. Maskless Printing of Miniature Polymer Thick Film Resistors for Embedded Applications, Available at: http://www.optomec.com/downloads/Optomec_Maskless_Printing_of_Resistors_for_Embedded_Applications.pdf (Accessed: 1st September 2013).
- [2.15] King, B., Renn, M. Aerosol Jet Direct Write Printing for Mil-Aero Electronic Applications, Available at: http://www.optomec.com/downloads/Optomec_Aerosol_Jet_Direct_Write_Printing_for_Mil_Aero_Electronic_Apps.pdf (Accessed: 1st September 2013).
- [2.16] Verheecke, W., Van, D.M.,vogeler, F.,Voet, A.,Valkenaers, H. (2012) 'Optimizing Aerosol Jet Printing of Silver Interconnects on Polyimide film for embedded electronics applications', Proceeding of 8th International DAAAM Baltic Conference "Industrial Engineering", Tallinn, Estonia, pp. 373-379.
- [2.17] Hoey, J., Lutfurakhmanov, A., Schulz, D.,Akhatov, I. (2012) 'A review on Aerosol-based Direct-write and its applications for microelectronics', Journal of Nanotechnology, Vol.2012.
- [2.18] Gong, Y., Tu, R., Goto, T. (2009) 'Microstructure and Preferred Orientation of Titanium Nitride Films Prepared by Laser CVD', Materials Transactions, 50(8), pp.2028-2034.
- [2.19] Remes, J. (2006) 'The development of Laser Chemical Vapor Deposition and Focused Ion Beam Methods for Prototype Integrated Circuit Modification', Oulu University Press.
- [2.20] Creighton, J.R., Ho, P. (2001) 'Chapter 1. Introduction to Chemical Vapor Deposition (CVD)', in Park, J.H., Sudarshan, T.S. (ed.) Chemical Vapor Deposition. : ASM International.
- [2.21] Mitchell, J., Park, S.J., Watson, C.A., Srisungsitthisunti, P., Tansarawiput, C., Qi, M., Stach, E., Yang, C., Xu, X. (2011) 'Laser direct write of silicon nanowires', Optical Engineering, Vol.50(10).
- [2.22] Lee, B. (2012) 'Micro-droplet deposition by UV-Pulsed laser induced forward transfer direct writing technology', Electronic Materials Letters, 8(6), pp.631-637.
- [2.23] Shaw-Stewart, J., Lippert, T., Nagel, M., Nuesch, F., Wokaun, A. (2012) 'Sequential Printing by Laser-induced Forward transfer to fabricate a polymer light-emitting diode pixel', Applied materials & interfaces, 4, pp.3535-3541.
- [2.24] Shaw-Stewart, J., Lippert, T., Nagel, M., Nuesch, F., Wokaun, A. (2011) 'laser-induced forward transfer of polymer light-emitting diode pixels with increased charge injection', Applied materials & interfaces, 3, pp.309-316.
- [2.25] Palla-papavlu, A., Dinca, V., Lippert, T., Dinescu, M. (2011) 'Laser induced forward transfer for materials patterning', Romanian reports in physics, vol. 63, supplement, pp. 1285-1301.
- [2.26] Colina, M., Serra, P., Fernandez-Pradas, J.M., Sevilla, L., Morenza, J.L. (2004) 'DNA deposition through laser induced forward transfer', Biosensors and Bioelectronics, 8(47).
- [2.27] Palla-papavlu, A., Dinca, V., Paraico, I., Moldovan, A., Shaw-Stewart, J., Scheneider, C., Kovacs, E., Lippert, T., Dinescu, M. (2010) 'Microfabrication of polystyrene microbead arrays by laser induced forward transfer', Journal of applied physics, 108(033111).
- [2.28] Kattamis, N., Mcdaniel, N., Bernhard, S., Arnold, C., (2011) 'Ambient laser direct-write printing of a patterned organo-metallic electroluminescent device', Organic Electronics, 12(7), pp.1152-1158.
- [2.29] Wang, Y., Bokor, J., Lee, A. (2004) 'Maskless Lithography Using Drop-On-Demand Inkjet Printing Method', Proc. SPIE 5374, Emerging Lithographic Technologies VIII, 628.
- [2.30] Delaney, J.T., Smith, P.J. and Schubert, U. (2009) 'Inkjet printing of proteins', Soft Matter, 5(24), pp.4866-4877.

- [2.31] Tseng, M.L., Wu, P.C., Sun, S., Chang, C.M., Chen, W.T., Chu, C.H., Chen, P.L., Zhou, L., Huang, D.W., Yen, T.J. and Tsai, D.P. (2012) 'Fabrication of multilayer metamaterials by femtosecond laser-induced forward-transfer technique', *Laser Photonics Rev*, 6(5), pp. 702-707.
- [2.32] Lee, B.G. (2012) 'Micro-Droplet Deposition by UV-Pulsed Laser Induced Forward Transfer Direct Writing Technology', *Electronic Materials Letters*, 8(6), pp.631-637.
- [2.33] Greer, J.A. (2011) 'Design challenges for matrix assisted pulsed laser evaporation and infrared resonant laser evaporation equipment', *Applied Physics A: Materials Science & Processing*, 105(3), pp.661-671.
- [2.34] Arnold, C.B., Serra, P., Pique, A. (2007) 'Laser Direct-Write Techniques for Printing of Complex Materials', *MRS Bulletin*, Vol 32, pp. 23-31.
- [2.35] Pique, A., Weir, D.W., Wu, P.K.,Pratap, B., Arnold, C.B., Ringeisen, B.R., McGill, R.A., Auyeung, R.C.Y., Kant, R.A. and Chrisey, D.B. (2002) 'Direct-Write of Sensor Devices by a Laser Forward Transfer Technique', *Proceedings of SPIE LASE 2002*, San Jose, California, Vol.4637, pp.361-368.
- [2.36] Pique, A., Auyeung, R.C.Y., Stepnowski, J.L., Weir, D.W., Arnold, C.B., McGill, R.A. and Chrisey, D.B. (2003) 'Laser processing of polymer thin films for chemical sensor applications', *Surface and Coatings Technology*, 163-164, pp. 293-299.
- [2.37] Tseng, A.A. (2005) Recent Developments in Nanofabrication Using Focused Ion Beams, *Small*, 1(10), pp. 924-939.
- [2.38] Li, B., Clark, P.A., and Church, K.H. (2007) 'Robust Printing and Dispensing Solutions with Three Sigma Volumetric Control for 21st Century Manufacturing and Packaging', *MRS Proceedings*, Vol.1002.
- [2.39] Li, B., Clark, P.A., Church, K.H. (2007) 'Robust Direct-Write Dispensing Tool and Solutions for Micro/Meso-scale Manufacturing and Packaging', *Proceedings of the 2007 International Manufacturing Science And Engineering Conference (MSEC2007)*, Atlanta, Georgia, USA.
- [2.40] Li, B., Roy, T.D., Smith, C.M., Clark, P.A., Church, K.H. (2007) 'A robust true direct-print technology for tissue engineering', *Proceedings of the 2007 International Manufacturing Science And Engineering Conference (MSEC2007)*, Atlanta, Georgia, USA.
- [2.41] Ginger, D.S., Zhang, H. and Mirkin, C.A. (2003) 'The evolution of Dip-Pen Nanolithography', *Angewandte Chemie International Edition*, 43(1), pp. 30-45.
- [2.42] Rozhok, S., Piner, R., and Mirkin, C.A. (2003) 'Dip-Pen Nanolithography: What Controls Ink Transport?', *The Journal of Physical Chemistry B*, 107, pp. 751-757.
- [2.43] Haaheim, J., Eby, R., Nelson, M., Fragala, J., Rosner, B., Zhang, H., and Athas, G. (2005) 'Dip Pen Nanolithography (DPN): process and instrument performance with NanoInk's Nscriptor system', *Ultramicroscopy*, Vol.103, pp. 117-132.
- [2.44] Saha, S., Culpepper, M., (2011) 'Characterization of the Dip Pen Nanolithography Process for Nanomanufacturing', *Journal of Manufacturing Science and Engineering*, 133(4).
- [2.45] Haaheim, J., Nafday, O. (2008) 'Dip Pen Nanolithography: A "Desktop Nanofab" Approach Using High-Throughput Flexible Nanopatterning', *Scanning*, Vol.30, pp.137-150.
- [2.46] Espinosa, H. (2011) 'NANO HIGHLIGHT: Nanofountain Probe for Large-scale Nanomanufacturing', *NSF Nanoscale Science and Engineering Grantees Conference*, Arlington, Virginia.
- [2.47] Kim, K.H., Moldovan, N., Ke, C., and Espinosa, D. (2004) 'A novel AFM chip for Fountain Pen Nanolithography - Design and Microfabrication', *Materials Research Society Symposium Proceedings*, 2003 Fall MRS Meeting, Vol.782.
- [2.48] Loh, O.Y., and Espinosa, H.D. (2010) 'Nanofountain Probes for Direct-Write Nanomanufacturing and In Vitro Single Cell Studies', *Proceedings of 3rd International Nanoelectronics Conference (INEC)*, Hong Kong, pp. 423-424.
- [2.49] Belmont, A.S., Sokuler, M., Haupt, K., Gheber, L.A. (2007) 'Direct writing of molecularly imprinted microstructures using a nanofountain pen', *Applied physics letters*, Vol.90.

- [2.50] Kang, W., McNaughton, R.L., Yavari, F., Minary-Jolandan, M., Safi, A., and Espinosa, H.D. (2013) 'Microfluidic Parallel Patterning and Cellular Delivery of Molecules with a Nanofountain Probe', *Journal of Laboratory Automation*.
- [2.51] Shang, S., Fearon, E., Wellburn, D., Sato, T., Edwardson, S., Dearden, G., & Watkins, K.G. (2011) 'A predictive thermal dynamic model for parameter generation in laser assisted direct write process', *Journal of Physics D: Applied Physics*, Vol.44.
- [2.52] Sato, T. (2011) *Laser assisted ink consolidation for direct write component fabrication*, Ph.D Thesis. University of Liverpool.
- [2.53] Kamyshny, A., Steinke, J., Magdassi, S. (2011) 'Metal-based inkjet inks for printed electronics', *The open applied physics journal*, Vol.4, pp. 19-36.
- [2.54] Dengler, S., Kubel, C., Schwenke, A., Ritt, G., and Eberle, B. (2012) 'Near-and off-resonant optical limiting properties of gold-silver alloy nanoparticles for intense nanosecond laser pulses', *Journal of Optics*, vol.14.
- [2.55] Shimadzu Corporation. Investigation of UV-irradiated Film Deterioration - Color Measurement and Haze Measurement, Available at: <http://www2.shimadzu.com/applications/UV/VIS/A435.pdf> (Accessed: 15th October 2012).
- [2.56] Zeus Inc. UV properties of plastics: Transmission & Resistance, Available at: http://www.zeusinc.com/UserFiles/zeusinc/Documents/Zeus_UV_Properties.pdf (Accessed: 1st September 2013).
- [2.57] Lee, S. (2002) 'CO₂ processing at 9 microns', *Industrial Laser solutions for manufacturing*, March.
- [2.58] Treffert Coatings GmbH. The role and use of pigments, NIR absorbers and additives, Available at: http://www.polybright.eu/file_153905.dat (Accessed: 1st September 2013).
- [2.59] A. Lopes, M. Navarrete, F. Medina, J.A. Palmer, E. MacDonald, and R.B. Wicker, "Expanding Rapid Prototyping for Electronic Systems Integration of Arbitrary Form," 17th Annual Solid Freeform Fabrication Symposium, University of Texas at Austin, August 14-16, 2006.
- [2.60] Perelaer, J, Schubert, U, Smith, P, Mager, D, Korvink, J, Soltman, D, Volkman, S, & Subramanian, V 2010, 'Printed electronics: The challenges involved in printing devices, interconnects, and contacts based on inorganic materials', *Journal Of Materials Chemistry*, 20, 39, p. 8446-8453.
- [2.61] Horvath, E, Henap, G, & Harsanyi, G 2012, 'MATERIALS AND TECHNOLOGICAL DEVELOPEMENT OF SCREEN PRINTING IN TRANSPORTATION', *International Journal For Traffic & Transport Engineering*, 2, 2, p. 133, Publisher Provided Full Text Searching File, EBSCOhost, viewed 2 January 2014.
- [2.62] Executive Data Control (2013) A Brief History Of Screen Printing, Available at: <http://www.edcmktg.com/history-of-screen-printing> (Accessed: 2nd January 2014).
- [2.63] Yasushi Sano. "Why Screen Printing?" *Converttech & e-Print* July/August 2012.
- [2.64] Marc Burgelman (1998). Thin film solar cells by screen printing technology. In: *Proceeding of the workshop microtechnology and thermal problems in electronics*, September 21-27 1998, Zakopane. pp. 129-135.
- [2.65] Yin, W, Lee, D, Choi, J, Cho, S, & Park, C 2008, 'Screen printing of silver nanoparticle suspension for metal interconnects', *Korean Journal Of Chemical Engineering*, 25, 6, p. 1358-1361, Scopus®, EBSCOhost, viewed 2 January 2014.
- [2.66] ASADA Mesh Co., Ltd. Development of Stainless Steel Wire Mesh and Improvement of Screen printing Technology, Available at: http://www.asada-mesh.co.jp/data_upload/1334013925.pdf (Accessed: 2nd January 2014).
- [2.67] Applied Materials Italia Srl (2013) *Screen Printing For Crystalline Silicon Solar Cells*, Available at: http://www.appliedmaterials.com/sites/default/files/Screen_Printing_Backgrounder_0.pdf (Accessed: 2nd January 2014).

- [2.68] Roberson, D, Wicker, R, Murr, L, Church, K, & MacDonald, E 2011, 'Microstructural and Process Characterization of Conductive Traces Printed from Ag Particulate Inks', *Materials* (1996-1944), 4, 6, pp. 963-979, Academic Search Complete, EBSCOhost, viewed 4 January 2014.
- [2.69] S. Kirkpatrick, "Percolation and conduction", *Reviews of Modern Physics*, vol. 45, no. 4, pp. 574-588, January 1973, doi:10.1103/RevModPhys.45.574.
- [2.70] Jeffrey E. Steif. A mini course on percolation theory, Available at: <http://www.math.chalmers.se/~steif/perc.pdf> (Accessed: 4th January 2014).
- [2.71] Saraf, R, Roldan, J, Jagannathan, R, Sambucetti, C, Marino, J, & Jahnes, C 1995, 'Polymer/metal composite for interconnection technology', *Proceedings - Electronic Components And Technology Conference*, p. 1051-1053, Scopus®, EBSCOhost, viewed 4 January 2014.
- [2.72] Banfield, J., "Understanding and Measuring Electrical Resistivity in Conductive Inks and Adhesives", *SGIA Journal*, 6, 29-36 (2000).
- [2.73] Ye, L, Thölen, A, Lai, Z, & Liu, J 1999, 'Effect of Ag particle size on electrical conductivity of isotropically conductive adhesives', *IEEE Transactions On Electronics Packaging Manufacturing*, 22, 4, p. 251, Scopus®, EBSCOhost, viewed 5 January 2014.
- [2.74] J. Nicolics, M. Mündlein. "Electrically Conductive Adhesives" in "Micro- and Opto-Electronic Materials and Structures: Physics, Mechanics, Design, Reliability, Packaging, Volume 2", Springer-Verlag, 2007, 571 - 610.
- [2.75] Christopher Wargo. Characterization of Conductors for Printed Electronics, Available at: <http://www.nanopchem.com/pdf/understanding.pdf> (Accessed: 4th January 2014).
- [2.76] Faddoul, R, Reverdy-Bruas, N, & Bourel, J 2012, 'Silver content effect on rheological and electrical properties of silver pastes', *Journal Of Materials Science: Materials In Electronics*, 23, 7, p. 1415-1426, Scopus®, EBSCOhost, viewed 6 January 2014.
- [2.77] Roberson, D, Wicker, R, & MacDonald, E 2012, 'Ohmic curing of printed silver conductive traces', *Journal Of Electronic Materials*, 41, 9, p. 2553-2566, Scopus®, EBSCOhost, viewed 6 January 2014.
- [2.78] Conductive Low-Cost Ink Project (CLIP). CLIP newsletter: Why do we need low-cost conductive inks?, Available at: <http://www.clip-fp7.eu/images/CLIP%20newsletter%20Jan%202013.pdf> (Accessed: 4th January 2014).
- [2.79] Scott E. Gordon, Jay R. Dorfman, Daniel Kirk, Kerry Adams. *Advances in Conductive Inks across Multiple Applications and Deposition Platforms*, Available at: <http://www.smtnet.com/library/files/upload/Conductive-Inks-Advances.pdf> (Accessed: 4th January 2014).
- [2.80] Sigma-Aldrich Corporation. Available at: <http://www.sigmaaldrich.com> (Accessed: 4th January 2014).
- [2.81] David Pile (2011) 'Organic electronics: Laser-induced electrode fabrication', *Nature Photonics*, 5, pp. 199.
- [2.82] Wang, J, Duan, H, Huang, Z, & Karihaloo, B 2006, 'A scaling law for properties of nano-structured materials', *Proceedings Of The Royal Society A: Mathematical, Physical And Engineering Sciences*, 462, 2069, p. 1355-1363, Scopus®, EBSCOhost, viewed 6 January 2014.
- [2.83] Buffat, P, & Borel, J 1976, 'Size effect on the melting temperature of gold particles', *Physical Review A*, 13, 6, p. 2287-2298, Scopus®, EBSCOhost, viewed 6 January 2014.
- [2.84] Bieri, N, Poulidakos, D, Chung, J, & Grigoropoulos, C 2005, 'An experimental investigation of microresistor laser printing with gold nanoparticle-laden inks', *Applied Physics A: Materials Science And Processing*, 80, 7, p. 1485-1495, Scopus®, EBSCOhost, viewed 6 January 2014.
- [2.85] Jolke Perelaer and Ulrich S. Schubert (2010). *Inkjet Printing and Alternative Sintering of Narrow Conductive Tracks on Flexible Substrates for Plastic Electronic Applications, Radio Frequency Identification Fundamentals and Applications Design Methods and Solutions*, Cristina Turcu (Ed.), ISBN: 978-953-7619-72-5, InTech, DOI: 10.5772/7983. Available from: <http://www.intechopen.com/books/radio-frequency-identification-fundamentals-and-applications-design-methods-and-solutions/inkjet-printing-and-alternative-sintering-of-narrow-conductive-tracks-on-flexible-substrates-for-pla>

- [2.86] Qi, S, Vaidhyanathan, B, & Hutt, D 2013, 'Conventional and microwave-assisted processing of Cu-loaded ICAs for electronic interconnect applications', *Journal Of Materials Science*, 48, 20, p. 7204-7214, Scopus®, EBSCOhost, viewed 7 January 2014.
- [2.87] Pique, A. and Chrisey, D.B. (2002) *Direct-Write Technologies for Rapid Prototyping Applications: Sensors, Electronics, and Integrated Power Sources*, San Diego: Academic Press.
- [2.88] Eiroma, K., Hakola, L., Hast, J., Maaninen, A. and Petaja, J. 2007. *UV Curing for Printed Electronics*. Radtech Report, pp. 31-34.
- [2.89] Eerik, H, Esa, H, & Matti, M 2013, 'The Effect of Laser Sintering Process Parameters on Cu Nanoparticle Ink in Room Conditions', *Optics And Photonics Journal*, 04, p. 40, Directory of Open Access Journals, EBSCOhost, viewed 7 January 2014.
- [2.90] Wolf, F, Perelaer, J, Stumpf, S, Schubert, U, Bollen, D, & Kriebel, F 2013, 'Rapid low-pressure plasma sintering of inkjet-printed silver nanoparticles for RFID antennas', *Journal Of Materials Research*, 28, 9, p. 1254-1261, Scopus®, EBSCOhost, viewed 7 January 2014
- [2.91] Perelaer, J, Hendriks, C, Schubert, U, & De Laat, A 2008, 'Inkjet-printed silver tracks: Low temperature curing and thermal stability investigation', *Journal Of Materials Chemistry*, 18, 27, p. 3209-3215, Scopus®, EBSCOhost, viewed 7 January 2014.
- [2.92] Wu, S, Xu, L, Yung, K, & Ding, X 2008, 'Fabrication of polymer silver conductor using inkjet printing and low temperature sintering process', *IEEE Transactions On Electronics Packaging Manufacturing*, 31, 4, p. 291-296, Scopus®, EBSCOhost, viewed 7 January 2014.
- [2.93] Greer, J, & Street, R 2007, 'Thermal cure effects on electrical performance of nanoparticle silver inks', *Acta Materialia*, 55, 18, p. 6345-6349, Scopus®, EBSCOhost, viewed 7 January 2014.
- [2.94] Kim, M, Hwang, J, Kang, H, Kang, K, Lee, S, & Moon, S 2009, 'Laser sintering of the printed silver ink', 2009 IEEE International Symposium On Assembly And Manufacturing, ISAM 2009, 2009 IEEE International Symposium on Assembly and Manufacturing, ISAM 2009, p. 155-158, Scopus®, EBSCOhost, viewed 8 January 2014.
- [2.95] Kim, T, Hwang, J, & Moon, S 2010, 'Laser curing of the silver/copper nanoparticle ink via optical property measurement and calculation', *Japanese Journal Of Applied Physics*, 49, 5 PART 2, p. 05EA091-05EA096, Scopus®, EBSCOhost, viewed 8 January 2014.
- [2.96] Lee, D, Kim, D, Moon, Y, & Moon, S 2013, 'Effect of laser-induced temperature field on the characteristics of laser-sintered silver nanoparticle ink', *Nanotechnology*, 24, 26, Scopus®, EBSCOhost, viewed 8 January 2014.
- [2.97] Maekawa, K, Yamasaki, K, Niizeki, T, Mita, M, Matsuba, Y, Terada, N, & Saito, H 2012, 'Drop-on-Demand Laser Sintering With Silver Nanoparticles for Electronics Packaging', *IEEE Transactions On Components, Packaging & Manufacturing Technology*, 2, 5, pp. 868-877, Business Source Complete, EBSCOhost, viewed 8 January 2014.
- [2.98] Eerik, H, Esa, H, & Matti, M 2013, 'The Effect of Laser Sintering Process Parameters on Cu Nanoparticle Ink in Room Conditions', *Optics And Photonics Journal*, 04, p. 40, Directory of Open Access Journals, EBSCOhost, viewed 8 January 2014.
- [2.99] Ko, S, Pan, H, Grigoropoulos, C, Luscombe, C, Fr chet, J, & Poulidakos, D 2007, 'Air stable high resolution organic transistors by selective laser sintering of ink-jet printed metal nanoparticles', *Applied Physics Letters*, 90, 14, Scopus®, EBSCOhost, viewed 8 January 2014.
- [2.100] Chung, J, Bieri, N, Ko, S, Grigoropoulos, C, & Poulidakos, D 2004, 'In-tandem deposition and sintering of printed gold nanoparticle inks induced by continuous Gaussian laser irradiation', *Applied Physics A: Materials Science & Processing*, 79, 4-6, pp. 1259-1261, Academic Search Complete, EBSCOhost, viewed 8 January 2014.
- [2.101] Ko, S, Pan, H, Grigoropoulos, C, Chung, J, & Poulidakos, D 2007, 'Fabrication of multilayer passive and active electric components on polymer using inkjet printing and low temperature laser processing', *Sensors And Actuators, A: Physical*, 134, 1, p. 161-168, Scopus®, EBSCOhost, viewed 8 January 2014.
- [2.102] Ferro 3309F Silver Conductor; Technical Data Sheet. Ferro Corporation: Cleveland, OH, USA, 2001.

- [2.103] DuPont CB028 Silver Conductor; Technical Data Sheet. DuPont: Wilmington, DE, USA, 2009.
- [2.104] Josh. (2010) Flexible Organic ElectroLuminescent Display: Fabrication of a 32x32 Passive-Matrix Display. Carleton University.
- [3.1] Goodfellow Corporation. Polymer properties, Available at: <http://www.goodfellow.com> (Accessed: 1st September 2013).
- [3.2] Coonrod, J. Understanding PCBs for HIGH-FREQUENCY Applications, Available at: <http://www.rogerscorp.com/documents/2236/acm/articles/Understanding-PCBs-for-High-Frequency-Applications.pdf> (Accessed: 3rd September 2013)
- [3.3] FEI Company. FEI Sells Phenom(TM) Product Line, Available at: <http://investor.fei.com/releasedetail.cfm?ReleaseID=421591> (Accessed: 1st September 2013).
- [3.4] Thermo Nicolet Corporation. Introduction to Fourier Transform Infrared Spectrometry, Available at: <http://mmrc.caltech.edu/FTIR/FTIRintro.pdf> (Accessed: 4th September 2013).
- [3.5] Keithley Instruments. Instrumentation and Techniques for Measuring High Resistivity and Hall Voltage of Semiconducting Materials, Available at: <http://www.keithley.co.uk/data?asset=50094> (Accessed: 28th September 2013).
- [3.6] Center of Micronanotechnology, EPFL. Manuel pour optical profiler Veeco WYKO NT1100, Available at: http://cmi.epfl.ch/metrology/Wyko_NT1100.php (Accessed: 20th September 2013).
- [3.7] Microworld, Four Point Probe Resistivity. Available at: <http://www.four-point-probe.eu/> (Accessed: 14th April 2014).
- [3.8] Four Point Probes, Finite-Size Corrections for 4-Point Probe Measurements. Available at: <http://four-point-probes.com/4-point.pdf> (Accessed: 23rd January 2014).
- [3.9] IFA, Polyethylene terephthalate. Available at: [http://gestis-en.itrust.de/nxt/gateway.dll/gestis_en/530566.xml?f=templates\\$fn=default.htm\\$3.0](http://gestis-en.itrust.de/nxt/gateway.dll/gestis_en/530566.xml?f=templates$fn=default.htm$3.0) (Accessed: 14th April 2014).
- [3.10] Veeco, Basics of Interferometry. Available at: http://cmi.epfl.ch/metrology/files/Wyko/Interferometry_Basics.pdf (Accessed: 14th April 2014).
- [3.11] Elcometer, Elcometer 501 Pencil Hardness Tester Operating Instructions.
- [3.12] FLIR, The ultimate infrared handbook for R&D professionals: A resource guide for using infrared in the Research and Development Industry. Available at: http://www.flir.com/uploadedFiles/Thermography/MMC/Brochures/T559243/T559243_APAC.pdf (Accessed: 14th April, 2014).
- [3.13] Radiological & Environmental Management, Purdue University, Scanning Electron Microscope. Available at: <http://www.purdue.edu/rem/rs/sem.htm> (Accessed: 14th April 2014).
- [3.14] Oxford instruments, Silicon Drift Detectors Explained. Available at: http://www.oxford-instruments.com/OxfordInstruments/media/nanoanalysis/brochures%20and%20thumbs/OI_AppNote_SDD_Explained.pdf?returnurl=%2fproducts%2fmicroanalysis%2fenergy-dispersive-x-ray-systems-eds-edx%2feds-for-sem%2fsdd&overlay=true (Accessed: 14th April 2014).
- [3.15] PerkinElmer, Technical note: FT-IR Spectroscopy - Attenuated Total Reflectance (ATR). Available at: http://www.utoronto.ca/~traceslab/ATR_FTIR.pdf (Accessed: 14th April 2014).
- [4.1] Shang, S. (2012) A Predictive Thermal Dynamic Model for Parameter Generation in the Laser Assisted Direct Write Process, PhD Thesis. University of Liverpool.
- [4.2] Enthone, ENTHONE 60 data sheet. Available at: <http://allenwoodsgroup.com/pdf/60SERIES.pdf> (Accessed: 14th April 2014).
- [4.3] Baxenden, Trixene BI 7963 data sheet.

- [4.4] Merad, L, Cochez, M, Margueron, S, Ferriol, M, Bourson, P, Jauchem, F, & Benyoucef, B 2009, 'In-situ monitoring of the curing of epoxy resins by Raman spectroscopy', *Polymer Testing*, 28, 1, p. 42-45, Scopus®, EBSCOhost, viewed 24 April 2014.
- [5.1] Cameo Chemicals, NOAA. Diethylene Glycol Monobutyl Ether, Available at: <http://cameochemicals.noaa.gov/chris/DME.pdf> (Accessed: 30th August 2013).
- [5.2] Hexcel Corporation. HexFlow®VRM37 Datasheet, Available at: http://www.hexcel.com/Resources/DataSheets/RTM-Data-Sheets/VRM37_eu.pdf (Accessed: 27th August 2013).
- [5.3] (2002) 'News: Light-absorbing nanoparticle labels', *ANALYTICAL CHEMISTRY*, pp. 564A. Available at: <http://cdn-pubs.acs.org/doi/pdfplus/10.1021/ac022145p> (Accessed: 14th April 2014).
- [5.4] Boyer, D, Tamarat, P, Maali, A, Lounis, B, & Orrit, M 2002, 'Photothermal imaging of nanometer-sized metal particles among scatterers', *Science*, 297, 5584, p. 1160-1163.
- [5.5] Scriven, L. E. & Sternling, C.V., 1960, 'The Marangoni Effects', *Nature*, 187, p. 186-188.
- [5.6] MIT, Lecture 4: Marangoni flows. Available at: <http://web.mit.edu/1.63/www/LectureNotes/Surfacetension/Lecture4.pdf> (Accessed: 14th April, 2014).
- [5.7] Lautrup, B (2009) 'Chapter 5: Surface Tension', in Lautrup, B (ed.) *Physics of Continuous Matter*. : CRC Press, pp. 69-94.
- [5.8] Trefethen, L, 'Surface Tension in Fluid Mechanics'. Available at: <http://web.mit.edu/hml/ncfmf/04STFM.pdf> (Accessed: 14th April, 2014).
- [5.9] Calvert, J.B., 'Surface Tension'. Available at: <http://mysite.du.edu/~jcalvert/phys/surftens.htm> (Accessed: 14th April, 2014).
- [5.10] Chung, J, Ko, S, Bieri, N, Grigoropoulos, C, & Poulikakos, 'Microconductors by combining laser curing and printing of gold nanoparticle inks'. Available at: <http://www.me.berkeley.edu/ltl/pdf/%5BEtc%2003%20Seicence%5D%20MICROCONDUCTORS%20BY%20COMBINING%20LASER%20CURING.pdf> (Accessed: 14th April, 2014).
- [5.11] Layertec, 'Reflectivity of different metals'. Available at: <http://www.layertec.de/en/capabilities/coatings/metallic> (Accessed: 14th April 2014).
- [5.12] Baxenden Chemicals Ltd, 'Urethane Surface Coatings - Blocked Isocyanates'. Available at: http://www.baxchem.co.uk/files/documents/Baxenden_BlockedISO.pdf.pdf (Accessed: 14th April 2014).
- [6.1] University of California, Berkeley. Introduction to Finite Element Modelling, Available at: <http://www.me.berkeley.edu/~lwlin/me128/FEMNotes.pdf> (Accessed: 15th October 2012).
- [6.2] COMSOL AB. COMSOL product Suite, Available at: <http://comsol.com/products> (Accessed: 4th September 2013).
- [6.3] Cheng, J. (2010) Ultrafast picosecond laser micromachining of metallic materials, Ph.D Thesis, University of Liverpool.
- [6.4] HyperPhysics, Georgia State University, The Wiedemann-Franz Law. Available at: <http://hyperphysics.phy-astr.gsu.edu/hbase/thermo/thercond.html> (Accessed: 14th April 2014).
- [6.5] National Bureau of Standards, Thermal Conductivity of Selected Materials. Available at: <http://www.nist.gov/data/nsrds/NSRDS-NBS-8.pdf> (Accessed: 14th April 2014).

Appendix 1.

Procedures of calibrating the emissivity of an IR camera (Selected from the instructional manual for FLIR SC 660 Thermal Camera)

32 Thermographic measurement techniques

32

32.1 Introduction

An infrared camera measures and images the emitted infrared radiation from an object. The fact that radiation is a function of object surface temperature makes it possible for the camera to calculate and display this temperature.

However, the radiation measured by the camera does not only depend on the temperature of the object but is also a function of the emissivity. Radiation also originates from the surroundings and is reflected in the object. The radiation from the object and the reflected radiation will also be influenced by the absorption of the atmosphere.

To measure temperature accurately, it is therefore necessary to compensate for the effects of a number of different radiation sources. This is done on-line automatically by the camera. The following object parameters must, however, be supplied for the camera:

- The emissivity of the object
- The reflected apparent temperature
- The distance between the object and the camera
- The relative humidity
- Temperature of the atmosphere

32.2 Emissivity

The most important object parameter to set correctly is the emissivity which, in short, is a measure of how much radiation is emitted from the object, compared to that from a perfect blackbody of the same temperature.

Normally, object materials and surface treatments exhibit emissivity ranging from approximately 0.1 to 0.95. A highly polished (mirror) surface falls below 0.1, while an oxidized or painted surface has a higher emissivity. Oil-based paint, regardless of color in the visible spectrum, has an emissivity over 0.9 in the infrared. Human skin exhibits an emissivity 0.97 to 0.98.

Non-oxidized metals represent an extreme case of perfect opacity and high reflexivity, which does not vary greatly with wavelength. Consequently, the emissivity of metals is low – only increasing with temperature. For non-metals, emissivity tends to be high, and decreases with temperature.

32.2.1 Finding the emissivity of a sample**32.2.1.1 Step 1: Determining reflected apparent temperature****32**

Use one of the following two methods to determine reflected apparent temperature:

32.2.1.1.1 Method 1: Direct method

- 1** Look for possible reflection sources, considering that the incident angle = reflection angle ($a = b$).

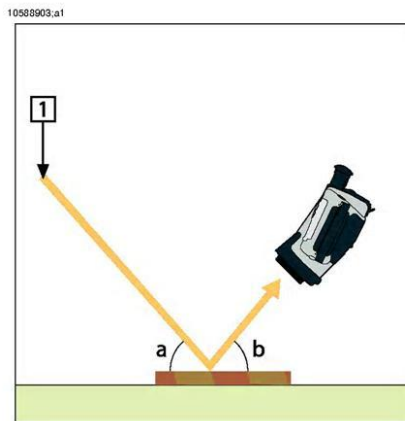


Figure 32.1 1 = Reflection source

- 2** If the reflection source is a spot source, modify the source by obstructing it using a piece of cardboard.

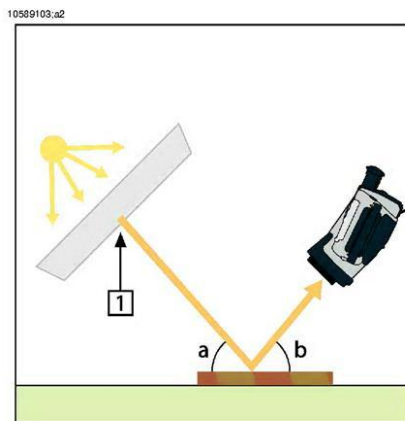


Figure 32.2 1 = Reflection source

3 Measure the radiation intensity (= apparent temperature) from the reflecting source using the following settings:

- Emissivity: 1.0
- D_{obj} : 0

You can measure the radiation intensity using one of the following two methods:

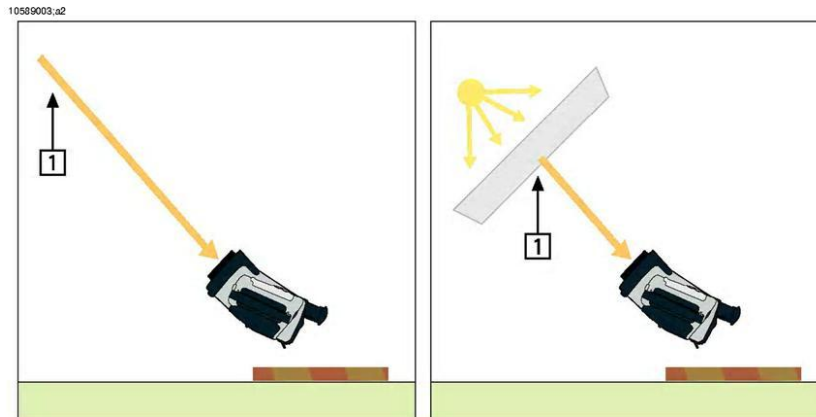


Figure 32.3 1 = Reflection source

Note: Using a thermocouple to measure reflected apparent temperature is not recommended for two important reasons:

- A thermocouple does not measure radiation intensity
- A thermocouple requires a very good thermal contact to the surface, usually by gluing and covering the sensor by a thermal isolator.

32.2.1.1.2 Method 2: Reflector method

1	Crumble up a large piece of aluminum foil.
2	Uncrumble the aluminum foil and attach it to a piece of cardboard of the same size.
3	Put the piece of cardboard in front of the object you want to measure. Make sure that the side with aluminum foil points to the camera.
4	Set the emissivity to 1.0.

32

32 – Thermographic measurement techniques

5 Measure the apparent temperature of the aluminum foil and write it down.

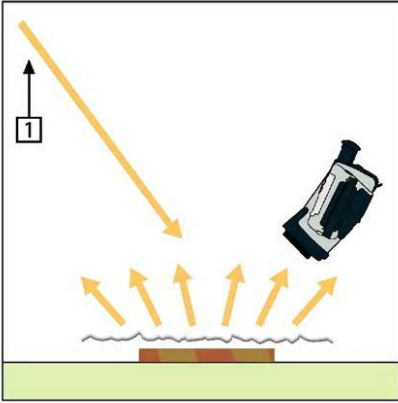


Figure 32.4 Measuring the apparent temperature of the aluminum foil

32.2.1.2 Step 2: Determining the emissivity

1	Select a place to put the sample.
2	Determine and set reflected apparent temperature according to the previous procedure.
3	Put a piece of electrical tape with known high emissivity on the sample.
4	Heat the sample at least 20 K above room temperature. Heating must be reasonably even.
5	Focus and auto-adjust the camera, and freeze the image.
6	Adjust Level and Span for best image brightness and contrast.
7	Set emissivity to that of the tape (usually 0.97).
8	Measure the temperature of the tape using one of the following measurement functions: <ul style="list-style-type: none"> ■ Isotherm (helps you to determine both the temperature and how evenly you have heated the sample) ■ Spot (simpler) ■ Box Avg (good for surfaces with varying emissivity).
9	Write down the temperature.
10	Move your measurement function to the sample surface.
11	Change the emissivity setting until you read the same temperature as your previous measurement.
12	Write down the emissivity.

Note:

- Avoid forced convection
- Look for a thermally stable surrounding that will not generate spot reflections
- Use high quality tape that you know is not transparent, and has a high emissivity you are certain of
- This method assumes that the temperature of your tape and the sample surface are the same. If they are not, your emissivity measurement will be wrong.

32.3 *Reflected apparent temperature*

This parameter is used to compensate for the radiation reflected in the object. If the emissivity is low and the object temperature relatively far from that of the reflected it will be important to set and compensate for the reflected apparent temperature correctly.

32.4 *Distance*

The distance is the distance between the object and the front lens of the camera. This parameter is used to compensate for the following two facts:

- That radiation from the target is absorbed by the atmosphere between the object and the camera.
- That radiation from the atmosphere itself is detected by the camera.

32.5 *Relative humidity*

The camera can also compensate for the fact that the transmittance is also dependent on the relative humidity of the atmosphere. To do this set the relative humidity to the correct value. For short distances and normal humidity the relative humidity can normally be left at a default value of 50%.

32.6 *Other parameters*

In addition, some cameras and analysis programs from FLIR Systems allow you to compensate for the following parameters:

- Atmospheric temperature – *i.e.* the temperature of the atmosphere between the camera and the target
- External optics temperature – *i.e.* the temperature of any external lenses or windows used in front of the camera
- External optics transmittance – *i.e.* the transmission of any external lenses or windows used in front of the camera

Appendix 2.

Approximated calculation of proportional mass percent of carbon and oxygen elements in D58 silver ink

D58 silver ink is an epoxy-based silver conductive ink manufactured by Gwent Electronic Materials, Ltd. (GEM). As shown in **Tables 1** and **2**, D58 silver ink contains silver flakes (59% by weight), resin complex containing epikote resin and blocked isocyanate (26% by weight), and organic solvent (15% by weight). Therefore the proportional mass percent of carbon and oxygen elements in D58 silver ink can be approximated by the calculation of the proportional mass percent of carbon and oxygen elements in resin complex and solvent of the D58 silver ink.

Table 1. Approximated ink composition of D58 silver ink (source: GEM).

	Mass percent (wt%)
Silver flake	59
Resin complex	26
Solvent	15

Table 2. Approximated resin complex composition of D58 silver ink (source: GEM).

	Mass percent (wt%)
Epikote	12
Blocked Isocyanates	14

As the chemical molecular formulas for resin complex and solvent are known, therefore the mass percent of elements in resin complex and solvent can be demonstrated in **Table 3**.

Table 3. Elements in Resin complex and Solvent in D58 silver ink (Source: GEM).

Material	Symbol	Number of Atoms	Atomic Mass	Mass Percent (wt%)
Epikote	C	18	12.01078	67.38
	O	3	15.99943	14.96
	H	21	1.007947	6.6
	Cl	1	35.4532	11.05
Blocked Isocyanate	C	45	12.01078	55.21
	O	18	15.99943	29.42
	H	66	1.007947	6.79
	N	6	14.0067	8.58
Solvent	C	8	12.01078	59.23
	O	3	15.99943	29.59
	H	18	1.007947	11.18

Therefore, as shown in **Tables 1-3**, the total proportional mass percent of carbon and oxygen elements in Resin complex and Solvent of the silver ink can be calculated as (1) and

(2). As Energy Dispersive X-ray Spectroscopy (EDX) results show only proportional percent for each element in measured sample, therefore In order to make a direct comparison to EDX results, the correction factor (3) and normalized proportional mass percent of ink components in uncured D58 silver ink corrected base on the correction factor are required, the normalized proportional mass percent of uncured D58 ink is shown in **Table 4**.

Carbon (wt%)

= *Carbon absolute mass percent in ink component*

* *Mass percent of ink component in D58 silver ink*

(1)

Oxygen (wt%)

= *Oxygen absolute mass percent in ink component*

* *Mass percent of ink component in D58 silver ink*

(2)

Correction Factor (CF)

$$= \frac{100}{(\text{Absolute mass percent of Ag in ink} + \text{Absolute mass percentage of C + O in ink})}$$

(3)

Table 4. The normalized proportional mass percent of uncured D58 epoxy-based silver ink.

	Absolute Mass Percent of Silver in Ink	Absolute Mass Percent of Carbon and Oxygen in Ink	Correction Factor (CF)	Normalized Proportional Mass Percent of Silver in Ink	Normalized Proportional Mass Percent of Carbon and Oxygen in Ink
Uncured D58 ink	59.00	35.05	1.063264	62.73	37.27

The ideal case for curing D58 silver ink, is to perfectly remove all the containing solvent, therefore the absolute mass percent of carbon and oxygen in ink is the mass percent of carbon and oxygen of resin complex only, the value of correction factor and the normalized proportional mass percent of ink component in this perfectly solvent removed D58 ink are shown in **Table 5**.

Table 5. The normalized proportional mass percent of ideally cured D58 epoxy-based silver ink.

	Absolute Mass Percent of Silver in Ink	Absolute Mass Percent of Carbon and Oxygen in Ink	Correction Factor (CF)	Normalized Proportional Mass Percent of Silver in Ink	Normalized Proportional Mass Percent of Carbon and Oxygen in Ink
Ideal cured D58 ink (no solvent)	59.00	23.10	1.218027	71.86	28.14

Appendix 3.

Thermal Conductivity of Silver (Source: National Bureau of Standards)

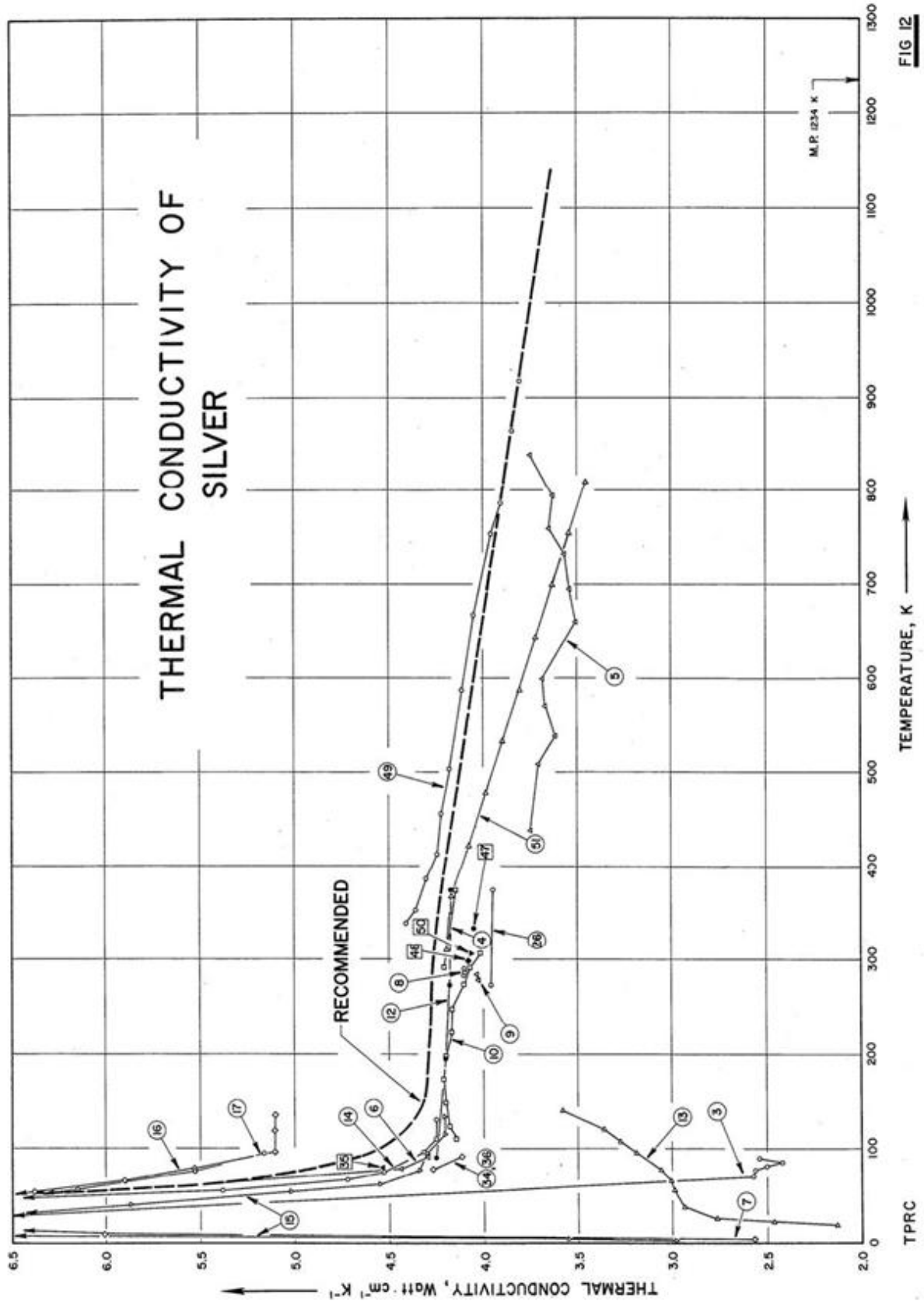


FIG 12